STUDY OF SOME BIO-MATERIALS SYSTEMS: CRYSTALLINE AND NANO-PARTICLE PROPERTIES

Thesis submitted to the

SAURASHTRA UNIVERSITY

For

The award of the degree of

DOCTOR OF PHILOSOPHY

in

PHYSICS

by

POORVESH MADHUKANT VYAS

(M. Sc.)

Guided by

Dr. M. J. Joshi

Professor & Head
Department of Physics, Saurashtra University,
Rajkot – 360 005

JULY 2012

Statements Under O.Ph.D.7 of Saurashtra University

The contents of this thesis is my own work carried out under the supervision of ***Dr. M. J. Joshi*** and leads to some contributions in Physics supported by necessary references.

(Poorvesh M. Vyas)

This is to certify that the present work submitted for Ph. D. Degree of the Saurashtra University, Rajkot, by ***Shri Poorvesh M. Vyas*** has been the result of about five years of work under my supervision and is a valuable contribution in the field of “Solid State Physics and Materials Science”.

(Dr. M. J. Joshi)
Professor
Department of Physics
Saurashtra University
Rajkot, 360 005

तमित्सुहव्यमङ्गिरः सुदेवं सहसो यहो ।

जना आहुः सुबर्हिषम् ॥ ५ ॥

ऋ मंडण–१, सूक्त–७४, मंत्र–५

Dear like life, son of a noble mighty person, let us serve you who are shining like fire and whom men call full of divine attributes and liberal donor, endowed with good knowledge and full of most acceptable virtues.

Purport Men should acquire scientific knowledge from a wellknown person among the learned, should learn its application and teach it to others.

Dedicated to

God like Figures

My Parents

And

My Teachers

ACKNOWLEDGEMENT

First and foremost the author is heartily thankful to the **Almighty God** for the abundant blessings. The author expresses his deep sense of gratitude and sincere thanks to his enthusiastic guide **Dr. Mihir J. Joshi,** Professor & Head, Department of Physics, Saurashtra University, Rajkot, who introduced him to the field of *"Crystal Growth & Nano Technology",* particularly, in the multidisciplinary research work on bio - material as well as Active Pharmaceutical Ingredients (API) crystals and nano particles, which requires integrating data, theories, methodologies, perspectives and concepts from multiple disciplines like physics, chemistry, material science, life sciences, *Ayurveda*, pharmacology and medicine as well. **Dr. Joshi** has not only guided him in the most profound manner with continuous encouragement, inspiration and love with close family touch during entire course of the work but also enlightened the author through his wide knowledge and has certainly played a major role to inculcate a scientific career in a true sense and shaped the author as a true researcher…! Author appreciates all his contributions of time, ideas, and constructive comments, to make his Ph.D. experience fruitful and stimulating.

The author is highly indebted to **Prof. Hiren H. Joshi,** Head (On Sabbatical Leave), Physics Department, Saurashtra University, Rajkot, and the former Head of the Department **Prof. K. N. Iyer** for their keen interest and providing the necessary facilities to work day and night at the Crystal Growth Laboratory in the Department of Physics.

The author expresses his sincere thanks to other faculty members of the Physics Department **Prof. H. P. Joshi**, **Prof. D. G. Kuberkar**, **Dr. G. J. Baldha, Dr. K. B. Modi** and **Dr. J. A. Bhalodia**, for their kind help and cooperation during the experimental work.

The author wishes to express his gratitude to **Prof. B. S. Shah**, **Prof. B. J. Mehta** and **Dr. L. K. Maniar** for providing motivation to do further

research work at every stage and also whole hearted wishes and encouragements during the entire work.

The author expresses his gratitude towards **Dr Ashok B. Vaidya and Dr. Rama A. Vaidya** (Kasturba Health Society, ICMR Advanced Center for Reverse Pharmacology in Traditional Medicine, Mumbai), **Prof. H. S. Joshi and Dr. Y. T. Naliapara** (Chemistry Department, Saurashtra University) for becoming mentors in interdisciplinary work, useful discussions and supply of APIs in enough quantity whenever it was required (which is very difficult to produce in grams). The author acknowledges **Prof. Vrinda S. Thakar** (Bioscience Department) for fruitful discussions on growth inhibition studies and providing the aseptic medium for experiment and herbal extract preparation.

The author is thankful to **Prof. Rajnikant, Dr. Vivek Gupta and Dr. Shweta Kohli** (Department of Physics & Electronics, University of Jammu, Jammu) for helping him in Single Crystal XRD data collection and analysis; **Dr. Ashwin Raut, Dr. Amonkar, Dr. Chhaya Godse, Dr. Namyata Pathak, Ms. Priyanka Mertia** and whole team of Kasturaba Health Sociey, Mumbai, for their help in discussion on pharmacology as well as biomaterials; **Prof. Sagayraj** (Loyola College, Chennai) and **Dr. Rajesh** (Engineering College, Madurai) for their help in dielectric data collection; **Dr. Utpal Joshi** (Physics Department, Gujarat University) for his help in taking the AFM images of cholesterol crystals; **Dr. Jayesh Govani** (Department of Physics, University of South Dakota, Vermilion, USA) and **Dr. V. N. Mani** (CMET, Hyderabad) for their quick and unending support.

The author is also thankful to University Grants Commission (**UGC**) for providing Meritorious Fellowship under BSR scheme and Department of Science and Technology (**DST**) for providing financial assistance to participate in **9th International Workshop on Crystal Growth of Organic Materials (CGOM 9), Singapore.**

The author express his gratitude to his colleagues from Chemistry Department, Saurashtra University, Dr. Aksahy Pansuriya, Dr. Jignesh Akbari, Dr. Satish Tala, Dr. Vipul Audichya and form Bioscience Department,

Saurashtra University, Dr. Lalit Chariya and Mr. Viral Mandaliya for their support in synthesizing materials as well as support for inhibition study by sacrificing their research work.

The author is grateful to his senior research colleagues of "Crystal Growth Laboratory", namely, **Dr. V. S. Joshi** (Principal, R.K. Parikh Arts & Science College, Petlad), **Dr. R. M. Dabhi** (Virani High-school, Rajkot), **Dr. K. C. Joseph** (St Xavier's School, Jamnagar), **Dr. B. B. Parekh** (Pt. Deendayal Petroleum University, Gandhinagar), **Dr. S. R. Suthar** (Science College, Mehsana), **Dr. H. J. Pandya** (Physics Department, Saurashtra University, Rajkot), **Dr. S. J. Joshi** (Head, Physics Department, Bahauddin Science College, Junagadh), **Dr. D. J. Dave** (M. N. Virani Science College, Rajkot), **Dr. K. D. Parikh** (M. P. Shah Arts and Science College, Surendranagar), **Dr. C. K. Chauhan** (Officer on Special Duty, Gujarat Educational Innovation Commision & Asst. Prof. in Science College, Gandhinagar) and also to the present co-workers Ms. Kashmira P. Tank, Ms. Sonal R. Vasant, Mr. Rakesh R. Hajiyani, Mr. Hiren S. Jani, Ms. Bhoomika V. Jogiya, Mr. Dhaval Khunti, Mr. Kaushal Mehta, Mr. Ravindra Gohel, Mr. Pushpakant Solanki, Mr. Ravi Mansuria and Ms. Urvisha Tarpara and all the M. Sc. Project students of Crystal Growth Laboratory, for their friendly support and kind cooperation throughout the research work. A special remembrance and thanks to **Late Shri Jigneshbhai A. Shah** (Himmatnagar Science College, Himmatnagar) for his continuous inspiration and motivation.

The author is thankful to the office staff and non teaching staff of Physics Department for their kind support.

The author also extends his sincere thanks to **Mr. Harendra Joshi** (Ex – servicemen, Indian Army) for introducing him to the field of science and monitoring of his progress throughout his study and **Dr. Raghuvir J. Joshi** (Author's mama) for useful discussion on cholesterol and herbal formulations.

The author also expresses his heartfelt gratitude towards the parents of his guide – **Mr. Janakrai Joshi (*Dadaji*)** and ***Ba*** for their wholehearted blessings. The author cannot forget the moral support provided by his Guide's

better – half Mrs**. Shilpa M. Joshi** and daughter **Ms. Krutika M. Joshi** and the whole family.

Finally, last but not least, author would like to express his love and appreciation to his near and dear family members - a powerful source of inspiration and energy, to whom this thesis is dedicated, for their years of sacrifices and lots of prayers. The author heartily expresses his gratitude to his Grand Father **Late Jayashankar L. Vyas** and beloved parents **Mr. Madhukant J. Vyas** and **Mrs**. **Malti M. Vyas.** Author is also thankful to his sister and brother in law – **Mita & Amitkumar** and their two cute children **Isha & Nikhil** for providing inspiration. Author is also thankful to his sister's in laws **Mr. Vasantbhai M. Thaker** and **Mrs. Madhuben V. Thaker** to give moral support during the most tedious job of thesis writing in peaceful atmosphere at their home.

Perhaps, if the author forgot someone to acknowledge… so, just in that case: thanks to whom it concerns…!

Poorvesh M. Vyas
Rajkot
July 2012.

Content

ABSTRACT

The thesis entitled, “STUDY OF SOME ORGANIC BIO-MATERIALS SYSTEMS: CRYSTALLINE AND NANO-PARTICLE PROPERTIES”, representing an elaborated report of the author’s research work will be covering following eight chapters.

Chapter – I : Brief Introduction to Crystal Growth and Synthesis of Nano – Particles

This chapter gives the brief introduction to the subject and explains the objectives and the significance of the study. This chapter presents brief out line of various crystal growth technique, with focus on solution growth technique and gel growth technique, which is also one kind of modified version of solution growth technique. The crystals are grown for the present investigation by slow solvent evaporation and gel growth method. Bio-crystallization usually occurs in the slow and steady process in the soft tissues, cavities or vessels. Single diffusion gel growth technique provides the simplified *in vitro* model. This chapter also presents brief out line of various nano synthesis technique, with focus on microemulsion technique. The nano particles in the present investigation were synthesized by microemulsion technique. Microemulsions are self-assembled nano-scale entities. Microemulsion is isotropic, transparent and thermodynamically stable system composed of water, oil and surfactant and facilitates the growth of nano-particles in micelles. The microemulsion can be a potential system for drug delivery. As noted earlier by applying the microemulsion the total dose of the drug can be reduced and the side effects can be minimized.

Chapter – II : Characterization Techniques

This chapter describes experimental techniques used to characterize the grown crystals and synthesized nano particles. These techniques are powder X – Ray Diffraction (XRD), Single Crystal X – Ray Diffraction, Electron microscopy studies including Scanning Electron Microscopy (SEM), Transmission Electron Microscopy (TEM), Atomic Force Microscopy (AFM), Fourier Transform Infrared Microscopy (FTIR), Dynamic Light Scattering (DLS), Thermal studies including Thermo Gravimetric Analysis (TGA), Differential Thermal Analysis (DTA) and Differential Scanning Calorimetry (DSC) and Dielectric Study.

Chapter: III: Synthesis and Characterization of n-butyl 4 - (3, 4 – dimethoxyphenyl)– 6 – methyl – 2 – thioxo – 1,2,3,4 tetrahydropyrimidine – 5 – carboxylate Crystals and Nano – particles

This chapter deals with the synthesis and characterization of **n**-butyl 4 - (3, 4 – dimethoxyphenyl) – 6 – methyl – 2 – thioxo – 1,2,3,4 tetrahydropyrimidine – 5 – carboxylate (n – butyl THPM) crystals and nano particles. Crystals were grown by using slow solvent evaporation technique. N – butyl THPM crystals were pale yellowish, semitransparent, coagulated crystals were grown at the bottom of the vessel having maximum dimensions 2.0 mm x 1.5 mm. The grown crystals were characterized by Powder XRD, FTIR and Thermal Studies. Thermodynamic and Kinetic parameters were calculated by using Coats – Redfern formula and dielectric study was carried out. n – butyl THPM shows triclinic crystal system with unit cell parameters a = 7.1689Å, b = 10.3378 Å, c = 10.2246 Å, α = 103.78°, β = 107.56°,

γ = 92.66°. SEM study shows the grown crystals were coagulated nature and was composed of fine needle type structure. Nano particles of n – butyl THPM were synthesized by using w/o microemulsion technique. Synthesized nano particles were characterized by powder XRD, TEM, FTIR, thermal studies and Dielectric study. Thermodynamic and Kinetic parameters were calculated. Synthesized nano – particles were having size from 18 – 62 nm, which was confirmed by using TEM. The results were discussed in detail.

Chapter – IV: Synthesis and Characterization of 1-phenyl-3-(propan-2-yl)-1H-pyrazol-5-ol Crystals and Nano – particles

This chapter describes the synthesis and characterization of 1-phenyl-3-(propan-2-yl)-1H-pyrazol-5-ol crystals and nano particles. Single crystals were grown by using slow solvent evaporation technique. 1-phenyl-3-(propan-2-yl)-1H-pyrazol-5-ol grown crystals were yellowish, transparent and having maximum dimensions 5 mm x 4 mm. The grown crystals were characterized by Single Crystal XRD, Powder XRD, FTIR, thermal studies and dielectric studies. Thermodynamic and Kinetic parameters were calculated by using Coats – Redfern Formula. 1-phenyl-3-(propan-2-yl)-1H-pyrazol-5-ol exhibited triclinic crystal system. FTIR showed the C – H, C = O, C = C and =N – N - stretching. Nano particles of 1-phenyl-3-(propan-2-yl)-1H-pyrazol-5-ol were synthesized by using w/o microemulsion technique. Synthesized nano particles were characterized by powder XRD, TEM, FTIR, thermal studies. Thermodynamic and Kinetic parameters were calculated. Synthesized nano – particles were having size from 11 – 42 nm, which was confirmed by using TEM. The results were discussed in detail.

Chapter – V: Synthesis and Characterization of Cholesterol Crystals and Nano Particles

The chapter deals with the growth and characterization of cholesterol crystals and nano particles. The cholesterol crystals were grown by single diffusion gel growth technique in silica hydro gel medium, which provides the simplified *in vitro* model. In the present study, the silica gel was chosen as it remains stable and does not react with the supernatant solutions within it or with the product crystal formed. The grown crystals were very thin, transparent, platelets having size 35 mm × 5 mm. The grown crystals were characterized by powder XRD, SEM, AFM, FTIR, thermal studies and dielectric studies. Thermodynamic and Kinetic parameters were calculated by using Coats – Redfern formula. Nano particles of cholesterol were synthesized by using water/n-butanol/triton X – 100 microemulsions. Synthesized nano particles were characterized by powder XRD, TEM, FTIR, DLS and thermal studies; Thermodynamic and Kinetic parameters were obtained from thermogram. Synthesized nano particles were having nearly spherical morphology with sizes varied from 15 – 31 nm. From the calculation it was found that 0.22 cholesterol nano particle per water core was available, which indicated there were some empty water cores also.

Chapter – VI Growth Inhibition Study of Cholesterol Crystals

This chapter describes the growth inhibition study of cholesterol crystals. The effect of herbal extract on the growth of cholesterol crystals was studied by measuring the length and breadth of growing cholesterol crystals at fixed interval of time totaling to 192 hours. *In vitro* single diffusion gel growth

technique was used to study the growth and inhibition behaviour of cholesterol crystals in the presence of herbal extract of *Fagonia cretica Linn.* The details of the studies will be discussed in this chapter. This study incorporated multidisciplinary interests and may be used for formulating the strategy for prevention of cholesterol. The results were discussed.

Chapter – VII: Synthesis and Characterization of Curcumin Nano particles

This chapter deals with the synthesis and characterization of curcumin nano particles. Curcumin is a major component in the roots of turmeric. Curcumin is very well known for its antioxidant, antitumor, antiarthritic, antiamyloid, anti ischemic, anti – inflammatory nature. It also shows good effect against malaria, cervical cancer, pancreatic cancer, colon cancer, psoriasis, etc. Synthesize nano particles were characterized by powder XRD, TEM, FTIR and thermal studies. Thermal and kinetic parameters were calculated. The curcumin nano particles were found to be of size 20 – 35 nm.

Chapter – VIII: Conclusions

This chapter gives an overall view of the results and general conclusions. Also, the scope of the future work is discussed.

Chapter – I

Brief Introduction to Crystal Growth and Synthesis of Nano – Particles

1. Introduction

When I look around the world on this day

Many Things have evolved from yesterday

No longer can I keep with the new

When I don't understand what's due!

The world is getting faster than before

Everything is smaller and there is more.

But when will this madness stop in its steps

Till we fall into never – ending traps!

In this situation that we are in

Caused by desires to forward and win.

We had been the one driving force behind

Only we can't put it in our minds

Technology will not slow tomorrow

When showing – off is all we can follow

- Aurias

Technology along with pure sciences has brought enormous changes in the human life. The burning desire to do something new and improve the quality of the human life has acted as power house for technology. Technology has crossed all the borders to integrate not only all sciences and engineering but other disciplines also. Technology has impact on economy, marketing, environment, health, defense and individual and family social life. The present author has attempted to briefly review the two technologies, i.e., crystal (growth) technology and nano technology. The former technology is

concerned with the growth of large size, good quality single crystals for different applications. The boom in semiconductor industry is due to the availability of technology to grow device grade semiconductor materials crystals. Notwithstanding, the latter one, nanotechnology, is concerned with the synthesis and applications of nano – sized materials. These both technologies are far apart from each other so far as the material dimensions are concerned. They have unique application and importance.

1.1 Crystal Growth: An Introduction

A crystal is a solid material whose constituent atoms, molecules, or ions are arranged in an orderly repeating pattern extending in all three spatial dimensions. A systematic and scientific study of crystals including process of crystallization, internal structure, external morphology, properties and classification of crystals is known as *"Crystallography"*. The study of the formation of crystals is covered under the subhead *"Crystal Growth"*. The process of crystal formation is known as *crystallization*. The growth of crystals occurs either in nature or artificially in a laboratory. The Mother Nature grows a variety of crystals in the crust of Earth, which are mainly the natural mineral crystals including diamond and precious stones. Mostly these crystals were grown from the molten state by freezing. It is also possible to form crystals directly from a gas without passing through the liquid state; example is, the hoarfrost, i.e., ice crystals which are grown from water vapour in the air. There are other examples of crystals grown in nature, which are famous *Amarnath Shivalinga* of ice in Himalayan cave, large crystals grown around Dead Sea in Israel and gigantic mineral crystals in Naica caves, Chihuahua State of Mexico.

Today, the growth of crystals does not remain the phenomena only occurring in nature, but it has become a well advanced as well as widely used technology. There always has been a requirement of good quality crystals for various applications. The demand of the modern day science and technology has tempted scientists to synthesize and grow several new varieties of crystals. The requirement for better, cheaper, and larger single crystals has driven extensive research and development in crystal growth. This has brought the field of crystal growth into the lime light. As a result the congeries of crystals is ever expanding day by day.

Nowadays crystals are the back bone of modern technological development. The world crystal production was estimated to be more than 20,000 ton per year in the year 1999 [1]. Out of that the largest share of about 60% was from semiconductor materials, for instance, silicon, gallium arsenide, indium phosphate, gallium phosphate, cadmium telluride and its alloys. As can be seen in Figure 1.1 (a), optical crystals, scintillator crystals, and acousto-optic crystals had about equal shares of 10%, whereas laser and nonlinear-optic crystals and crystals for jewelry and watch industry had shares of a few % only. According to another survey in the year 2004, the bulk crystal demand in Western Europe was around 6000 metric tons with value of 1 billion US$. A chart is shown in figure 1.1 (b).

However, over the last decade the demands on synthetic biomaterials have increased significantly with the progress in fields of medicine, material science and engineering, biochemistry, pharmaceutics and nanotechnology.

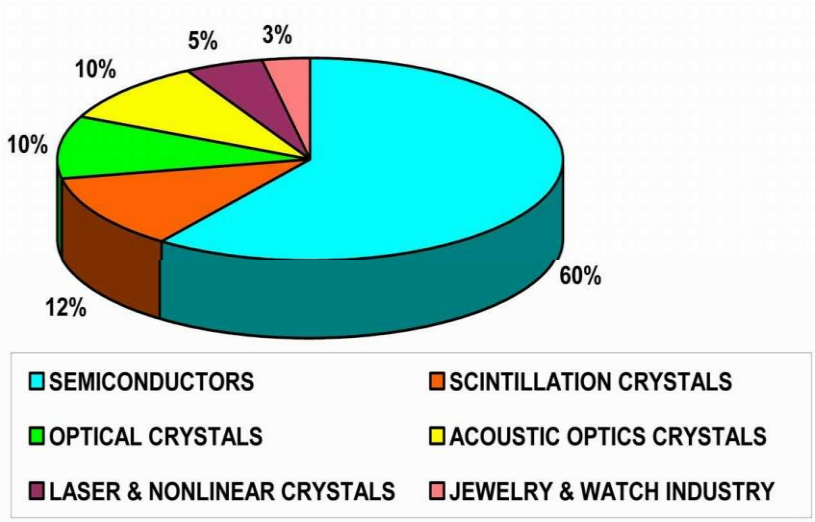

Figure 1.1 (a) Estimated shares of world crystal production in 1999 [1]

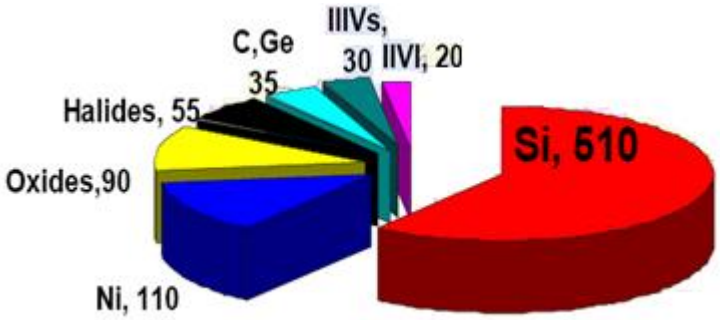

Figure 1.1 (b) Turnover of single crystals in W. Europe in the year 2004 [2]

Furthermore, crystal growth is divided into five major areas by H. J. Scheel, namely, [3] :

1. Fundamental, theoretical and experimental crystal growth studies.

2. Laboratory crystal growth for preparing research samples.

3. Industrial fabrication of single crystals, their characterization and machining

4. Fabrication of metallic / dendritic crystals (e.g. turbine blades).

5. Mass crystallization (salt, sugar, chemicals).

1.2 Crystal Growth Technique

Crystal growth techniques range from a simple inexpensive processes to complex, sophisticated and expensive processes, where the crystallization time ranges from minutes, hours, days and to months. The process of crystal

growth is a controlled change of state, or phase change, to the solid state. This transition may occur from the solid, liquid or vapour state. Hence, depending on the phase transitions involved in the process, the crystal growth methods can generally be classified into three basic categories [4]:

Solid Growth : S → S processes involving solid to solid phase transitions.

Melt Growth : L → S processes involving liquid to solid phase transitions.

Vapour Growth : V →S processes involving vapour to solid phase transitions.

The development and refinement of methods of crystal growth to achieve useful products have relied heavily on empirical engineering and on trial and error methods. Crystal growth still remains, by and large, as an art along with a science [5]. A phalanx of crystal growers has developed various crystal growth techniques after their pain staking efforts of years together. Table 1.1 shows the classification scheme for various growth techniques as summarized by Laudise, which is very important for the neophytes [6].

The designing and development of various crystal growth techniques of the present day is a result of continuous and fruitful modifications occurring since last several decades and still today the modification process is continuing. Table 1.2 shows the multi-disciplinary nature and complexity of crystal growth processes as explained by Scheel [7].

Schieber [8] has well explained the required three aspects of crystal growth: (i) Theory of nucleation and growth, (ii) Experimental crystal growth and (iii) Characterization of crystals.

There are many well written books available on subjects like fundamentals of crystal growth [9]; different crystal growth techniques, their

theories, characterization and applications [10-16] and understanding the growth mechanism [17].

Table 1.1 Crystal Growth Techniques

Mono – component		Poly – component	
A	**Solid-solid (solid growth)** 1. Strain annealing 2. Devitrification 3. Polymorphic-phase change	**A**	**Solid-solid (solid growth)** 1. Precipitation from solid solution
B	**Liquid-solid (melt growth)** 1. Conservative (a) Directional solidification *(Bridgman-Stockbarger)* (b) Cooled seed *(Kyropoulos)* (c) Pulling *(Czochralski)* 2. Non conservative (a) Zoning *(horizontal, vertical, float zone, growth on a pedestal)* Verneuil *(Flame fusion, plasma, arc image)*	**B**	**Liquid-solid (melt growth)** 1. Growth from solution *(evaporation, slow cooling and temperature differential)* (a) Aqueous solvents (b) Organic solvents (c) Molten-salt solvents (d) Solvents under hydrothermal (e) Other organic solvents *2.* Growth by reaction (a) Chemical reaction (b) Electrochemical reaction
C	**Gas-solid (vapor growth)** 1. Sublimation-condensation 2. Sputtering	**C**	**Gas-solid (vapor growth)** 1. Growth by reversible reaction *(temperature change, concentration change)* (a) Van Arkel *(hot wire processes)* 2. Growth by irreversible reaction (b) Epitaxial processes

Even books are available with wonderful photographs of crystals [18]. The authors Stangl and Stang [19] have considered the growth of a variety of beautiful crystals as the growth of flowers in a garden.

Various crystal growth techniques have been discussed in detail by several authors [20,21]. The different techniques of each category are found in reviews and books by Faktor and Garrett [22] on vapour growth, Brice [23] on melt growth, Henisch [24] on gel growth, Buckley [25] on solution growth and Elwell and Scheel [26] on high temperature solution growth.

A review on the advances in crystal growth techniques is given by Mirkin and Moreno [27]. Recently, a *"Handbook of Crystal Growth"* is published [28], which describes the fundamentals of crystal growth and defect formation; bulk growth from the melt, solution, and vapor; epitaxial growth; crystallization from gels; modeling of growth processes and defects; and techniques of defect characterization.

Table 1.2 Multi-Disciplinary Nature and Complexity of Crystal Growth

Multi-Disciplinary Nature of Crystal Growth
• Theoretical Physics (especially thermodynamics, non-equilibrium, thermodynamics, statistical mechanics) • Solid-State Physics • Crystallography and Crystal Chemistry • Materials Science & Engineering • Chemistry (all fields) including Chemical Engineering • Mechanical & Electrical Engineering (especially hydrodynamics, machine design, process control) • Mineralogy • Metallurgy
Complexity of Crystal Growth
• Phase Transformation from Fluid (melt, solution, vapour) to Crystal • Scaling Problem: Control of surface on nm scale in growth system of~m size, hampers numerical simulation • Complex Structure & Phenomena in Melts and Solutions • Multi-Parameter Processes: Optimize and compromise

The predecessors of the present author [29–36] have discussed various growth techniques in detail; therefore, it is avoided in the present

thesis. Among various techniques of growing crystals, solution growth and gel growth technique occupies a prominent place owing to its versatility and simplicity. The present author has employed the Solution growth technique to grow the crystals of Organic Active Pharmaceutical Ingredients (API) and gel growth technique to grow cholesterol crystals; therefore, these techniques are discussed in somewhat more elaborately, hereby.

1.3 Brief Outline of Crystal Growth Theory

The conventional theory of crystal growth starts from the observation that the low index crystallographic planes exhibit a much lower surface energy than the other planes due to the dense atomic packing of these planes. At absolute zero temperature, the crystal tends to be bounded by planes of low indices which are as smooth as possible so as to represent the state of lowest energy. As the temperature is raised from the absolute zero, atoms leave their sites and arrive at the surface continuously and also diffuse out from the interior of the bulk of the material, creating vacancies. Due to this, a large number of atoms will be arriving and leaving the surface continuously, the crystal exhibiting all kinds of planes. If now the vapour pressure is increased above the pressure corresponding to that temperature, more atoms will arrive than leave the surface and the crystal will start growing. The addition of a new atom to the surface, where there are no kinks or steps in energetically a very unfavorable process. Only in the case when an atom, which has arrived at the surface, migrates to a kink or a step before it evaporates also has a chance to be permanently attached to the surface. This is described in figure 1.2 (b). When all the kinks are filled by such a process the surface becomes smooth and the

growth can then proceed only by the accidental formation of an island to which the atoms can again join at the kinks. This is shown figure 1.2 (b).

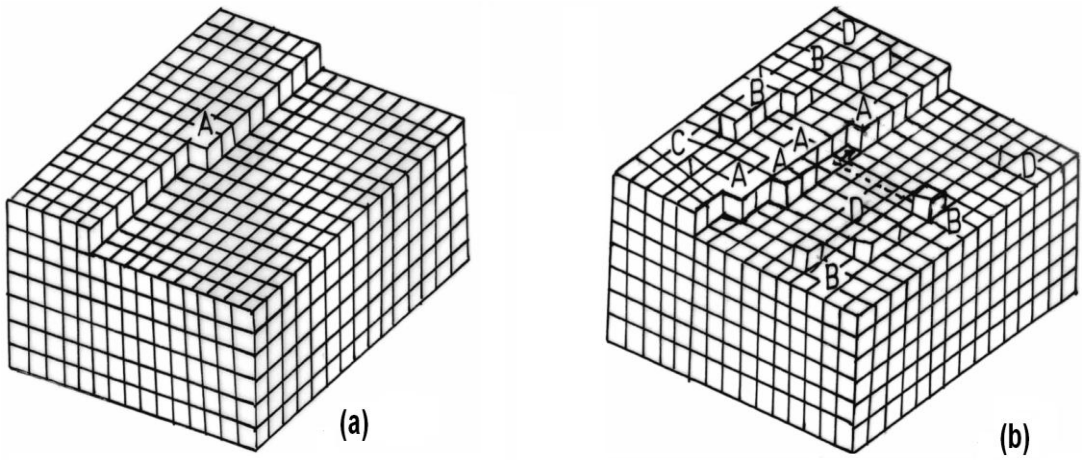

Figure 1.2 (a) Step on a perfect crystalline surface, (b) Step with kinks and vacancies

The critical size of such a nucleus is found to be dependent on the vapour pressure *p* as,

$$R_C = \frac{\gamma a^3}{kT\,log(p/p_o)} \qquad (1.1)$$

Where, γ = surface tension, a = lattice parameter, p_0 = equilibrium vapour pressure.

The formation of a critical nucleus increases the surface free energy by a factor $2\pi\gamma Rc/kT$ and by the action of thermal fluctuations can be expected to occur at a rate proportional to $\exp(2\pi\gamma Rc/kT)$, which is a very small factor. According to this theory, the growth rate cannot be expected to occur below 25 % vapour pressure, however, experimentally it has been found to occur at as low as 1% super saturation.

For low super-saturation σ_i, the growth rate is given as,

$$R = \frac{C}{\sigma_i}\sigma^2 \qquad (1.2)$$

And for high value of σ, it is assumed $\sigma_i \approx \sigma$ then,

$$R = C\sigma \qquad (1.3)$$

To explain this discrepancy, Frank [37] and Burton [38] introduced the idea of nucleation in the presence of a dislocation. The step formed on a surface, where a screw dislocation exists, provides a self–perpetuating step for the atoms to be accommodated without the necessity of a two dimensional nucleus each time a layer is completed. In this process the step will not remain straight because this requires its speed of motion to be proportional to the distance from the dislocation, whereas this is more or less uniform. Due to this the step lags behind at the edge and winds itself into a spiral. The growth rate is, therefore, the number of turns it makes in a second, which is proportional to the square of the super-saturation. This has been confirmed by many experiments. This spiral growth is shown in figure 1.3.

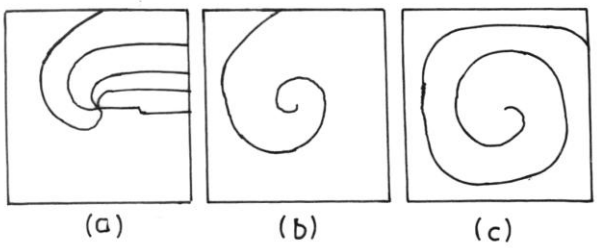

Figure 1.3 Growth spirals

The shape of the spiral depends upon the type and structure of the crystal on which it grows. Owing to the change in growth rate with crystallographic direction, the spiral, many a times assumes a polygonal shape. The possibility of two or more dislocations near each other gives rise

to different spiral structures or closed loops of growth steps due to two dislocations of which some have a configuration which generally resembles that of a dislocation arrangement around a Frank-Read source. Also, double pitch spirals are observed due to close dislocations of the same sign. As the predecessor [32] of the present author has already discussed this in detail, the discussion at length is avoided hereby. Various authors have discussed this theory in detail in their books [5, 38–40].

1.4 Growth from Liquid

The crystal growth from liquid can be classified into six categories namely.

(a) Melt growth
(b) High temperature solution growth (Flux growth)
(c) Hydrothermal growth
(d) Gel growth
(e) Electro-crystallization and
(f) Low temperature solution growth.

There are number of growth methods in each category, which are mentioned in table 1.1. Among various methods of growing single crystals, solution growth at low temperature occupies a prominent place owing to its versatility and simplicity. Growth from solution occurs close to equilibrium conditions and hence crystals with perfection can be grown.

Low Temperature Solution Growth

Solution growth is particularly suited to those materials, which experience decomposition at high temperatures and undergo phase transformations below the melting point.

Crystal growth from solution is more widely used than growth from the melt or from the vapour phase. In this technique, a saturated solution of the material in an appropriate solvent is taken and the growth takes place after the solution is supersaturated by evaporating the solvent (isothermal method) or by lowering the temperature of solution (non-isothermal method). The low temperature aqueous solution has been used for centuries to grow crystals of NaCl and Cane Sugar. Though the rate of crystallization is low, the growth of crystals from solution at room temperature has many advantages over the other growth methods. Since growth is carried out at room temperature, the structural imperfections in solution grown crystals are relatively low [20]. After undergoing so many modifications and refinements, the process of solution growth now yields good quality crystals for a variety of applications. Low temperature solution growth can be subdivided into the following methods:

(a) Slow cooling method
(b) Slow evaporation method
(c) Temperature gradient method
(d) Sankarnarayan Ramasamy method.

Slow Cooling Method

Slow cooling is the easiest method to grow bulk single crystals from solution. However, the principal disadvantage of slow cooling method is the need to use a range of temperatures. The possible range of temperature is usually narrow and hence much of the solute remains in the solution at the end of the growth run. The use of wide range of temperatures may not be desirable because the properties of the grown crystals may vary with temperature. Temperature stability may be increased by keeping the solution in large water bath or by using a vacuum jacket. This technique needs only

two vessels for the solution in which the crystals grow. The height, radius and volume of the vessel are so chosen as to achieve the required thermal stability. Achieving the desired rate of cooling is a major technological hurdle. This method also requires a programmable temperature controller. In spite of these disadvantages, the method is widely used with great success [20]. The temperature at which crystallization begin is usually within the range 45-75 ^{o}C and the lower limit of cooling is the room temperature.

Slow Evaporation Technique

In this method, the saturated solution is kept at a particular temperature and provision is made for evaporation.

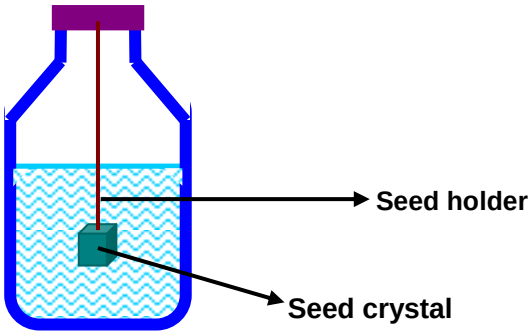

Figure 1.4 Manson Jar (Crystallizer)

If the solvent is non-toxic like water, it is easy to allow evaporation into the atmosphere. The slow evaporation technique has the advantage to grow crystal at a fixed temperature. The basic apparatus Manson Jar Crystallizer used for the solution growth technique is shown in figure 1.4. The height, radius and volume of the vessel are properly chosen to achieve the required crystal size. A saturated solution heated slightly above its saturation temperature is poured into a screw-cap jar and a seed tied to a piece of thread is introduced to achieve the growth of the crystals. In case of organic crystals, the

organic solvents like acetone, chloroform and ethanol or methanol can be used [12,21].

Temperature Gradient Method

This method involves the transport of the materials from hot region containing the source material to be grown to a cooler region where the solution is supersaturated and the crystal grows [12]. The main advantages of the method are:

a. Crystal grows at fixed temperature.
b. This method is insensitive to changes in temperature, provided both the source and the growing crystal undergo the same change.
c. Economy of solvent and solute.

On the other hand, changes in the small temperature difference between the source and the crystal zones have a large effect on the growth rate.

Sankarnarayan-Ramasamy Method

In slow evaporation method, researchers are struggling to get bigger size crystals. An attempt has been made by Sankaranarayanan and Ramasamy to overcome this problem and have introduced a new method (SR method) to grow a large size crystal from solution by the principle of slow evaporation [41]. This novel uni-axial SR solution growth method has attracted many researchers due to the growth of nearly defect free transparent bulk single crystals along a particular axis. Simple experimental techniques, unidirectional growth, 100% solute-solid conversion, minimum thermal stress and prevention of the microbial growth are the interesting features of this technique.

1.5 Criteria for Optimizing Solution Growth Parameters

The growth of good quality single crystals by slow evaporation and slow cooling techniques require the optimized conditions and the same may be achieved with the help of the following norms: (i) Material purification, (ii) Solvent selection, (iii) Crystal habit, (iv) Solution preparation, (v) Seed preparation and (vi) Agitation.

Material Purification

An essential prerequisite for achieving success in crystal growth is the availability of high purity materials that is both solute and solvents. Otherwise the impurity may be incorporated into the crystal lattice resulting in the formation of flaws and defects. Sometimes impurities may slow down crystallization process by being adsorbed on the growing face of the crystal, which changes the crystal habit [42]. A careful repetitive use of standard purification methods of recrystallization followed by filtration of the solution would increase the level of purity.

Choice of Solvents

An ideal solvent should yield a prismatic growth habit and possesses characteristics such as:

- High solute solubility
- High and positive temperature co-efficient of solute solubility
- Low volatility, lower density than that of bulk solute and low viscosity
- Non corrosiveness, Non-toxicity and Non Flammability.

Crystal Habit

The growth of the crystal at approximately equivalent rates along all the directions is a prerequisite for its accurate characterization. This will result in a large bulk crystal from which samples of any desired orientation can be cut. Further, such large crystals should also be devoid of dislocation and other defects. These imperfections usually become isolated into defective regions surrounded by large volumes of high perfection when the crystals grow in with a bulk form. In the crystals which grow as needles or plates, the growth dislocations propagate along the principal growth directions of the crystals [43].

Change of habit in such crystals, which naturally grow as needles or plates, can be achieved by any one of the following ways:

- Changing the temperature of growth
- Changing the pH of solution.
- Adding a habit-modifying agent.
- Changing the solvent.

Preparation of the Solution

For solution preparation, it is necessary to have an accurate solubility temperature data of the material. The saturated solution is prepared in accordance with the solubility curve. It is tested for saturation by suspending a small seed crystal in the solution. The temperature of the solution is slightly raised above the saturated temperature to dissolve any unwanted nuclei or any surface damage on the seed. The temperature is then lowered to the equilibrium temperature in order to initiate the crystal growth. Sintered glass filters of different pore size are used for solution purification. The clear

solution saturated at the desired temperature is taken in a growth vessel. The seed crystal is suspended in the solution. The growth vessel is perfectly or partially closed during crystallization.

Preparation of Seed

Defects present in an imperfect seed propagate into the bulk of the crystal, which decreases the quality of the crystal. Therefore, a proper care is needed to prepare the seed crystals. The quality of the crystal is usually slightly better than that of the seed. Seed crystals are prepared by self-nucleation under slow evaporation from the saturated solution, which is shown in figure 1.5. During this process, the surface of the seed inevitably gets damaged. This problem can be overcome by dissolving the deformed surface layers of the seed crystal, before commencing the growth. There would be a formation of many seeds from the solution as the concentration is high. But seeds of good visual quality free from inclusions and imperfections are selected for growth.

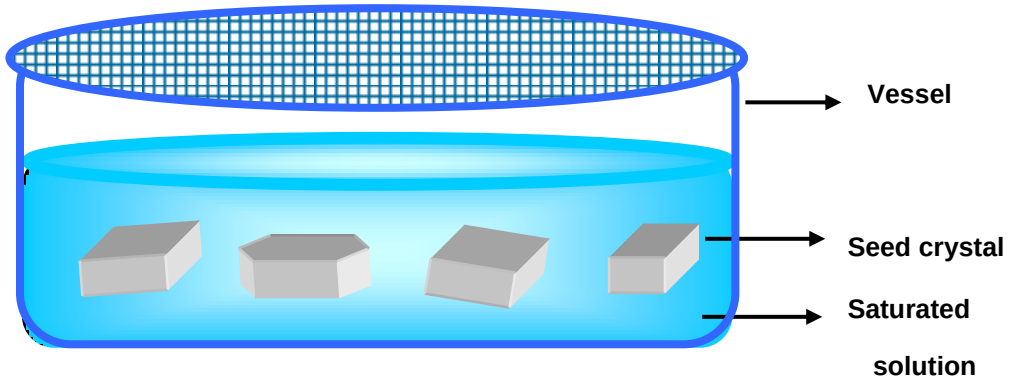

Figure 1.5 The preparation of seed crystal

Agitation

To have regular and uniform growth, the level of super-saturation has to be maintained equally around the surface of the growing crystal. An uneven

growth leads to localized stresses at the surface generating imperfection in the bulk crystals. Moreover, the concentration gradients, existing in the growth vessel at different faces of the crystal, cause fluctuations in super-saturation, which seriously affect the growth rate of individual faces. The gradient at the bottom of the growth vessel exceeds the meta-stable zone width, resulting in spurious nucleation. The degree of formation of concentration gradients around the crystal depends on the efficiency of agitation of the solution. This is achieved by agitating the saturated solution in either direction at an optimized speed using a stirrer motor. There are several methods for stirring and also many designs have been developed which are discussed by Chernov [21].

1.6 Advantages of Low Temperature Solution Growth Technique

The low-temperature solution growth technique has the following merits:

- Simple growth apparatus.
- Growth of strain and dislocation free crystals.
- Permits the growth of prismatic crystals by varying the growth conditions.
- This is the only method which can be used for substances the undergo decomposition before melting.

The technique has the following limitations:

- The growth substance should not react with solvent.

This method is applicable for substances fairly soluble in a solvent.

1.7 Gel Growth Technique

The gel growth technique is a one kind of modified version of solution growth technique. In which the growth occurs due to reaction between two suitable reactants (solutions) in a gel medium or achieving super-saturation by diffusion in gel medium. It is the simplest technique under ambient conditions. This technique is well suited for the crystal growth of compounds, which are sparingly soluble and decompose at fairly low temperatures. Crystals with dimensions of several mm can be grown in a period of 3 to 4 weeks. Crystal growth by the gel technique has attracted the attention of numerous researchers, as this technique is comparatively simple and can be set up in a laboratory with simple glass-wares and without any need of sophisticated instruments and high temperature furnaces.

The gel growth technique is elaborately described by Henisch [24], Henisch *et al.* [44], P.S. Raghavan and P. Ramasamy [10] as well as Patel and Rao [45]. An attempt has been made by the present author to review the gel growth technique briefly.

1.8 Types of Gels

Out of four states of matter - solid, liquid, gas and plasma, the three states of matter-solid, liquid and gas are more familiar. Even there are many exotic materials, which are having bizarre properties and find various applications. One of the exotic states of matter is gels. They are neither solids nor liquids. In early stage, gel has been defined as a two component system of a semi solid nature rich in liquid [46]. A gel may also be defined as a semisolid formulation having an external solvent phase, a polar (organo-gels)

or non-polar (hydro-gel), immobilized within the spaces available of a three dimensional networked structure [47]. Recently, according to IUPAC 2007 recommendations gel is defined as non-fluid colloidal network or polymer network that is expanded throughout its whole volume by a fluid [48]. A characteristic property of gel is that they contain a conspicuously high percentage of solvent and little solid matter. The gel forming substances and solvents stabilize each other in the gel structure. Most gels are mechanically and optically isotropic, except when under strain.

As shown in Table 1.3, gels can be classified according to constituent (matrix) phase, solvent phase and cross-linkages.

Table 1.3 Classifications of Gels

Classification of Gel		
Constituent Or Matrix Phase	**Surfactant Bilayers**	
	Polymers	• Neutral Gel • Synthetic Gel • Hybrid Gel
Solvent Phase	**Solid - Liquid**	• Hydro-gel (Water Solvent) • Organo-gel (Organic Solvent) • Lio-gel (Oily Solvent) • Alco-gel (Alcohol Solvent)
	Solid - Gas	• Xero – Gel (Air) • Aero – Gel (Air)
	Solid - Solid	• Polymer – Gel (Polymer)
Cross-linkage	**Physical Gel** (Noncovalently Crosslinked Polymer Networks)	• Coulombic Interaction • Hydrogen Bonding • Coordinate Bonding • Hydrophobic Bonding
	Chemical Gel (Covalently Crosslinked Polymer Networks)	• Covalent crosslinking

1.9 Gelling Mechanism

The gelation, i.e., gelling process, can be achieved by many ways, such as, cooling of a sol, chemical reaction, addition of precipitation agents and incompatible solvents. Gelatin is a good example of a substance, which is readily soluble in hot water and can be gelled by cooling provided that the concentration exceeds about 10%. Formation of gel can be obtained by the action of two reagents in concentrated solution; preparation of silica gel is an example for this. The process of gelling takes an amount of time, which can vary widely, from minutes to many days, depending on the nature of the materials, its temperature and history [24]. For silica gel, this has been described and documented by Treadwell and Wieland [49]. Silica gel structures depend significantly on the method of preparation. Mechanical properties of fully set gels can vary widely, depending on the density and on the precise conditions during gelling. For the diffusion of reagents through the gel medium, the most important operative parameter is the size of the diffusing particles relative to the pore size in the gel. Another one is the amount of interaction between the solute and internal the gel surfaces.

1.10 Structure of Silica Hydro Gel

It is the general observation of the researchers that gels, in particular, silica gels are the best, efficient and the most versatile media for growing variety of crystals [24, 44, 50-60].

Silica gels are chemical gels because all inter-atomic bonds are covalent. When sodium meta-silicate goes into aqueous solution, mono-silicic acid is produced in accordance with the dynamic equilibrium,

$Na_2SiO_3 + 3H_2O \rightarrow H_4SiO_4 + 2NaOH$ …. (1.4)

This mono-silicic acid can polymerize with the liberation of water,

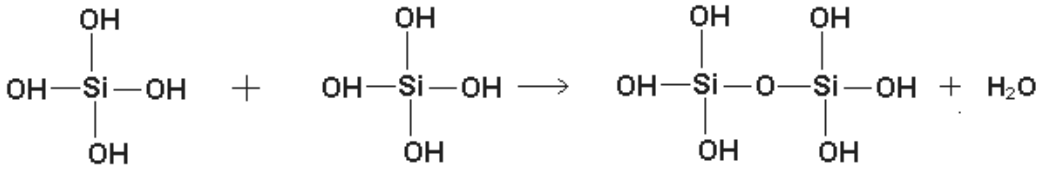

This can occur repeatedly and a three dimensional network of Si-O links is established as silica hydro-gel.

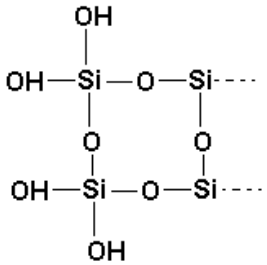

As the polymerization process continues, water accumulates on top of the gel surface. This phenomenon is known as *Syneresis*. Much of the water has its origin in the above condensation process, and some may arise from purely mechanical factors connected with a small amount of gel shrinkage. The well known stability of the silicon-oxygen bonds is responsible for the fact that the polymerization is largely irreversible [24].

The time required for gelation is very sensitive to pH. As the gelation is a gradual process, there is no unique definition for gelation time. It is known that two types of ions are produced during the gelation; $H_3SiO_4^-$ and $H_2SiO_4^{-2}$, in relative amount which depends on the hydrogen ion concentration. The

latter one, favored by high pH values, is in principle more reactive, but higher charge implies a greater degree of repulsions. The $H_3SiO_4^-$ is favored by moderately low pH values and found to be responsible for initial formation for long chain polymerization products [61]. Between these chains the cross-linkages are formed in due course and these contribute to the sharp increase of viscosity that signals the onset of gelation. Because of their low mobility, very long chains will cross-link more slowly than short chains. At very low pH values, the tendency towards polymerization is diminished and chain formation is slowed. Gelation time is strongly dependent on temperature [46]. This has been described in detail by Henisch [24].

A weak acid is generally preferred to adjust the pH values, because pH of the set gel changes only slightly with time and, secondly, the mineral acids tend to spoil the growing crystals. It is noteworthy that in less acidic gel solutions the reaction between the acid and sodium meta-silicate occurs with liberation of hydroxyl ions and thus pH of the solution rapidly increases with the process of polymerization, while in highly acidic gel there is no change in pH except due to very little difference in dissociation of acids of different complexities as well as requirements of reaction mechanism. Hence pH has profound influence on the gel structure [53]. Parikh *et al* [62] reported the effect of gel solution pH on the gel setting time.

Silica gels are irreversible, elastic and resist to deformation. Moreover, silica hydro – gel reduces heterogeneous and secondary nucleations [63]. Also the gel does not react with crystals grown.

1.11 Classification of Gel Growth Methods

Crystal growth in gel has been mainly classified into the following five different methods.

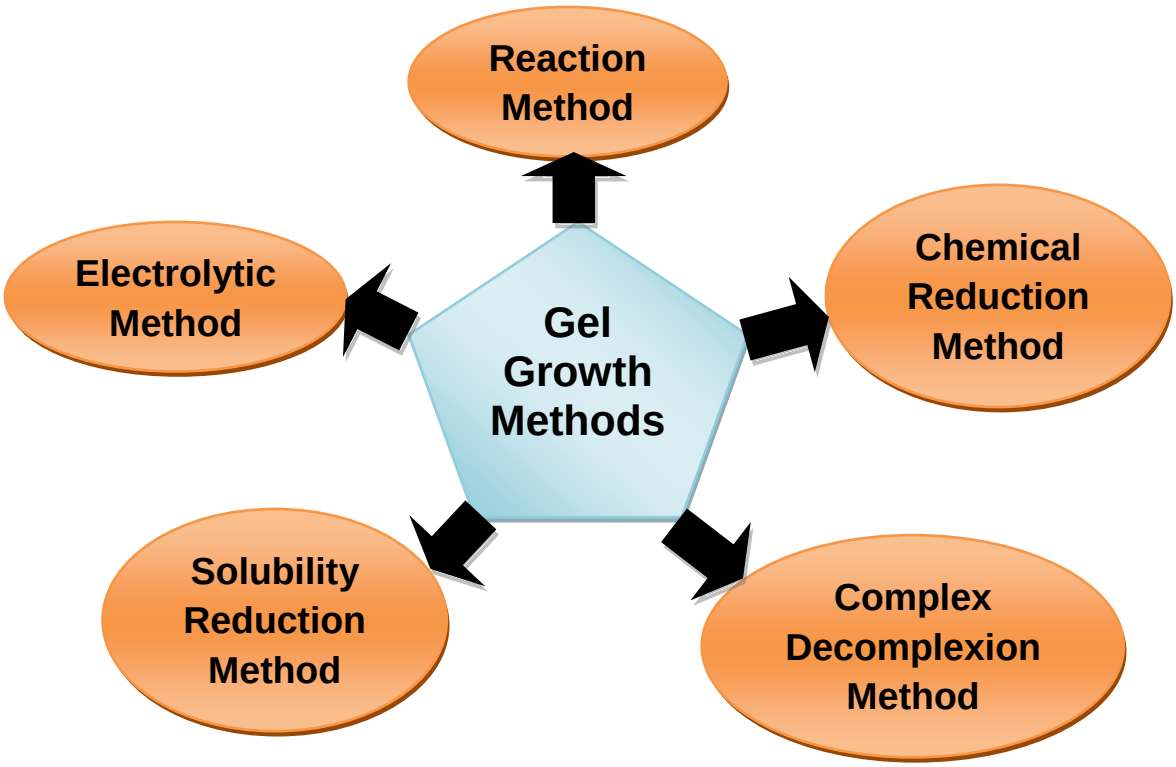

Crystal Growth by Reaction

This method is the basis of all methods of gel growth and can be described as crystal growth by chemical reaction. The crystals, which are insoluble or slightly soluble in water and decompose before reaching their melting points, can be conveniently grown by this method. Two basic requirements to grow single crystals by this method are; (i) the reactants used must be soluble in the solvent and the product crystal must be relatively less soluble, and (ii) the gel must remain stable in the presence of the reacting solutions and must not react with these solutions or with the product formed.

Two aqueous solutions of soluble salts are suitably chosen and allowed to diffuse through the gel, so that there can be a slow and controlled segregation of ions and molecules resulting into the precipitation of an insoluble phase as the crystal. The gel affords to limit the number of critical size nuclei and decreases the rate of crystal growth either by controlling the diffusion of reacting ions or by governing the reaction velocity on the surfaces of the growing crystals. Resulting chemical reaction can be expressed as,

$$A\,X + BY \rightarrow AY + B\,X \qquad \ldots. (1.5)$$

Where, A and B are the cations, X and Y are the anions.

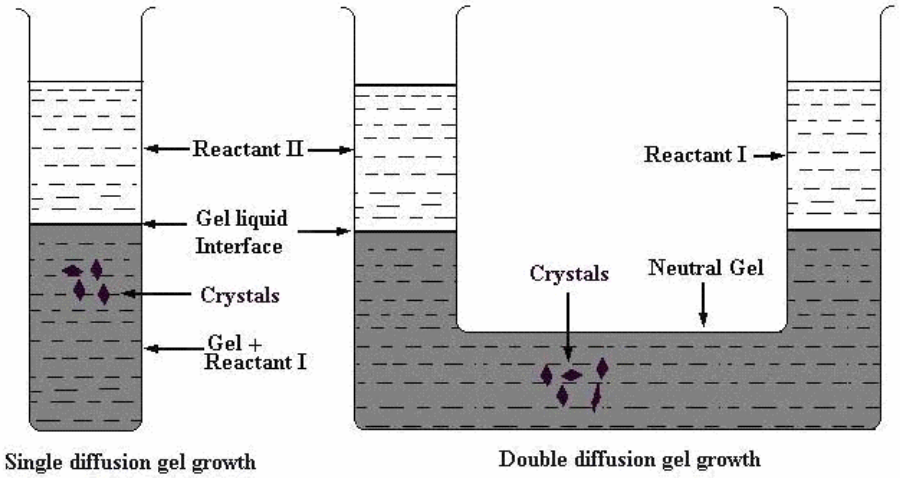

Figure 1.6 Crystal Growth by Chemical Reaction

This can be achieved by the test tube technique, in which one of the reactants is incorporated in the gel and the other reactant is diffused into it, or by the U tube technique as shown in Figure 1.6, or its modification in which the two reactants are allowed to react by diffusion into an essentially inactive gel.

Chemical Reduction Method

This method is suitable for growing only metal crystals from gel media. Hatschek and Simons [64] were the first to report the growth of gold crystals by adding 8 % oxalic acid solution over a set gel containing gold chloride solution. By this particular method crystals of Nickel, Cobalt [65], Selenium, Lead and Copper have been obtained.

Complex Decomplexion Method

This method requires first forming a chemical complex of the material of the crystals to be grown with aqueous solutions of some suitable substance, called complexing agent, in which the former is homogeneously mixable and then providing externally a condition conducive to de-complexing or dissociation of the complex formed. A standard procedure adopted for decomplexion is to increase the dilution steadily, while complex solution is diffused through the gel. Crystal growth by this method was first attempted by O' Connor *et al* [66] for the growth of cupric halide crystals.

Solubility Reduction Method

This method is applicable to grow single crystals of highly water soluble substances. The growth of ammonium dihydrogen phosphate (ADP) single crystals by this method has been first reported by Gloker and Soest [67].

In this method, the substance to be grown is dissolved in water and is incorporated with the gel forming solution. Then a solution, which reduces the solubility of the substance, is added over the set gel to induce crystallization as in Figure 1.7.

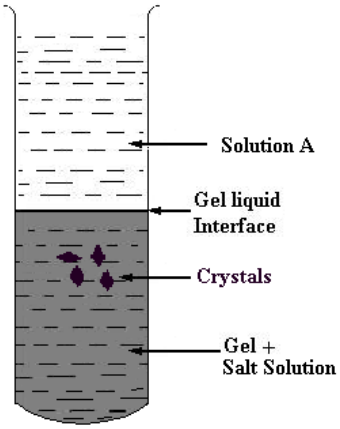

Figure 1.7 Crystal Growth by Solubility Reduction Method

For instance, potassium dihydrogen phosphate (KDP) crystals have been grown by adding ethyl alcohol over the gel containing a saturated solution of KDP [68]. Crystals are grown due to the reduction of solubility of KDP in the liquid phase by the diffusing alcohol.

Electrolytic Method

The electrolytic method can also be used for the growth of metallic crystals by selecting the gel medium for controlled growth. For this a very low d.c. electric current, usually of the order of 2-10 mA, is passed through a silica gel charged with suitable acid or electrolytic solution. Details are given in Figure 1.8.

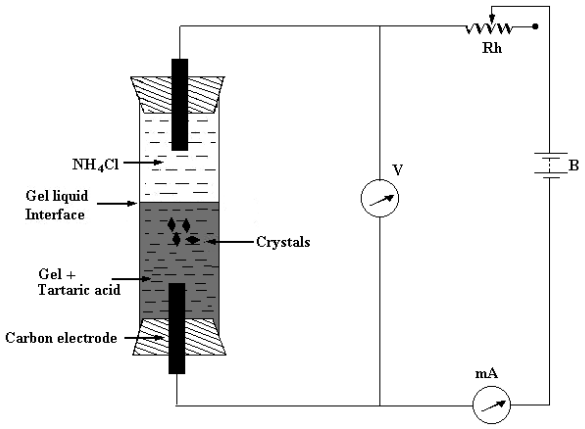

Figure 1.8 Crystal Growth by Electrolytic Method

It has been found that the pH of the gel medium, the concentration of the supernatant solution, the current density and the material used as electrode, have considerable influence on the habit of the crystals grown.

Micro – crystal Growth

Recently, the growth of micro – crystals in modified gel growth technique is reported by Parekh *et al.* [69]. In this technique a drop of gel solution is allowed to set on a glass slide. This drop of gel solution is protected by thin glass cover slip. The reacting solution is allowed to diffuse into this gel by gently bringing it into contact with the gel. The micro crystals grow within this drop of gel. The micro – crystals grow within this drop of gel. The growth of micro-crystals can be monitored continuously using optical microscope. The growth of crystals is quite rapid and requires minimum quantity of chemicals and simple laboratory equipments. This technique is schematically described in figure 1.9. This technique, however, does not introduce the new class, but any gel technique of particular class can be attempted.

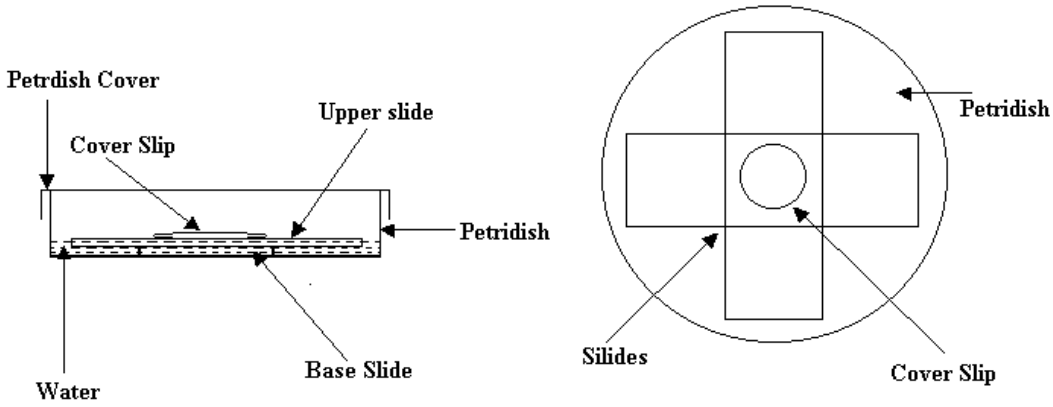

Figure 1.9 Set up for modified gel growth technique

1.12 Advantages and Limitations of Gel Growth

Gel method has the following main advantages:

(1) Thermodynamic consider reveals that as the growth proceeds at ambient temperature, the grown crystals would contain relatively less concentration of equilibrium defects.

(2) Crystals can be observed practically in all stages of their growth.

(3) The gel framework, which is chemically inert and harmless, acts like a three dimensional crucible in which the crystal nuclei are delicately held in the position of their formation and growth, thereby preventing damage, if any, due to impact with either the bottom or the walls of the container.

(4) By changing the conditions, crystals with different morphologies and size can be obtained.

(6) In as-much-as the gel reduces the speed of chemical reagents, crystals could be made to grow much larger than that are formed by a similar reaction in water or in molten stage by double decomposition process.

(9) As this method is extremely simple and inexpensive, good quality crystals can be grown even in small laboratories which do not possess sophisticated equipment.

Notwithstanding, the gel method has the following limitations also

(1) Growth period is usually very long.

(2) Crystal size is generally small, so large crystals cannot be grown by this method.

(3) When silica gel is used, gel inclusion occurs during growth in some crystals.

(4) The chance of lattice contamination by impurities from the gel itself are profusely increased.

1.13 Introduction to Nanotechnology

Nanotechnology is the term used to describe the creation and exploitation of materials with structural features in between those of atoms and bulk materials, with at least one dimension in the nanometer range (1 nm = 10^{-9} m). A schematic diagram of nano scale is given by figure 1.10. The properties of materials with nano metric dimensions are significantly different from those of atoms or bulk materials. Suitable control of the properties of nanometer-scale structures can lead to new science as well as new products, devices and technologies. The underlying theme of nanotechnology is miniaturization and the importance of which was pointed out by Feynman [70] as early as 1959 in his often-cited lecture entitled ‘‘There is plenty of room at the bottom’’. The challenge is to beat Moore’s law [71] and accommodate 1000 CDs in a wristwatch [72,73]. Since that many scientists and researchers have been investigating different effect caused by the small size of the particle. Nano-technology has become the cynosure across the globe for the technologists. Nanotechnology is a growing field that explores electrical, optical and magnetic activity as well as structural behavior at the molecular and sub-molecular level. One practical application of nano-technology, though there are many applications, is the science of constructing the computer chips and other devices using the nano-scale building blocks. The term nano-technology was introduced by Nori Taniguchi in 1974 at the Tokyo International Conference on Production Engineering [74].

Nano dimension is important because quantum mechanical properties of electrons, photons and atoms are evident at this scale. Nano-scale structures permit the control of fundamental properties of materials without

changing the chemical status of the material. Nano-structures such as nano-photonic devices, nano-wires, carbon nano-tubes, plasmonic devices will soon become the common technologies in near future.

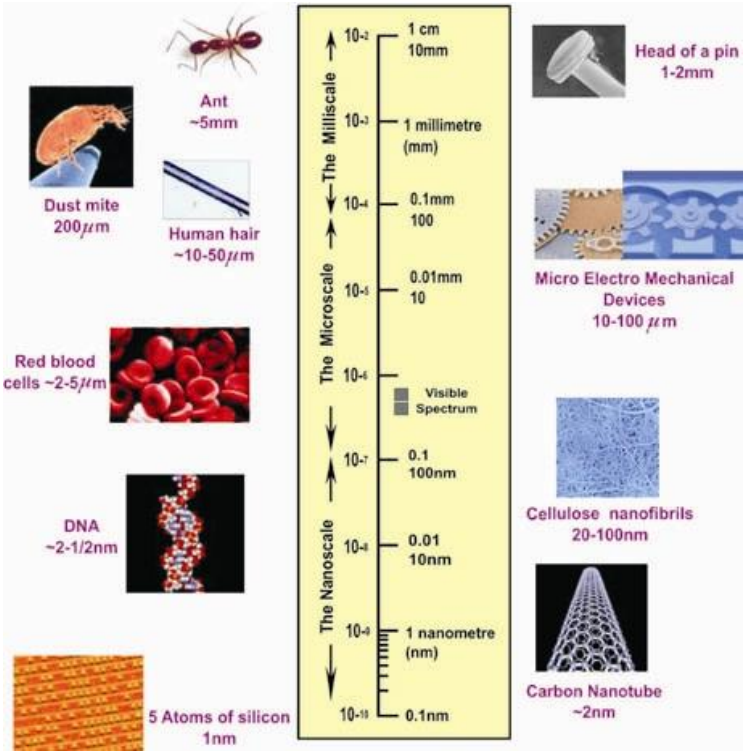

Figure 1.10 Schematic diagram of dimension of nano scale [75]

Nano-particles are of great scientific interest as they are effectively a bridge between bulk materials and atomic or molecular structures. A bulk material is having consistent physical properties regardless its size, but in contrast to this the nano-particles do not exhibit this. Size dependent properties are observed such as quantum confinement in semiconductor particles, surface plasmon resonance in some metal particles and super para-magnetism in magnetic materials.

The properties of materials change as their size approaches to the nano-scale, where the percentage of atoms on the surface of a material

becomes significant. Nano-particles have very high surface area to volume ratio. The interesting and sometimes unexpected properties of nano-particles are partly due to the high surface to volume ratio present in the material.

Nano-particles exhibit a number of special properties relative to the bulk one. For instance, the bending of copper wire, ribbon, etc. occurs with movement of copper atoms/ clusters at about 50 nm scale, however, copper nano-particles smaller than 50 nm are considered as super hard materials, that do not exhibit the same malleability and ductility those are offered by the bulk copper. However, the nano-scale is not always desirable for the benefit of properties; for example, nano-particles of ferroelectric materials smaller than 10 nm no longer distort as per the requirements and find no applications in memory storage.

Suspensions of nano-particles are possible because of the interaction of the particle surface with the solvent is strong enough to overcome differences in the density, which usually results in material either sinking or floating in a liquid. Nano-particles have bizarre visible properties because they are small enough to scatter visible light rather than absorb it, for example, gold nano- particles appear deep red to black in solution.

There are several general articles written by different authors [76–78] as well as several well written books are published [79–83].At the small end of the size range, the nano-particles are often called as clusters. Nano-spheres, nano-rods and nano-cups are a few of the shapes those are synthesized. If one dimension is reduced in the nano range keeping the other two dimensions large, then the achieved structure is quantum well. If two

dimensions are so reduced and one dimension remains large, the resulting structure is called as quantum wire. In the extreme case, all the three dimensions are reduced in the nano-meter range, which is called the quantum dot.

The word quantum is associated with these three types of nano-structures because the changes occurring in the properties arise from quantum mechanical nature of physics in the domain of the ultra small. These changes particularly affect the electronic properties, which is surveyed by Jacak *et al.* [84]. The quantum dots have applications in lasers, infrared detectors and superconductivity [85].

Different aspects, out comes, impacts, implications of nanotechnology are covered by Roco *et al.* [86] based on advances of last 10 years, present status and future vision for next decade using inputs from over 35 countries. Governance of nanotechnology is essential for realizing economic growth and other societal benefits of the new technology, protecting public health and supporting global collaboration and progress are to be considered. Moreover Roco *et al.* [87] provided a review on nano – technology research directions for societal need in the year 2020 based on international studies.

It is interesting to note that the global market for nanotechnology was 10.5 billion US$ in 2006 and is expected to be nearly 30.4 billion US$ in 2015.

1.14 Changes in properties at Nano Scale

Surface effect also increases with decreasing particle size, but these effects arise due to the relative increase in surface area to volume ratio, as

the particle dimensions decrease. For a sphere, the surface to volume ratio goes as $3/r^3$. Hence, the surface to volume ratio for a spherical particle with a diameter of 1 nm is 1000 times larger than that with a diameter of 1 μm. Examples of volume effects include the changes in magnetic properties if the particles are smaller than the magnetic domain; the changes in optical properties if the particles are smaller than the wavelength of light, and the changes in electrical properties if the particles are comparable to the mean free path of electrons [88]. The result is that surface atoms have different properties. As the ratio of surface atoms increases, at nano scale, the material properties will be affected.

Optical Properties

One of the most fascinating and useful aspects of nanomaterials is their optical properties. Applications based on optical properties of nanomaterials include optical detector, laser, sensor, imaging, phosphor, display, solar cell, photocatalysis, photoelectrochemistry, biomedicine, etc.

The optical properties of nanomaterials depend on parameters such as feature size, shape, surface characteristics, and other variables including doping and interaction with the surrounding environment or other nanostructures. Figure 1.11 exemplifies the difference in the optical properties of metal and semiconductor nanoparticles. With the CdSe semiconductor nanoparticles, a simple change in size alters the optical properties of the nanoparticles [89]. When metal nanoparticles are enlarged specifically, their optical properties change as observed for the different samples of gold nanospheres and nano rods as shown in UV – Vis spectra of figure 1.11.

However, in the case of nano rods, the optical properties change dramatically [89].

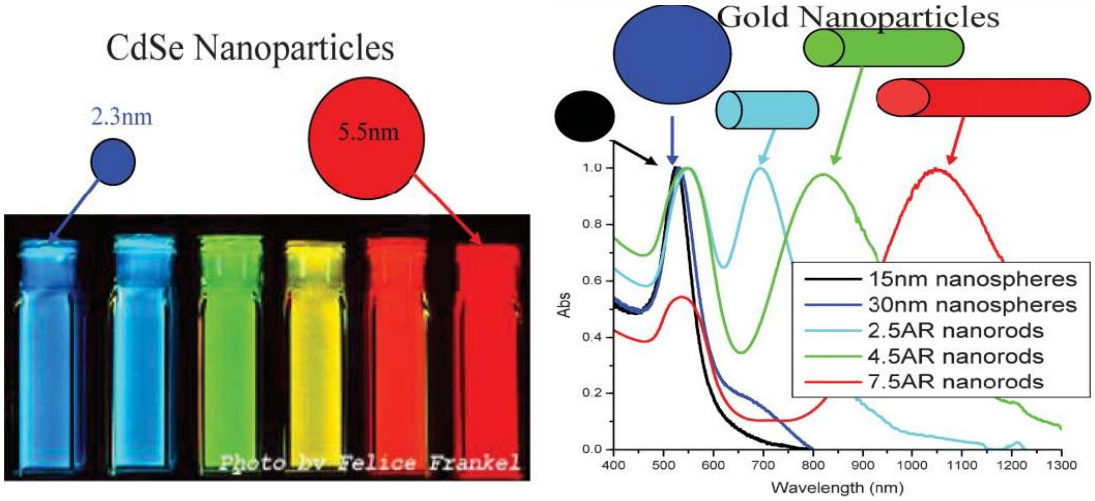

(a) (b)

Figure 1.11 (a) Fluorescence of (CdSe) ZnS quantum dots of various sizes and (b) absorption spectra of gold nanoparticles [89]

Electrical Properties

An electrical property of nanoparticles deals with fundamentals of electrical conductivity in nanotubes and nano-rods, photoconductivity of nano-rods, electrical conductivity of nano-composites. One interesting method which can be used to demonstrate the steps in conductance is the mechanical thinning of a nano-wire and measurement of the electrical current at a constant applied voltage. With decreasing diameter of the wire, the number of electron wave modes contributing to the electrical conductivity is becoming increasingly smaller by well-defined quantized steps.

In electrically conducting carbon nanotubes, only one electron wave mode is observed which transport the electrical current. As the lengths and

orientations of the carbon nanotubes are different, which provides two sets of information: (i) the influence of carbon nanotube length on the resistance; and (ii) the resistances of the different nanotubes. As the nanotubes have different lengths, then with increasing protrusion of the fiber bundle an increasing number of carbon nanotubes will touch the surface of the mercury droplet and contribute to the electrical current transport as shown in figure 1.12. [90]

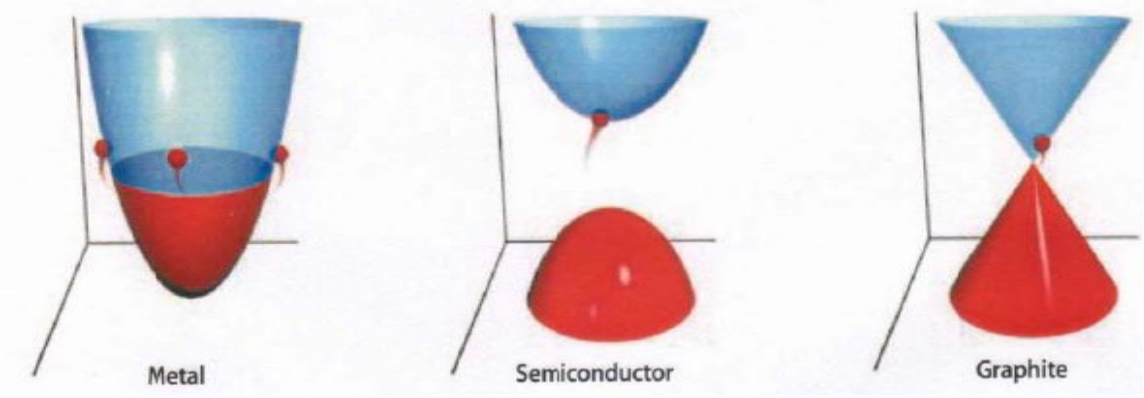

Figure1.12 Electrical behavior of naotubes [90].

Mechanical Properties

Mechanical properties of nanoparticles deals with influence of porosity, influence of grain size, super-plasticity, filled polymer composites, particle-filled polymers, polymer-based nano-composites filled with platelets, carbon nanotube-based composites. It is problematic to produce macroscopic bodies with a high density and a grain size in the range of less than 100 nm. However, two materials have attracted much greater interest as they will undoubtedly achieve industrial importance.

These materials are polymers which contain nanoparticles or nanotubes to improve their mechanical behaviors and severely plastic-deformed metals, which exhibit astonishing properties. However, because of

their larger grain size, the latter are generally not accepted as nanomaterials. Experimental studies on the mechanical properties of bulk nanomaterials are generally impaired by major experimental problems in producing specimens with exactly defined grain sizes and porosities. Therefore, model calculations and molecular dynamic studies are of major importance for an understanding of the mechanical properties of these materials.

Filling polymers with nanoparticles or nano-rods and nanotubes, respectively, leads to significant improvements in their mechanical properties. Such improvements depend heavily on the type of the filler and the way in which the filling is conducted. The latter point is of special importance, as any specific advantages of a nano-particulate filler may be lost if the filler forms aggregates, thereby mimicking the large particles. Particulate filled polymer-based nanocomposites exhibit a broad range of failure strengths and strains. This depends on the shape of the filler, particles or platelets, and on the degree of agglomeration. In this class of material, polymers filled with silicate platelets exhibit the best mechanical properties and are of the greatest economic relevance. The larger the particles of the filler or agglomerates, the poorer are the properties obtained. On the other hand, by using carbon nanotubes it is possible to produce composite fibers with extremely high strength and strain at rupture. Among the most exciting nano-composites are the polymer-ceramic nano-composites, where the ceramic phase is platelet-shaped. This type of composite is preferred in nature, and is found in the structure of bones, where it consists of crystallized mineral platelets of a few nanometers thickness that are bound together with collagen as the matrix [91].

Magnetic Properties

Bulk gold and platinum are non-magnetic, but at the nano size they are magnetic. Surface atoms are not only different to bulk atoms, but they can also be modified by interaction with other chemical species, that is, by capping the nanoparticles. This phenomenon opens the possibility to modify the physical properties of the nanoparticles by capping them with appropriate molecules. Actually, it should be possible that non-ferromagnetic bulk materials exhibit ferromagnetic-like behavior when prepared in nano range. In the case of Pt and Pd, the ferromagnetism arises from the structural changes associated with size effects.

However, gold nanoparticles become ferromagnetic when they are capped with appropriate molecules: the charge localized at the particle surface gives rise to ferromagnetic-like behavior.

Surface and the core of Au nanoparticles with 2 nm in diameter show ferromagnetic and paramagnetic character, respectively. The large spin-orbit coupling of these noble metals can yield to a large anisotropy and therefore exhibit high ordering temperatures. More surprisingly, permanent magnetism was observed up to room temperature for thiol-capped Au nanoparticles. For nanoparticles with sizes below 2 nm the localized carriers are in the 5d band. Bulk gold has an extremely low density of states and becomes diamagnetic, as is also the case for bare gold nanoparticles. This observation suggested that modification of the d band structure by chemical bonding can induce ferromagnetic like character in metallic clusters [91]. The capping of gold nanoparticles has brought many applications in medicine [92]

1.15 Approaches for synthesis of Nano Particles

1.15.1 Bottom-up Approach

Bottom-up, or self-assembly uses chemical or physical forces operating at the nano scale to assemble basic units into larger structures for nano-fabrication. As component size decreases in nanofabrication, bottom up approaches provide an increasingly important complement to top-down techniques. Inspiration for bottom-up approaches comes from biological systems where the catalysts, called enzymes, assemble amino acids to construct living tissue that forms and supports the organs of body. This approach enables to design new materials; those are built from simple atomic level constituents. Carefully arranged atoms provide opportunities to develop mechanical, electrical, magnetic and other properties that are not otherwise possible.

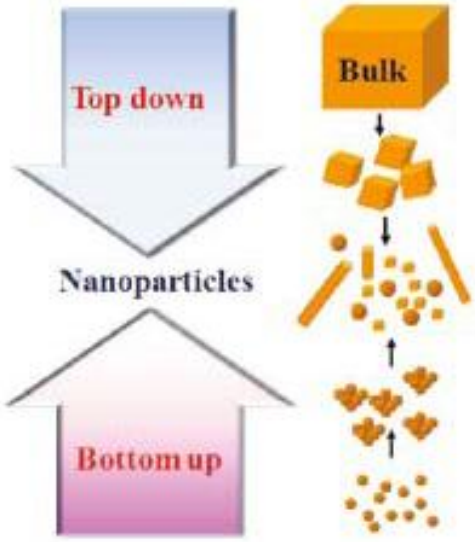

Figure 1.13 Two approaches for synthesis of nanoparticles [91]

1.15.2 Top-down Approach

This starts with a large scale object or pattern and gradually its dimension reduces. This can be accomplished by a technique called lithography which shines radiation through a template on to a surface coated

with a radiation sensitive resist; the resist is then removed and the surface is chemically treated to produce nano-structure. This technique involves fundamental study of chemistry and physics of large and complex structures, and then to investigate the fundamental building blocks of these structures which are smaller and simpler.

1.16 Synthesis Methods for Nano Structures

There are many techniques to synthesize the nano structure materials. A few of them are discussed over here, briefly.

Mechanical Grinding

Mechanical attrition is a typical example of 'top down' method of synthesis of nanomaterials, where the material is prepared not by cluster assembly but by the structural decomposition of coarser-grained structures as the result of severe plastic deformation. This has become a popular method to make nanocrystalline materials due to its simplicity, the relatively inexpensive equipment needed, and the applicability to essentially synthesis of all classes of materials. The major advantage often quoted is the possibility of easily scaling up the process to tonnage quantities of material for various applications. Similarly, the serious problems that are usually cited are; Contamination from milling media and/or atmosphere and to consolidate the powder product without coarsening the nanocrystalline microstructure.

Mechanical milling is typically achieved using high energy shaker, planetary ball, or tumbler mills. The energy transferred to the powder from refractory or steel balls depends on the rotational (vibrational) speed, size and

number of the balls, ratio of the ball to powder mass, the time of milling and the milling atmosphere. Nanoparticles are produced by the shear action during grinding.

Milling in cryogenic liquids can greatly increase the brittleness of the powders influencing the fracture process. As with any process that produces fine particles, an adequate step to prevent oxidation is necessary.

This method of synthesis is suitable for producing amorphous or nanocrystalline alloy particles, elemental or compound powders. If the mechanical milling imparts sufficient energy to the constituent powders a homogeneous alloy can be formed [91, 93].

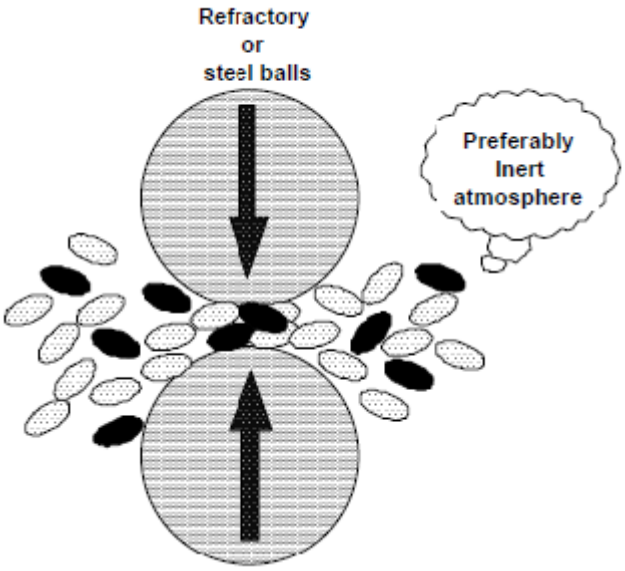

Figure 1.14 Schematic representation of the principle of mechanical milling

Sol-gel process

The sol-gel process, involves the evolution of inorganic networks through the formation of a colloidal suspension (sol) and gelation of the sol to form a network in a continuous liquid phase (gel). The precursors for

synthesizing these colloids consist usually of a metal or metalloid element surrounded by various reactive ligands. The starting material is processed to form a dispersible oxide and forms a sol in contact with water or dilute acid. Removal of the liquid from the sol yields the gel, and the sol/gel transition controls the particle size and shape. Calcination of the gel produces the oxide.

Sol-gel processing refers to the hydrolysis and condensation of alkoxide-based precursors such as $Si(OEt)_4$ (tetraethyl orthosilicate, or TEOS). The reactions involved in the sol-gel chemistry based on the hydrolysis and condensation of metal alkoxides M(OR)**z** can be described as follows:

$$MOR + H_2O \rightarrow MOH + ROH \text{ (hydrolysis)} \quad \ldots. (1.6)$$

$$MOH + ROM \rightarrow M\text{-}O\text{-}M + ROH \text{ (condensation)} \quad \ldots. (1.7)$$

Sol-gel method of synthesizing nanomaterials is very popular amongst chemists and is widely employed to prepare oxide materials. The sol-gel process can be characterized by a series of distinct steps.

The interest in this synthesis method arises due to the possibility of synthesizing nonmetallic inorganic materials like glasses, glass ceramics or ceramic materials at very low temperatures compared to the high temperature process required by melting glass or firing ceramics.

The major difficulties to overcome in developing a successful bottom-up approach is controlling the growth of the particles and then stopping the newly formed particles from agglomerating. Other technical issues are ensuring the reactions are complete so that no unwanted reactant is left on the product and completely removing any growth aids that may have been

used in the process. Also production rates of nano powders are very low by this process. The main advantage is one can get mono sized nano particles by any bottom up approach [91,93].

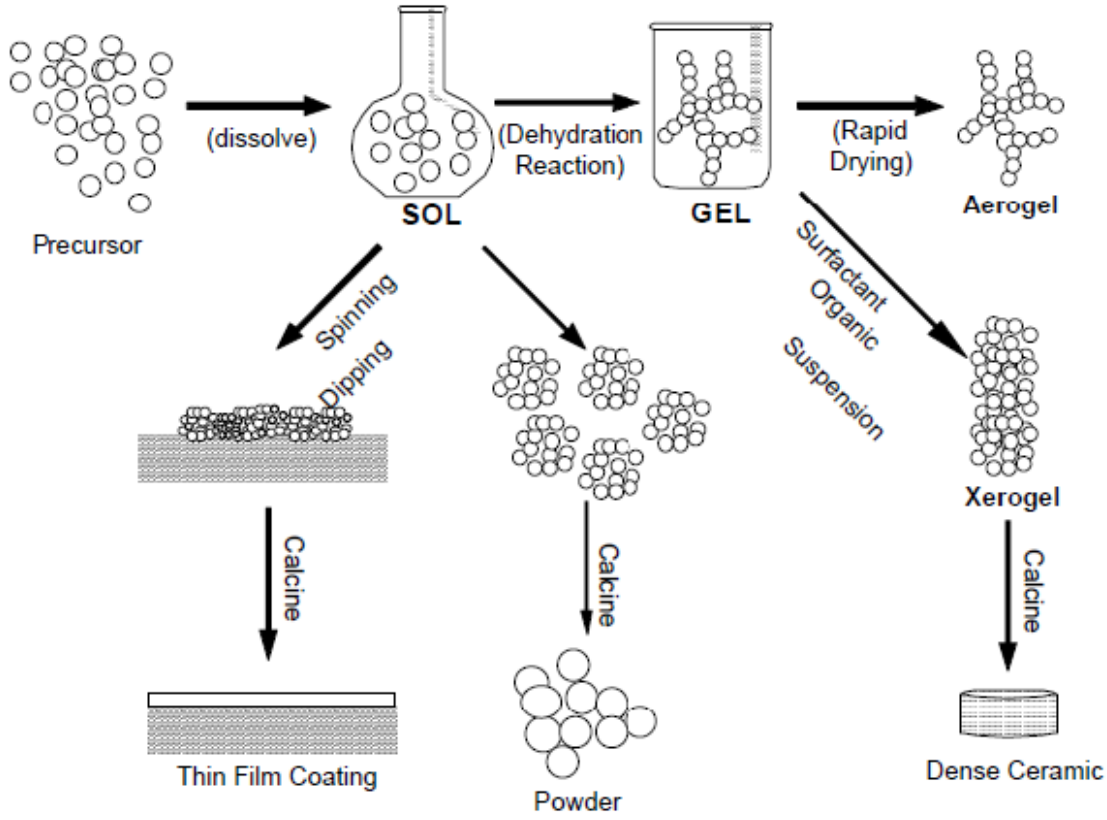

Figure 1.15 Various steps of sol-gel process of synthesis of nanomaterials [91]

Gas Phase Synthesis of Nanomaterials

The gas-phase synthesis methods are of increasing interest because they allow elegant way to control process parameters in order to be able to produce size, shape and chemical composition controlled nanostructures. In conventional chemical vapour deposition (CVD) synthesis, gaseous products either are allowed to react homogeneously or heterogeneously depending on a particular application.

1. In homogeneous CVD, particles form in the gas phase and diffuse towards a cold surface due to thermophoretic forces, and can either be scrapped of from the cold surface to give nano-powders, or deposited onto a substrate to yield what is called ***'particulate films'***.

2. In heterogeneous CVD, the solid is formed on the substrate surface, which catalyses the reaction and a dense film is formed.

In order to form nanomaterials several modified CVD methods have been developed. Gas phase processes have inherent advantages, some of which are noted here:

- An excellent control of size, shape, crystallinity and chemical composition
- Highly pure materials can be obtained
- Multicomponent systems are relatively easy to form
- Easy control of the reaction mechanisms

Most of the synthesis routes are based on the production of small clusters that can aggregate to form nano particles (condensation). Condensation occurs only when the vapour is supersaturated and in these processes homogeneous nucleation in the gas phase is utilized to form particles. This can be achieved both by physical and chemical methods [91].

Gas Phase Process

The simplest fashion to produce nanoparticles is by heating the desired material in a heat resistant crucible containing the desired material. This method is appropriate only for materials that have a high vapour pressure and

heated at temperatures that can be as high as 2000°C. Energy is normally introduced into the precursor by arc heating, electron beam heating or Joule heating. The atoms are evaporated into an atmosphere, which is either inert (e.g. He) or reactive (so as to form a compound). To carry out reactive synthesis, materials with very low vapour pressure have to be fed into the furnace in the form of a suitable precursor such as organometallics, which decompose in the furnace to produce a condensable material. The hot atoms of the evaporated matter lose energy by collision with the atoms of the cold gas and undergo condensation into small clusters via homogeneous nucleation. In case a compound is being synthesized, these precursors react in the gas phase and form a compound with the material that is separately injected in the reaction chamber. The clusters would continue to grow if they remain in the supersaturated region. To control their size, they need to be rapidly removed from the supersaturated environment by a carrier gas. The cluster size and its distribution are controlled by only three parameters:

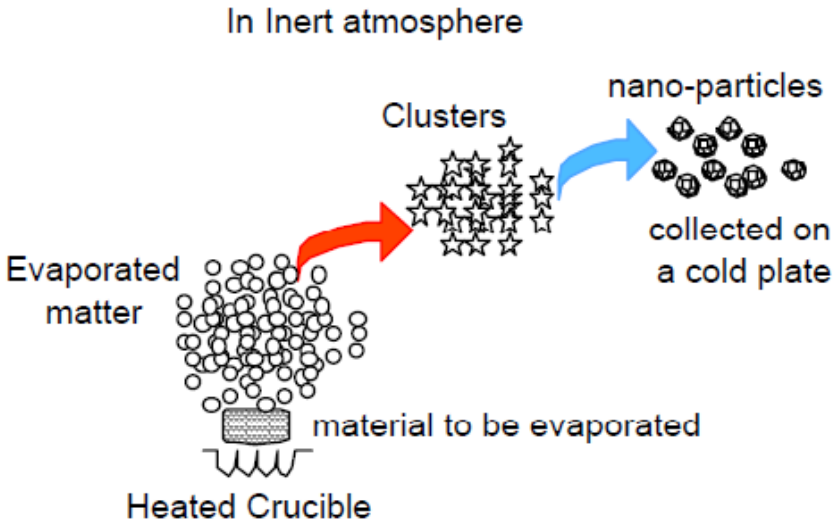

Figure 1.16 The gas phase process of synthesis of single phase nanomaterials from a heated crucible

1. The rate of evaporation (energy input),

2. The rate of condensation (energy removal),

3. The rate of gas flow (cluster removal).

Because of its inherent simplicity, it is possible to scale up this process from laboratory (mg/day) to industrial scales (tons/day) [91].

Flame Assisted Ultrasonic Spray Pyrolysis

In this process, precursors are nebulized and then unwanted components are burnt in a flame to get the required material, e.g., ZrO_2 has been obtained by this method from a precursor of $Zr(CH_3CH_2\ CH_2O)_4$. Flame hydrolysis, that is a variant of this process, is used for the manufacture of fused silica. In the process, silicon tetrachloride is heated in an oxy-hydrogen flame to give highly dispersed silica. The resulting white amorphous powder consists of spherical particles with sizes in the range 7-40 nm. The combustion flame synthesis, in which the burning of a gas mixture, e.g., acetylene and oxygen or hydrogen and oxygen, supplies the energy to initiate the pyrolysis of precursor compounds, is widely used for the industrial production of powders in large quantities, such as carbon black, fumed silica and titanium dioxide. However, since the gas pressure during the reaction is high, highly agglomerated powders are produced which is disadvantageous for subsequent processing [91].

A key for the formation of nanoparticles with narrow size distributions is the exact control of the flame in order to obtain a flat flame front. Under these conditions the thermal history, i.e., time and temperature, of each particle formed is identical and narrow distributions result. However, due to the

oxidative atmosphere in the flame, this synthesis process is limited to the formation of oxides in the reactor zone.

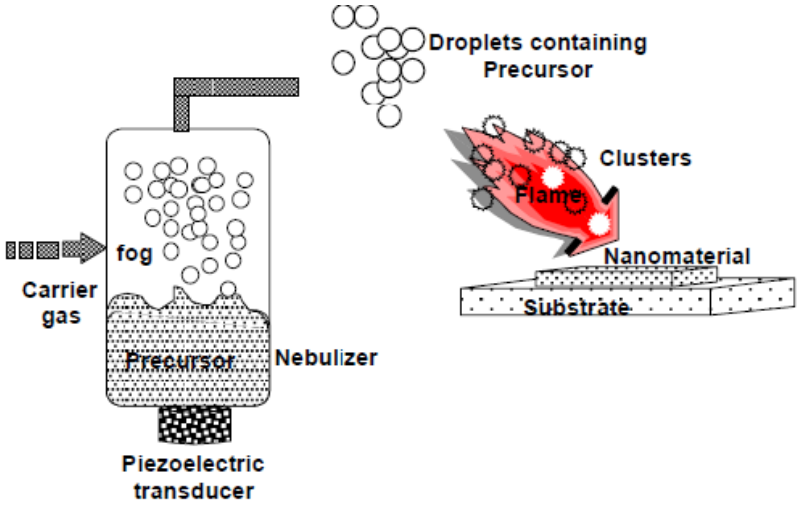

Figure 1.17 Flame assisted ultrasonic spray pyrolysis [91]

Gas Condensation Processing (GCP)

In this technique, a metallic or inorganic material, e.g. a suboxide, is vaporized using thermal evaporation sources such as crucibles, electron beam evaporation devices or sputtering sources in an atmosphere of 1-50 mbar He (or another inert gas like Ar, Ne, Kr). Clusters form in the vicinity of the source by homogenous nucleation in the gas phase and grow by coalescence and incorporation of atoms from the gas phase.

The cluster or particle size depends critically on the residence time of the particles in the growth system and can be influenced by the gas pressure, the kind of inert gas, i.e. He, Ar or Kr, and on the evaporation rate/vapour pressure of the evaporating material. With increasing gas pressure, vapour pressure and mass of the inert gas used the average particle size of the nanoparticles increases [89].

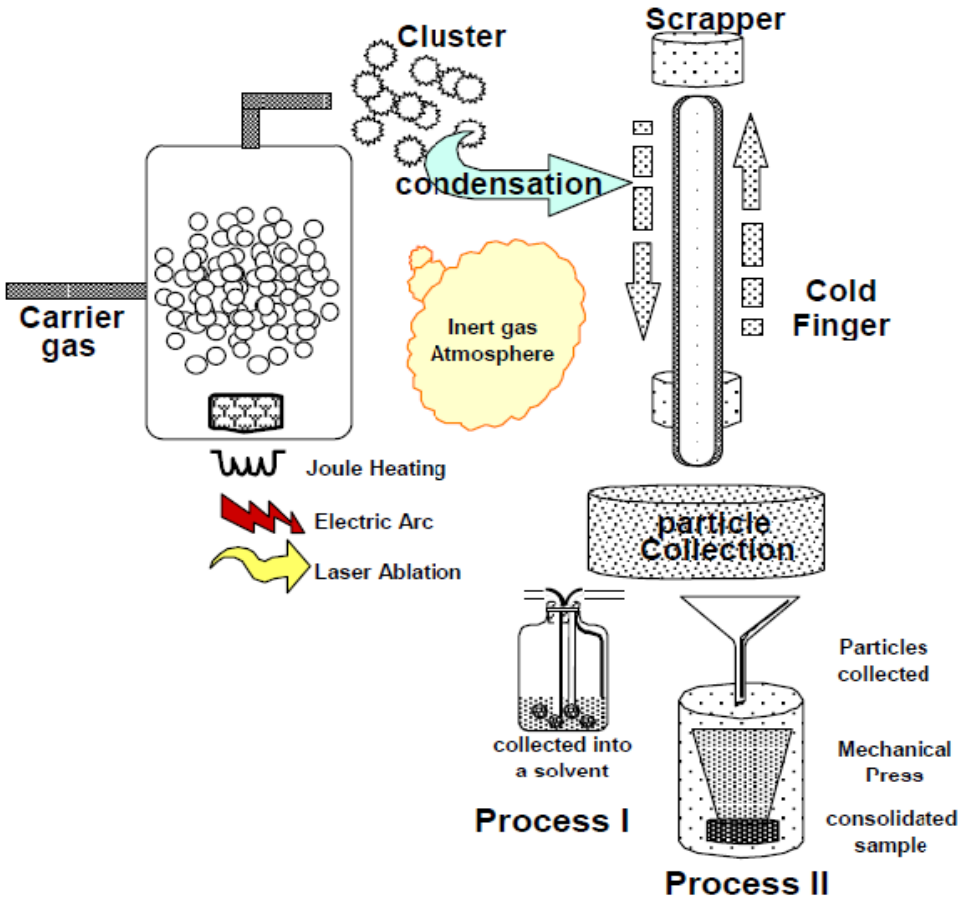

Figure1.18 The gas condensation synthesis of nanomaterials followed by consolidation in a mechanical press or collection in an appropriate solvent media

Chemical Vapour Condensation (CVC)

As shown schematically in Figure 1.19, the evaporative source used in GPC is replaced by a hot wall reactor in the Chemical Vapour Condensation (CVC) process. Depending on the processing parameters, nucleation of nanoparticles is observed during CVC of thin films and poses a major problem in obtaining good film qualities. It was intended to adjust the parameter field during the synthesis in order to suppress film formation and enhance homogeneous nucleation of particles in the gas flow. It is readily found that the residence time of the precursor in the reactor determines if films or

particles are formed. In a certain range of residence time both particle and film formation can be obtained.

Adjusting the residence time of the precursor molecules by changing the gas flow rate, the pressure difference between the precursor delivery system and the main chamber occurs. Then the temperature of the hot wall reactor results in the fertile production of nanosized particles of metals and ceramics instead of thin films as in CVD processing. In the simplest form a metal organic precursor is introduced into the hot zone of the reactor using mass flow controller [91].

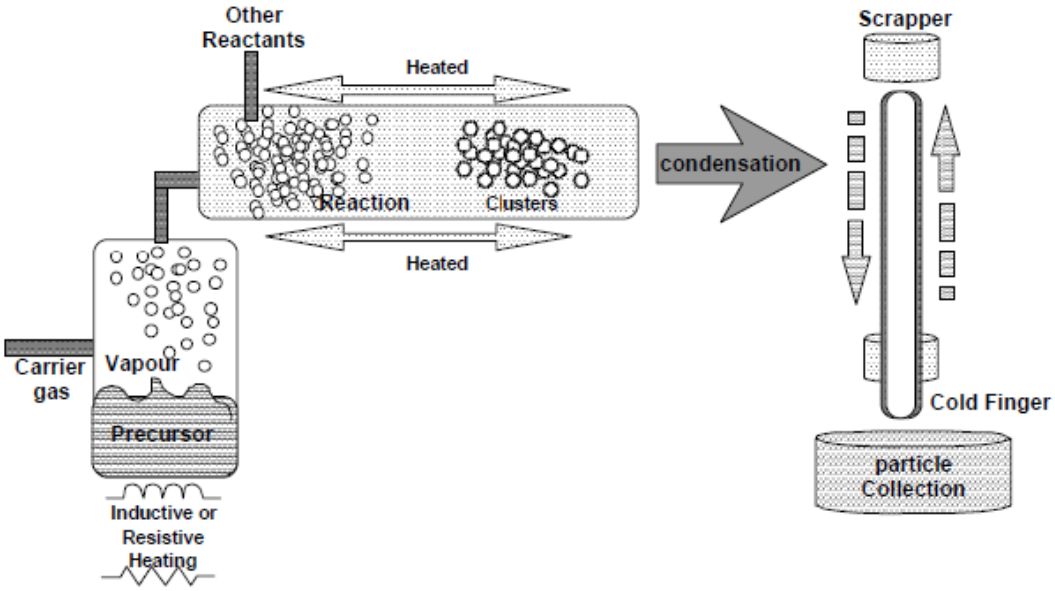

Figure 1.19 A typical CVC reactor [91]

Sputtered Plasma Processing

This method is a variation of the gas-condensation method excepting the fact that the source material is a sputtering target and this target is sputtered using rare gases and the constituents are allowed to agglomerate to produce nano material. Both dc (direct current) and rf (radio-frequency)

sputtering has been used to synthesize nanoparticles. Again reactive sputtering or multi-target sputtering has been used to make alloys and/or oxides, carbides, nitrides of materials. This method is specifically suitable for the preparation of ultrapure and non-agglomerated nanoparticles of metal.

Microwave Plasma Processing

This technique is similar to the previously discussed CVC method but employs plasma instead of high temperature for decomposition of the metal organic precursors. The method uses microwave plasma in a 50 mm diameter reaction vessel made of quartz placed in a cavity connected to a microwave generator. A precursor such as a chloride compound is introduced into the front end of the reactor. The major advantage of the plasma assisted pyrolysis in contrast to the thermal activation is the low temperature reaction which reduces the tendency for agglomeration of the primary particles. Additionally, it has been shown that by introducing another precursor into a second reaction zone of the tubular reactor, e.g., by splitting the microwave guide tubes, the primary particles can be coated with a second phase. For example, it has been demonstrated that ZrO_2 nanoparticles can be coated by Al_2O_3 [91].

Particle Precipitation Aided CVD

In this process, colloidal clusters of materials are used to prepare nanoparticles. The CVD reaction conditions are so set that particles form by condensation in the gas phase and collect onto a substrate, which is kept under a different condition that allows heterogeneous nucleation.

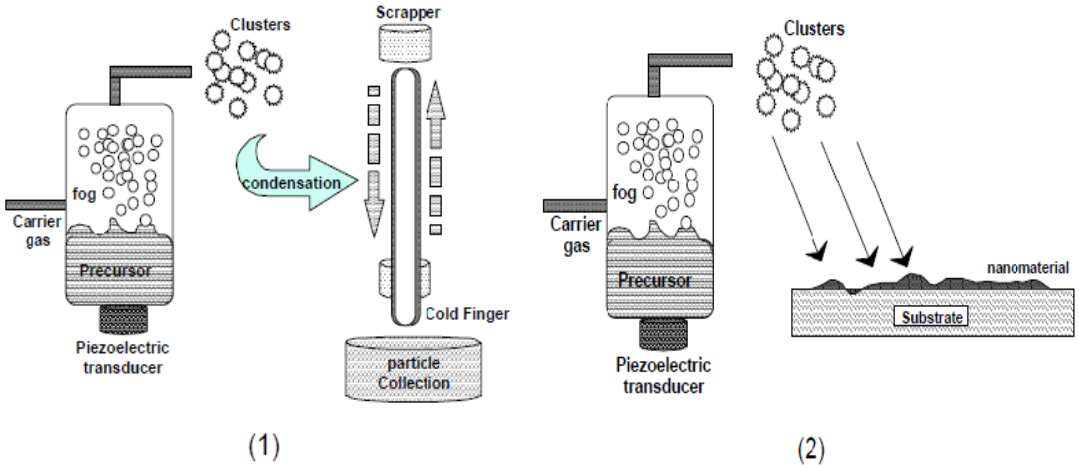

Figure 1.20 Schematic representations of (1) nanoparticle, and (2) particulate film formation

By this method both nanoparticles and particulate films can be prepared. This method has been used to form nanomaterials of SnO_2 by a method called pyrosol deposition process, where clusters of tin hydroxide are transformed into small aerosol droplets, following which they are reacted onto a heated glass substrate [89].

Laser Ablation

Laser ablation has been extensively used for the preparation of nanoparticles and particulate films. In this process a laser beam is used as the primary excitation source of ablation for generating clusters directly from a solid sample in a wide variety of applications. The small dimensions of the particles and the possibility to form thick films make this method quite an efficient tool for the production of ceramic particles and coatings and also an ablation source for analytical applications such as the coupling to induced coupled plasma emission spectrometry (ICP). The formation of the nanoparticles occurs following a liquification process, which generates

aerosols, followed by the cooling/solidification of the droplets resulting in the formation of fog. The general dynamics of both the aerosol and the fog favors the aggregation process and micrometer-sized fractal-like particles are formed. The laser spark atomizer can be used to produce highly mesoporous thick films and the porosity can be modified by the carrier gas flow rate. ZrO_2 and SnO_2 nano particulate thick films were also synthesized successfully using this process with quite identical microstructure. Synthesis of other materials such as lithium manganate, silicon and carbon has also been carried out by this technique [91].

1.17 Microemulsion

Micro emulsions are isotropic mixtures of oil, water and surfactant, usually, with a co – surfactant and the oil being a mixture of different hydrocarbons and olefins [95]. During more than the last five decades after the discovery of micro emulsions by Jack H. Shulman and co-workers at Columbia University in 1959 [96], there has been tremendous progress made in applying microemulsion techniques in a plethora of research and industrial process.

Microemulsions are self-assembled nano-scale entities [97–102]. On the basis of size alone, however, the term microemulsion is a misnomer, and has led to confusion. *Vis-à-vis* standard emulsions, which normally consist of dispersed droplet sizes in the low micron range (1- 20 μm), microemulsion dispersed domains are normally well-below 100 nm in diameter. More recently, nano-emulsions have gained attention as vehicles for controlled drug release and delivery. Despite the fact that these also consist of nano-scale

droplets (typically 20-200 nm), but they lack the thermodynamic stability of microemulsions [98,103].

As the author has used microemulsion technique for the synthesis of nano particles, therefore, this technique is discussed in somewhat detail. Oil and water are immiscible. They separate into two phases when mixed, each saturated with traces of the other component [104]. An attempt to combine the two phases requires energy input to establish water-oil contacts that would replace the water-water and oil-oil contacts. The interfacial tension between bulk oil and water can be as high as 30-50 dynes/cm [105]. To overcome this, surfactants can be used. Surfactants are surface-active molecules. They contain water-loving (hydrophilic) and oil-loving (lipophilic) moieties [106]. Because of this characteristic, they tend to adsorb at the water-oil interface. If enough surfactant molecules are present, they align and create an interface between the water and the oil by decreasing the interfacial tension [105].

An emulsion is formed when a small amount of an appropriate surfactant is mechanically agitated with the oil and water, which leads to two-phase dispersion where one phase exists as droplets coated by surfactant that is dispersed throughout the continuous, other phase. These emulsions are milky or turbid in appearance due to the fact that the droplet sizes range from 0.1 to 1 micron in diameter [106]. As a general rule, the type of surfactant used in the system determines which phase is continuous. If the surfactant is hydrophilic, then oil will be emulsified in droplets throughout a continuous water phase. The opposite is true for more lipophilic surfactants. Water will be emulsified in droplets that are dispersed throughout a continuous oil phase in this case [107].

Emulsions are kinetically stable, but are ultimately thermodynamically unstable. Over the time, they will begin to separate back into their two phases. The droplets will merge together, and the dispersed phase will sediment (cream) [106]. At this point, they degrade back into bulk phases of pure oil and pure water with some of the surfactant dissolved in preferentially in one of the two [105, 108].

The term *microemulsion* is applied to systems prepared by emulsifying oil in an aqueous surfactant and then adding a fourth component called a cosurfactant, which is generally an intermediate chain length alcohol such as pentanol or butanol. Microemulsions are quite distinct from previously mentioned emulsions in a number of ways, the main distinction being that emulsions are thermodynamically unstable and have a finite lifetime after which the emulsion breaks. Microemulsions on the other hand are thermodynamically stable compositions which form spontaneously or with gentle agitation once the correct composition reached. They have potentially infinite lifetimes which depend on storage conditions. Other distinctions include droplet size and the color of the system. Emulsion system generally have spherical droplets with diameters large enough to scatter white light and are therefore opaque in appearance, whereas microemulsions have droplet sizes of 100 nm or less and are transparent. Microemulsions can be either oil – in – water (O/W), water – in – oil (W/O) or a mixture of these two called a biocontinuous phase.

Microemulsion droplets differ from micellar aggregates in that the dispersed phase of a microemulsion is contained in the interior of the microemulsion droplet and these droplets tend to be slightly larger than

micelles. Micremulsions also have superior solubilizing power over micelles due to the presence of the dispersed phase and the larger droplet size. The formation of micelles depends on the concentration of surfactants in solution with micellization occuring once the *critical micellar concentration* (CMC) is reached.

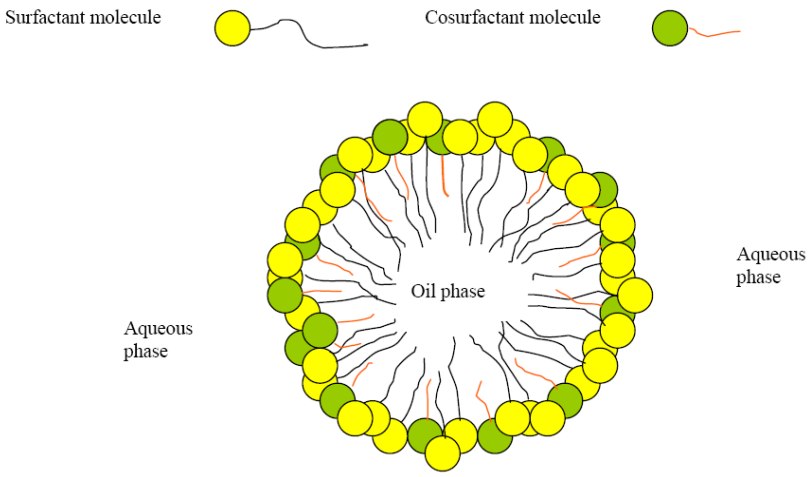

Figure 1.21 Cross sectional view of a spherical O/W microemulsion droplet

The formation of microemulsions however has very specific compositional requirements with concentrations of each component critical to their formation and to the type of microemulsion formed. Microemulsions can form spontaneously once the correct proportions of each component is reached and remains stable, implies that there is a minimum of interfacial free energy at the interface between the oil and aqueous phases which is occupied by the surfactant and cosurfactant.

Microemulsion Phase Diagrams

Phase diagrams are used to display regions in which different phases exist in three component systems. They are triangular in shape with each corner of the triangle representing 100% of each component. Although

microemulsions generally contain three key components: surfactant, oil and water.

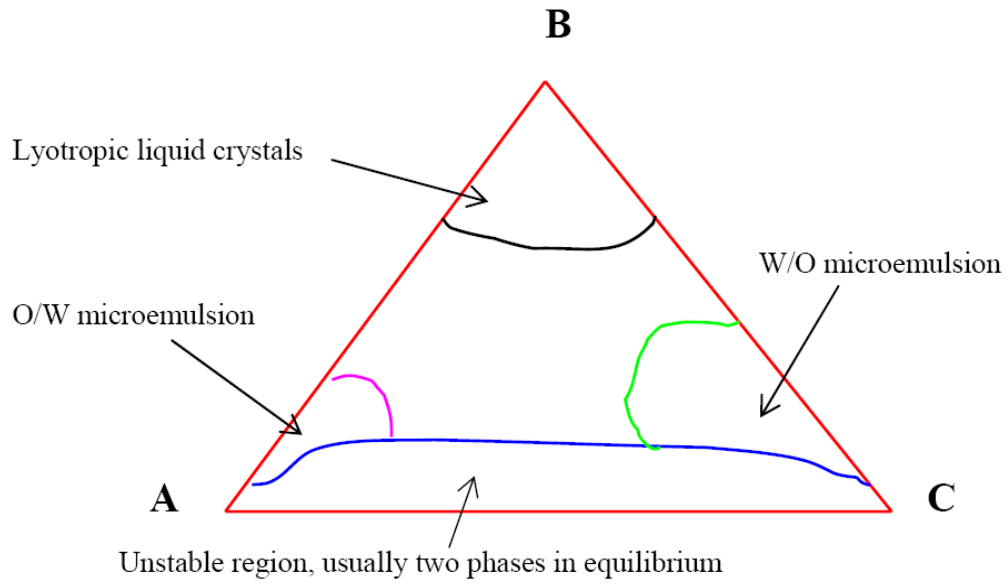

Figure 1.22 A three-component phase diagram indicating the composition of the various phases (A = 100% water; B = 100% surfactant; C = 100% oil)

The phase diagram in figure 1.22 is a representation of one that would be specific to three defined components at constant temperature and pressure. The character of a microemulsion and whether one will be formed is determined by variables such as the type and concentrationof the surfactant employed, temperature, the nature and concentration of the oil phase, aqueous electrolytes and the relative ratios of the component. The combined use of a range of these variables will generate distinct phase diagrams for each system used.

Applications of Microemulsion

Various applications of micro emulsion are summarized in the following figure. This indicates that the micro emulsion technique is a versatile technique finding applications in the numerous fields [108]

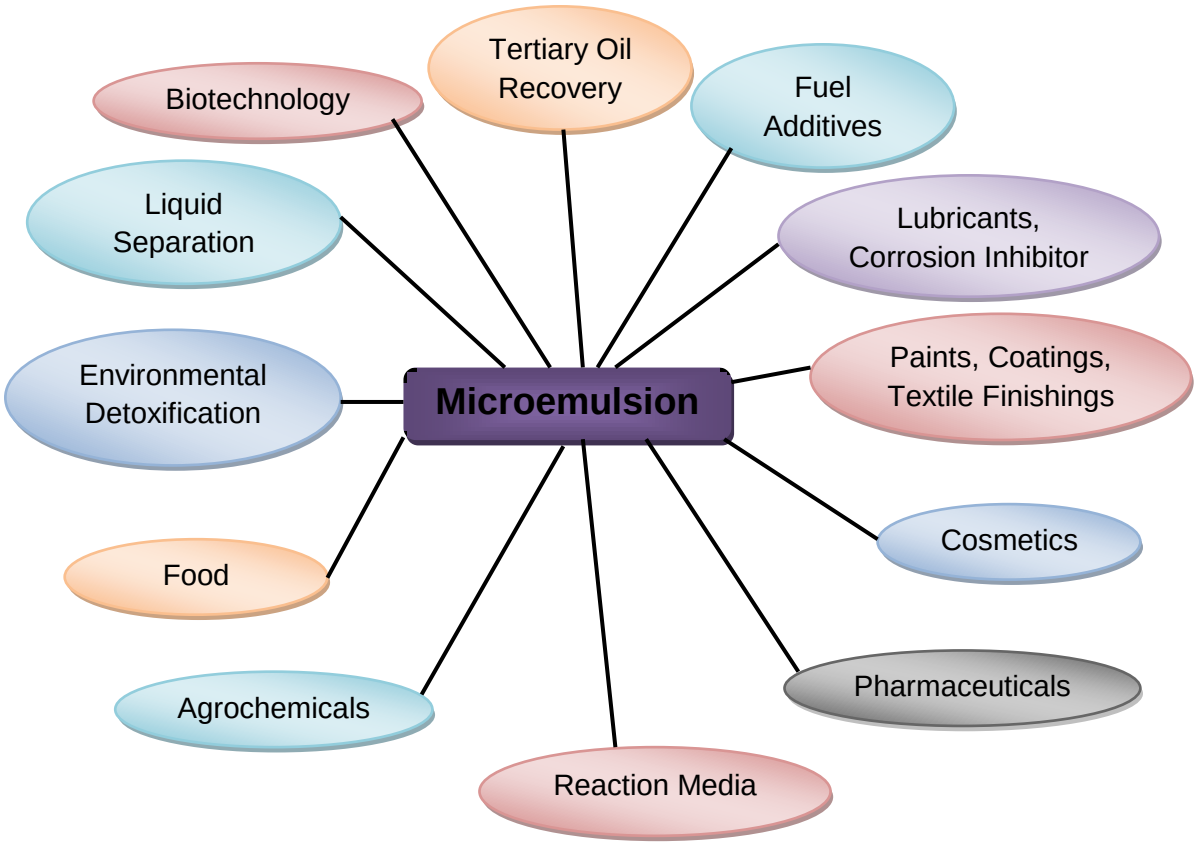

Advantage and Disadvantage of Microemulsion

Microemulsions have advantages as well as disadvantages. Because of the ease of microemulsion preparation, drugs that are thermo-labile are easily incorporated without the risk of degradation [109]. In drug delivery, microemulsions ultimately increase the surface area of drugs, which improves their solubilization and permeation behavior. They are shown to increase solubility and bioavailability of Class II and IV drugs of the biopharmaceutical drug classification system. Class II drugs have high solubility but low permeability and Class IV drugs have low solubility and low permeability [109]. Plasma concentration profiles and drug bioavailability have been shown to be more reproducible in microemulsion formulations [110,111]. The rate of penetration of drug is much faster from microemulsion systems than from other drug delivery vehicles, while having controlled drug release rates, slow

degradation, and target specificity [109]. Microemulsions have a higher solubilization capacity for both hydrophilic and hydrophobic compounds than simple micellar solutions. Because of their thermodynamic stability, they are more favorable than regular emulsions or suspensions since microemulsions can be established or manufactured with very little energy input and have a long shelf life [110].

Microemulsions have some disadvantages as well. Formation of microemulsions generally requires large amounts of surfactants and/or co-surfactants. All of these at high concentrations are, generally, irritating, if not slightly toxic, to the biological system [112, 113]. Many outside factors, such as temperature and pH, influence the stability of microemulsions as well. The effects of these factors must be examined for each potential formulation [108].

1. 18 Surfactants

Surfactants are materials which exhibit the characteristics of reducing the interfacial tension between two immiscible liquids by way of enhanced adsorption at the interface. These surfactants or ‘surface active reagents’ are usually amphiphilic organic compounds, i.e., in the same molecule possessing two distinct groups which differ greatly in their solubility relationships. Generally speaking, surfactants possess a hydrophobic tail group and a hydrophilic head group. The hydrophobic tail is usually a long chain hydrocarbon and the hydrophilic head is an ionic or highly polar group that imparts water solubility to the molecule. The unique amphiphilic structure of surfactants gives rise to some characteristic properties which fall into two broad categories.

(a) Adsorption, which is the tendency of a surfactant molecule to collect at an interface. The adsorption properties of surfactants means these molecules are usually found at the interface between oil and water phases with the hydrophilic head groups favoring inclusion in the water phase and the hydrophobic tails favoring inclusion in the oil phase.

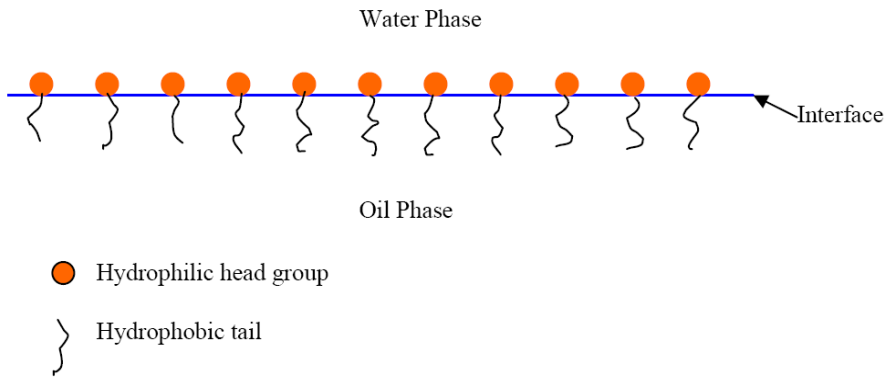

Figure 1.23 Adsorption of surfactant molecules at an oil/water interface

(b) Self – assembly, is the property of surfactants where they arrange themselves into organized strucutres in aqueous solutions, once a certain concentration is reached, usually referred to as the critical micalle concentration (CMC) [114]. At low concentrations, the surfactant molecules from solutions in water but some molecules will be adsorbed at the air/solution interface and onto the walls of the containing vessel. As the concentration is increased, the surface becom covered with a monolayer of surfactant molecules. Further increase in the concentration causes the normal dissolution processes to cease and the molecules in solutionbegin to aggregate into organized micelles, which occurs at a precisely defined concentration [115].

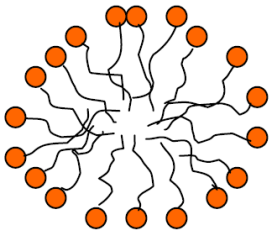

Figure 1.24 Spherical surfactant micelle

Micelles are often globular and roughly spherical in shape but ellipsoids, cylinders and bilayers or vasicles are also possible. The shape and size of a micelle depends on the molecular geometry of its surfactant molecules and solution conditions such as surfactant concentration, temperature, pH and ionic strength.

Surfactants can be classed in a number of ways but the most useful classification method is based on the nature of their hydrophilic head groups.

Anionic Surfactants

Anionic surfactants are the largest class of surfactants in general use today and have a head group composd of highly electro-negative atoms making these groups strongly polar, altogether, a small counter ion is also present which is ususally small cationsuch as sodium ion. This class of surfactant can be divided into subgroups such as alkali carboxylates or soaps, sulpbates such as aliphatic and alkylaryl sulphonates and to a lesser degree phosphates [116]. Figure 1.25 illustrates sodium dodecyl sulphate (SDS), a very commonly used anionic surfactant.

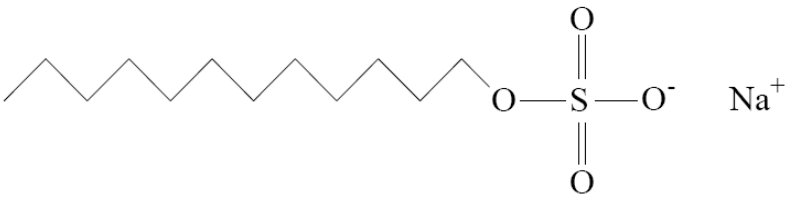

Figure 1.25 Structure of anionic surfactant, SDS

Cationic Surfactants

Cationic surfactants as the name suggests, possess positively charged head groups which usually contain a nitrogen atom or an amide group. There are two important categories of cationic surfactants, which differ mainly in the nature of the nitrogen containing group [116]. It consists of alkyl nitrogen compounds such as ammonium salts containing at least one long chain alkyl group, with halide, sulphate or acetate counter – ions. Figure 1.26 illustrates cetyltrimethylammonium bromide (CTAB), a commonly used cationic surfactant.

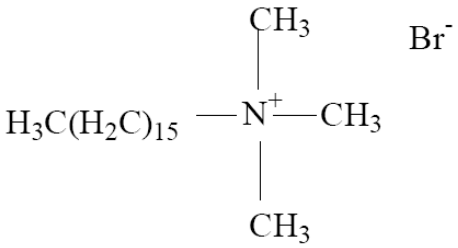

Figure 1.26 Structure of cationic surfactant, CTAB

Non – ionic surfactants

The two previously mentioned surfactants dissociate in water to produce a net charge on the head group of the molecule. This is not a necessary requirement for the existence of surface activity and non-ionic

surfactants can offer advantages over ionic surfactants. Non – ionic surfactans can be further divided into sub groups such as block copolymer non-ionic surfactants.

Zwitterionic surfactants

Zwitterionic or amphoteric surfactants contain, or have the potential to form, both positive and negative functional groups under specified conditions. The zwitterionic nature of these surfactants makes them very much compatible with other form of surfactants.

Aqueous Surfactant Structures

Surfactant molecules in solution exhibit unususal physical properties. In dilute solutions the surfactant acts as a normal solute but upon reaching a well defined concentration, abrupt changes in physical properties are observed. These properties include, osmotic pressure, turbidity, electrical conductance and surface tension.

1.19 Crystallization of Active Pharmaceutical Ingredients (API)

The study of crystalline properties of API is very important, which helps to identify the active sites for molecular binding during the action *in vivo*. Various physical properties such as thermal stability, dielectric properties, etc are helpful to understand the pharmaco-kinetics and increasing its shelf life. Generally, crystallization is carried out in the final stage during the manufacture of API. Moreover, the structure based approach requires effectively designed and commercially viable crystalline substances for optimal drug performance.

Characterization of grown pharmaceutical compound crystals or APIs is important. Thermogravimetry is used for assessing thermal stability and content of water as moisture or in crystallization form. Using Differential Scanning Calorimetry (DSC) a polymorphism in a compound can be predicted. Apart from this, DSC can be used for determination of solid – solid transition occuring before melting, melting of compound and associated mioisture [117]. The dielectric study of pharmaceutical compounds is focused mainly on four aspects: analysis of water, estimation of molecular mobility, estimation of the distribution of materials through out the system and general formulation characterization [118, 119]

1.20 Effect of nano size on API

The number of poorly soluble drugs and drug candidates (new chemical compounds) is rapidly increases. As per one estimate nearly 70% of molecules developed from synthesis have solubility problems and consequently face poor oral bioavailability and delivery problems. The poor solubility over here means that a compound is poorly soluble in case its oral single dose does not dissolve in 250 ml gastric/intestinal fluid or a compound can not be injected intravaneously in an acceptable injection volume for a single dose. At the beginning of the 1990s the drug nano crystals have been developed as more efficient approach to increase drug solubility and dissolution velocity. After successful trials and tests the first drug was marketed in the year 2000 as Rapamune® [120,121].

Reducing the particle size of an API is an efficient and reliable technique of improving the bioavailability of relatively insoluble drugs that is

often limited by poor dissolution rates. Thus by reducing particle size from micron to nanometer the surface area increases and hence the dissolution increases. The nanotechnology is effectively employed in medicine to achieve the targeted drug delivery, encapsulation of API, altered dosages, etc. [122-124].

The increase in the surface area leads to increse the dissolution rate according to Noyes – Whitney equation, which is expected to be achieved by increasing surface area to volume ratio in nano – particles. Another aspect is the increase in the saturation solubility of nano – sized compounds compared to micro – meter particles, precisely, the kinetic saturation solubility increases [120]. Further ahead, it is considered in the other opinion that the amorphous materials possess higher saturation solubility compared to crystalline material, for instance, itraconazole amorphous has 60 times higher solubility than the crystalline one [125]. Therefore, to obtain highest supersaturation, it can be considered the ideal drug nano particles will be not nano – crystalline but nano – amorhous. It is important to note, according to one market survey, that the market of nano pharmaceuticals has grown from $406 million in 2004 to $16.6 billion in 2014. In today's world economy, a pharmaceutical industry faces enormous pressure to deliver high-quality products to patients while maintaining profitability. Therefore, pharmaceutical companies are applying nanotechnology to enhance or supplement drug target discovery and drug formulation. Nano-pharmaceuticals reduce the cost of drug discovery, design and development and enhance the drug discovery process. This results into the improved Research and Development success rate, which enables faster introduction of new, cost-effective products to the marketplace.

The nano particles have following important advantages which are summerized by Bellare [126]

- Macrophage evasion
- Cross blood – brain barrier
- Slip through cell junction
- Bio – integrate
- Deliver large aliquots
- Enhance permeation and retention

The impact of nano biotechnology on the development of new drug delivery syatem has been reviewed by Kayser *et al.* [127]. Nano particles have been developed as an important strategy to deliver conventional drugs, recombinant, proteins, vaccines and more recently nucleotides. Nanoparticles and other colloidal drug delivery systems modify the kinetics, body distribution and drug release of an associated drug. While, other effects are tissue or cell specfic targeting of drugs and the reduction of unwanted side effects by a controlled release.

1.21 Reverse Pharmacology

There are two versions of the term Reverse Pharmacology available. The first one defines the discipline that involves research for the quest of receptors and action paths for the indogenios molecules discovered recently but which has yet unknown physiological roles. The second version, is a new and popular path ivolved in India. It implies the path of that begins with the robust documentation of experiential therapeutic varieties at the bedside in

Ayurveda, of Ayurveda and for Ayurveda. This is an organized follow up of Ayurvedic pharmacoepidemiology or observational therapeutics, based on the specific epistemeology [128]. Once hits are identified, exploratory studies are conducted with relevant safety/ efficacy markers, both from Ayurveda and modern medicine. The emergent would suggest that hits are indeed leads or not. Once the leads are defined at several levels of biological organization, the candidate extracts/molecules can be subjected to state of the art expermental and clinical models relevant to drug discovery [129].

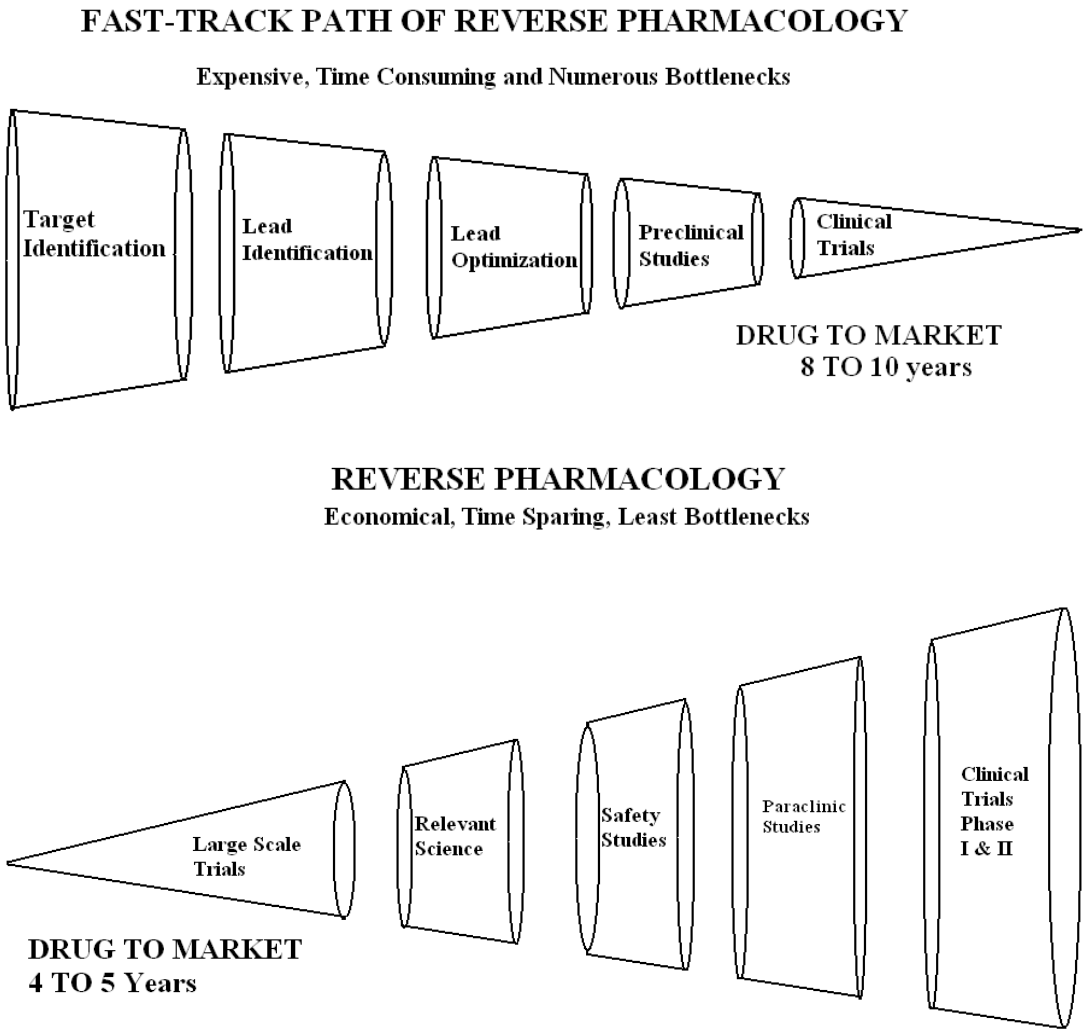

Reverse Pharmacology can be redefined as a trans discipline that initiates drug discovery and development from traditional knowledge/

practises at the bed side through rowbust and objective experiential documentation. Then it systamatically explores Ayurvedic and current scientific mechanisms as to satisfy, efficacy and therapeutic place for evolving either an extract or a molecule as a new drug [130].

The Reverse Pharmacology is discussed briefly as the growth inhibition of crystals in the presenrce of different inhibitors and herbal extracts forms its important component. Growth and deposition of various bio – crystals as well as bio – minerals invites different ailments such as urinary stones, arthritis, etc. Here the aim is not to grow large crystals but not to allow the growth of crystals and preferably the dissolution of crystals. For this growth inhibition studies of various bio – crystals the gel based crystal growth technique is found to be suitable [30, 32], which will be discussed in chapter VI.

1.22 Objective of the Present Study

Since the study of the present researcher is based on crystallization and nano particle synthesis of organic bio materials and APIs, it requires to cross the traditional boundary of the physics subject. The work carried out by the author is not only limited to growth and characterization of certain crystals (e.g., cholesterol), but it also covers the growth inhibition studies of the crystals to check the inhibitory effect of herbal extract selected. Therefore, this interdisciplinary research work requires integrating data, theories, methodologies, perspectives, and concepts from multiple disciplines like physics, chemistry, material science, botany, ayurveda, pharmacology, and medicine. The objectives envisaged to be achieved during the course of present research work are as follows.

- As pyrimidine and pyrazole based compounds find pharmaceutical applications the objective is to grow the crystals of Pyrimidine and Pyrazole moity compounds through solution growth technique and the synthesis of nano particles of the same compounds through microemulsion techniques.

- To grow cholesterol crystals by single diffusion gel growth technique, which provides simplified *in vitro* model of the highly complex growth of cholesterol *in vivo*, and characterize them by different techniques, Also, to synthesize cholesterol nano particles by micro emulsion technique and compare the characterizations of crystalline and nano – particles samples..
- To characterize the grown crystals and nano particles using techniques like powder X-ray diffraction (XRD), single crystal XRD, Transmission Electron Microscopy (TEM), Fourier Transform Infrared Spectroscopy (FT-IR), Thermo-gravimetric Analysis (TGA), Differential Thermal Analysis (DTA) and Differential Scanning Calorimetry (DSC), Dynamic Light Scattering (DLS) and dielectric study, with aim to compare their various properties and to understand the effect of particle size.
- To carry out growth inhibition study of cholesterol crystals in the presence of herbal extract of *Fagonia Cretica* Linn. This study hopefully will suggest same potent inhibitor for cholesterol crystals, which will have therapeutic implications from Reverse Pharmacology point of view.

- As curcumin is a natural pigment of turmeric and finds many therapeutical applications, the aim is to synthesize curcumin nano-particles and characterize them.

References

[1] H. J. Scheel, *J. Cryst Growth.*, **211** (2000) 1.

[2]www.kgbconsultingltd.com/downloads/manufacture_of_Bulk_crystals_In_ western Europe.pdf.

[3] H. J. Scheel, *The Development of Crystal Growth Technology*, in *Crystal Growth Technology*, Eds. H. J. Scheel, T. Fukuda, John Wiley & Sons Ltd., Chichester (2003).

[4] B. R. Pamplin, *Crystal Growth*, Peragamon Press, Oxford, UK (1975).

[5] J. J. Gilman, *The Art and Science of Growing Crystals*, John Wiley, NewYork, USA (1963).

[6] R. A. Laudise, *Techniques of Crystal Growth*, in *Proc. Int. Conf. Cryst. Growth*, Boston, Peragamon Press, Oxford, UK (1966).

[7] H. J. Scheel, *Historical Introduction*, in *Handbook of Crystal Growth*, Ed. D. T. J. Hurle, **Vol. 1**, Elsevier, Amsterdam, Netherland (1993).

[8] M. Schieber, *Introductory Remarks in Techniques of Crystal Growth* in *Proc. Int. Conf. Crystal Growth*, Boston, Pergamon Press, Oxford, UK (1966).

[9] J. P. van der Eerden, *Lecture Notes on Fundamentals of Crystal Growth,* World Scientific Publishing, Singapore (1993).

[10] P. S. Raghavan, P. Ramasamy, *Crystal Growth Process and Methods*, KRU Publication, Kumbhakonam,India (2000).

[11] B. Chalmers, *Principles of Solidification*, John Wiley, New York, USA (1964).

[12] N. Bardsley, D. Hurle, J. B. Mullin, *Crystal Growth : A Tutorial Approach,*

North-Holland Series in Crystal Growth, Vol. 2, Amstredam, Netherland (1979).

[13] A. V. Shubnikov, A. A. Chernov, N. N. Sheftall, *Growth of Crystals*, Kluwer Academic Publishers, Dordrecht, Netherland (1979).

[14] A. Majchrowski, *Single Crystal Growth, Characterization and Applications,* Ed. J. Zielinski, SPIE-International Society for Optical Engineering, Bellingham, Washington, USA (1999).

[15] K. Byrappa, T. Ohachi (Eds), *Crystal Growth Technology,* William Andrew, New York, USA (2003).

[16] D. T. J. Hurle, *Handbook of Crystal Growth*, **Vol. 1 – 3**, Elsevier Science, Amsterdam, Netherland (1994).

[17] T. Nishinaga, K. Nishioka, J. Harada, A. Sasaki, H. Takei, *Advances in Understanding of Crystal Growth Mechanism",* Elsevier, Amsterdam Netherland (1997).

[18] A. Holden, P. S. Morison, *Crystal and Crystals Growing*, MIT Press, Cambridge, UK (1982).

[19] J. Stangl, J. Stang, *Crystals and Crystal Gardens You Can Grow*, The Horn Book, Boston, USA (1990).

[20] J. C. Brice, *Crystal Growth Process,* John Wiley, New York, USA (1986).

[21] A. A. Chernov, *Modem Crystallography III- Crystal Growth,* Vol. 36, Springer- Verlag, Solid State Series, Berlin, Germany (1984).

[22] M. M. Faktor, I. Garrett, *Growth of Crystals from Vapour*, Chapmann and Hall, London, UK (1974).

[23] J. C. Brice, *The Growth of Crystals from Liquids,* North Holland, Amsterdam, Netherland (1973).

[24] H. K. Henisch, *Crystals in Gels and Liesegang Rings,* Cambridge Uni. Press, Cambridge, UK (1988).

[25] H. E. Buckley, *Crystal Growth*, John Wiley, New York, USA (1951).

[26] D. Elwell, H. J. Scheel, *Crystal Growth from High-Temperature Solutions*, Academic Press, London UK (1975).

[27] N. Mirkin, A. Moreno, *J. Mex. Chem. Soc.*, **49** (2005) 39.

[28] G. Dhanaraj, K. Byrappa, V. Prasad, M. Dudley, *Hand book of Crystal Growth*, Springer, Heidelberg, Germany (2010).

[29] S. Joseph, *Ph.D. Thesis,* Saurashtra University, Rajkot (1997).

[30] V. S. Joshi, *Ph.D. Thesis,* Saurashtra University, Rajkot (2001).

[31] R. M. Dabhi, *Ph.D. Thesis,* Saurashtra University, Rajkot (2002).

[32] B. B. Parekh, *Ph.D. Thesis,* Saurashtra University, Rajkot (2005).

[33] S. R. Suthar, *Ph.D. Thesis,* Saurashtra University, Rajkot (2007).

[34] D. J. Dave, *Ph.D. Thesis,* Saurashtra University, Rajkot (2011).

[35] K. D. Parikh, *Ph.D. Thesis,* Saurashtra University, Rajkot (2011).

[36] C. K. Chauhan, *Ph.D. Thesis,* Saurashtra University, Rajkot (2011).

[37] F. C. Frank, *Adv. in Phys. Phil. Mag. Suppl.,* **1** (1952) 91.

[38] W. K. Burton, *Penguin Sci. News*, **21** (1951) 285.

[39] A. R. Varma, *Crystal Growth and Dislocations.* Butterworths, London, UK (1953).

[40] P. Bennema, G. H. Gilmer, *Kinetics of Crystal Growth in Crystal Growth*; *An Introduction,* Ed. P. Hartman, North Holland, Amsterdam, Netherland (1973).

[41] K. Sankaranarayanan, P. Ramasamy, *J. Cryst. Growth.,* **280** (2005) 467.

[42] H. E. Buckley, *Crystal Growth*, John Wiley, New York, USA(1951).

[43] J. A. James, R. C. Kell, *Crystal Growth*, Ed. B. R. Pamplin, Peragamon Press, Oxford, UK (1975).

[44] H. K. Henisch, J. Dennis, J. I. Hanoka, *J. Phys. Chem. Solids.*, **26** (1965) 493.

[45] A. R. Patel, A. V. Rao, *Bull. Mater. Sci.*, **4** (1982) 527.

[46] A. E. Alexander, P. Johnson, *Colloid Science,* Vol. 2, Clarendon Press,Oxford, UK (1949).

[47] S. Sahoo, N. Kumar, C. Bhattacharya, S. S. Sagiri, K. Jain, K. Pal, S. S. Ray, B. Nayak, *Des. Monomers Polym.*, **14** (2011) 95.

[48] R. G. Jones, *Pure Appl. Chem.*, **79** (2007) 1801.

[49] W. D. Treadwell, W. Wieland, *Helv. Chem. Acta*, **13** (1930) 856.

[50] Z. Blank, W. Brenner, *Nature*, **222** (1969) 79.

[51] J. W. McCauley, R. Roy, *Am. Miner*., **59** (1974) 947.

[52] A. R. Patel, S. K. Arora, *J. Mater. Sci*, **11** (1976) 843.

[53] A. R. Patel, A. V. Rao, *J. Cryst. Growth*, **38** (1977) 288.

[54] S. Bhat, P. N. Kotru, *Mater. Sci. Eng.*, **B23** (1994) 73.

[55] V. S. Joshi, M. J. Joshi, *Cryst. Res. Technol.*, **38** (2003) 817.

[56] B. B. Parekh, P. M. Vyas, S. R. Vasant, M. J. Joshi, *Bull. Mater. Sci.*, **31** (2008) 143.

[57] S. L. Garud, K. B. Saraf, *Bull. Mater. Sci.*, **31** (2008) 639.

[58] S. N. Kalkura, S. Natarajan, *Crystallization from Gels* in *Springer Handbook of Crystal Growth* Eds. G. Dhanaraj, K. Byrappa, V. Prasad, M. Dudley, Springer-Verlag, Berlin Heidelberg, Germany (2010).

[59] D. K. Sawant, H. M. Patil, D. S. Bhavsar, J. H. Patil, K. D. Girase, *Arch. Phys. Res*., **2** (2011) 67.

[60] B. Cudney, S. Patel, A. McPherson, *Acta Cryst.*, **D50** (1994) 479.

[61] C. J. Plank, *J. Colloid Sci.*, **2** (1947) 413.

[62] K. D. Parikh, B. B. Parekh, D. J. Dave, M. J. Joshi, *Indian J. Phys.*, **80** (2006) 719.

[63] M. C. Robert, K. Provost, F. Lefaucheux, In *"Crystallization of Nucleic Acids and Proteins, a Practical Approach"*, Eds. A. Ducruix, R. Giege Oxford University Press, Oxford, UK (1992).

[64] E. Hatschek, Simon, *Kolloid Z*., **10** (1912) 265.

[65] P. F. Kurz, *Ohio J. Sci*., **66** (1966) 349.

[66] J. J. O'Connor, M. Dipietro, A. Armington, B. Rubin, *Nature*, **212** (1968) 68.

[67] D. A. Glocker, I. F. Soest, *J. Chem. Phys*., **51** (1969) 3143.

[68] B. Brezina, J. Havrankova, *Mater. Res. Bull*., **87** (1971) 537.

[69] B. B. Parekh, M. J. Joshi, A. B. Vaidya, *Curr. Sci.,* **93** (2003) 373.

[70] R. P. Feynman, Miniaturization, Reinhold, New York, USA (1961).

[71] P. L. Packman, *Science*, **285** (1999) 2079.

[72] G. M. Whitesides, *Nanotechnology: Art of the Possible*, Technology Review, Technology Review Inc., Cambridge,MA, Nov/Dec (1998).

[73] C. N. R. Rao, A. K. Cheetham, *J. Mater. Chem.*, **11** (2001) 2887.

[74] D. Minoli, "*Nanotechnology Applications to Telecommunications and Net working,*" Wiley Inter-science, Hoboken, USA (2006).

[75] http://www.sustainpack.com/images/scales.gif.

[76] C. C. Koch, D. G. Morris, K. Lu and A. Inoue, *MRS Bulletin* (1999).

[77] J. Lue, *J. Phys. Chem. Solids*, **62** (2001)1599.

[78] D. Awschalom, S. Von Molnar, *Physical Properties of Nano-scale Magnets Nanotechnology*, Ed.G. Timp, Springer- Verlag, Heidelberg, Germany (1999).

[79] A. Nabok, *Organic and Inorganic Nanostructures*,Artec House, Boston, USA (2005).

[80] C. P. Poole Jr and F. J. Owens, *Introduction to Nano-technology* Wiley Intersciences, Hoboken, USA (2003).

[81] S. N. Khanna, *Handbook of Nano Phase Materials*, Marcel Decker,New York, USA (1997).

[82] M. Ratner and D. Ratner D, *Nanotechnolgy*, Pearson, Singapore (2003).

[83] T. Pradeep, *Nano: The Essentials, Understanding Nano-science and Technology*,Tata - McGraw Hill, New York, USA (2007).

[84] L. Jacak, P. Hawrylak, A. Wojs, *Quantum Dots,*Springer – Verlag, Berlin, Germany (1998).

[85] M. Henini, *Materials Today,* (2002) 48.

[86] M. C. Roco, B. Harthron, D. Guston, P. Shapira, *J. Nanopart. Res.,* DOI: 10 – 1007/s11051-011-0454-4

[87] M. C. Roco, C. A. Mirkin, M. C. Hersam, *J. Nano – Part. Res,* **13** (2011) 897.

[88] N. Ichinose, Y. Ozaki and S. Kashuv, *Superfíne Particle Technology*, Springer –Verlag, Berlin, Germany (1992).

[89] S. Eustis, M. A. El – Sayed, *Chem. Soc. Rev.*, **35** (2006) 209.

[90] P. G. Collins, P. Avouris, *Scientific American*, **62** (2000) 283.

[91] http://www.nccr.iitm.ac.in/2011.pdf.

[92] W. Cai, T. Gao, H. Hong, J. Sun, *Nanotechnology,* **1** (2008) 17.

[93] C. L. De Castro, B. S. Mitchell, *Synthesis, Functionalization and Surface treatment of Nano particles, Ed. M. I. Baraton,* American Scientific Publishers, USA (2002).

[94] R. Nagar, *B. Tech Thesis,* NIT Rourkela, India (2002).

[95] A. Chandra, *Microemulsions: An Overview,* (1992); http://www.pharmainfo.net/reviews/microemulsions-overview

[96] J. H. Schulman, W. Stockenius, L. M. Prince, *J. Phys. Chem.,* **63** (1959) 1677.

[97] M. Polizelli, V. Telis, L. Amaral and E. Feitosa, *Coll. & Surf. a-Physicochem.& Engng. Aspects,* **275** (2006) 230.

[98] J. Flanagan, H. Singh, *Crit. Rev. in Food Sci. and Nutrition,* **46** (2006) 221.

[99] S. Friberg, R. Venable, *Microemulsions*, *Encyclopedia of Emulsion Technology,* P. Becher, Ed.,.Dekker, New York, USA (1983).

[100] F. Karamustafa, N. Celebi, *J. of Microencap.,* **25** (2008) 315.

[101] S. Moulik, B. Paul, *Adv. in Coll. and Interf. Sci.,* **75** (1998) 99.

[102] E. Ruckenstein, J. Chi, *J. of the Chem. Soc.-Faraday Trans. II,* **71** (1975) 1690.

[103] N. Berry, *Ph. D. Thesis*, Ryerson University, Canada (2011).

[104] I. Capek, *Adv Colloid Interf. Sci*, **80** (1999) 85.

[105] W. M. Gelbart, A. BenShaul, *J. of Phy. Chem.*, **100** (1996) 13169.

[106] K. Holmberg, *Handbook of Applied Surface and Colloid Chemistry*, Wiley Chichester, New York, USA (2002).

[107] W. D. Bankcroft, *J. of Phy. Chem.*, **17** (1913) 501.

[108] C. L. Zachar, *Ph. D. Thesis*, The University of Tolenado, USA (2010).

[109] K. R. Jadhav, I. M. Shaikh, K. W. Ambade, V. J. Kadam, *Curr Drug Deliv,* **3** (2006) 267.

[110] S. Shafiq,F. Shakeel, S. Talegaonkar, F. J. Ahmed, R. K. Khar, M. Ali, *Eur J Pharm Biopharm*, **66** (2007) 227.

[111] M. J. Lawrence, G. D. Rees, *Adv Drug Deliv Rev*, **45 (**2000) 89.

[112] L. Djordjevic, M. Primorac, M. Stupar, D. Krajisnik, *Int J Pharm*, **271** (2004) 11.

[113] F. Shakeel, S. Baboota, A. Ahuja, J. Ali, M. Agil, S. Shafiq, *AAPS Pharm SciTech*, **8** (2007) E104.

[114]http://www.kcpc.usyd.edu.au/discovery/9.5.5-short/9.5.5introsurfactants.html

[115] R. J. Hunter, *Introduction to Modern Colloid Science*, Oxford University Press, New York, USA (1993).

[116] D. Myers, *Surfactant Science and Technology*, 2nd edition, VCH publishers, New York, USA (2006).

[117] D. A. Skoog, F. J. Holler, T. A. Nieman, *Principle Instrumental Analysis,* Saundrs College Publishing, Philadelhia, USA (1998).

[118] R. A. Storey, I. Ym`en, *Solid State Characterization of Pharmaceuticals*, John Wiley & Sons Ltd, West Sussex, UK (1988).

[119] S. Barker, M. D. Antonijevic, *Thermal Analysis – Dielectric Techniques in Solid State Characterization of Pharmaceuticals*, John Wiley & Sons Ltd, West Sussex, UK (1988).

[120] C. Keck, S. Kobierski, R. Mauludin, R. H. Müller*, Dosis,* **24** (2008) 124.

[121] C. M. Keck, R. H. Müller, *Eu. J. Pharma. Biopharm.,* **62** (2008) 3.

[122] J. Lee, *J. Pharm. Sci.,* **92**, (2003) 2057.

[123] A. J. Domb, Y. Tabata, M. N. V. Ravi Kumar, S. Farber, *Nano Particles for Pharmaceutical Applications,* (2007),ISBN 1-58883-089-6.

[124] D. Fairhurst, M. A. Mitchnik, *Cosmet Toilet,* **110** (1995) 47.

[125] B – J Cha, J – G Oh, S – E Kim, *Eur. Patent,* EP 0991646 (2002).

[126] J. Bellare, *Nanotechnology in modern, traditional and alternative medicines,* Preceedings, The ICMR Strategic thrust symposium, Mumbai, India (2012).

[127] O. Kayser, A. Lemke, N. Hernandez – rejo, *Curr. Pharma. Biotechnol.,* **6** (2005) 3.

[128] R. A. Vaidya, A. B. Vaidya, B. Patwardhan, G. Tillu, Y. Rao, *J. Asso. Physician India*, **51** (2003) 528.

[129] B. Patwardhan, R. A. Mashelkar, *Drug. Discovery Today,* **14** (2009) 804.

[130] A. D. B. Vaidya, *Ayurveda in Transition,* **1** (2010) 27.

Chapter – II

Experimental Techniques

2.1 Introduction

Nowadays, scientists and engineers have an impressive array of powerful and elegant tools for acquiring quantitative and qualitative informations about the composition and structure of matter. There are variety of crystals grown and nano – particles synthesized, which are having numerous applications in science and technology. It is always important to characterize these crystals and nano - particles at different angles of interests by different instruments [1].

The present chapter gives a brief review of different experimental characterization techniques, which are used by the present author to characterize the grown crystals and synthesized nano – particles.

2.2 Crystal Growth

The crystals for the present investigations have been grown by the solution growth and single diffusion sodium metasilicate gel column. These particular techniques are briefly reviewed in chapter – I and will be discussed in the following chapters.

2.3 Synthesis of Nano particles

The nano – particles in the present investigation have been synthesized by microemulsion technique. This particular technique is discussed in the following chapters.

2.4 X – Ray Diffraction by Powder Method

X-rays were discovered by Wilhelm Conrad Roentgen, the first Nobel laureate in physics, in 1895 [2]. In 1912, Max von Laue, a German physicist and a Nobel laureate, discovered that crystalline substances act as three dimensional diffraction gratings for X-ray wavelengths. After Laue's pioneering research, the field developed rapidly, most notably by the contribution from a pair of father and son physicists, namely, William Henry Bragg and William Lawrence Bragg, respectively. In 1912-1913, the W. L. Bragg developed a well known Bragg's law, which connects the observed scattering with reflections from evenly spaced planes within the crystal [3, 4]. The use of X-ray techniques for qualitative and quantitative analysis of materials is now completing more than its century. Following these discoveries two major fields of materials analysis have developed. One of them is the method of powder XRD, which was devised independently in 1916 by Peter Joseph William Debye, a Nobel laureate, and P. Scherrer [5] in Germany and in 1917 by A. W. Hull [6, 7] in United States. In the late 1930s, the powder XRD technique was recognized as a powerful technique for phase identification and chemical analysis. There was then a dramatic increase of interest in powder methods during the 1970s, following the introduction by Rietveld in 1967 of his powerful *Rietveld method* for refining crystal structures from X-ray and neutron powder diffraction data [8,9]. While the broad definition of X-ray techniques covers many techniques based on the scatter, emission and absorption properties of X-radiation (X-ray). The powder method derives its name from the fact that the specimen is typically in the form of a microcrystalline powder. Since single crystals are not always available, this method is more suitable for structural

determination of various substances. Any material which is made up of an ordered array of atoms gives a particular diffraction pattern. The powder XRD, which is also known as *Debye – Scherer method* is a non-destructive technique widely used for the characterization of a variety of crystalline materials. Powder XRD has become an important tool for rapid identification of polymorphs and formed compounds in pharmaceutical industry. Powder XRD opens tremendous possibilities for characterization of materials and stimulates an interdisciplinary dialogue and collaboration among physicists, mineralogists, crystallographers, chemists, pharmacists and material scientist.

Generally, the method is applied to data collected under ambient conditions, but *in situ* diffraction as a function of an external constraint, such as temperature, pressure, stress, electric field, atmosphere, etc, is important for the interpretation of solid state transformations and materials behaviors. Various types of micro and nano crystalline materials can be characterized by powder- XRD, including organic and inorganic materials, drugs, minerals, zeolites, catalysts, metals and ceramics. The physical states of the materials can be loose powders, thin films, poly-crystalline and bulk materials. By properly using this technique one can yield a great deal of structural information about the material under investigation. For most applications, the amount of information which is possible to extract depends on the nature of the sample microstructure (crystallinity, structure imperfections, crystallite size and texture) the complexity of the crystal structure (number of atoms in the asymmetric unit cell and unit cell volume), the quality of the experimental data (instrument performances and counting statistics) [10].

The fundamental law, which governs the x-ray diffraction phenomenon, is the Bragg's Law and the equation is as follows;

$$\Delta S = n\lambda = 2d\sin\theta \quad \text{or} \quad d = \frac{n\lambda}{2\sin\theta} \qquad \ldots. (2.1)$$

When X-ray is incident on the crystalline powdered sample it gets diffracted according to the above mentioned equation in form of cones, which is exhibited in Figure 2.1.

Basically, this powder method involves the diffraction of monochromatic X-ray by a powdered specimen. Usually 'monochromatic' means the strong characteristic K component of the filtered radiation from an X-ray tube operated above the K excitation potential of the target material.

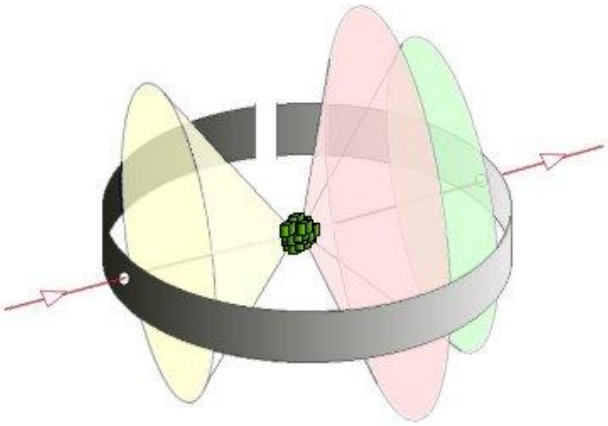

Figure 2.1 Powder Sample Diffract X-ray Beam in Cones

The "Powder" can mean either an actual, physical powder held together with suitable binder or any specimen in polycrystalline form. Figure 2.2 gives the schematic representation of powder method.

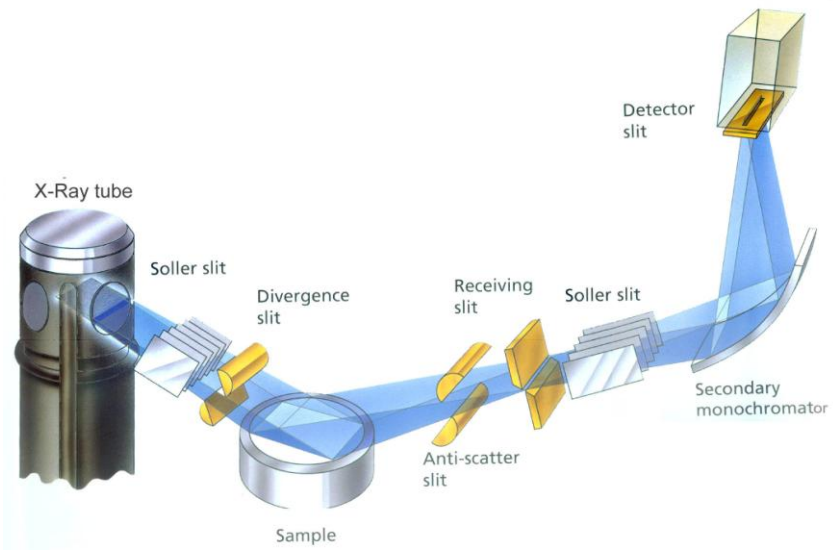

Figure 2.2 The Principle of Powder X-ray Diffraction

There are many applications of the powder method, which are summarized in table 2.1. Fundamentally this method provides a way of investigating, within limits, the crystallography of the crystal in the powder form. The powder method can be used as a tool to identify crystals, since the powder XRD patterns produced by a crystalline substance is a characteristic of that particular substance. One of the most important uses of the powder method is in the identification of an unknown material. If a set of standard diagrams of known substances, or tabular representations of them, available, then it is possible to identify a pure substance with the aid of a set of rules for finding an unknown diagram. The ASTM data cards as well as JCPDS data files are available for large number of substances for identifications and comparison. Statistical study of the relative orientations of the individual crystals of an aggregate is one of the important secondary uses of the powder method [11]. Identification of phases can be done by powder technique without solving crystal structure or assigning indices to the reflections. There are numerous computer soft-wares available for powder XRD analysis. There

are several well written books available on X – Ray diffraction [12], powder photographic method [13,14], basics of X – Ray diffraction [15], a practical approach to X- Ray diffraction [16] and review of progress of X- Ray diffraction [17].

Table 2.1 Applications of Powder XRD [18]

Diffraction Line Parameter	Applications
Peak Position	Unit-cell parameter refinement Pattern indexing Space group determination (*2θ* / absent reflections) Anisotropic thermal expansion Macro stress: sin2*ψ* method Phase identification (*d* / *I*)
Intensity	Phase abundance Reaction kinetics Crystal structure analysis (whole pattern) Rietveld refinement (whole pattern) Search/match, phase identification Preferred orientation, texture analysis
Width / Breadth and Shape	Instrumental resolution function Microstructure: line profile analysis Microstructure (crystallite size, size distribution, lattice distortion, structure mistakes, dislocations, composition gradient) Crystallite growth kinetics Three-dimensional microstructure (whole pattern)
Non-ambient and dynamic diffraction	*In situ* diffraction under external constraints reaction kinetics.

However, there are certain limitations of powder XRD, such as limited sensitivity (a phase present in quantities lower than 5% by weight is difficult to detect), peak overlaps may occur for high angle reflections and for non – isometric crystals the analysis of unit cell parameters and indexing pattern is difficult.

The present author has analyzed crystalline and nano – particle samples by powder X-ray analysis PHILIPS X'PERT Modular Powder

Diffractometer (MPD) system as shown in figure 2.3 in the Department of Physics, Saurashtra University. The CuKα radiation was used. The crystal structures were determined by a computer software Powder-X.

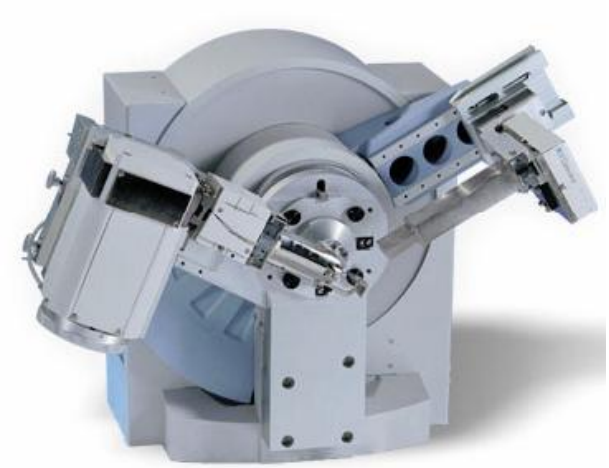

Figure 2.3 X-ray Powder Diffractometer [19]

2.5 Single Crystal X-ray Diffraction Method

The oldest and the most precise method of X-ray crystallography is "*Single-crystal X-ray diffraction*", in which a beam of X-rays is deflected from a single crystal, producing a "*diffraction pattern*", a regular array of spots called "reflections". The arrangement of atoms is determined from the position and brightness of the set of reflections that can be observed as the crystal gradually rotates, together with supplementary data. For single crystals of sufficient purity and regularity, X-ray diffraction data can determine the positions of most atoms in a crystal structure to within a few tenths of an Ångstrom. If one wants to know three-dimensional structures of biological molecules-one needs to crystallize them, then place them into the X-ray beam and to interpret the obtained diffraction pattern.

The investigation of crystal and molecular structure by X-ray diffraction techniques has been one of the most fruitful scientific activities in the recent years. Single crystal X-ray diffraction is a non-destructive analytical technique which provides detailed information about the internal lattice of crystalline substances, including unit cell dimensions, bond-lengths, bond angles, torsion angles, etc. This has been well explored in new drug designing and identifying structures of unknown biological macromolecules, enzymes, proteins, viruses, etc. the great deal of activities are being carried out globally in this direction.

There are numerous books available on the application of X – Ray Crystallography to solve the structure of protein and macromolecules [20 - 23]. However, the classic paper was published by Wyckoff and Corey [24] way back in 1936.

During 1975-80, the technological developments, which took place in the field of crystallography, paved the way for a very sophisticated X-ray machine that is known as *Computer Controlled Single Crystal X-ray Diffractometer.* A diffractometer is an instrument, which measures the intensities of diffracted beams individually by counting the number of X-ray photons that arrive at a suitably placed detector. The term "*four circle*" means four rotational motions such as ϕ, ω, θ, χ. of these ϕ, ω, χ are associated with the crystal and 2θ with the counter. The crystal is placed at the point of intersection of the four circles. A detector, usually a scintillation counter, intercepts the diffracted beam and the intensity is recorded electronically. Goniometer head holding the single crystal is carried by ϕ - circle, which is mounted on the χ-circle. The χ-circle is mounted on the ω circle, which is

coaxial with the *2θ*-circle. An outline of the conventional crystal X-ray diffractometer is shown in Figure 2.4.

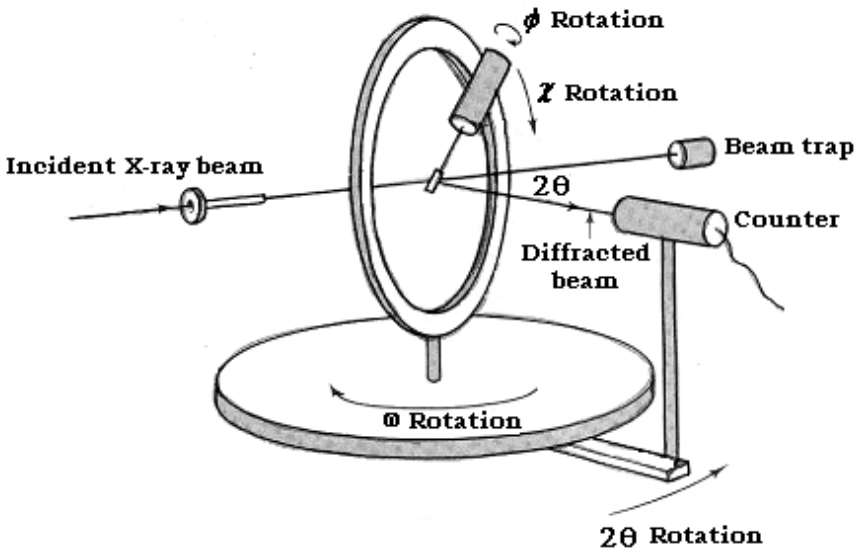

Figure 2.4 Conventional Single Crystal X-ray Diffractometer

There are two basic geometries used by the four-circle instrument

Eulerian geometry

The goniometer is mounted on a ω - circle, lying in the horizontal plane, and so having a vertical rotation axis. Perpendicular to this is the vertical *χ-circle*, having a horizontal axis. The goniometer head itself is mounted on the *ϕ - circle*, located on the inside of *χ*. Finally the *θ-circle* which is concentric with *ω* carries the detector which may be proportional or scintillation counter.

Kappa geometry

Another way to orient the crystal in space is that of the CAD4 diffractometer and its successor MACH3, made by Enraf-Nonius. The *ω* and *θ* are identical to those of the Eulerian instruments. The *K* circle is replaced

by the *K - circle* the axis of which is tilted at 50º to the horizontal. It supports an arm carrying the goniometer head, with the ϕ - axis tilted at 50º to *K*.

The accuracy of both the unit cell parameters and the subsequent intensity measurements is dependent on a stable and accurate centering of the crystal. Knowing the approximate cell dimensions from the photographic method and accurate centering of the crystal, the diffractometer first calculates orientation matrix, which is a 3 x 3 matrix, which gives the components of the three reciprocal axes in the three directions of the goniometer's axial system. It, therefore, contains the basic data for the definition of the reciprocal unit cell and its orientation in space. Once it is known, the position of each reciprocal lattice point may readily be calculated. The usefulness of this technique is that it provides the record of reflections and intensities electronically. The data so obtained constitutes the raw data to which various corrections, viz. background, Lorentz, polarization, absorption and extinction corrections are applied. After the application of suitable corrections the data are considered clean and hence becomes an input to the crystal structure realization.

Figure 2.5 View of X'Calibur Single Crystal X – Ray Diffactometer

The illustrative view of single crystal XRD set – up is shown in figure 2.5. The salient features of single crystal XRD set – up are

A Kappa geometry; 4-circle diffractometer; A CCD area detector; An instrument cabinet with electronics rack; System software installed on PC workstation; A water chiller for the CCD detector (type KMW200CCD); A water chiller for the X-ray tube and X-ray generator (type KMW3000C).

In the present work, well-defined single crystals having a good morphology were selected for three-dimensional crystal intensity data collection. The crystal selection was made by using a Leica polarizing microscope. The data were collected on *X'calibur diffractometer*. The diffractometer and CCD area detector are mounted inside a cabinet. The cabinet experimental area is mounted on top of the electronic rack. Water chillers for the CCD detector and the X- ray generator are positioned to the side of the instrument. The *PC workstation* (Figure 2.5) is located close to the instrument to allow a clear view of the diffractometer and convenient access to it. X-rays are generated by a sealed tube, which is powered by the high voltage X-ray generator. The X-ray optics consist of *a high speed shutter* located next to the tube shield, *a monochromator* for selecting a specified bandwidth from tube spectrum and *a collimator* for limiting beam divergence. The sample can be viewed with the video microscope, which is attached to the stand doming the instrument. The X-rays enters the detector through a Beryllium Window to the vacuum-sealed detector unit. A scintillation screen transforms the X-ray photons to light, which is conducted via a fibre optic reduction taper towards the scientific grade CCD chip. The CCD signal is digitized to 18-bit resolution (17-bit for Sapphire 3 and Onyx) by a correlated

double sampling circuit with analog-to-digital converter located in the detector head. The data transfer is done via a fiber optic data link to the frame buffer located in the PC workstation. The control program reads the data from the frame buffer to the PC workstation and stores it for further data analysis to the hard disk.

The diffractometer provides reflections of a large number of individual planes and their corresponding intensities are recorded electronically with the help of a CCD camera. The radiation used for data collection is Mo Kα radiation (λ= 0.71073Å). The data collection and cell measurement are carried at 293 (2) K.

After the data have been collected, corrections for instrumental factors, Lorentz polarization effects, X-ray absorption must be applied to the entire data set. This integration process also reduces the raw frame data to a smaller set of individual integrated intensities. *CrysAlis*^{Pro} software is for data collection and space group determination. The intensity data so collected on a diffractometer are raw in nature and the same is cleaned by using data reduction program, *CrysAlisRED*.

Once the data have been collected, then the initial structure of the given compounds is solved. Various computer programs and steps can be done to attain the best possible fit between the observed and calculated structure factors [25]. In the present investigation, the machine, i.e., X'calibur, is a brand product of *M/S OXFORD DIFFRACTION U.K*. was used for the single crystal XRD. The analysis was performed using the facility at Department of Physics & Electronics, University of Jammu, Jammu.

2.6 Electron Microscopy

Electron Microscopes are scientific instruments that use a beam of highly energetic electrons to examine objects on a very fine scale. Since its invention in the year 1931, electron microscope has been a valuable tool in biology, medicine and material science. This wide spread use of electron microscopes is based on the fact that they permit the observation and characterization of materials on a nanometer (nm) to micrometer (μm) scale.

Electron Microscopes were developed due to the limitations of Optical or Light Microscopes which are usually having 500x or 1000x magnification and a resolution of 0.2 micrometers. Electron Microscopes function exactly as their counterparts except that they use a focused beam of electrons instead of light to “image” the specimen and gain information of its structure and composition. Electron microscope has high resolving power and large magnification, for example, resolution power $\lambda = (150/\varphi)$ Å, suppose $\varphi = 100$ kV then λ is 0.04 Å. The electrons are behaving as waves as per the de - Broglie hypothesis, which is well explored in electron microscopy. The basic steps involved in all electron microscopes are the following: A stream of electrons is formed in high vacuum (by electron guns). This stream is accelerated towards the specimen, into a thin, focused, monochromatic beam by using metal apertures and magnetic lenses. The sample is irradiated by the beam and interactions occur inside the irradiated sample. These interactions and effects are detected and transformed into an image.

Basically, there are two different types of electron microscopes available viz., the Scanning Electron Microscopes (SEM) and the

Transmission Electron Microscopes (TEM). In the TEM, an electron beam is passed through an extremely thin section of the specimen, which gives two – dimensional cross – section of the specimen. Whereas the SEM, in to the TEM in contrast, visualize the surface structure of the specimen. Several books are available on electron microscopy covering SEM, TEM and X – Ray microanalysis [26 - 30].

The biggest advantage of electron microscopes is that they have a higher resolution and higher magnification (up to 2 million times). In SEM a greater depth of field compared to light microscopes is achieved. The higher resolution may also give the human eye the subjective impression of a higher depth of field.

The Sample preparation is often much more elaborate. It is often necessary to coat the specimen with a very thin layer of metal (such as gold). The metal is able to reflect the electrons. The energy of the electron beam is very high and hence the sample is exposed to high radiation, and which destroys the living cells and does not allow observing functioning normally.

2.6.1 Scanning Electron Microscope (SEM)

A Scanning Electron Microscope (SEM) is a powerful magnification tool that utilizes focused beams of electrons to obtain information. The high – resolution, three – dimensional images produced by SEMs provide topographical, morphological and compositional information makes them invaluable in a variety of scientific and industrial applications. The first SEM debuted in 1942 with the first commercial instruments around 1965. Its late development was due to the electronics involved in “scanning” the beam of

electrons across the sample. The SEM is often the first analytical instrument used when a "quick look" at a material is required when the light microscope no longer provides adequate resolution. In the SEM an electron beam is focused into a fine probe and subsequently raster scans over a small rectangular area. As the beam interacts with the sample, it creates various signals (secondary electrons, internal currents, photon emission, etc.), all of which can be appropriately detected. These signals are highly localized to the area directly under the beam. By using these signals to modulate the brightness of a cathode ray tube, which is raster scanned in synchronism with the electron beam, an image is formed on the screen. This image is highly magnified and usually has the **"**look**"** of a traditional microscopic image, but it is with a much greater depth of field. With ancillary detectors, the instrument is capable of elemental analysis. The block diagram of SEM is shown in figure 2.6.

Electron Gun

The first and basic part of SEM is the source of electrons. It is usually a V – shaped filament made up of LaB_6 or W (tungsten), which is wreathed with Wehnelt electrode (Wehnelt Cap). Due to negative potential of the electrode, the electrons are emitted from a small area of the filament (point source). A point source is important because it emits monochromatic electrons (with similar energy). The two usual types of electron guns are used, viz., the conventional electron guns and the field emission guns (FEG).

In conventional electron guns, a positive electrical potential is applied to the anode and the filament (cathode) is heated until a stream of electrons is

produced. The electrons are accelerated by the positive potential down the column and because of the negative potential of cap; all electrons are repelled toward the optic axis.

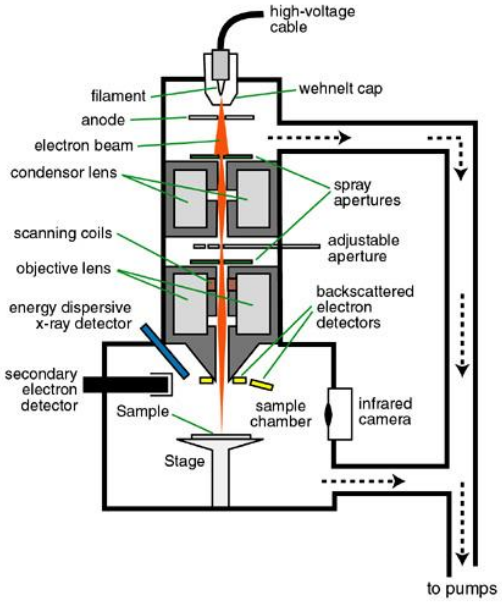

Figure 2.6 Schematic Diagram of Scanning Electron Microscope (SEM)

Electron – Specimen Interactions

When an electron beam interacts with the atoms in a sample, individual incident electrons undergo two types of scattering phenomena, i.e., the elastic scattering and the inelastic scattering as shown in figure 2.7. In the elastic scattering, only the trajectory changes and the kinetic energy and speed remain constant. In the case of elastic scattering, some incident electrons will actually collide and displace from their orbits (shells) around nuclei of atoms comprising the sample. This interaction places the atom in an excited state. Specimen interaction is what makes Electron microscopy possible. The inelastic interactions noted on top side of the diagram are utilized when

examining thick or bulk specimens (SEM), while on the bottom side are those examined in thin or foil specimens (TEM).

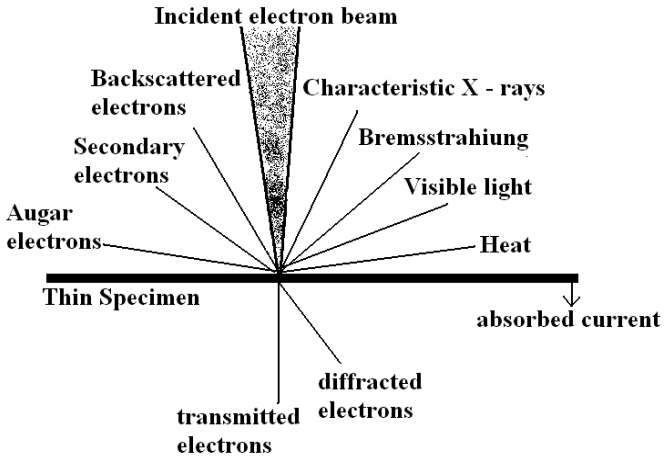

Figure 2.7 Effects produced by electron bombardment on a material

Reactions Exploited in SEM

Secondary Electrons

When the sample is bombarded with electrons, the strongest region of the electron energy spectrum is due to secondary electrons. The secondary electron yield depends on many factors and is generally higher for high atomic number targets and at higher angles of incidence. Secondary electrons are produced when an incident electron excites an electron in the sample and loses most of its energy in the process. The excited electron moves towards the surface of the sample undergoing elastic and inelastic collisions until it reaches the surface, where it can escape if it still has sufficient energy.

Backscattered Electrons

Backscattered electrons consist of high – energy electrons originating in the electron beam that are reflected or back – scattered out of the

specimen interaction volume. The production of backscattered electrons varies directly with the atomic number of the specimen. This differing production rates causes higher atomic number elements to appear brighter than lower atomic number elements. The interaction is utilized to differentiate parts of the specimen that have different average atomic number.

Relaxation of Excited Atoms

When the sample is bombarded by the electron beam of the SEM, electrons are ejected from the atoms on the specimens surface. A resulting electron vacancy is filled by an electron from a higher shell and an X – ray is emitted to balance the energy difference between the two electrons. The EDS (Electron Dispersive Scanning) X – ray detector (EDX) measures the number of emitted x – rays versus their energy. The energy of the X – ray is characteristic of the element from which the x – ray was emitted. In practice EDX is most often used for qualitative elemental analysis, simply to determine which elements are present and their relative abundance.

Operation of SEM

In SEM, a source of electrons is focused in vacuum into a fine probe that is rastered over the surface of the specimen. The electron beam passes through scan coils and objective lens that deflect horizontally and vertically so that the beam scans the surface of the sample. As the electrons penetrate the surface, a number of interactions occur that can result in the emission of electrons or photons from or through the surface.

Figure 2.8 Typical SEM Set – up

A reasonable fraction of the electrons emitted can be collected by appropriate detectors and the output can be used to modulate the brightness of a cathode ray tube (CRT) whose X – and Y – inputs are driven in synchronism with the X – Y voltages rastering the electron beam. In this way an image is produced on the CRT; every point that the beam strikes on the sample is mapped directly onto a corresponding point on the screen. In the present study SEM of model Philips XL30 ESEM TMP was used, which is shown in figure 2.8. this set – up is available at SICART, Vallabh Vidyanagar, Gujarat.

2.6.2 Transmission Electron Microscopy

The *Transmission Electron Microscope* (TEM) operates on the same basic principles as the optical microscope but it uses electrons instead of light. TEM uses electrons as *light source* and their much lower wavelength makes it possible to get a resolution of thousand times better than with an optical microscope. Electron microscopy allows one to visualize objects that are as small as 1 nm. Here the specimen is bombarded by electrons emitted by a suitable source and collimated by the optics. Electron gun is used as a source

of electrons and electro-magnetic lenses are used to deflect electrons, namely, a condenser that concentrates the beam. The first TEM was built by Max Knoll and Ernst Ruska in 1931, with this group developing the first TEM with resolving power greater than that of light in 1933 and the first commercial TEM in 1939. Earnst Ruska won Nobel Prize in Physics in 1986 for the development of electron microscope. A schematic diagram of TEM is shown in figure 2.9 and a photograph of typical set – up is shown in figure 2.10.

In figure 2.9, *Virtual Source* at the top represents the electron gun, producing a stream of monochromatic electrons.

This stream is focused to a small, thin, coherent beam by the use of condenser lens. This condenser lens actually consists of two condenser lenses out of which the first lens (usually controlled by the *spot size knob*) largely determines the *spot size* and the second lens (usually controlled by the *intensity or brightness knob*) actually changes the size of the spot on the sample from a wide dispersed spot to a pinpoint beam.

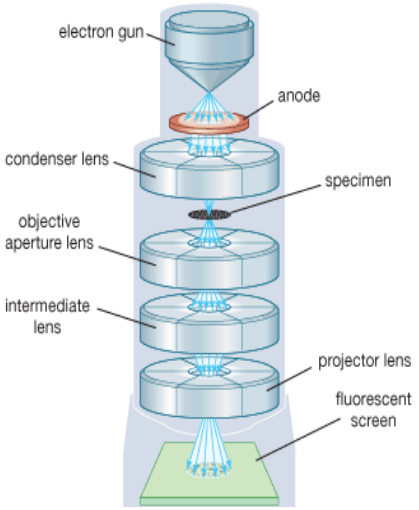

Figure 2.9 Internal Mechanism **Figure 2.10** Typical TEM Set – up

The beam is restricted by the condenser aperture (usually user selectable), knocking out the high angle electrons (far from the optic axis). The beam strikes the specimen and a part of it is transmitted. This transmitted portion is focused by the objective lens into an image optional objective and the selected area metal apertures can restrict the beam. The Objective aperture is enhancing the contrast by blocking out high-angle diffracted electrons, whereas the selected area aperture is enabling the user to examine the periodic diffraction of electrons by ordered arrangements of atoms in the sample. The image is passed down the column through the intermediate and projector lenses, being enlarged all the way. The image strikes the phosphor screen and the light is generated, allowing the user to see the image. The darker areas of the image represent those areas of the sample that fewer electrons transmitted through (thicker or denser) medium; on the other hand, the lighter areas of the image represent those areas of the sample that more electrons transmitted through (thinner or less dense) medium [31]. Apart from the fluorescent screen one can use photographic film, or a CCD camera for detection.

TEMs are capable of imaging at a significantly higher resolution than optical microscopes, owing to the small de - Broglie wavelength of electrons. This enables the user of instrument to examine fine detail – even as small as a single column of atoms. TEM forms a major analysis method in a range of scientific fields, in both physical and biological sciences. TEMs find application in cancer research, virology, materials science as well as semiconductor research and nanotechnology.

At smaller magnifications TEM image contrast is due to absorption of electrons in the material, owing the thickness and composition of the material. Notwithstanding, a higher magnifications the complex wave interactions modulate the intensity of the image, which require expert analysis of observed images. Alternate modes of use allow the TEM to observe modulations in chemical identity, crystal orientation, electronic structure and sample induced electron phase shift as well as the regular absorption based imaging [32]. The newer High Resolution TEM (HRTEM) is now available for finer details at higher resolutions. In the present investigation, Philips Tecnai 20 set – up from SICART, Vallabh Vidyanagar, Gujarat, was used. Which is having resolution up to 2 Å, magnification up to 7,50,000x and accelerating voltage 200 kV.

2.7 Atomic Force Microscopy (AFM)

The AFM was invented by Binning, Quate and Gerber in 1986 with the goal of addressing the limitation of STM to imaging conducting samples [33]. The AFM is a very high – resolution type of scanning probe microscopy, with demonstrated resolution of fractions of a nanometer, more than 1000 times better than the optical diffraction limit. The AFM is one of the foremost tools for imaging, measuring and manipulating matter at the nanoscale. The information is gathered by “feeling” the surface with a mechanical probe. Piezoelectric elements that facilitate tiny but accurate and precise movements on (electronic) command enable the very precise scanning. The AFM consists of a cantilever with a sharp tip at its end, which is used to scan the specimen surface. The cantilever is typically made up of silicon or silicon nitride with a tip radius of curvature of the order of nanometers. When the tip is brought into

proximity of sample surface, forces between the tip and the sample lead to a deflection of the cantilever according to Hooke's law. The forces measured, in AFM depending on the condition, include mechanical contact force, van der Waals forces, capillary forces, chemical bonding, electrostatic forces, magnetic forces, etc. Apart from the force, additional quantities may simultaneously be measured through the use of specialized types of probe. Typically, the deflection is measured using a laser spot reflected from the top surface of the cantilever into an array of photodiodes.

The other methods use optical interferometry or piezoresistive AFM cantilevers. These cantilevers are fabricated with piezoresistive elements, that act as a strain in the AFM cantilever due to deflection can be measured, but this method is not as sensitive as laser deflection or interferometry. If the tip is scanned at a constant height, a risk will exist that the tip collides with the surface, causing damage. Hence, in most cases a feedback mechanism is employed to adjust the tip – to – sample distance to maintain a constant force between the tip and the sample. Traditionally, the sample is mounted on a piezoelectric tube that can move the sample in *z* direction for maintaining a constant force, and the *x* and *y* directions for scanning the sample. Alternatively a 'tripod' configuration of three piezo crystals may be employed, with each responsible for scanning in the x, y and z directions. This eliminates some of the distortion effects seen with a tube scanner. In newer designs, the tip is mounted on a vertical piezo scanner while the sample is being scanned in X and Y using another piezo block. Figure 2.11 shows the operating principal diagram of AFM.

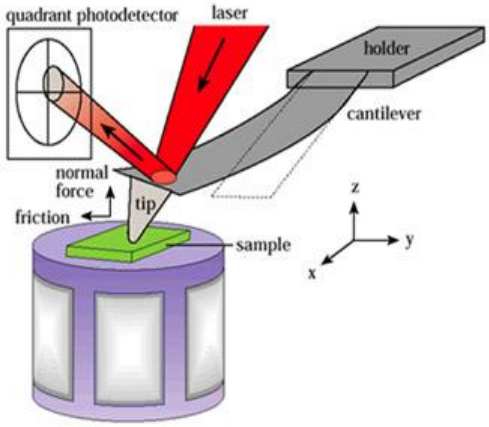

Figure 2.11 Schematic diagram **Figure 2.12** Photograph of AFM set – up

The AFM can be operated in a number of modes, depending on the application. In general, possible imaging modes are divided into static (contact) modes and a variety of dynamic (non – contact) modes where the cantilever is vibrated.

Contact mode

The primary modes of operation are contact mode. In contact mode, an AFM tip makes soft “physical contact” with the surface. The tip is attached to the end of a cantilever with a low spring constant, which is lower than the effective spring constant holding the atoms of the sample together. As the scanner gently traces the tip across the sample (or the sample under the tip), the contact force causes the cantilever to bend to accommodate changes in topography. In contact mode operation, the tip deflection is used as a feedback signal. Because the measurement of a static signal is prone to noise and drift, the low stiffness cantilevers are used to boost the deflection signal. Thus static mode AFM is almost always done in contact where the overall force is repulsive. In contact mode, the force between the tip and the surface

is kept constant during scanning by maintaining a constant deflection. Figure 2.12 shows an instrument of contact mode AFM.

Non – contact mode

When lifting the probe by at least one nanometer from the sample surface, only long-range interactions remain. The relevant forces result in general from van der Waals interactions, electro- and magnetostatic interactions, and, under ambient conditions, often from the formation of liquid capillaries. Information of the atomic or nanoscale surface structure gets completely lost.

While van der Waals forces are relatively small and capillary forces can be avoided by either choosing a sufficiently large working distance or by working on clean surfaces, electro- and magnetostatic interactions can yield relatively strong forces. This provides important information about the electrical or magnetic charge distribution in the near-surface regime of the sample. Since these charge distributions can be manifold, the lateral variation as well as the range of the resulting interactions is very different on different samples. Near-field operation means, in this context, that only charges in probe and sample within a certain volume around the probe apex contribute to contrast formation. In other words, if the static interaction is modeled in terms of a multipole expansion of the charge distribution, one usually finds monopole, dipole and higher contributions which all have to be taken into account up to a certain degrees. Thus, for the magnetostatic interaction, it is very frequently found that the resulting forces are not simply dipole forces but that the monopole term dominates contrast formation.

The AFM has several advantages over the SEM. Unlike the electron microscope which provides a two dimensional projection or a two dimensional image of a sample, the AFM provides a true three – dimensional surface profile. Additionally, samples viewed by AFM do not require any special treatments that would irreversibly change or damage the sample. While an electron microscope needs an expensive vacuum environment for proper operation, most AFM modes can work perfectly well in ambient air or even a liquid environment. This makes it possible to study biological macromolecules and even living organisms. In principle, AFM can provide higher resolution than SEM. It has been shown to give true atomic resolution in ultra – high vacuum and more recently, in liquid environments. High resolution AFM is comparable in resolution to scanning tunneling microscopy and transmission electron microscopy.

A disadvantage of AFM compared with the SEM is the image size. The SEM can image an area in the order of millimeters by millimeters with a depth of field of the order of millimeters. The AFM can only image a maximum height in the order of 10 – 20 micrometers and a maximum scanning area of around 150 by 150 micrometers [34 - 36]. Some books have discussed the AFM technique at length [37-39].

In the present study the author has used contact type AFM of model Nanosurf AG available at Physics Department, Gujarat University, Ahmedabad. The minimum lateral and Z resolution is 0.1 nm and 0.21 nm, respectively.

2.8 Fourier Transform Infrared Spectroscopy (FT - IR)

The term ‘spectroscopy’ is generally used for the analytical techniques based on the interaction of electromagnetic radiation with matter and variation of particular physical quantity with frequency of radiation. In spectroscopy the measurements of absorbance or transmittance of electromagnetic radiation, due to interaction with sample by molecules, are carried out in a gas or vapour state or dissolved molecules/ions or solid depending upon requirement. Spectroscopy is used for both qualitative and quantitative investigations.

Multiplex types of instruments employ the mathematical tool of *Fourier Transform* [40]. The apparatus of Fourier Transform Infrared (FT-IR) spectrometer is derived from *Michaelson interferometer,* which is shown in figure 2.16. The main components of the FT-IR spectrometers are: (1) drive mechanism, (2) beam splitters, and (3) sources and (4) transducers or detectors. In Figure 2.13 a parallel beam of radiation is directed from the source to the interferometer, consisting of a beam splitter (B) and two mirrors (M_1 and M_2). It is well known that for monochromatic radiation the interference patterns are obtained.

The constructive or destructive interference is produced depending on the relative path lengths B to M_1 and B to M_2. When mirror M_2 moves smoothly towards or away from B, a detector sees radiation of changing intensity.

If *white* radiation is used, the obtained interference patterns can be transferred back to the original frequency distribution. This is achieved by a

mathematical process known as *Fourier transform*, nowadays, this process is carried out by a computer or microprocessor of the spectrometer. Under these conditions, the detector response fluctuates at a rate, which depends upon the rate of movement of mirror and the wavelength of radiation.

In general, any combination of frequencies with corresponding amplitudes will produce an interferogram containing all the spectral information of the original radiation. The interferogram is the Fourier transform of the spectrum and the task of the computer is to apply the *inverse Fourier transform*.

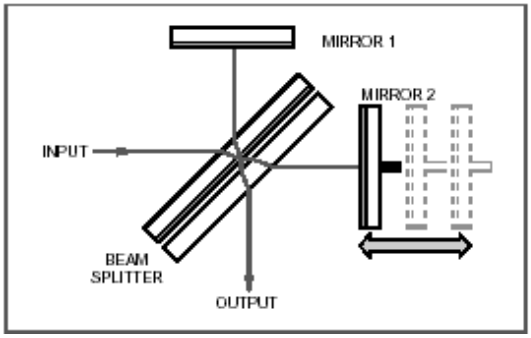

Figure 2.13 Schematic diagram of Michelson interferometer

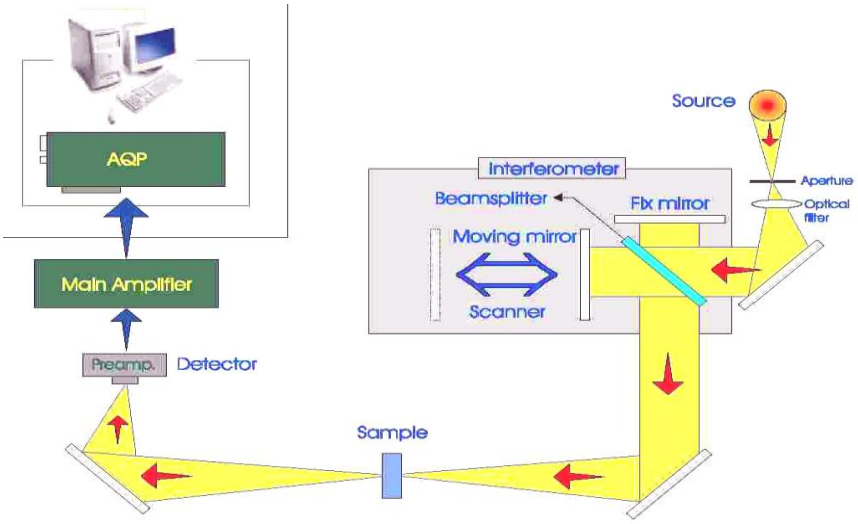

Figure 2.14 The schematic diagram of FT-IR [41]

Interferometric or Fourier transform spectroscopy makes use of all the frequencies from the source simultaneously, rather than sequentially as in scanning instrument. This was first proposed by Fellgett and hence also called as *Fellgett advantage FTS*.

The Fellgett advantage is an improvement in signal to noise ratio of $(M)^{1/2}$, where M is the number of resolution elements desired in the particular spectrum. It is worth noting that the resolving power of Fourier transform instrument is constant over the entire spectrum, whereas it varies with frequency in the conventional technique [42]. Sensitivity is dramatically improved with FT-IR for many reasons. The detectors employed are much more sensitive, the optical throughput is much higher which results in much lower noise levels, and the fast scans enable the co-addition of several scans in order to reduce the random measurement noise to any desired level (referred to as signal averaging). These instruments employ a He-Ne laser (helium-neon laser) as an internal wavelength calibration standard (referred to as the Connes Advantage). The use of a helium - neon laser as the internal reference in many FT-IR systems provides an automatic calibration in an accuracy of better than 0.01 cm^{-1}. These instruments are self-calibrating and never need to be calibrated by the user. Energy-wasting slits are not required in the interferometer because dispersion or filtering is not needed. Instead, a circular optical aperture is commonly used in FT-IR systems. The beam area of an instrument is usually 75 to 100 times larger than the slit width of a dispersive spectrometer. Thus, more radiation energy is made available. This constitutes a major advantage for many samples or sampling techniques that are energy-limited. The interferometer in FT-IR modulates all the frequencies.

The un-modulated stray light and sample emissions (if any) are not detected. Fourier transform spectroscopy is providing simultaneous and almost instantaneous recording of whole spectrum in the magnetic resonance, microwave and infrared regions. *Fourier Transform (FT) Spectroscopy* is equally applicable to both emission and absorption spectroscopy.

These advantages, along with several others, make measurements made by FT-IR extremely accurate and reproducible. Thus, it is a very reliable technique for positive identification of functional groups of virtually any sample (solid, liquid or gas). The sensitivity benefits enable identification of even the smallest of contaminants. In addition, the sensitivity and accuracy of FT-IR detectors, along with a wide variety of software algorithms, have dramatically increased the practical use of infrared for quantitative analysis. Thus, FT-IR technique has brought significant practical advantages to infrared spectroscopy in qualitative and quantitative analysis. In case of FT-IR background solvent or solid matrix must be relatively transparent in the spectral region of interest. Molecule must be active in the IR region. When exposed to IR radiation, a minimum of one vibrational motion must alter the net dipole moment of the molecule in order for absorption to be observed. IR-active atmospheric components (CO_2, H_2O) will appear in the spectrum. However, usually, a "Background" spectrum is run, and then automatically subtracted from every spectrum. FT-IR cannot detect atoms or mono atomic entities contain no chemical bonds. Usually aqueous solutions are very difficult to analyze- water is a strong IR absorber.

Infrared (IR) and FTIR spectroscopy are covered at length by various authors in their books [1, 40, 43 - 45]. The present author has used Nicolet

6700 FT-IR spectrometer (as shown in figure 2.15) having optical resolution of 0.04 cm^{-1}, in the range from 400 cm^{-1} to 4000 cm^{-1} in KBr disc medium. The FT-IR set up available at Physics Department of Saurashtra University was used for the analysis.

Figure 2.15 Nicolet 6700 FT-IR spectrometer

2.6. Dynamic Light Scattering (DLS)

Dynamic Light Scattering is also known as *Photon Correlation Spectroscopy* (PCS) or also known as *Quasi Elastic Light Scattering* (QELS). This technique is one of the most popular methods used to determine the size of particles. Shining a monochromatic light beam, such as a laser, onto a solution with spherical particles in Brownian motion causes a Doppler Shift when the light hits the moving particle and as a result changing the wavelength of the incoming light. This change is related to the size of the particle. It is possible to compute the sphere size distribution and give a description of the motion of particle in the medium by measuring the diffusion coefficient of the particle and using the autocorrelation function.

This method has several advantages: first of all the experiment duration is short and it is almost all automatized so that for routine measurements an extensive experience is not required. Moreover, this method has modest development costs. Commercial "particle sizing" systems mostly operate at only one angle (90°) and use red light (675 nm). Usually, in these systems the dependence on concentration is neglected. Using more sophisticated equipment (projector, short wavelength light source), the methods can be not only considerably extended, but also be made more complicated and expensive.

According to the semi-classical light scattering theory, when light impinges on matter, the electric field of the light induces oscillating polarized electrons in the molecules. As a result, the molecules provide a secondary source of light and subsequently scatter light. The frequency shifts, the angular distribution, the polarization, and the intensity of the scattered light are determined by the size, shape and molecular interactions in the scattering material, which is possible, with the aid of electrodynamics and theory of time dependent statistical mechanics, to get information about the structure and molecular dynamics of the scattering medium through the light scattering characteristics of the system.

When a beam of light passes through a colloidal dispersion, the particles or droplets scatter some of the light in all directions. When the particles are very small compared with the wavelength of the light, the intensity of the scattered light is uniform in all directions (Rayleigh scattering); whereas for the larger particles (above approximately 250 nm diameter), the intensity is angle dependent (Mie scattering).

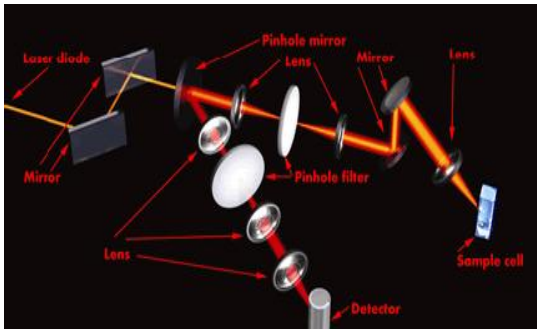

Figure 2.16 Internal Mechanism of DLS **Figure 2.17** Typical DLS Set – up

If the light is coherent and monochromatic, i.e., a laser, it is possible to observe time-dependent fluctuations in the scattered intensity using a suitable detector such as a photomultiplier capable of operating in photon counting mode. These fluctuations arise from the fact that the particles are small enough to undergo random thermal (Brownian) motion and the distance between them is therefore constantly varying. Constructive and destructive interference of light scattered by neighboring particles within the illuminated zone gives rise to the intensity fluctuation at the detector plane which, as it arises from particle motion, contains information about this motion.

Analysis of the time dependence of the intensity fluctuation can therefore yield the diffusion coefficient of the particles from which, through the Stokes - Einstein equation, knowing the viscosity of the medium, the hydrodynamic radius or diameter of the particles can be calculated. The time dependence of the intensity fluctuation is most commonly analyzed using a digital correlator. Such a device determines the intensity autocorrelation function, which can be described as the ensemble average of the product of the signal with a delayed version of itself as a function of the delay time. The *signal* in this case is the number of photons counted in one sampling interval.

At short delay times, correlation is high and, over time as particles diffuse, correlation diminishes to zero and the exponential decay of the correlation function is the characteristic of diffusion coefficient of the particles. Data are typically collected over a delay range of 100ns to several seconds depending upon the particle size and viscosity of the medium.

Analysis of the autocorrelation function in terms of particle size distribution is done by numerically fitting the data with calculations based on assumed distributions. A truly mono-disperse sample would give rise to a single exponential decay for that fitting a calculated particle size distribution is relatively straightforward. In practice, polydisperse samples give rise to a series of exponentials and several quite complex schemes have been devised for the fitting process. One of the methods most widely used today is known as *Non-Negatively Constrained Least Squares* (NNLS); the Brookhaven correlator software includes this along with several other approaches to the problem. Several books have discussed the details of DLS at length with applications [46 - 48].

The present author has used Nanotrac NPA – 253 combination set – up (as shown in figure 2.17) available at Physics Department of Saurashtra University with particle size range available from 1 nm to 6500 nm. For the analysis water as a dispersion medium having viscosity 8.90×10^{-3} dyn s/ cm^2 and refractive index 1.33 was used.

2.9 Thermal Studies

According to widely accepted definition of thermal analysis (Thermo analytical), it is a group of techniques in which physical properties of a

substance and/or its reaction products are measured as a function of temperature whilst the substance is subjected to a controlled temperature program [1]. According to International Confederation for Thermal Analysis and Calorimetry (ICTAC), thermal analysis is defined as a group of techniques in which a property of the sample is monitored against time or temperature while the temperature of the sample, in a specified atmosphere, is programmed [49]. Nearly over a dozen thermal methods can be identified, which differ in the properties measured and temperature programs [50-52]. These methods find widespread use for both quality control and research applications of various substances, such as, polymers, pharmaceuticals, crystals, clays, minerals, metals and alloys.

2.9.1 Classification of Thermal Analysis Techniques

Thermal analysis techniques involve the measurement of various properties of materials subjected to dynamically changing environments under predetermined condition of heating rate, temperature range and gaseous atmosphere or vacuum. Classification of thermal analysis techniques is as shown in table 2.2. Among all the thermal methods, the most widely used techniques are TGA, DTA and DSC, which are employed in inorganic and organic chemistry, metallurgy, mineralogy and other areas.

In certain cases, the use of a single thermo analytical technique may not provide sufficient information to solve the problem on hand and hence the use of other thermal techniques, either independently or simultaneously, for complementary information becomes necessary. For example, both differential thermal analysis (DTA) and thermo gravimetric analysis (TGA) are

widely used in studies involving physicochemical changes accompanied by variation in the heat content and the weight of the material.

Table 2.2 Classification of Thermal Analysis Techniques

Techniques Based On Variation of Physical Property	**Thermal Analysis (Thermo Analytical) Techniques**	
	Abbreviated Name	**Full Form**
Classical Techniques		
MASS	**TG / TGA**	Thermo-Gravimetry / Thermo Gravimetric Analysis
	DTG	Derivative Thermo-Gravimetry
		Isobaric Mass-Change Determination
	EGD	Evolved Gas Detection
	EGA • **TG – FT-IR** • **TG – MS**	Evolved Gas Analysis • Thermo Gravimetric Analysis Coupled to a Fourier Transform Infrared Spectrophotometer • Thermo Gravimetric Analysis Coupled to a Mass Spectrometer
		Emanation Thermal Analysis
		Thermo-Particulate Analysis
TEMPERATURE	**DTA**	Differential Thermal Analysis
	DDTA	Derivative Differential Thermal Analysis
		Heating Curve Determination • Heating Rate Curve • Inverse Heating Rate Curve
ENTHALPY	**DSC**	Differential Scanning Calorimetry
	DSM/NC	Differential Scanning Micro / Nano Calorimetry
DIMENSIONS	**TD**	Thermo- Dilatometry • Differential Dilatometry • Derivative Dilatometry

2.9.2 Thermo Gravimetric Analysis (TGA)

Thermo gravimetric analysis is a technique in which the mass of a substance is measured as a function of temperature or time while the substance is subjected to a controlled temperature program. The curve obtained in a thermo gravimetric analysis is called thermogram (TG) and its first derivative is called a derivative thermogram (DTG).

Modern commercial TG instrument consists of following main parts:

(1) A sensitive analytical balance

(2) A temperature programmable furnace

(3) A purge gas system for providing suitable gas atmosphere

(4) A microprocessor for instrument control, data acquisition and display

The null-point weighing mechanism is employed since the sample remains in the same zone of furnace irrespective of changes in mass. The furnace is normally an electrical resistive heater and the temperature range for most of the furnace is from ambient to 1000-2000 °C. The rate of heat exchange between the furnace and the sample depends on the heating rate which influences the TG curve in a number of ways. A slower rate gives a better resolution of the closely lying steps, while the faster heating rate merges such steps.

One of the objectives of TG and DTA is to delineate as accurately as possible the various temperatures associated with the thermal behavior of a given substance, i.e., temperature of decomposition, stability range of an intermediate compound and the temperature at which the reaction get completed. As noted earlier that the TGA involves change in weight with respect to temperature, the acquired data obtained as a plot of mass or loss of mass in percentage as a function of temperature is considered as a thermal spectrum, or a thermogram, or a thermal decomposition curve. These thermograms characterize a system in terms of temperature dependence of its thermodynamic properties and physical-chemical kinetics. Since the TGA involves measurement of a change in weight of a system as the temperature is increased at pre-determined rate, changes in weight are a result of the rupture and/or formation of various physical and chemical bonds at elevated

temperatures that lead to the release of volatile products or the formation of heavier reaction products. From such curves, parameters concerning the thermodynamics and kinetics of the various chemical reactions can be evaluated; moreover, the reaction mechanism, the intermediate and final reaction products can be identified. Usually, the temperature range is from ambient to 1200 °C with inert or reactive atmospheres. The derivative in TG is often used to pinpoint completion of weight-loss steps or to increase resolution of overlapping weight-loss occurrences. The shape of thermogravimetric curve of a particular compound is influenced by the heating rate of the sample and the atmosphere surrounding it [1,53,54].

The TGA finds applications in the study of thermal degradation, decomposition, dehydration of different samples. The chemical reaction resulting in changes of mass such as absorption, adsorption and desorption can also be studied

2.9.3 Differential Thermal Analysis (DTA)

DTA is a technique in which the temperature difference between a substance and a reference material is measured as a function of temperature whilst the substance and reference material are subjected to a controlled temperature program [1,49]. DTA provides information on the chemical reactions, phase transformations, and structural changes that occur in a sample during a heat-up or a cool-down cycle. The DTA measures the differences in energies released or absorbed, and the changes in heat capacity of materials as a function of temperature. The graph of DTA signal, i.e. differential thermocouple output in micro volts on the Y-axis plotted versus the sample temperature in °C on the X-axis gives the results of DTA.

Modern thermo-balances are often equipped so as to record the DTA signal and the actual thermo-gravimetric measurement, simultaneously. In addition to showing the energetic nature of weight loss events, the DTA signal can also show thermal effects that are not accompanied by a change in mass, e.g. melting, crystallization or a glass transition. Transition temperatures are measured precisely using the DTA. The DTA identifies the temperature regions and the magnitude of critical events during a drying or firing process such as binder burnout, carbon oxidation, sulfur oxidation, structural clay collapse, Alpha to Beta quartz transition, carbonate decompositions, recrystallizations, melting and cristobalite transitions, melting, solidification or solidus temperature, glass transition temperature (TG), curie point, energy of reaction, heat capacity, and others. The transition enthalpy is estimated from the DTA curve using the heat capacity of the heat sensitive plate as a function of temperature.

2.9.4 Differential Scanning Calorimetry (DSC)

DSC is a technique in which the difference in energy inputs into a substance and a reference material is measured as a function of temperature whilst the substance and reference material are subjected to a controlled temperature program [1,49]. A DSC analyzer measures the energy changes that occur as a sample is heated, cooled or held isothermally, together with the temperature at which these changes occur. The graph of heat flow in mJ/s on the Y-axis plotted versus temperature at a fixed rate of change of temperature in °C on the X-axis shows the output of the DSC. Usually, for the power compensation DSC curve, heat flow rate should be plotted on the ordinate with endothermic reactions upwards, and for the heat-flux DSC curve

with endothermic reactions downwards. The energy changes enable the user to find and measure the transitions that occur in the sample quantitatively, and to note the temperature where they occur, and so to characterize a material for melting processes, measurement of glass transitions and a range of more complex events.

There are two methods of carrying out DSC, namely, (i) Power compensated DSC, and (ii) Heat-flux DSC. Power-compensated DSC is the method usually discussed in textbooks, though most practical instruments are based on heat-flux DSC. However, in practice these usually give equivalent results. In the present study the heat flux type of DSC was used.

Power-Compensated DSC

In this method, the sample and reference are in separate furnaces, each with a heater coil and a thermocouple. The aim is to maintain both at the same temperature, even during a thermal event in the sample. The difference in power supplied to the two furnaces to maintain zero temperature differential between the sample and the reference is measured.

Heat-Flux DSC

The sample and reference are both within the same furnace and are connected by a low-resistance heat-flow path. If any difference in temperature develops, heat flows in proportion to that temperature difference.

DTA and DSC are sister techniques which provide fast, convenient analysis of the glass characteristic temperatures such as T_g and temperatures of phase changes, for instance, devitrification and melting. DSC is rather more versatile than DTA. DSC allows quantitative determination of heat capacity, the enthalpy of a phase transformation, the heat of fusion of a crystal phase.

2.9.5 Experimental Procedure

In the present study, the thermal analysis TG, DTA and DSC of the grown crystals were carried out to determine simultaneous changes of mass and caloric reactions using PC controlled Linseis Simultaneous Thermal Analyzer (STA) PT-1600, in the atmosphere of air from 35 °C to 900 °C at a heating rate of 15 °C/min. TA-WIN and WIN-STA software used for testing and analysis. The set up for thermal analysis is shown in figure 2.18, which is available at Physics Department of Saurashtra University.

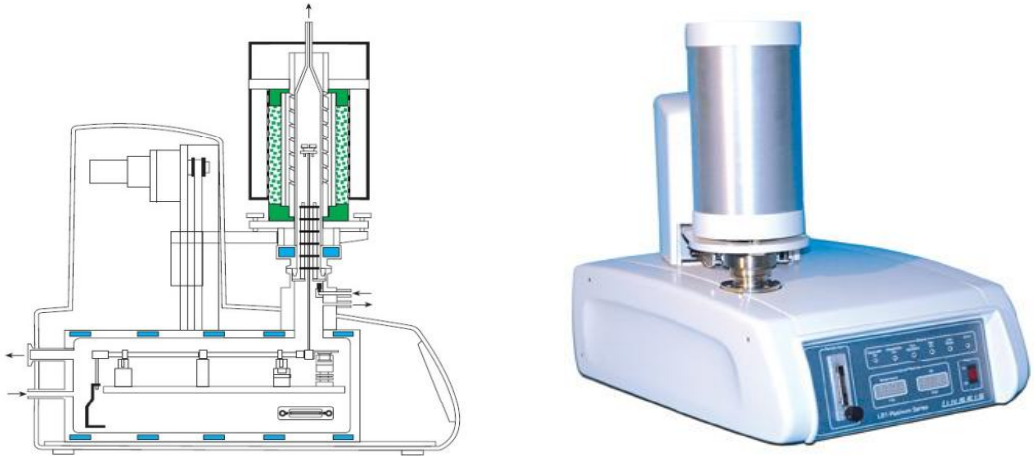

Figure 2.18 Linseis Simultaneous Thermal Analyzer PT-1600

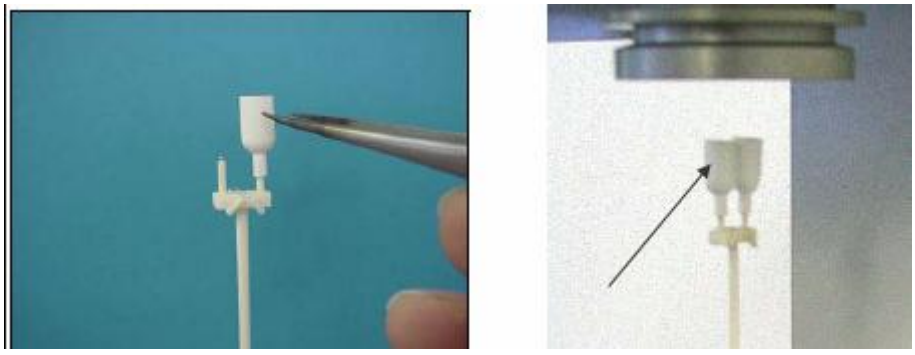

Figure 2.19 Measuring head and crucible

After switching on computer and thermo balance, one has to open furnace using LIFT switch. As shown in the figure 2.19, the measuring head, carries two equal crucibles, one for the reference material and one for the

sample substance, each one is sitting on a thermocouple. Carefully remove used crucible and clean it thoroughly. Insert a fine powder of the grown crystals under investigation in the sample crucible in the right side. The sample is evenly distributed in the bottom of the sample crucible. Take Al_2O_3, with equal amount in reference crucible in the left. The two thermocouples are wired such as to measure the temperature difference between the sample and the reference material. The absolute temperature is measured with the reference thermocouple. Good thermal contact between the sample and heat flux sensor is an indispensable requirement for optimum results. Since the test parameters have a significant influence in thermo analytical investigations, the parameters such as calibration, sample preparation, sample weight, reference material, sample chamber temperature, temperature program and atmosphere should be well considered. Calibration of the instrument is a prerequisite for quantitative analysis of STA measurements.

2.10 Dielectric Studies

Every material has a unique set of electrical characteristics depending upon the type of the materials belongs to, such as the dielectric properties, permittivity, permeability, resistivity, conductivity, etc. A material is classified as “dielectric” if it has the ability to store energy when an external electric field is applied. In other words, materials, which are electric insulators or in which an electric field can be sustained with a minimum dissipation of power, are known as dielectric materials. Simply, dielectrics are insulating materials. In dielectrics all the electrons are bound to their parent molecules and there are no free charges. Even with normal voltage or thermal energy the electrons are not released. Dielectrics are nonmetallic materials of high specific resistance

and have negative temperature coefficient of resistance. The dielectric characteristics of the material are important to study the lattice dynamics in the crystal. It is important to note that permittivity and permeability are not constant. They can change with frequency, temperature, orientation, mixture, pressure, and molecular structure of the material. Many authors discussed various dielectric properties, dielectric applications and dielectric theories in details [55-62]. Classical theory of dielectric constant was given by Kachhava and Saxena [63]. Also the predecessors of the present author have described the dielectric properties in detail [19,64-67], therefore, it is avoided in the present thesis.

Dielectric constant (*k*) or Relative Permittivity (ε_r)

Dielectric constant is defined as the ratio of the capacitance (*C*) of a capacitor filled with the given material to the capacitance (C_0) of an identical capacitor in a vacuum without the dielectric material. The dielectric constant can also be defined as the ratio of the permittivity of the dielectric material (ε) to the permittivity of vacuum (ε_o). The dielectric constant is, therefore, also known as the *relative permittivity* (ε_r) of the material. Sometimes it is also referred as the *absolute permittivity.*

Dielectric constant, $k = \varepsilon_r = \frac{C}{C_0} = \frac{\varepsilon}{\varepsilon_0}$ …. (2.2)

Since the dielectric constant is just a ratio of two similar quantities, it is dimensionless and is always greater than 1. It is a measure of polarization in the dielectric material. It denotes a large-scale property of dielectrics without specifying the electrical behaviour on the atomic scale. In the present study dielectric constant was calculated using following formula

Dielectric constant, $k = \varepsilon_r = \dfrac{Cd}{\varepsilon_0 A}$ ….. (2.3)

Where, where *C* is the capacitance, *d* is the thickness of the pellet, ε_0 is the vacuum dielectric constant (permittivity of free space, ε_0 = 8.854 x 10^{-12} F/m) and *A* is the area of the pellet.

Complex Relative Permittivity (ε^*)

Permittivity is determined by the ability of a material to polarize in response to the field and, thereby, reduce the total electric field inside the material. Thus, permittivity relates to the ability of material to transmit (or permit) an electric field. The response of normal materials to external fields generally depends on the frequency of the field. This frequency dependence reflects the fact that the polarization of material does not respond instantaneously to an applied field. The response must always be causal which can be represented by a phase difference. For this reason permittivity is often treated as a complex function. The response of materials to alternating fields is characterized by a complex permittivity,

$$\varepsilon^* = \varepsilon' - j\varepsilon'' = |\varepsilon| e^{-j\delta} \quad \text{…. (2.4)}$$

Where ε' is the real part of the relative permittivity (i.e. the dielectric constant), which is related to the stored energy within the medium; and ε'' is the imaginary part of the relative permittivity, which is related to the dissipation (or loss) of energy within the medium. Equation (2.4) expresses the complex permittivity in two ways, as real and imaginary or as magnitude and phase.

Dielectric Loss

The dielectric loss is a loss of energy which eventually produces a rise in temperature of a dielectric placed in an alternating electrical field. In other

words it is a measure of the energy absorbed by dielectric. It is the electrical energy lost as heat in the polarization process in applied AC electric field. The ratio of imaginary part to the real part of the relative permittivity is known as dielectric loss or the dissipation factor *D*.

$$D = \tan\delta = \frac{\varepsilon''}{\varepsilon'} \qquad \text{…. (2.5)}$$

The dissipation factor is measured along with the capacitance at room temperature using the LCR meter.

a. c. Conductivity and a.c. Resistivity

The a.c. conductivity is one of the studies done on solids in order to characterize the bulk resistance of the crystalline sample. The values of a. c. conductivity and a. c. resistivity were calculated for the different frequencies of the applied electric field using the following formulae,

a. c. conductivity, $\sigma_{ac} = \frac{2\pi fcDt}{A}$ …. (2.6)

where, *f* is the frequency, *C* is the capacitance, *D* is the dissipation factor or dielectric loss or *D* = *tan* δ*, t* is the thickness of the pellet and *A* is the area of the pellet.

a. c. resistivity, $\rho_{ac} = \frac{1}{\sigma_{ac}}$ …. (2.7)

Figure 2.20 HIOKI 3532 LCR HITESTER

In the present investigation the dielectric study was carried out by measuring different parameters such as capacitance and dielectric loss of the pressed pellets of samples of known dimension at room temperature on HIOKI 3532 LCR HITESTER. A precession Inductance, Capacitance and Resistance (LCR) meter using specially designed sample older, within the frequency range from 50 Hz to 5 MHz. Figure 2.20 shows the photograph of the set up. The powdered samples were pelletized by using a die of 1 cm diameter and applying 2 tone pressure. The pellets were placed in a suitably design spring loaded holder.

Reference

[1] D. A. Skoog, F. J. Holler and T. A. Nieman, *Principles of Instrumental Analysis,* Saundrs College Publishing, Philadelphia, USA (1998).

[2] W. C. Roentgen, *Ann. Phys. Chem.*, **64** (1898) 1.

[3] W. L. Bragg, *Nature*, **90** (1912) 410.

[4] W. L. Bragg, *Proc. Cambridge Philos. Soc.*, **17** (1913) 43.

[5] P. Debye and P. Scherrer, *Physik. Z*, **27** (1917) 277.

[6] A. W. Hull, *Phys. Rev.*, **9** (1917) 84.

[7] A. W. Hull, *J. Am. Chem. Soc.*, **41** (1919) 1168.

[8] H. M. Rietveld, *Acta Cryst.*, **22** (1967) 151.

[9] H. M. Rietveld, *J. Appl. Cryst.*, **2** (1969) 65.

[10] D. Louër and E. J. Mittemeijer, *Powder Diffraction in Material Science; The Role of Europe,* Material Science Forum, **37-38** *V – X* (2001).

[11] L. V. Azaroff and M. J. Buerger, *The Power Method in X-ray Crystallography*, Mc Graw-Hill, New York, USA (1958).

[12] B. D. Cullity, *Elements of X- Ray diffraction,* Addison – Wesley, Boston, USA (1956).

[13] H. P. Klug and L. E. Alexander; *X-ray Diffraction Procedures,* 2nd ed., Wiley, New York, USA (1974).

[14] L. V. Azaroff and M. J. Buerger; *The Power Method in X-ray Crystallography*,

Mc Graw-Hill, New York, USA (1958).

[15] B. E. Warren, *X – Ray Diffraction*, Dover, New York, USA (1969).

[16] C. Suryanarayana, M. Grant Norton, *X – Ray Diffraction : A Practical Approach,* Plenum press, New York, USA (1998).

[17] P. P. Ewald, *Fifity years of X – Ray Diffraction,* IUCR XVIII Congress, Glasgow, Scotland (1999).

[18] T. Irusan, D. Arivuoli, P. Ramasamy, *Cryst. Res. Technol.,* 25 (1990) K104.

[19] C. K. Chauhan, Ph. D. Thesis, Saurashtra University, Rajkot (2011).

[20] J. Drenth, *Principles of Protein Crystallography,* Springer, New York, USA, (2007).

[21] R. S. Rowlett, *Protein X – Ray Crystallography Methods,* Colgate University, New York, USA (2005).

[22] E. E. Lattman, P. J. Poll, *Protein Crystallography – A Concise Guide,* John – Hopkins Univ. Press, Maryland, USA (2008).

[23] N. Kasai, M. Kakudo, *X – Ray Diffraction by Macromolecules,* Springer, New York, USA, (2005).

[24] R. W. G. Wyckoff and R. B. Corey, *J. Biol. Chem.,* **116** (1936) 51.

[25] S. Kohli, *Ph. D. Thesis,* Jammu University, Jammu (2011).

[26] D. B. Williams, C. B. Carter, *Transmission Electron Microcopy: A Text book of Material Science*, Springer, New York, USA (2009).

[27] J. Goldstein, D. E. Newbury, D. C. Joy, C. E. Lyman, P. Echlin, E. Lifshin, L. Sawyer, J. R. Michael, *Scanning Electron Microscopy and X – Ray Microanalysis,* Springer, New York, USA (2003).

[28] L. Reimer, H. Kohl, *Transmission Electron Microscopy: Physics of Images formation*, Springer, New York, USA (2008).

[29] V. Kazmiruk, *Scanning Electron Microscopy,* INTECH (2012).

[30] A. H. Zewail, J. H. Thomas, *4 – D Electron Microscopy: Imaging in space and time,* Imp. Colg. Press, London, UK (2010).

[31] P. Hawkes (Ed.), *The Beginnings of Electron Microscopy,* Academic Press, London, UK, (1985).

[32] D. Williams and C. B. Carter, '*Transmission Electron Microscopy',* 1 – Basics, Plenum Press, New York, USA (1996).

[33] G. Binning, C. F. Quate, C. Gerber, *Phys. Rev. Lett.*, **56** (1986) 930.

[34] T. Pradeep, *Nano: the essentials*, Tata McGraw – Hill, 5th Edition, New Delhi, India (2010).

[35] S. M. Lindsay, Introduction to nano Science, Oxford University Press, Oxford, UK (2010).

[36] A. D. L. Humphris, M. J. Miles and J. K. Hobbsb, *Appl. Phys. Lett.*, 86, (2005) 034106.

[37] P. Eaton, *Atomic Force Microscopy,* Oxford Univ. Press, Oxford, UK (2010).

[38] S. H. Cohen, M. T. Bray, M. L. Lightbody, *Atomic Force Microscopy, Scanning Tunneling Microscopy,* Springer, New York, USA (1995).

[39] S. Morita, R. Wiesendanger, E. Meyer, *Non – Contact Atomic Force Microscopy,* Springer, New York, USA (2002).

[40] B. C. Smith, '*Fourier Transform Infrared Spectroscopy',* CRC Press, Boca Raton, (1996).

[41] www.emt.uni-linz.ac.at/. ../index_ftir.html

[42] B. K. Sharma, '*Spectroscopy',* Goel Publ., Meerut, India (1997).

[43] N. B Colthup, L. H. Doly, S. E. Wiberley, *Introduction to Infrared and Raman Spectroscopy,* Academic Press, London, UK (1975).

[44] G. Socrates, *Infrared Characteristic Group Frequencies,* John Wiley, Chichester, UK (1980).

[45] R. R. Griffiths, *Chemical Infrared Fourier Transform Spectroscopy,* Academic Press, London, UK (1972).

[46] B. J. Berne, R. Pecora, *Dynamic Light Scattering with Applications to Chemistry, Biology & Physics*, Dover, New York, USA (2000).

[47] R. Pecora, *Dynamic Light Scattering: Application of Photon Correlation Spectroscopy,* Springer, New York, USA (1985).

[48] W. Brown, *Dynamic Light Scattering: The Method and Some Applications,* Clarendon Press, Oxford, UK (1993).

[49] J. O. Hill, *"For Better Thermal Analysis",* 3rd Ed., International Confederation for Thermal Analysis, New Castle, Australia (1991).

[50] W. W. Wendlandt, *"Thermal Analysis"*, Wiley, New York, USA (1985).

[51] M. E. Brown, *"Introduction to Thermal Analysis: Techniques and Applications".* Chapman and Hall, New York, USA (1988).

[52] P. J. Haines, *"Thermal Methods of Analysis",* Blackie, London, UK (1995).

[53] Wendlandt; S. M. Khopkar, *"Basic Concepts of Analytical Chemistry"*, Wiley

Eastern, New Delhi, India (1984).

[54] L. Erdey, *"Gravimetric Analysis",* Pergamon Press, New York, USA (1963).

[55] H. Frohlic, *"Theory of Dielectrics"*, Clarendon Press, Oxford, UK (1949).

[56] J. C. Anderson, *"Dielectric"*, Chapman and Hall, London, UK (1963).

[57] P. J. Harrop, *"Dielectrics",* Butterworth, London, UK (1972).

[58] B. Tareev, *"Physics of Dielectric Materials"*, Mir Publishers, Moscow, Russia (1975).

[59] L. Solymar, D. Walsh, *"Lectures on the Electrical Properties of Materials"*, Oxford University Press, New York, USA (1984).

[60] Kwan Chi Kao, *Dielectric Phenomenon in solids,* Elsevier, London, UK (2004).

[61] H. C. Grant, R. J. Sheppard , G. P. South, *Dielectric study of Biological Molecules in Solution,* Snippet (1978).

[62] P. S. Ho, J. Leu, W. W. Lee, *Low Dielectric Constant Materials for IC Applictions,* Springer, New York, USA (2003).

[63] C. M. Kachhava, S. C. Saxena, *Ind. J. Phys*., **41** (1967) 440.

[64] B. B. Parekh, *Ph.D. Thesis,* Saurashtra University, Rajkot (2005).

[65] S. R. Suthar, *Ph.D. Thesis,* Saurashtra University, Rajkot (2007).

[66] D. J. Dave, *Ph.D. Thesis,* Saurashtra University, Rajkot (2011).

[67] K. D. Parikh, *Ph.D. Thesis,* Saurashtra University, Rajkot (2011).

Chapter – III

Synthesis and Characterization of n-Butyl 4-(3, 4-dimethoxyphenyl) –6–methyl–2–thioxo– 1,2,3,4 tetrahydropyrimidine – 5 – carboxylate Crystals and Nano – Particles

3.1 Introduction

Pyrimidine is a heterocyclic aromatic organic compound similar to benzene and it contains two nitrogen atoms at position 1 and 3 of the six member ring. It is isomeric with two other forms of diazine. Pyridazine is with nitrogen atoms at position 1 and 2, while pyrazine is with nitrogen atoms at position 1 and 4.

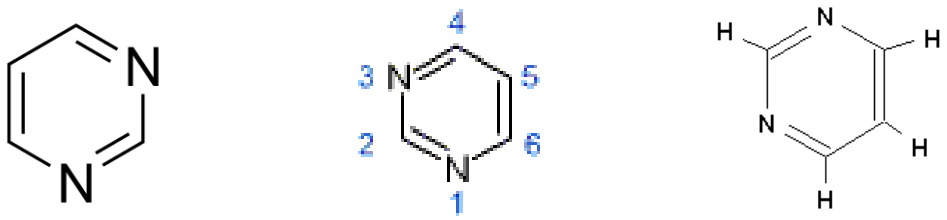

Figure 3.1 Pyrimidine structure

A pyrimidine has many properties in common with pyridine, as the number of nitrogen atoms in the ring increases the ring π – electrons become less energetic and electrophilic aromatic substitution becomes more difficult, whereas the nucleophilic aromatic substitution becomes easier. Pyrimidines are structural components in many natural compounds, such as nucleotides, nucleic acids, vitamins, proteins and antibiotics. In all organisms pyrimidine nucleotides performs essential roles in cell metabolisms as well as in nucleic acids such as activation of sugars for polysaccharide and phospholipid

synthesis and glycosylation of proteins and lipids. In mammals pyrimidines are crucial for detoxification reaction in liver. They are also considered as modulators of blood flow and have functions in the peripheral and central nervous system [1].

The current state of knowledge of pyrimidine metabolism has been reviewed by Löffler *et al.* [2]. They discussed the need to define which enzymes of the pyrimidine pathways are disrupted in more clinical situations such as rheumatoid arthritis, malignancy or infection and to develop better analogues targeting such enzymes.

Pyrimidines serve essential functions in human metabolisms as ribonucleotide bases in RNA (uracil and cytosine) and deoxyribonucleotide bases in DNA (cytosine and thymine) and are linked by phosphodiester bridges to purine nucleotides in double – standard DNA, in both the nucleus and the mitochondria. Since pyrimidines and purine (deoxy) nucleotides are building blocks of RNA and DNA, the biosynthesis of pyrimidine has been addressed by large number of researchers [3-6]. Since disorders in mitochondrial energy metabolism can entrail serve impairment to pyrimidine biosynthesis, it is advisable to include improvement of pyrimidine status in therapy protocols.

Synthetic pyrimidine analogs acts as antimetabolites and by selective interference in metabolic pathways of RNA and DNA synthesis, the synthetic or natural enzymes inhibitors can combat infection, virus, tumor and autoimmune diseases [1].

Pyrimidine derivatives possess wide range of biological properties such as antiviral [7], antitumor [8], antibacterial [9], anti-inflammatory [10]; anti-hypertensive [11], anti-cardiovascular agents[12], calcium channel blocking [13] and neuropeptide Y (NPY) antagonists [14]. Several marine alkaloids with interesting biological activities containing the dihydropyrimidine – 5 – carboxylate core have been isolated [15 – 17]. Also, appropriately functionalised dihydropyrimidine have emerged as orally active and hypertensive agents [18 – 20]. Other derivatives show interesting biological activities in several marine natural products, which contain the dihydropyrimidine - 5 - carboxylate core [12]. Crystals of 5-(2- amino-4-(2 furyl) pyrimidin-5-yl)-1-methylpyridin-2(1H)-one were found suitable for active ingredient of preventing and therapeutic agent for constipation [21]. The dihydropyrimidine core structure was found to posses adrenergic agonistic, mitotic kinesin inhibiting, antibacterial, fungicidal and other interesting pharmacological application [22 – 23]. Polypyrimidine exhibits high electron affinity [24], which makes it an attractive candidate for incorporation into a π - conjugated system. An elegant step-by-step synthetic strategy for the synthesis of pyrimidine-containing oligophenylenes has been reported by Gommper *et al.* [25] which is very useful as an electron transporting material in OLED (Organic LED) devices.

It is important to study the crystals of Active Pharmaceutical Ingredient (API) because in the pharmaceutical industry crystallization is one of the most popular method of preparation and purification of solid oral dosage forms. Crystalline forms of API are thermodynamically stable, since their molecules are arranged in a regular, repeating pattern. It is also well known that common

way to administer API is the oral route [26]. During storage, amorphous form will tend to revert to more stable crystalline form [27 – 32].

It is interesting to study the effect of particle size of API on dosage. Reducing the particle size of API is an efficient and reliable method of improving bioavailability of relatively insoluble drugs that is many times limited by poor dissolution rates. As per the Noyes – Whitney equation, the dissolution rates linearly depends on surface area. Therefore, the reduction in particle size to nanometers increases the surface area and as a result increase in dissolution rate can be achieved. The typical unit operation for oral solid dosage forms are developed for micro particle range. However, the introduction of nanoparticles will require significant efforts to understand their behaviour and modify the current unit operations. Therefore, comparison between the physical properties of nano – particles and micro – particles can help transition from micro – formulation to nano – formulation processes. This has been discussed by several authors [33 - 34].

In 1893, Pietro Biginelli discovered a multicomponent reaction which leads to partly reduced pyrimidine derivatives [35]. Since that time, the 'Biginelli reaction' has been known as an efficient *one – pot* reaction protocol for 3,4 – dihydropyrimidine – 2 (1H)- one and its derivatives. n-Butyl 4-(3, 4-dimethoxyphenyl) –6–methyl–2–thioxo– 1,2,3,4 tetrahydropyrimidine – 5 – carboxylate abbreviated as (n – butyl THPM) as a being Dihydro Pyrimidine abbreviated as (DHPM) derivative it shows most of the properties shown by the dihydropyrimidine derivatives. It is also found from Computational Studies on Tetrahydropyrimidine-2-one that it may act as HIV-1 Protease Inhibitors

[36]. Studies on 5-(4'-hydroxybenzylidenoimino)-4, 6-diketo-4, 5, 6, 7-tetrahydropyrimidine-[4,5-d]-3-methyl-isothiazole shows that it exerts slight hypotensive effect on the circulatory system for smooth muscle organs and central nervous system [37]. Two lead(II) 2,4-dioxo-1,2,3,4-tetrahydropyrimidine-5-carboxylate complexes also exhibit different topologies and fluorescent properties [38].

Considering various applications of Tetrahydropyrimidine (THPM) compounds, the novel compound n – butyl THPM was selected by the present author for crystal growth and various characterizations were carried out. To identify the change in properties of n – butyl THPM based on the particle size, the nano particle of n – butyl THPM were synthesized by micro – emulsion method and further characterized by various techniques.

3.2 Recent Study on Some Pharmaceutical and Organic Crystals

As it has been noted earlier in Chapter – I, that many physical and chemical properties of API are governed by the crystalline nature and crystalline properties. Therefore, the present author has attempted to cover the recent study of API crystals and some organic molecules crystals before beginning the discussion of growth of some API crystals in this chapter as well as in the following chapters.

In the crystallization of APIs several issue are of prime importance such as nucleation and crystallization parameters, polymorphism, effect of various processes, crystal size and morphology, etc.

The lactose monohydrate is widely used as a pharmaceutical excipient and the drug delivery system requires the excipient to be of narrow particle size distribution with regular particle shape. Application of ultrasound is known to increase or decrease the growth rate of certain crystal faces and control the crystal size distribution. The effect of various process parameters on crystal size and morphology of lactose in ultra – sound assisted crystallization is reported by Patel and Murthy [39]. The effect of seed loading on the mean crystal size of acetyl salicylic acid (aspirin) in a continuous – flow – crystallization set – up is studied by Eder *et al.* [40]. Moreover, cyclodextrin induced changes in crystal habit of acetyl salicylic acid in aqueous solution is reported by Iohara *et al.* [41].

Polymorphism is also an important issue during crystallization of APIs polymorphism is the ability of a solid material to exist in more than one form or crystal structure. Controlling polymorphism is very crucial in crystallization of APIs for bulk applications. Recently, Brun *et al.* [42] attempted to analyze the process parameters and achieved control of polymorphism in crystallization of caffeine. Also the polymorphism of nifedipine is studied keeping in view the crystal structure and the reversible transition of the metastable β – polymorph by Gunn *et al.* [43].

For crystallization to occur from solution, it requires super-saturation, which can be achieved commonly in industry by (1) solution cooling, (2) addition of a second solvent to reduce the solubility of a solute (also known as antisolvent), (3) chemical reaction and (4) change in pH. The super critical anti – solvent (SAS) approach is frequently adopted in crystallization APIs and

effect of process parameters is reported [44]. The estimation of nucleation kinetics for anti – solvent crystallization of paracetamol in methanol/water solution is reported [45]. Apart from this, the primary nucleation and growth mechanism of cloxacillin sodium in methanol – butyl acetate system is studied [46].

Another important aspect in pharmaceutical compound crystallization is of co – crystals. The simplest definition of a co – crystal is a crystalline structure made up of two or more components in definite stoichiometric ratio, where each component is defined as atom, ion or molecule. Further extending the definition that the co – crystals consist of two or more components that form a unique crystalline structure having unique properties. The most widely studied co – crystals find applications in drug development and specifically in the formation, design and implementation of APIs. Changing the structure and composition of the API will have significant influence on the properties, particularly, the bioavailability of drugs. Brittain [47] has recently reviewed the co – crystal systems of pharmaceutical interest. There are several co – crystal system reported in the recent one year, e. g. sulfamerazine with sulfamethazine [48] and Pyrazinamide – Diflurisal [49].

The characterization of grown crystals of APIs or organic molecular solids is important for this application point of view and helps to identify the strength or weakness in terms of the properties of the known or existing compounds. The crystal growth and characterization studies are reported for 1- (2 – thiophen) – 3 – (2,3,5 – trichlorophenyl) – 2 – propen – 1 – one [50] and N – (2 - hydroxybenzyldene) acetohydrazide [51]. Recently, the crystal

growth and structure determination of the natural high potency sweetener Rebaudioside A is carried out by Upreti *et al.* [52]. Altogether, the growth, spectral and thermal study of well known drug molecule crystal ibuprofen is conducted by Ramakutty and Ramachandran [53] very recently.

It is indeed a mammoth task to extensively review the complete literature, however, an humble attempt has been made over hereto briefly review the literature of last one or two years before beginning the discussion of growth and characterization of some APIs and organic crystals in this chapter as well as in the following chapters.

3.3 Synthesis of n – butyl THPM crystals

3.3.1 Synthesis

To obtain n-butyl THPM powder, n- butyl acetoacetate powder was synthesized first, which was obtained by transesterification of ethyl acetoacetate with n – butyl alcohol by using Biginelli condensation. To synthesize n-Butyl THPM, a mixture of n – butyl acetoacetate (1.58g, 10mmol), benzaldehyde (1.06g, 10mmol) and thiourea (1.14g, 15mmol) in absolute ethanol (20ml) containing 2 to 3 drops of HCl as a catalyst was refluxed for 15 – 18 hours. All AR grade chemicals were used for the synthesis. Then the reaction precipitates were obtained, which were filtered out and washed with cold ethanol in order to yield a pale yellowish solid powder of n – butyl THPM. The n-butyl THPM powder was re-crystallized several times to increase the purity. The synthesis of n – butyl THPM was carried out by collaborators in Chemistry Department of Saurashtra University. The fragmentations in mass spectrum suggested the formulation of

the said compound. Figure 3.2 shows the molecular structure of n – butyl THPM.

The n-butyl THPM crystals were grown by the solution growth technique using slow solvent evaporation. Chloroform was selected as a solvent after trying different organic solvents. Pale yellowish, semitransparent, coagulated crystals were grown at the bottom of the vessel having maximum dimensions 2.0 mm x 1.5 mm. Figure 3.3 shows the type of the crystals grown.

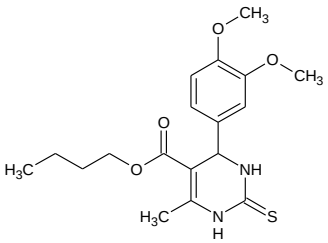

Figure 3.2 Molecular Structure of n – butyl THPM

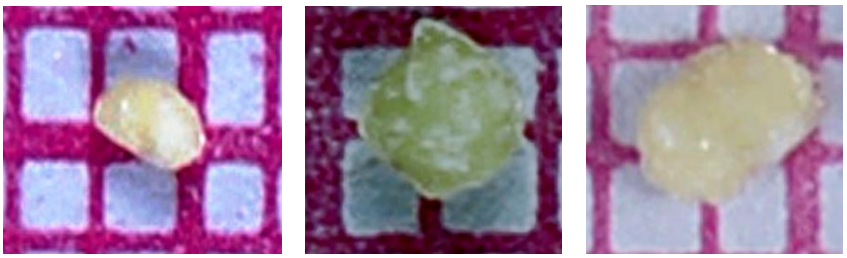

Figure 3.3 The grown crystals of n – butyl THPM on graph paper

3.4 Powder XRD Study of n – Butyl THPM Crystals

Powder X-ray Diffraction (XRD) is perhaps the most widely used x-ray diffraction technique for characterizing inorganic and organic crystalline materials. As the name suggests, the sample is usually in a powder form, consisting of fine grains of single crystalline material to be studied. The

technique is also used widely for studying particles in liquid suspensions or polycrystalline solids (bulk or thin film materials) [54]. The term 'powder' really means that the crystalline domains are randomly oriented in the sample. Therefore, when the 2-D diffraction pattern is recorded, it shows concentric rings of scattering peaks corresponding to the various *d* spacings in the crystal lattice. The positions and the intensities of the peaks are used for identifying the underlying structure (or phase) of the material. The method has been traditionally used for phase identification, quantitative analysis and the determination of structure imperfections. In recent years, applications have been extended to new areas, such as the determination of crystal structures and the extraction of three-dimensional micro-structural properties [55].

Among the many experimental techniques available for the identification of solid forms, including polymorphs, solvates, salts, co-crystals and amorphous forms, the Powder XRD stands out as a generally accepted “gold standard.” It does not mean that Powder XRD should be used to the exclusion of other experimental techniques. When studying solid forms, powder XRD has applications throughout the drug development and manufacturing process, ranging from discovery studies to lot release. The utility of XRD becomes evident when one considers the direct relationship between the measured XRD pattern and the structural order and/or disorder of the solid. There are several benefits [56]:

- Identification of existing forms of Active Pharmaceutical Ingredient (API).

- Characterization of the type of order present in the API (crystalline and/or amorphous).
- Determination of physical and chemical stability.
- Identification of the solid form of the API in the drug product.
- Identification of excipients present in a drug product.
- Monitoring for solid form conversion upon manufacturing.
- Detection of impurities in a drug product.
- Quantitative analysis of a drug product.

Gurskaya *et al.* [57] studied the x – ray diffraction of three 1,2,3,4-tetrahydropyrimidine-2-ones derivatives: As the grown crystals were coagulated in nature and the single crystal XRD was not possible, the powder XRD study was carried out on n- butyl THPM crystals. Figure 3.4 is the powder XRD pattern of n-butyl THPM, which suggests that the sample is highly crystalline in nature. The crystal structure was obtained by assuming the unit cell parameters of the nearest similar compound, that is, dihydropyrimidine – 5 – carboxylate core [58] as a reference to fit the reflections in the powder XRD pattern using software powder x. All major reflections in the XRD pattern were fitted and assigned the corresponding crystallographic plane. The n – butyl THPM crystals exhibited triclinic system with the estimated unit cell parameters as, a = 7.1689Å, b = 10.3378 Å, c = 10.2246 Å, α = 103.78°, β = 107.56°, γ = 92.66°.

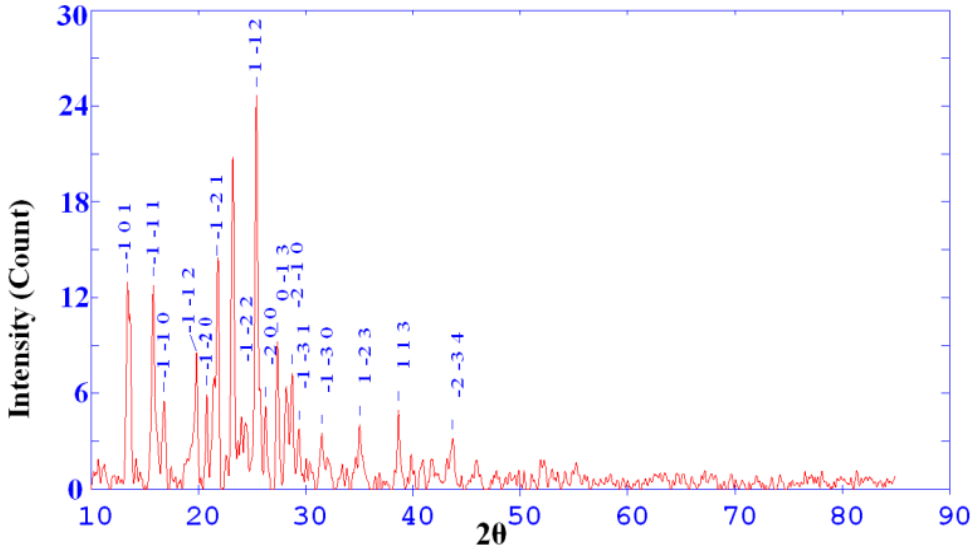

Figure 3.4 Powder X – Ray Diffraction pattern of n – butyl THPM Crystals

3.5 FT-IR Spectral Study of n – butyl THPM Crystals

Infrared spectroscopy is a very powerful analytical tool for examining both inorganic and organic materials [59 – 61]. It is an easy way to identify the presence of certain functional groups in a molecule. Also, one can use the unique collection of absorption bands to confirm the identity of a pure compound or to detect the presence of specific impurities. Infrared spectroscopy reveals information about molecular vibrations that cause a change in the dipole moment of molecules. It offers a fingerprint of the chemical bonds present within materials. When radiation passes through a sample (solid, liquid or gas), certain frequencies of the radiation are absorbed by the molecules of the substance leading to the molecular vibrations. The frequencies of absorbed radiation are unique for each molecule which provides the characteristics of a substance.

FT-IR spectroscopy is the further advancement of IR spectroscopy by using the mathematical concept of *Fourier Transform* through proper

electronic circuit and computer interfacing. From the earliest days of infrared spectroscopy it was observed that functional groups of atoms could be associated with definite characteristic absorption bands, i.e., the absorption of infrared radiation over certain frequency intervals. The infrared spectrum of any given substance is interpreted by the use of the known group frequencies and thus it will be easy to characterize the substance as one containing a given type of group or groups. Although group frequencies occur within narrow limits, interference or perturbation may cause a shift of the characteristic bands due to (a) the electro negativity of neighboring groups or atoms, (b) the spatial geometry of the molecule, or (c) the mechanical mixing of vibrational modes.

Functional groups sometimes have more than one characteristic absorption band associated with them. On the other hand, two or more functional groups may absorb in the same region and hence, in general, can only be distinguished from each other by means of other characteristic infrared bands, which occur in non-overlapping regions.

Absorption bands may be considered as having two origins, these being the fundamental vibrations of (a) functional groups, e.g. C=O, C=C, C≡N, $-CH_2-$, $-CH_3-$, and (b) skeletal groups, i.e. the molecular backbone or skeleton of the molecule e.g., C-C-C-C. Absorption bands may also be aroused from stretching vibrations, i.e., vibrations involving bond-length changes, or deformation vibration, i.e., vibrations involving bond-angle changes, of the group. Each of these, in some cases, may be considered as arising from symmetric or asymmetric vibrations.

For a given functional group, the vibration bands due to stretching occur at higher frequencies than those due to deformation. This is because more energy is required to stretch the group than to deform it due to the bonding force directly opposing the change.

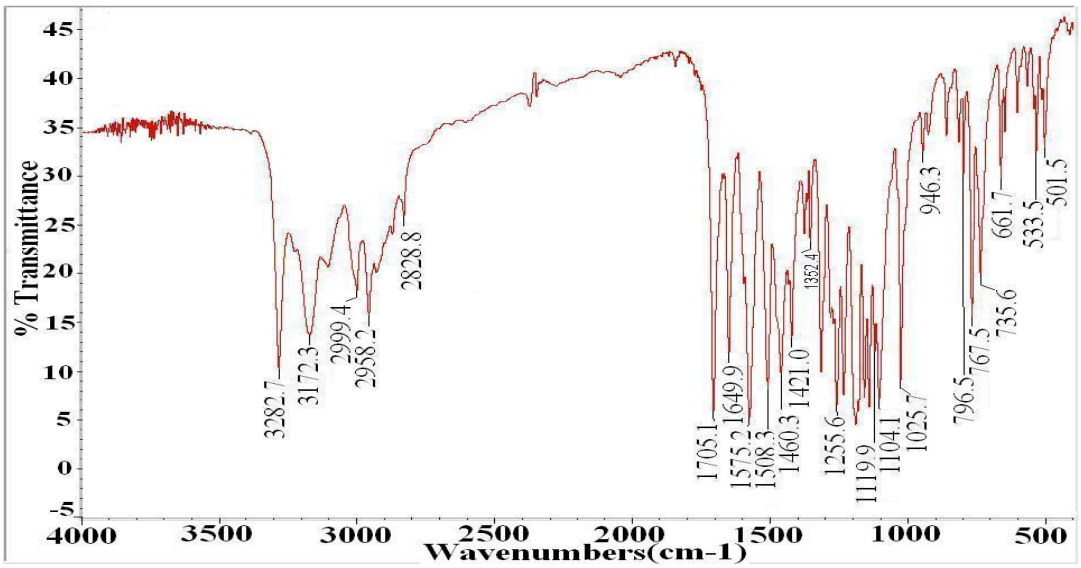

Figure 3.5 FT-IR spectrum of n – butyl THPM Crystals

Figure 3.5 shows the FT – IR spectrum of n-butyl THPM crystals. The analysis of spectrum suggests that the absorptions occurring at 3282.7 cm^{-1} and 3172.3 cm^{-1} show - NH bending. The absorption occurring at 2999.4 cm^{-1} is due to stretching vibration of – CH_3. The absorptions taking place at 2958.2 cm^{-1} and 2828.8 cm^{-1} are due to C – H stretching vibration of – CH_2 and the absorption at 1705.1 cm^{-1} is due to C = O stretching vibration of ester. Whereas, the absorptions situated at 1649.9 cm^{-1}, 1575.2 cm^{-1} and 1508.3 cm^{-1} show C = C aromatic ring skeleton vibrations. The absorption at 1460.8 cm^{-1} is assigned to C – H bending vibration of – CH_2 and the absorption at 1352.4 cm^{-1} is due to C – H bending vibration of – CH_3. Altogether, the absorptions occurring at 1255.6 cm^{-1}, 1119.9 cm^{-1}, 1104.1 cm^{-1} and 1025.7

cm^{-1} are due to C – O stretching vibrations of esters and the absorptions at 946.3 cm^{-1}, 796.5 cm^{-1}, 767.4 cm^{-1} and 661.7 cm^{-1} are attributed to either out of plane bending vibrations or aromatic substitution.

3.6 SEM Study of n – butyl THPM crystals

From the visual observation and under optical microscope observations, it was found that the grown crystals of figure 3.3 were coagulated in nature and hence for finer observation SEM study was conducted.

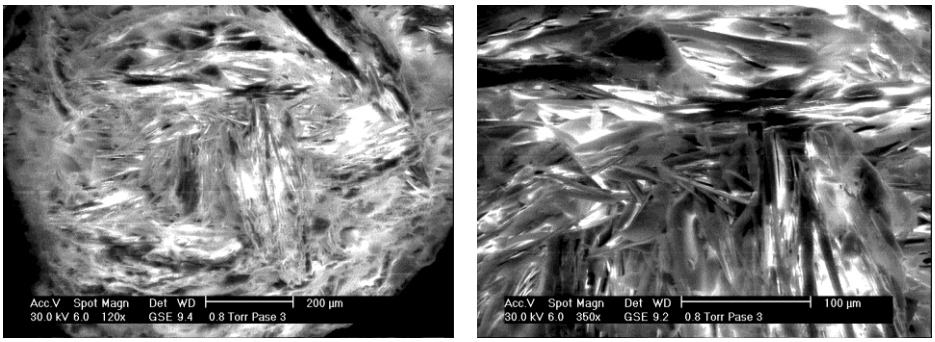

(a) (b)

Figure 3.6 SEM images of n – butyl THPM Crystals

Figure 3.6 (a) shows the Scanning Electron Microscopy (SEM) image of the grown crystal at 120x magnification, suggesting that the aggregated needles form the crystalline mass, which is further exhibited in Figure 3.6 (b) with clear nature at higher magnification of 350x. The needles were aligned in more than one specific orientation.

3.7 TG – DTA – DSC Study of n – butyl THPM Crystals

Thermo-gravimetric analysis (TGA) is a very useful technique to assess the thermal stability of various substances; many workers have demonstrated its usefulness [62 - 65].

In TGA, the weight of a sample in a controlled atmosphere is recorded continuously as a function of temperature or time, as the temperature of the sample is increased (usually linearly with time). A plot of mass or mass percent as a function of temperature is called a thermogram, or a thermal decomposition curve, or a pyrolysis curve. Often a pyrolysis occurs through many-stepped mechanisms, where the temperature ranges for each step overlap, resulting in irregular weight-temperature curve that may be difficult to analyze. Also, in many cases the trace follows a characteristics path common to a wide range of decomposition processes, which includes many polymer pyrolysis. The sample weight drops slowly as pyrolysis begins, then drops precipitously over a narrow range of temperature and finally turns back to zero slope as the reactants are used up.

Differential Thermal Analysis (DTA) is the analytical technique in which the temperature differential between the sample and a nonreactive reference material is monitored while the two substances are subjected to the identical heating program. Unlike TG, DTA does not require a change in mass of the sample in order to obtain meaningful information. DTA can be used to study any process in which heat is absorbed or evolved. Among the endothermic processes that can be studied using DTA are melting, boiling and sublimation. Absorptive processes are often exothermic and can be studied by using DTA. Thermal curves obtained with DTA show peaks corresponding to processes in which the temperature of the sample is increased or decreased relative to the temperature of the reference substance. Upward deflection usually corresponds to exothermic reactions and downward deflection to endothermic

reaction. The temperatures at which the peaks are observed in thermal curve can be used for qualitative analysis.

Differential Scanning Calorimetry (DSC) is the technique in which the temperatures of a sample and reference substance are controlled at identical values while the amount of heat that is added to the other substance is monitored. DSC can be used to measure enthalpimetric changes associated with physical and chemical transitions. In the drug industry DSC is used to determine the purity of some drugs [66].

Thermal study of different pyrimidine compounds have been reported by several authors [67,68]. As the pyrimidine based compounds find pharmaceutical applications it is important to assess the thermal stability and the presence of moisture. The thermal decomposition behavior of n-butyl THPM was similar to the reported for other pyrimidine based compounds. Figure 3.7 shows the thermogram of n-butyl THPM crystalline powder.

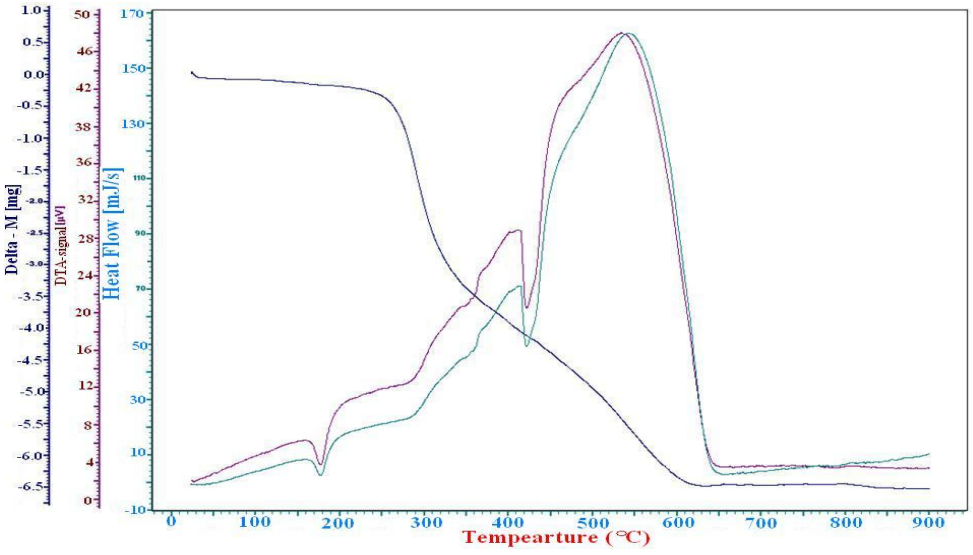

Figure 3.7 TG – DTA – DSC of n – butyl THPM Crystals

The TG plot of n – butyl THPM shows that the sample remains stable up to 150 ^{o}C and then it slowly starts decomposing and beyond 260^{0} C it

starts decomposing rapidly. The complete decomposition takes place within 630 ^{o}C. The DTA plot indicates that the decomposition process of n –butyl THPM occurs through two endothermic reactions at 175.7 ^{o}C and 420.6 ^{o}C, respectively. A broad exothermic peak is observed at 540.3 ^{o}C. From the DSC plot several thermodynamic parameters were calculated by using the software TA evaluation available with the set up. For the first endothermic reaction at 175 ^{0}C, the enthalpy, the change in heat capacity and the heat change are calculated and found to be 75.20 J/g, 1.93 J/gK and -33.72 μVs/mg, respectively. This may be due to some phase change occurring without significant breaking of the bonds resulting into marginal weight loss, which may be due to melting of a sample. Similarly, for the second endothermic reaction at 420 ^{0}C, the values of enthalpy, change in heat capacity and heat change are found to be -467.63 J/g, 18.98 J/gK and -104.25 μVs/mg, respectively. This may be due to decomposition of the sample. After the second endothermic reaction an exothermic reaction is observed at 533 ^{0}C, which may be due to complete decomposition of the sample into the gaseous phase and reaction within the products.

3.8 Kinetic Parameters of n – butyl THPM Decomposition

Usually, the kinetic parameters can be evaluated from the TGA curve by applying several equations [68 – 70], which were proposed by different authors on the basis of different assumptions to the kinetics of the reaction and the Arrhenius law. These equations are (i) Coats and Redfern Relation [51], (ii) Horowitz and Metzger Relation [69] and (iii) Freeman - Carroll Relation [70]. However, in the present investigation, the Coats and Redfern

relation is used because it facilitates not only to evaluate the activation energy and order of reaction but also the frequency factor. By using this equation one can select any temperature value at which one desires to evaluate kinetic parameters, unlike the standard software calculated at the particular peak values. It also helps further to evaluate the thermodynamic parameters. The Coats and Redfern formula is as follows:

$$\log_{10}\left(\frac{1-(1-\alpha)^{1-n}}{T^2(1-n)}\right)=\left\{\log_{10}\left(\frac{AR}{aE}\right)\left(\frac{1-2RT}{E}\right)\right\}-\left\{\frac{E}{2.3RT}\right\} \quad \text{.... (3.1)}$$

where, α is the fraction of original substance decomposed at time t, that is, $\alpha = (W_o - W) / (W_o - W_f)$; W_o is the initial weight, W is the weight at time t, W_f is the final weight; E is the activation energy of the reaction, A is the frequency factor, a is the heating rate in K/min, R is the gas constant, n is the order of reaction and T is the absolute temperature. Here, it should be noted that the equation 3.1 is valid for all values of n except $n = 1$.

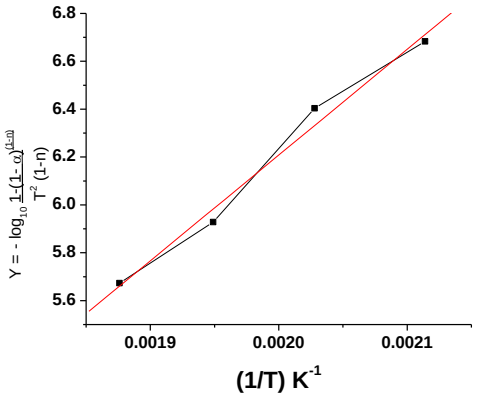

Figure 3.8 Coats and Redfern plot for linear fit

The plots of Y = $-\log_{10}[\{1-(1-\alpha)^{1-n}\}/\{T^2(1-n)\}]$ versus X = $1/T$, were straight lines for different values of n, however, the best linear fit plot gives the

correct value of *n*. The value of activation energy is obtained from the slope of the best linear fit plot. Figure 3.8 shows the Coats and Redfern plot. The values of activation energy *E*, frequency factor *A* and order of reaction *n* are as tabulated in table 3.1 for temperature 260 ^{o}C.

Table 3.1 Kinetic parameters of n – butyl THPM

Samples	Kinetic Parameters
n – butyl THPM crystals	Order of reaction (n) = 0.75
	Activation energy (E) = 22.81 $kJK^{-1}Mol^{-1}$
	Frequency factor (A) = 5.32×10^{18}

3.9 Thermodynamic Parameters of Decomposition

Various thermodynamic parameters were calculated by applying well known formulae, as described in detail by Laidler [71]. The standard entropy of activation $\Delta^{\#}S°$ (here, superscript # is for activation and superscript ° is for standard), i.e. entropy change associated with the activation reaction, can be calculated by the formula,

$$\Delta^{\#}S° = 2.303 \times R \times \log_{10}\left(\frac{Ah}{kT_m}\right) \quad \text{…. (3.2)}$$

where, *A* is the frequency factor, *k* is the Boltzmann constant, *h* is the Plank's constant, *R* is the gas constant, T_m is the absolute temperature in K.

The standard enthalpy of activation $\Delta^{\#}H°$ can be calculated by the formula,

$$\Delta^{\#}H° = E - 2RT \quad \text{… (3.3)}$$

Enthalpy is a state function whose absolute value cannot be known. $\Delta^{\#}H°$ can be ascertained, either by direct method or indirectly. An increase in the enthalpy of a system, for which $\Delta^{\#}H°$ is positive, is referred to as an endothermic process. Conversely, loss of heat from a system, for which $\Delta^{\#}H°$ has a negative value, is referred to as an exothermic process.

The energy difference between the transition state of a reaction and the ground state of the reactants is known as standard Gibbs energy of activation. The standard Gibbs energy of activation $\Delta^{\#}G°$ can be calculated as

$$\Delta^{\#}G° = \Delta^{\#}H° - T\,\Delta^{\#}S° \quad \ldots (3.4)$$

The standard change in internal energy of activation $\Delta^{\#}U°$ can be calculated by the following formula

$$\Delta^{\#}U° = E - R\,T \quad \ldots (3.5)$$

Table 3.2 gives the values of different thermodynamic parameters of dehydration and decomposition calculated at 260 ^{o}C temperature. Positive values of $\Delta^{\#}S°$ and $\Delta^{\#}H°$ suggest spontaneous reaction at high temperature.

Table 3.2 Thermodynamic Parameters of n – butyl THPM

Samples	Thermodynamic Parameters
n – butyl THPM crystals	Standard Entropy $\Delta^{\#}S° = 110.49$ Jkmol^{-1}
	Standard Enthalpy $\Delta^{\#}H° = 15.61$ kJmol^{-1}
	Standard Gibbs free energy $\Delta^{\#}G° = -3.22$ kJmol^{-1}
	Standard change in internal energy $\Delta^{\#}U° = 19.21$ kJmol^{-1}

3.10 Dielectric Study of n – butyl THPM Crystals

Materials, which are electrical insulators or in which an electric field can be sustained with minimum dissipation of power, are known as dielectric materials. In the general sense, dielectric includes all materials except the condensed state of metals.

Dielectric properties are very important for materials characterization, particularly, for pharmaceutical compounds and crystalline materials. In pharmaceutical compounds, such as in polymorphs and solvates characterizations, the contribution of dielectric spectroscopies to study the details of all molecular movements specific of morphous of crystalline phase is essential and probably will become indispensable in future developments of pharmaceutical sciences. In this regard the study has been carried out correlating the existing knowledge between the molecular mobility of a selected model amorphous new chemical entities (NCE) and its crystallization kinetics determined with temperature [72,73]. The dielectric and calorimetric analysis were carried out by Mantheni *et al.* [74]. Also, the dielectric behaviour of Tinidazole in acetone has recently been reported by Castillo *et al.* [75]. As the present compound n – butyl THPM is expected to possess certain pharmaceutical applications, the dielectric study has been carried out.

The value of dielectric constant was calculated by using the following formula,

$$C = \frac{\varepsilon A}{t} = \frac{\varepsilon_0 K A}{t} \qquad \text{... (3.6)}$$

$$K = \frac{Ct}{\varepsilon_0 A}, \quad \text{.... (3.7)}$$

Where, C = Capacitance, ε = Relative permittivity, A = Area of sample, and ε_0 = Permittivity of free space and K = Dielectric constant.

The value of dielectric constant (K) of material is usually composed of four contributions; which are from electronic, ionic, dipolar and space-charge polarizations. However, all these may be active in low frequency region. The nature of the variation of K with frequency indicates which contribution is prevailing. The space-charge contribution depends on the purity and perfection of the crystal. The dipolar orientational effect can be sometimes seen up to 10^{10} Hz. The ionic and electronic polarizations always exist below 10^{13} Hz [76]. Figure 3.9 shows the variation of K with frequency of applied field. The dielectric constant decreases rapidly as frequency increases. The nature of the plots in the figure 3.9 suggest space-charge polarization is active in low frequency region, which is reflected in terms of rapid decrease in the value of dielectric constant with increase in frequency and its higher values in the low frequency region. This also further suggests that the dipoles can not comply with the varying field and hence the decreasing nature is exhibited, which is a common feature in many compounds such as 4 - (2 - hydroxyphenylamino) – pent - 3en – 2 – one (HPAP) [77], zinc tartrate [78] and zinc doped nano – hydroxyapatite [79].

More-or-less, the same type of nature is observed for the variation of dielectric loss (*tan δ*) with the frequency of applied field as shown in the figure 3.10.

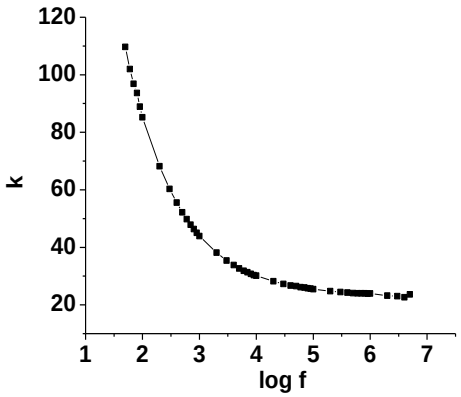

Figure 3.9 Plot of Dielectric Constant versus log f

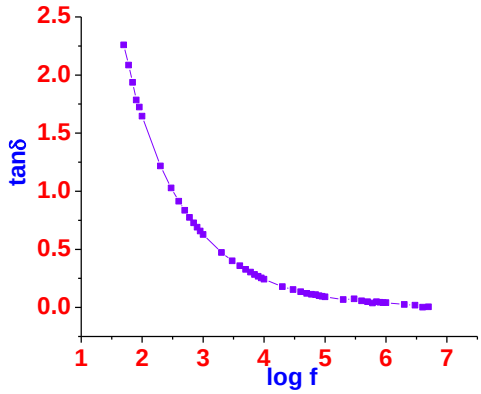

Figure 3.10 Plot of Dielectric loss versus log f

Recently, an a.c. conductivity and dielectric constant measurements of bulk pyronine G (Y) is reported by Yaghmour [80]. The author observed that the dielectric constant and dielectric loss decreased by increasing frequency and the a.c. conductivity was due to the correlated barrier hopping. Usually, typical current carriers in organic solids are through π- conjugated systems and the electrons can move via π-electron cloud, especially, by hopping, tunneling and other related mechanisms. The variation of a. c. conductivity σ_{ac} shows that it increases as the frequency increases and the opposite nature is observed for a. c. resistivity as shown in figure 3.11

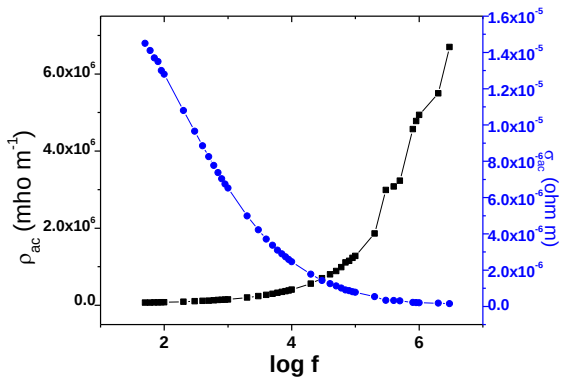

Figure 3.11 Plot of a. c. conductivity and a. c. resistivity versus log f

3.11 Synthesis and Characterization of n – butyl THPM Nano particles

The n – butyl THPM nanoparticles were synthesized by using w/o microemulsion technique because microemulsions are isotropic, transparent and thermodynamically stable systems composed of water, oil and surfactant and facilitates the growth of nano-particles in micelles. Microemulsions find large number of applications, which are reviewed by Pal and Moulik [81]. The internal structures and dynamics of micro – emulsions are having important properties, which are investigated by variety of methods. The microemulsion can be a potential system for drug delivery. As noted earlier by applying the microemulsion the total dose of the drug can be reduced and the side effects can be minimized [82].

3.12 Hypothesis for the Mechanisam of Nanoparticle Formation

The synthesis of organic nanoparticles such as cholesterol and retinol by precipitating them directly in water cores through w/o microemulsion was discussed in detail elsewhere [83,84]. Debuigne *et al.* [85] and Bayrak and Iscan [86] have proposed the hypothesis of the growth of nanoparticles by microemulsion technique. Mainly, there are three hypotheses proposed for the organic nanoparticles containing micelles [87] which are; (i) the nanoparticles are in the organic phase and are in direct contact with the polar head of the surfactants, (ii) the nanoparticles are surrounded by water and (iii) the nanoparticle are surrounded by surfactant tails having their polar heads toward the water phase and the water is also in contact with a second layer of surfactant polar layers.

In the present hypothesis the formation of n-butyl THPM nanocrystalline particles is proposed through several stages. In the first stage, Triton X - 100 and n-butanol were added one by one in a specific amount in double distilled water so that the aqueous cores were surrounded by oil and the surfactant. In the second stage, n-butyl THPM, dissolved in appropriate solvent was diffused into empty micelles during continuous stirring. In the third stage, the n-butyl THPM precipitated in the aqueous cores due to its insolubility in water. In the fourth stage, the displacement of the solvent from micelles to the surrounding took place, and in the fifth stage the exchange of organic molecules between the aqueous cores occurred as a result of collision between different droplets due to stirring. In stages six, seventh and eighth, the formed nanoparticles are stabilized by surfactant molecules.

Various workers [83,85] have proposed the hypothesis of the growth of nanoparticles by microemulsion technique. In the present study the hypothesis of synthesis of n – butyl THPM nano particles is presented as follows. As shown in figure 3.12 in the first stage the aqueous cores are surrounded by the surfactant. In the second stage the organic molecules (n – butyl THPM) dissolved in the appropriate solvent (chloroform) is added drop by drop into the empty micelles under continuous stirring.

In the second stage the organic molecules (n – butyl THPM) dissolved in the appropriate solvent (chloroform) is added drop by drop into the empty micelles under continuous stirring. The solution goes to the aqueous cores (by diffusion) and penetrates inside by crossing the interfacial film. The solvent

certainly plays a role in the transport of the organic molecule inside the aqueous cores.

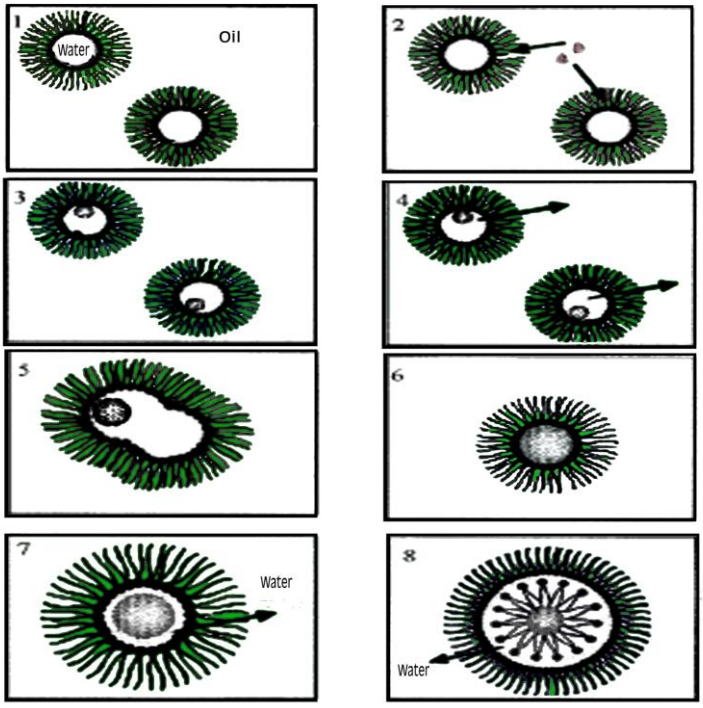

Figure 3.12 Schematic Diagram of hypothesis of Microemulsion

In the third stage the organic material precipitates in the aqueous core because of its insolubility in water. The nuclei are thus formed. The fourth stage shows the deplacement of the solvent. In the fifth stage exchange of n – butyl THPM molecules between the aqueous cores as a result of collisions between droplets. Then the so formed nuclei and lastly in the sixth, seventh and eighth stages the nanoparticles are stabilized by surfactant molecules.

3.13 Phase Diagram

A phase diagram is a type of chart used to show conditions at which thermodyanmically distinct phases can occur at equillibrium. The

microemulsion region is usually characterized by constructing a ternary-phase diagram. Three components are the basic requirement to form a microemulsion: an oil phase, an aqueous phase and a surfactant. The relative amounts of these three components can be represented in a ternary phase diagram.

The three components composing the system are each found at an apex of the triangle, where their corresponding volume fraction is 100%. Moving away from that corner reduces the volume fraction of that specific component and increases the volume fraction of one or both of the two other components. Each point within the triangle represents a possible composition of a mixture of the three components or pseudo-components, which may consist of one, two or three phases. These points combine to form regions with boundaries between them, which represent the "phase behavior" of the system at constant temperature and pressure.

The phase diagram, however, is an empirical visual observation of the state of the system and may, or may not, express the true number of phases within a given composition. Apparently clear single phase formulations can still consist of multiple iso-tropic phases. Since these systems can be in equilibrium with other phases, many systems, especially, those with high volume fractions of both the two immiscible phases, can be easily destabilized by anything that changes this equilibrium, e.g., high or low temperature or addition of surface tension modifying agents.

However, examples of relatively stable microemulsions can be found. It is believed that the mechanism for removing acid build up in car engine oils

involves low water phase volume, water-in-oil (w/o) microemulsions. Theoretically, transport of the aqueous acid droplets through the engine oil to micro-dispersed calcium carbonate particles in the oil should be most efficient when the droplets are small enough to transport a single hydrogen ion (the smaller the droplets, the greater the number of droplets, the faster the neutralisation). Such microemulsions are probably very stable across a reasonably wide range of elevated temperatures [88].

Here in this case phase diagram of triton X – 100/water/ n – butanol was constructed as shown in figure 3.13.

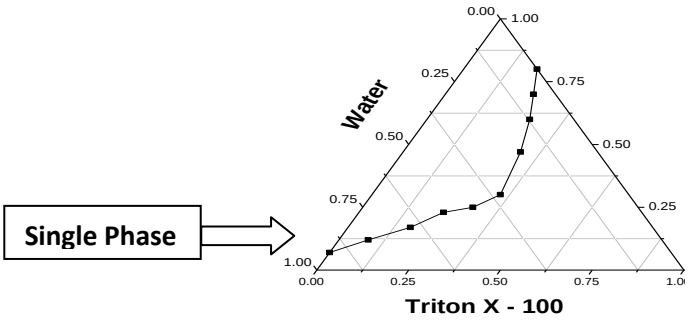

Figure 3.13 Ternary diagram of Triton X – 100/ Butanol /Water system (Large Domain shows the existence of the microemulsion at room temperature)

The Triton X – 100/n – butanol/water ternary diagram was constructed by varying the volume of the three liquids in a stepwise systematic manner in such a way that the total volume remained constant and it was found that the single phase existed in a large area. To construct the ternary phase diagram triton X – 100 was dissolved in appropriate amount of water in such a way that the molar ratio (R) = [H_2O] / surfactant was maintained at six, thereafter, the desired amount of n – butanol was added. This resulting mixture remained in

the single phase region. This phase diagram was earlier reported for triton X – 100/n-butanol/water by Jesus *et al.* [89] and similar other systems such as CTAB/Hexanol/water, Triton X – 100/Decanol/water, AOT/Heptane/ water [85].

3.14 Synthesis

n – butyl THPM crystalline material was used for the synthesis of nano particles. The solution of n – butyl THPM made in suitable organic solvent (chloroform) was added in drop-wise manner into this mixture with continuous stirring. Within 15-20 minutes n – butyl THPM nano crystalline particles were formed between liquid - liquid interface of the solutions, which were filtered by using filter paper of no. 42 and air dried. The yield of synthesized nano – particles was around 80%.

3.15 Powder XRD Study of n – butyl THPM Nano particles

Figure 3.14 shows the powder X – Ray Diffraction (XRD) pattern of n – butyl THPM nano particles. The peak broadening shows that the formed material is nano in nature. For the analysis of powder XRD pattern a software powder x was used. The unit cell parameters of the chemically near by structure compound 8-ethyl-5,8-dihydro-5-oxo-2-(1-pyrrolidinyl)pyrido [2,3-d] pyrimidine -6- carboxylic acid were taken as a reference. The n– butyl THPM nano particles showed triclinic crystal system with estimated unit cell parameters as, a = 7.1980 Å, b = 10.3378 Å, c = 10.2246 Å, α = 103.78 º, β = 107.56 º, γ = 92.66 º.

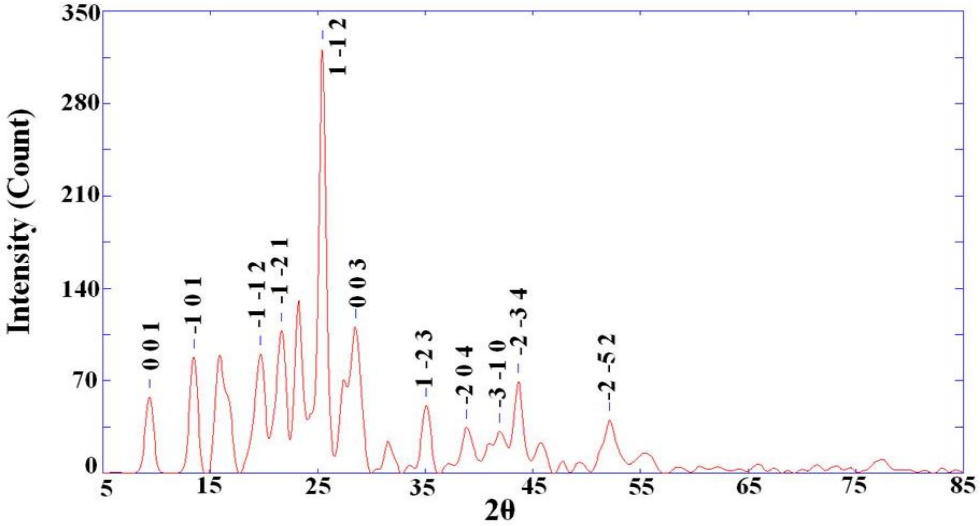

Figure 3.14 Powder XRD pattern of n – butyl THPM nano particles

The average particle size of n – butyl THPM nano particles was determined from the powder XRD pattern by employing the Scherrer's formula given as follows,

$$D = \frac{K\lambda}{\beta cos\theta} \qquad \text{.... (3.8)}$$

Where, *D*= Average diameter, *K*= Shape factor, *λ* = Wavelength of source used, *β* = FWHM (Full Width Half Maximum) and *θ*= Angle of the peak for particular Bragg reflection. From the Scherrer's formula the average particle size of n-butyl THPM nano particles was found to be of 35 nm.

3.16 TEM study of n – butyl THPM Nano particles

The Transmission Electron Microscopy (TEM) study was carried out to determine the exact size and morphology of the synthesized n – butyl THPM nanocrystalline particles. The TEM images of different size nano particles are shown in Figures 3.15 (a) and 3.15 (b), which indicate nano particles of 18.36nm and 61.75 nm, respectively. TEM results suggested that the particles were having nearly spherical type morphology and their size varied from 15 nm – 65 nm. From the images of Figures 3.15 (a) and 3.15 (b), one can find

that the large size nano particles in Figure 3.15 (b) are having more precise spherical type morphology. In the present study, instead of mono-disperesed nanoparticles, different size of nanoparticles was obtained. The possible explanation for that could be given hereby. The microemulsion is expected to tolerate a limited quantity of organic molecules in order to form nano particles without phase separation. The initial microemulsion is expected to be thermodynamically stable. If the number of organic molecules per aqueous core increases then this interaction with surfactant molecules increases at the interface. The optimal radius of curvature is then disturbed and the phase separation occurs more readily for specific molar ratio (R) factor, as soon as the organic molecules come into contact with aqueous core, the nuclei formation takes place due to the insolubility of organic molecules in water.

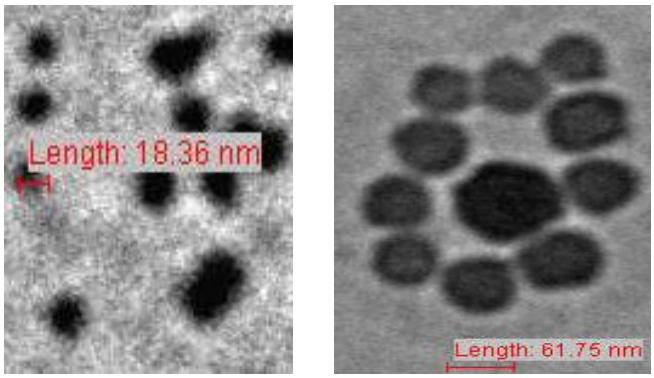

(a) (b)

Figure 3.15 TEM images of n – butyl THPM nano particles

The nano particles later on grows to a certain favored size and are stabilized in the same manner with surfactants in spite of their presence in both immiscible phases. The magnetic stirring is expected to influence this and different sizes of nano particles are stabilized rather than the same size of nano particles.

3.17 FT-IR Spectral study of n – butyl THPM Nano particles

FT – IR spectrum of n – butyl THPM nanocrystalline particles is shown in figure 3.16. The analysis of spectrum suggests that the absorptions occurring at 3282.4 cm^{-1} and 3171.9 cm^{-1} show – NH bending, the absorption occurring at 2999.2 cm^{-1} is due to C – H stretching vibration of – CH_3, the absorption taking place at 2957.5 cm^{-1} is due to C – H stretching vibration of – CH_2 and the absorption at 1704.7 cm^{-1} is due to C = O stretching vibration of ester. Whereas, the absorptions situated at 1649.9 cm^{-1}, 1574.9 cm^{-1} and 1508.2 cm^{-1} show C = C aromatic ring skeleton vibrations. The absorption at 1420.8 cm^{-1} is assigned to C – H bending vibration of – CH_2 and the absorption at 1366.1 cm^{-1} is due to C – H bending vibration of – CH_3.

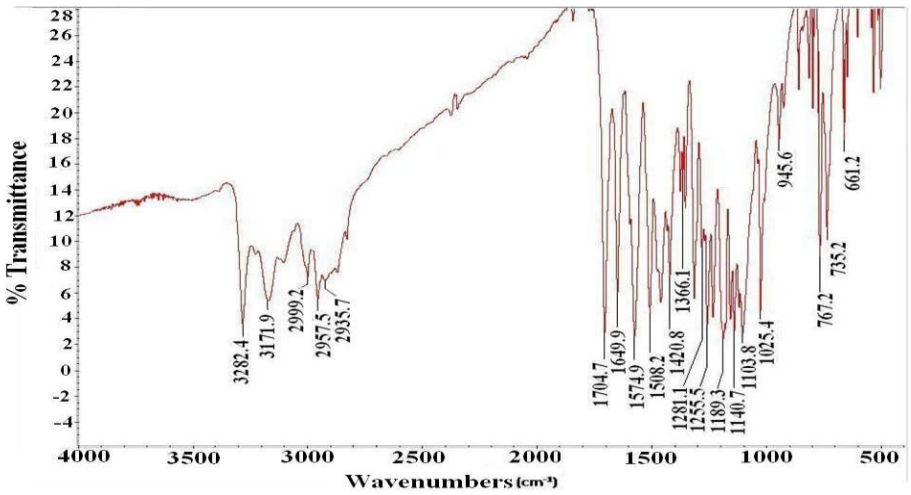

Figure 3.16 FT – IR spectrum of n – butyl THPM nanoparticles

Altogether, the absorptions occurring at 1281.1 cm^{-1}, 1255.5 cm^{-1}, 1189.3 cm^{-1}, 1140.7 cm^{-1}, 1103.8 cm^{-1} and 1025.4 cm^{-1} are due to C – O stretching vibrations of esters and the absorptions at 945.6 cm^{-1}, 767.2 cm^{-1}, 735.2 cm^{-1} and 661.2 cm^{-1} are attributed to the out of plane bending vibration or aromatic substitution.

Comparing FTIR spectra of n – butyl THPM crystalline sample and nano – particles sample, it can be observed that no major changes are observed. Very small changes are observed within 940 cm^{-1} to 650 cm^{-1} range, however, they cannot be firmly attributed to the nano – crystalline nature.

3.18 TG – DTA – DSC of n – butyl THPM Nano particles

Thermal stability of n – butyl THPM nanocrystalline particles was assessed by employing the TGA, DTA and DCS as shown in figure 3.17. It can be noticed from the thermogram that a minor weight loss of the order of 0.2 percent of weight is observed within 160 ^{o}C - 180 ^{o}C, which corresponds to a sharp endothermal peak at 177.5 ^{o}C temperature with 102.62 J/g enthalpy. This suggests some minor phase change in the sample. This endothermic peak is comparatively small in crystalline sample. The sample then remains almost stable up to 250 ^{o}C with 0.05 percent weight loss. Thereafter, it decomposes rapidly to a small stage around 400 ^{o}C corresponding to a sharp endothermal peak indicating phase transition may be in terms of melting of the sample. The values of enthalpy, change in heat capacity and heat change are found to be – 101.70J/g, 0.8966J/gk and -47.98 µVs/mg, respectively. The melting point of n-butyl THPM was measured by open capillary technique and was found to be 364 ^{o}C.

Finally, it decomposes up to 620 ^{o}C and the remaining weight percent is 9.3 of its original weight. This decomposition stage corresponds to a broad exothermic peak, which may be due to the combustion of organic chemicals

as the combustion of organic chemicals takes place quickly and generates an exothermic peak.

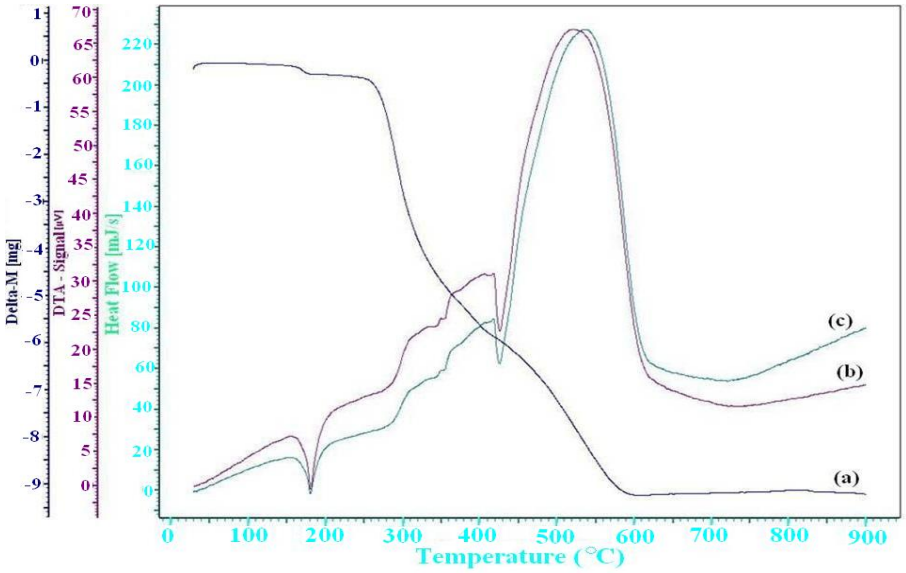

Figure 3.17 (a)Thermogram (b) DTA (c) DSC of n – butyl THPM

Following this almost stable state achieved up to the end of the analysis. Decomposition illustrated by the loss of mass in the temperature range 280 ^{o}C – 580 ^{o}C may be due to the liberation of gaseous fragments and removal of surfactant. Comparing various thermal parameters of crystalline n – butyl THPM and nano – crystalline n – butyl THPM samples of figures 3.7 and 3.17, one finds that the values of thermal parameters are more in the nano – crystalline materials.

The same nature of the thermogram was observed for n-butyl THPM nanocrystalline particles even after six months, which suggests good stability of the samples, a suitable parameter for pharmaceutical applications.

3.19 Kinetic parameters of n – butyl THPM nano particles

Kinetic parameter of n – buty THPM nano particles were calculated by using Coats – Redfern relation [68] as discussed in section 3.8 The plot of $\log_{10}$ [{1-(1-α)$^{1-n}$}/ {T^2 (1-n)}] versus 1/T is shown in figure 3.18 The values of activation energy were obtained from the slope of the best linear fit plot. The values of activation energy *E*, frequency factor *A* and order of reaction *n* were obtained as tabulated in table 3.3.

As the activation energy is considered as a barrier to be surmounted to form reaction products [90], the higher values of activation energy suggests slower reaction rate and hence more stability.

It is noticed from the table 3.3 activation energy of nano particles is higher than the crystalline material, which indicates that nano particles of n – butyl THPM are more stable then the crystalline material.

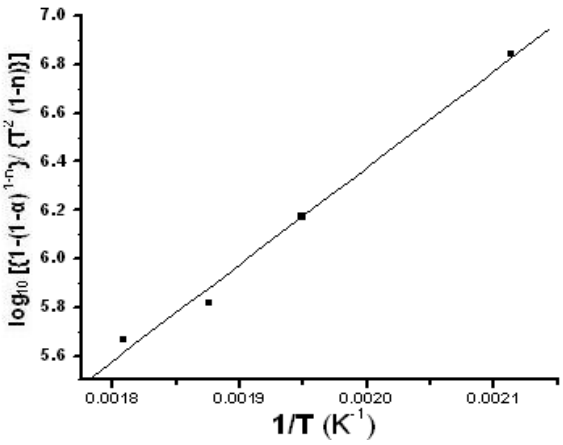

Figure 3.18 Linear fitted plot of C – R relation for n – butyl THPM nanoparticles

Table 3.3 Kinetic Parameters of n – butyl THPM nano particles

Samples	Kinetic Parameters
n – butyl THPM nano particles	Order of reaction (n) = 0.75
	Activation energy (E) = 76.15 $kJK^{-1}Mol^{-1}$
	Frequency factor (A) = 6.77×10^{20}

3.20 Thermodyanmic parameters of n – butyl THPM nano particles

Various thermodynamic parameters such as standard entropy of activation $\Delta^{\#}S°$, standard enthalpy of activation $\Delta^{\#}H°$, standard Gibbs energy of activation $\Delta^{\#}G°$ and standard internal energy of activation $\Delta^{\#}U°$ were calculated by applying well known formulae, as described in detail by Laidler [54] as mentioned in section 3.9. Table 3.4 gives the values of thermodynamic parameters of various decomposition for n – butyl THPM nano particles, at 260 ^{o}C.

Here positive values of $\Delta^{\#}$ S° and $\Delta^{\#}$ H° depict the spontaneous reaction and negative value of $\Delta^{\#}$ G°shows the reaction take place at higher temperature.

Table 3.4 Thermodynamic Parameters of n – butyl THPM nano particles

Samples	Thermodynamic Parameters
n – butyl THPM nano particles	Standard Entropy $\Delta^{\#}$ S° = 149.38 $Jkmol^{-1}$
	Standard Enthalpy $\Delta^{\#}$ H° = 67.62 $kJmol^{-1}$
	Standard Gibbs free energy $\Delta^{\#}$ G°= - 9.01 $kJmol^{-1}$
	Standard change in internal energy $\Delta^{\#}$ U° = 71.88 $kJmol^{-1}$

With comparison to table 3.4 with table 3.2, the values of various thermodynamic parameters are higher in n – butyl THPM nano – particle than n – butyl THPM crystals, which indicates higher stability of nano – particles [91].

3.21 Dielectric Studies of n – butyl THPM Nano particles

Every material has an unique set of electrical characteristics which is dependent on its dielectric properties. The dielectric constant of a material is associated with the energy storage capability in the electric field in the material and the loss factor is associated with the energy dissipation, i.e. conversion of electrical energy to heat energy in the material. Figure 3.19 is a plot of variation of dielectric constant with frequency of applied field. From this plot one can notice that as the frequency increases the dielectric constant initially decreases rapidly and then above 10kHz range decreases very slowly. This type of behavior suggests higher space charge polarizability at lower frequency region. This may be due to the electronic exchange in the ions of the nano-crystalline sample gives the local displacement of electrons in the direction of applied field, which results into the polarization. As the frequency of applied field increases the dipoles can not comply with the varying field and hence the reduction in dielectric constant is observed. The nano-structured materials have enhanced crystal field due to its surface bond contraction and the rise in surface area to volume ratio. As the particle size decreases the crystal field increases and subsequently the dielectric constant decreases. This effect can be seen clearly by comparing figures 3.9 and 3.19, the value

of dielectric constant is comapratively less in nano n – butyl THPM than in crystalline samples.

Figure 3.20 shows the plot of dielectric loss (*tan δ*) of n – butyl THPM nanocrystalline particles versus log f at room temperature. From this plot one can observe that as the frequency increases the dielectric loss decreases.

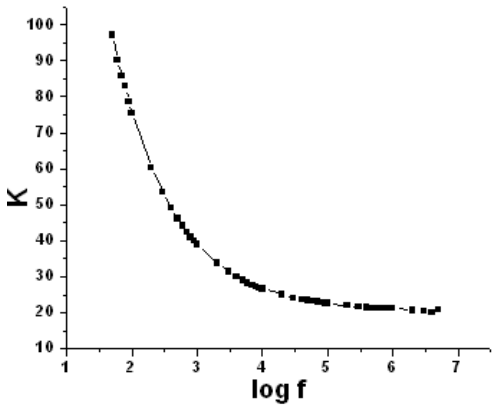

Figure 3.19 Plot of Dielectric Constant versus log f

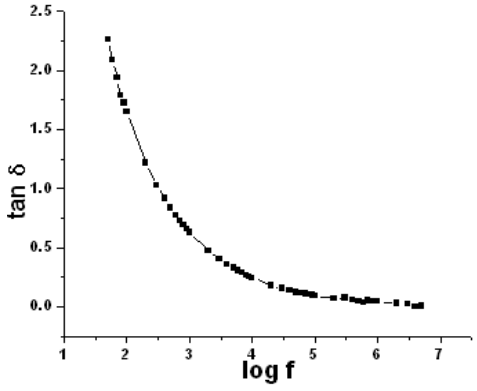

Figure 3.20 Plot of Dielectric Loss versus log f

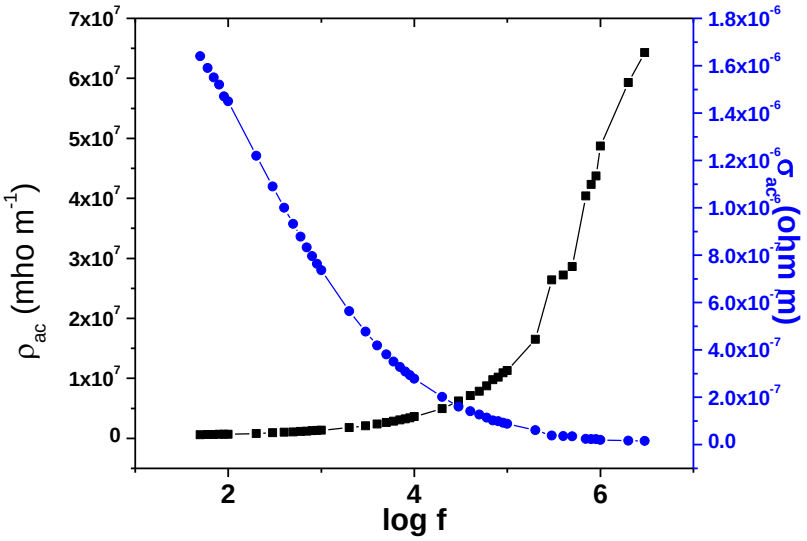

Figure 3.21 a.c. resistivity and a.c. conductivity versus log f

The variation of a. c. conductivity and a. c. resistivity with frequency of applied field is shown in figure 3.21 This shows that as the frequency of the

applied field increases the a. c conductivity increases. The nature of the a. c. resistivity is just opposite to the nature of the a. c. conductivity. Comparing the values of ρ_{ac} and σ_{ac} of n – butyl THPM nano particles with crystalline samples, it is found that the values are more in nano paricles.

3.22 Conclusions

(1) n – butyl THPM material was synthesized by using the mixture of n-butylacetoacetate, benzaldehyde and thiourea and few drops of HCl was used as a catalyst.

(2) Crystals of n – butyl THPM were grown by using slow solvent evaporation technique. Pale yellowish, semi transparent, coagulated crystals having maximum size 2.0 mm x 1.5 mm were grown.

(3) n – butyl THPM crystals showed the triclinic crystal system with unit cell parameter as, a = 7.1689Å, b = 10.3378 Å, c = 10.2246 Å, α = 103.78°, β = 107.56°, γ = 92.66°.

(4) FT-IR spectrum of the n – butyl THPM crystals revealed the presence of functional groups and confirmed the presence of –NH bending, C – H stretching, C = O stretching, C = C aromatic ring skeleton and C – O stretching vibrations.

(5) SEM study suggested that the crystalline bulk sample was of coagulated nature and was composed of fine needle type structure.

(6) From the TGA it was found that the crystalline material remained stable up to 150 ^{o}C thereafter it started decomposing slowly up to 260 ^{o}C and then it decomposed completely into gaseous products up to 630 ^{o}C. DTA plot

showed two endothermic reactions at 175.7 ^{o}C and 420.6 ^{o}C and an exothermic reaction at 540.3 ^{o}C. Various thermal parameters were calculated from DSC.

(7) By applying the Coats and Redfern relation to the decomposition stage, the values of kinetic parameters were calculated at 240 ^{o}C. The value of order of reaction, activation energy (*E)* and frequency factor (*A) n* were found to be 0.75, 22.81 kJ $K^{-1}Mol^{-1}$ and 5.32 x 10^{18}, respectively.

(8) The thermodynamic parameters for the decomposition process were also evaluated. The value of standard entropy, standard enthalpy, standard Gibbs energy and standard change in internal energy of activation were found to be, 110.49 $Jkmol^{-1}$, 15.61 kJmol $^{-1}$, -3.22 kJmol $^{-1}$ and 19.21 kJmol $^{-1}$, respectively. The positive values of standard entropy and standard enthalpy suggested spontaneous nature of reaction at high temperature.

(9) The dielectric constant and dielectric loss decreased as the frequency increased. As the frequency increased the a. c. conductivity increased while the a. c. resistivity decreased.

(10) The nano particles of n – butyl THPM were synthesized by using w/o microemulsion technique with the mixture of water/ n – butanol/ triton X – 100. Ternary phase diagram was constructed by varying the proportion of all the three solutions.

(11) Broadening in the Powder XRD pattern confirmed the nano structured nature. n – butyl THPM nano-particle showed triclinic crystal system with unit

cell parameters as, a = 7.1980 Å, b = 10.3378 Å, c = 10.2246 Å, α = 103.78^{o}, β = 107.56^{o}, γ = 92.66^{o}

(12) The average particle size of the n – butyl THPM nanoparticles was calculated by using Scherrer's formula to a particular reflection in powder XRD pattern and it was found to be 35 nm.

(13) TEM study was carried out to study the exact size and morphology of the particles. From TEM it was found that the n – butyl THPM nano – particles were having spherical morphology with sizes varied from 18 nm – 62 nm.

(14) FT – IR spectrum of the n – butyl THPM nano – particle showed the same absorptions as shown in crystalline material. This showed there was no inclusion or presence of any extra bonding. No conclusive effect was noted in FTIR spectrum due to the nano structured nature.

(15) TG of n – butyl THPM nanoparticles showed minor weight loss around 160 ^{o}C – 180 ^{o}C, which might be due to phase transition. After that the sample remained almost stable up to 280 ^{o}C thereafter it decomposed rapidly and at 620 ^{o}C complete decomposition took place. DTA showed two endothermal peaks at 177.5 ^{o}C and 400 ^{o}C and an exothermic reaction at 580 ^{o}C. DSC showed the entropy and heat change of these endothermic and exothermic reactions.

(16) Kinetic parameters of the n – butyl THPM nanoparticles were calculated by Coats – Redfern formula. It was found that the order of reaction, activation energy (E) and frequency factor (A), 0.75, 76.15 kJ $K^{-1}Mol^{-1}$ and 6.77 x 10^{20},

respectively. With comparison to crystalline sample the higher value of activation energy suggested more stable nature.

(17) The thermodynamic parameters for the decomposition process were also evaluated. The value of standard entropy, standard enthalpy, standard Gibbs energy and standard change in internal energy of activation were found to be, 149.38 $Jkmol^{-1}$, 67.62 $kJmol^{-1}$, - 9.01 $kJmol^{-1}$ and 71.88 $kJmol^{-1}$, respectively. These values were higher than those for the crystalline samples further indicating stable nature of nano – particles.

(18) The dielectric constant and dielectric loss of the n – butyl THPM nanoparticles were dependant on the frequency. It was found that as the frequency increased the a. c. conductivity increased while the a. c. resistivity decreased.

(19) The lower values of dielectric constant for nano particles might be due to the increase in crystal field in nano – structured samples than in crystalline samples.

Refferences

[1] M. Löffler, E. Zameitat, *Encyc. Biol. Chem.*, **3** (2004) 600.

[2] M. Löffler, L. D. Fairbanks, E. Zameitat, A. M. Marinaki, H. Anne Simmonds, *Trends in Mol. Med.,* **11** (2005) 430.

[3] S. S. Cohen, J. Lichtenstein, H. D. Barner, M. Green, *J. Biol. Chem.,* **228** (1957) 611.

[4] G. E. Shabaugh III, *Am. J. Clin. Nutr.,* **32** (1979) 1290.

[5] V. Jankowski, M. Tölle, R. Vanholder, G. Schönfelder, M. Van Der Giet, L. Henning, H. Schlüter, M. Paul, W. Zidek, J. Jankowski, *Nature Med.,* **11** (2005) 223.

[6] V. Jankowski, T. Günthner, S. Herget – Rosenthal, W. Zidek, J. Jankowski, *Sem. In Dialysis*, **22** (2009) 396.

[7] A.Holý, I. Votruba, M. Masojídková, G. Andrei, R. Snoeck, L. Naesens, E. D. Clercq, J. Balzarini, *J. Med. Chem.*, **45** (2002) 1918.

[8] A. G. E. Amr , A. M. Mohamed, S. F. Mohamed, N. A. Abdel-Hafez, A. El-Fotooh, G. Hammam, *Bioorg. and Med. Chem.*, **14** (2006) 5481.

[9] J. Zimmermann, Mohlin, G. Caravatti, U. S. Patent, 5516775 (1996).

[10] C. O. Kappe ,Tetrahedron, 49, 6937 (1993).

[11] G. C. Rovnyak, K. S. Atwal, A. Hedberg, S. D. Kimball, S. Moreland, J. Z. Gougoutas, B. C. O'Reilly, J. Schwartz, M. F. Malley, *J. Med. Chem.*, **35** (1992) 3254.

[12] E. L. Khania, G. O. Sillisnietse, Ya Ya Ozel, G. Dabur, A. A. Yakimenis, *Khim. Pharm. Zh.*, **78** (1978) 1321.

[13] H. Cho, M. Ueda, K. Shima, A. Mizuno, M. Hayashimatsu, Y. Ohnaka, Y. Takeuchi, M. Hamaguchi, K. Aisaka, *J. Med. Chem.*, **32** (1989) 2399.

[14] M. A. Bruce, G. S. Pointdexterand, G. Johnson, *PCT Int. WO,* 9833791(1998).

[15] B. B. Snider, Z. Shi, *J. Org. Chem.*, **58** (1993) 3828.

[16] A. D. Patil, N. V. Kumar, W. C. Kokke, M. F. Bean, A. J. Freyer, C. DeBrosse, S. Mai, A. Truneh, D. J. Faulkner, B. Carte, A. L. Breen, R. P. Hertzberg, R. K. Johnson, J. W. Westley, B. C. M . Potts, *J. Org. Chem.*, **60** (1995) 1182.

[17] Y. Kashman, S. Hirsh, O. J. McConnel, I. Ohtani, K. Takenori, K. Kakisawa, A. Ptimycolin, *J. Am. Chem. Soc.*, **111** (1989) 8925.

[18] K. S. Atwal, B. N. Swanson, S. E. Unger, D. M. Floyd, S. Moreland, A. Hedberg, B. C. O'Reilly, *J. Med. Chem.*, **34** (1991) 806.

[19] G. C. Rovnyak, K.S. Atwal, A. Hedberg, S. D. Kimball, S. Moreland, J. Z. Gougoutas, B. C. O'Reilly, J. Schwartz, M. F. Malley, *J. Med. Chem.*, **35** (1992) 3254.

[20] G. J. Grover, S. Dzwonczyk, D. M. McMullen, D. E. Normandin, C. S. Parham, P. G. Sleph, S. J. Moreland, *Cardiovasc. Pharmacol.*, **26** (1995) 289.

[21] H. Harda, H. Ishihara, Y. Sato, H. Chiba, Y. Komatsu, S. Inoue, N. Ozeki, *US Patent*, 5443311 (1995).

[22] C. O. Kappe, *Eur. J. Med. Chem.*, **35** (2000) 1043.

[23] D. Dallinger, A. Stadler, C. O. Keppe, *Pure Appl. Chem.*, **76** (2004) 1004.

[24] T. Kanbara, T. Kushida, N. Saito, I. Kuwajima, K. Kubota, T. Yamamoto, *Chem. Lett.*, **21** (1992) 583.

[25] R. Gommper, H. J. Mair, K. Polborn, *Synthesis* **1997** (1997) 696.

[26] K. Adrjanowicz, K. Kaminski, M. Paluch, P. Wlodarczyk, K. Grazybowska, Z. Wojnarowska, L. Hawelek, W. Sawicki, P. Lepek, R. Lunio, *J. Pharma. Sci.*, **99** (2010) 828.

[27] E. Fukokova, M. Makita, S. Yamamura, *Chem. Pharm. Bull.*, **35** (1987) 2943.

[28] D. Craig, P. Royall, V. Kett, M. Hopton, *Int. J. Pharm.*, **179** (1999) 179.

[29] P. Gupta, A. K. Bansal, *AAPS PharmSciTech*, **6** (2005) 32.

[30] M. Yoshioka, B. C. Hancock, G. Zografi, *J. Phrm. Sci.*, **83** (1994) 1700.

[31] L. Stubberud, R. T. Forbes, *Int. J. Pharm.*, **163** (1998) 145.

[32] H. Imaizumi, N. Nambu, T. Nagai, *Chem. Pharm. Bull.*, **28** (1980) 2565.

[33] R. W. Lee, J. McShane, J. M. Shaw, R. W. Wood, *Water insoluble drug formulation,* Ed. R. Liu, Inter Pharm Press, Buffalo Grove, USA (2000).

[34] J. Lee, *J. Pharm. Sci.*, **92** (2003) 2057.

[35] P. Biginelli, Gazz. Chim. Ital. **23** (1893) 360.

[36] A. C. Nair, P. Jayatilleke, X. Wang, S. Miertus, W. J. Welsh, *J. Med. Chem.*, **45** (2002) 973.

[37] Z. Machoń , J. Giełdanowski, Z. Wieczorek, G. Raberger, S. H. Kowalczyk-Bronisz, B. Błaszczyk, M. Zimecki, M. Mordarski, L. Fiszer-Maliszewska, J. Wieczorek, *Arch Immu. Ther Exp (Warsz).,* **31** (1983) 769.

[38] Z. Chen, J. Yan, H. Xing, Z. Zhang, F. Liang, *J. Solid State Chem.*, **184** (2011) 1063.

[39] S. R. Patel, Z. V. P. Murthy, *Cryst. Res. Technol.*, **46** (2011) 243.

[40] R. J. P. Eder, E. K. Schmitt, J. Grill, S. Radl, M. Grumber – Woelfler, J. G. Khinast, *Cryst. Res. Technol.,* **46** (2011) 227.

[41] D. Iohara, K, Yoshida, K. Yamaguchi, M. Anraku, K. Motoyama, H. Arima, K. Uekama, F. Hirayama, *J. Cryst. Growth. Des.,* **12** (2012) 1985.

[42] G. W. Brun, A. Mutin, E. Cassel, R. M. F. Vargas, M. Jose Cocero, *J. Cryst. Growth. Des.,* **12** (2012) 1943.

[43] E. Gunn, I. A. Guzei, T. Coi, L. Yu, *J. Cryst. Growth. Des.,* **12** (2012) 2037.

[44] S. Careno, O. Boutin, E. Badens, *J. Cryst. Growth.,* **342** (2012) 34.

[45] C. T. O'Clardha, J. F. Frawley, N. A. Mitchell, *J. Cryst. Growth.,* **328** (2011) 50.

[46] M. Zhi, Y. Wang, J. Wang, *J. Cryst. Growth.,* **314** (2011) 213.

[47] H. G. Brittain, *J. Cryst. Growth. Des.,* **12** (2012) 1046.

[48] J. Lu, Y. P. Li, J. Wang, Z. Li, S. Rohani, C. B. Ching, *J. Cryst. Growth.,* **335** (2011) 110.

[49] A. O. L. Evora, R. A. E. Castro, T. M. R. Maria, M. T. S. Rosado, M. R. Silva, A. M. Beja, J. Canotilho, M. E. S. Eusebio, *J. Cryst. Growth. Des.*, **11** (2011) 4780.

[50] H. R. Manjunath, P. C. Rajesh Kumar, S. Naveen, V. Ravindrachary, M. A. Sridhar, T. S. Prasad, P. Karegoudar, *J. Cryst. Growth.,* **327** (2011) 161.

[51] H. Zhang, Y. Sun, X. Chen, X. Yan, B. Sun, *J. Cryst. Growth.,* **324** (2011) 196.

[52] M. Upreti, J. P. Smit, E. J. Hagen, V. N. Smolenskaya, I. Prakash, *J. Cryst. Growth. Des.*, **12** (2012) 990.

[53] S. Ramakutty, E. Ramachandran, *Cryst. Res. Technol.,* **47** (2012) 31.

[54] http://www.mrl.ucsb.edu/mrl/centralfacilities/xray/xray-basics/#x2

[55]http://www.mf.mpg.de/de/abteilungen/mittemeijer/english/commentary/Powder%20 Diffraction%20in%20Mat.Sci.pdf

[56] I. Ivanisevic, R. B. McClurg, P. J. Schields, *Pharmaceutical Sciences Encyclopedia: Drug Discovery, Development, and Manufacturing*, Ed. S. C. Gad, John Willey & Sons, (2010).

[57] G. V. Gurskaya, V. E. Zavodnik, A. D. Shutalev, *Crystallography Reports*, **48** (2003) 92.

[58] T. H. Quiroz, S. H. Ortega, M. S. García, *Anal. Chem.*, **15** (1999) 105.

[59] G. Socrates; '*Infrared Characteristics Group Frequencies'*, John Wiley, Chichester, UK(1980).

[60] R. R. Griffiths; '*Chemical Infrared Fourier Transform Spectroscopy'*, Academic Press, New York, USA (1972).

[61] K. Nakamoto; '*Infrared and Raman Spectra of Inorganic and Coordination Compounds'*, John Wiley 5th Ed., New Jersey, USA (1997).

[62] D. A. Anderson, E. S. Freeman, *J. Polymer Sci*., **54** (1961) 253.

[63] H. C. Anderson, *S. P. E. Trans*., **1** (1962) 202.

[64] H. D. Anderson, *Nature*, **191** (1961) 1088.

[65] C. D. Doyle, *Anal. Chem*., **33** (1961) 77.

[66] R. D. Braun, *Pharm Med Press*, 2010.

[67] M. N. Marino, J. M. Salas, *J. of Therm. Anal.,* **29** (1984) 1053.

[68] A. W. Coats, J. P. Redfern, *Nature*, **201** (1964) 68.

[69] H. H. Horowitz, G. Metzger, *Anal. Chem.*, **35** (1963) 1464.

[70] E. S. Freeman, B. Carroll, *J. Phys. Chem.*, **62** (1958) 394.

[71] K. J. Laidler, *"Chemical Kinetics",* 3rd Ed., Harper and Row, New York, USA (1987).

[72] J. Aliè, J. Menegotto, P. Cardon, H. Duplaa, A. Caron, C. Lacabanne, M. Bauer, *J. Pharma. Sci,* **93** (2004) 218.

[73] J. Menegotto, J. Aliè, C. Lacabanne, M. Bauer, *Dielectric News,* **19** July 2004.

[74] D. R. Mantheni, M. P. K. Maheshwaram, H. F. Sobhi, N. I. Perera, A. T. Riga, M. E. Mattews , K. Alexander, *J. Ther. Anal. Cal.,* DOI 10.1007/s10973 – 011 – 1423 – y7

[75] M. V. Castillo, M. A. Checa, M. E. Manzur, F. H. Feretti, E. F. Vargas, F. Martinez, A. Yurquina, *Vitae Revisista de la fac. de Qim – Farma,* **17** (2010) 299.

[76] D. Enakshi, K. V. Rao, *J. Mater. Sci. Lett.*, **4** (1985) 1298.

[77] B. B. Parekh, D. H. Purohit, P. Sagayaraj, H. S. Joshi, M. J. Joshi, *Cryst. Res. Technol.*, **42** (2007) 407.

[78] R. M. Dabhi, B. B. Parekh, M. J. Joshi, *Ind. J. Phys.*, **79** (2005) 503.

[79] K. P. Tank, P. Sharma, D. K. Kanchan, M. J. Joshi, *Cryst. Res. Technol.,* **46** (2011) 1309.

[80] S. J. Yaghmour, *Eur. Phys. J. Appl. Phys.*, **49** (2010) 10402.

[81] B. K. Pal, S. P. Moulik, *Current Science*, **80** (2001) 990.

[82] P. M. Vyas, S. R. Vasant, R. R. Hajiyani, M. J. Joshi, *AIP Conf. Proceed.*, **1276** (2010) 198.

[83] C. Destrée, J. Ghijsen, J. B. Nagy, *Langmuir,* **23** (2007) 1965.

[84] L. Jeunieau, F. Debuigne, J. B. Nagy, *Surf. Sci. Ser.,* **100**, (2001) 609.

[85] F. Debuigne, L. Jeunieau, M. Wiame, J. B. Nagy, *Langmuir,* **16** (2000) 7605.

[86] Y. Bayrak, M. Iscan, *J. Surf. Deter.,* **7** (2004) 363.

[87] S. P. Moulik, B. K. Paul, Adv. *Colloid. Inter. Sci.*, **78** (1998) 99.

[88] http://en.wikipedia.org/wiki/Microemulsion

[89] A. Jesus, A. V. Zmozinski, J. A. Barbar, M. G. R. Vale, M. M. Silva, *Energy Fuels,* **24** (2010) 2109.

[90] R. S. Boikess, E. Edelson, *Chemical Principles,* Harper and Row, New York, USA (1978).

[91] A. S. Kazanskaya, V. A. Skoblo, *Calculations of Chemical Equilibria,* Mir Publication, Moscow, Russia (1978).

Chapter – IV

Synthesis and Characterization 1-phenyl-3-(propan-2-yl)-1H-pyrazol-5-ol Crystals and Nano – Particles

4.1 Introduction

Pyrazole refers to the class of simple aromatic ring organic compounds of the heterocyclic series characterized by a 5-membered ring structure composed of three carbon atoms and two nitrogen atoms in adjacent positions. Being so composed and having pharmacological effects on humans, they are classified as alkaloids, although they are rare in nature. In 1959, the first natural pyrazole, 1- pyrazolyl-alanine, was isolated from seeds of watermelons [1]. The typical pyrazole structures are shown in figure 4.1 (a) and (b).

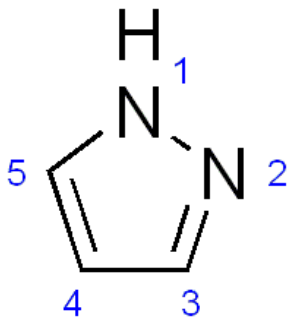

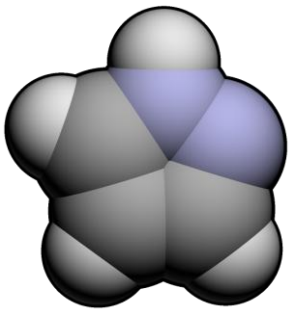

Figure 4.1 (a) Pyrazole structure **Figure 4.1** (b) 3D – diagram of Pyrazole

The biological properties of pyrazoles are reviewed extensively [2]. Several pyrazoles and its substituted derivatives are potential inhibitors and deactivators of liver alcohol dehydrogenase [3]. Difenamizole possess analgesic activity greater than that of Aspirin [4]. In addition, a variety of pyrazole derivatives have been synthesized as a new class of Cox – 1/ Cox –

2 inhibitors. Although Cox – 2 inhibitors have anti – inflammatory properties, their greatest effect appear to be associated with pain relief and symptoms of osteoarthritis. Therefore, it may be postulated that the moderately selective Cox – 2 inhibitors are a safer alternative to the patients with cardiovascular disease. This is being used at present as an effective anti – inflammatory drug [5]. Pyrazole derivatives also posses antibacterial [6], p-38α MAP kinase inhibitory [7], monoamine oxidase inhibitory [8], insecticidal [9, 10], anti cancer [11, 12], anti – HIV [13, 14], herbicidal [15, 16] etc. activities. This gave a great impact to search for potential pharmacologically active drugs carrying pyrazole substituent. Pyrazolyl pyrazolone derivatives were found to possess potent activities such as anti-inflammatory [17, 18], antimicrobial [19, 20], antiallergic [21, 22], antidiabetic [23, 24], cardio – vascular [25, 26], diuretic [2,27,28], antioxidant agent [29] and brain connabinoid receptor (CB1) [30].

Looking at various pharmaceutical applications of various pyrazole compounds, the present author reports hereby the growth of 1-phenyl-3-(propan-2-yl)-1H-pyrazol-5-ol single crystals and their characterizations by various techniques. Moreover, the synthesis and characterization of nano particles of the same compound is also reported.

4.2 Synthesis of 1-phenyl-3-(propan-2-yl)-1H-pyrazol-5-ol single crystals

4.2.1 Synthesis of 1-phenyl-3-(propan-2-yl)-1H-pyrazol-5-ol

1-phenyl-3-(propan-2-yl)-1H-pyrazol-5-ol has been synthesized by using a mixture of methyl-isobutyl acetate (0.01 mole) and phenyl hydrazine (0.01 mole) in methanol (10 ml). In this mixture two drops of acetic acid were added and the solution was reflux for 5 h. After completion of the reaction, the

solvent was removed under vacuum and the resulting solid was air dried in to a powder form, which was used for the further growth of single crystals. All AR grade chemicals were used for the synthesis. Synthesis of 1-phenyl-3-(propan-2-yl)-1H-pyrazol-5-ol was carried out by collaborators in Chemistry Department of Saurashtra University. The fragmentations in mass spectrum suggested the formation of the compound, which is not included in this thesis. Figure 4.2 shows the expected molecular structure of 1-phenyl-3-(propan-2-yl)-1H-pyrazol-5-ol.

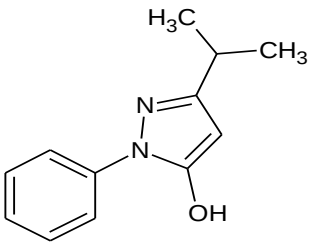

Figure 4.2 Molecular structure of 1-phenyl-3-(propan-2-yl)-1*H*-pyrazol-5-ol

4.2.2 Crystal Growth of 1-phenyl-3-(propan-2-yl)-1H-pyrazol-5-ol

For the growth of single crystals, the synthesized material was dissolved in the mixture of chloroform and methanol, with the ratio of chloroform: methanol was selected as 8:2. This mixture was selected as a solvent after trying different organic solvents. The growth of 1-phenyl-3-(propan-2-yl)-1*H*-pyrazol-5-ol crystals was carried out by using slow solvent evaporation technique. Glass container of 50 ml was selected as a crystallization apparatus containing saturated solution of 1-phenyl-3-(propan-2-yl)-1*H*-pyrazol-5-ol, this was covered by lid to allow slow and controlled evaporation of solvent. This was placed in a constant temperature water bath of accuracy ± 0.01^0 C. After 20 days yellowish, transparent, crystals were

grown having maximum dimensions of 5 mm x 4 mm, which are shown in figure 4.3.

Figure 4.3 Grown single crystals of 1-phenyl-3-(propan-2-yl)-1*H*-pyrazol-5-ol

4.3 Tautomerism

Tautomers are isomers of organic compounds that readily interconvert by a chemical reaction called tautomerization [31,32]. This reaction commonly results in the formal migration of a hydrogen atom or proton, accompanied by a switch of a single bond and adjacent double bond. The concept of tautomerizations is called *tautomerism*. Because of the rapid interconversion, tautomers are generally considered to be the same chemical compound. Tautomerism is a special case of structural isomerism and can play an important role in non-canonical base pairing in DNA and especially RNA molecules. In annular tautomerism, there are four situations possible for solid state: (i) the most common is that where only one tautomer is present in the crystal and only one kind of crystal can be obtained, (ii) both tautomers are present in the crystal, (iii) two or eventually more polymorphs of the same tautomers can be isolated and (iv) both tautomers crystallize in the different crystal types (desmotropy) [33]. The tautomerism in 1-phenyl-3-(propan-2-yl)-1*H*-pyrazol-5-ol crystal is observed and reported in the subsequent section.

4.4 Single crystal X – Ray Diffraction of 1-phenyl-3-(propan-2-yl)-1*H*-pyrazol-5-ol crystal

A light yellow rectangular plate-shaped single crystal of the 1-phenyl-3-(propan-2-yl)-1*H*-pyrazol-5-ol measuring 0.30x0.20x0.10 mm was picked up for X-ray intensity data collection on a CCD area-detector diffractometer (*X'calibur system)* which is equipped with graphite monochromated MoK_{α} radiation (λ=0.71073Å). A total number of 23149 reflections were collected of which 4611 reflections were treated as observed (I > 2σ(I)). Data were corrected for Lorentz-polarization and absorption factors. The crystal structure was solved by direct methods using SHELX 97 and refined by full-matrix least-squares methods using SHELX 97 [34]. The final refinement cycle yielded an R-factor of 0.0405 [wR (F^2) =0.1044] for the observed data. The residual electron density ranges from -0.188 to 0.194e $Å^{-3}$. The crystallographic data are summarized in Table 4.1.

It is found that this compound undergoes tautomerism by proton transfer between the hydroxyl O atom and the N2 atom forming two tautomers, keto form (molecule I) and enol form (molecule II) as shown in figure 4.4, and the two different tautomeric forms of the same molecule cocrystallized in a 1:2 ratio.

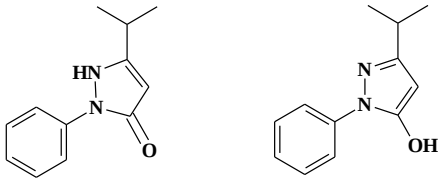

Molecule I Molecule II

Figure 4.4 Chemical structure of 1-phenyl-3-(propan-2-yl)-1,2-dihydro-pyrazol-5-one (molecule-I) and 1-phenyl-3-(propan-2-yl)-1H-pyrazol-5-ol (molecule-II)

An ORTEP view of all the three molecules [35] [molecule – I (keto form); molecule – IIA and molecule – IIB (enol form with two independent molecules in the asymmetric unit)] is shown in figure 4.5. Selected bond lengths, bond angles and torsion angles are given in Table 4.2. When compound – I undergoes tautomerization during crystallization to afford corresponding enol via proton transfer reaction, an appreciable decrease in the N2-C3 and C4-C5 distance is observed [N2-C3=1.346(2) Å *versus* N2A-C3A=1.326(2) Å; N2B-C3B=1.327(2) Å and C4-C5=1.411(2) Å *versus* C4A-C5A= 1.368(2) Å; C4B-C5B=1.368(2) Å]. A concomitant increase in the C3-C4 and C5-O5 distance has also been observed [C3-C4=1.366(2) Å *versus* C3A-C4A=1.397(2) Å; C3B-C4B=1.399(2) Å and C5-O5=1.261(2) Å *versus* C5A-O5A= 1.326(2) Å; C5B-O5B=1.325(2) Å]. Hence the above mentioned C-C, C-N, and C-O bond lengths (Table 4.2) help establish the keto form of molecule I and the enol form of molecule – IIA and molecule – IIB, respectively. In addition, the magnitude of planarity for the molecules in keto and enol forms is different. The pyrazole and the phenyl rings are inclined at an angle of 28.04(5)^{o} in molecule – I, 47.38(5)^{o} in molecule – IIA and 49.32(6)^{o} in molecule – IIB.

The six C-C bond lengths in the phenyl ring lie in the range: 1.378(2)Å – 1.386(2)Å, molecule – I; 1.370(3)Å – 1.387(2)Å, molecule – IIA; 1.371(3)Å – 1.383(3)Å, molecule – IIB. The pyrazole ring and the phenyl ring are individually planar with maximum deviations from the respective least squares planes of: -0.023(1)Å for C5 and -0.008(2)Å for C14 (molecule – I); -0.004(2)Å for C3A and -0.008(2)Å for C14A (molecule – IIA); 0.006(1)Å for C3B and 0.011(2) Å for C14B (molecule – IIB).

Table 4.1 Crystal and experimental data

Chemical formula: $C_{12}H_{14}N_2O$ .2 $C_{12}H_{14}N_2O$

Formula weight = 606.76

T = 293 K

Crystal system: triclinic Space group: P-1

a = 11.1593(3) Å *α* = 73.333(3)°

b = 11.2247(3) Å *β* = 88.286(2)°

c = 14.1140(4) Å *γ* = 82.767(2)°

V = 1680.13(8)Å^3 *Z* = 2

D_x = 1.199g/cm^3 D_m (floatation) = not measured

Radiation: Mo *K*ɑ̨ (λ = 0.71073 Å)

μ (Mo *K*a) = 0.078 mm–1 *F*(000) = 648

Crystal size = 0.3 X 0.2 X 0.1 mm^3

No. of reflections collected = 23149

No. of independent reflections = 5862

θ range for data collection: 3.44 to 24.99 °

Data/Restraints/Parameters = 5862/0/542

Goodness-of-fit on F^2 = 1.016

R indices [$I > 2\sigma(I)$]: *R*1 = 0.0405, *wR*2 = 0.0966

R indices (all data): *R*1 = 0.0556, *wR*2 = 0.1044

$(\Delta/\sigma)_{max}$ = 0.001 for y H83

$(\Delta\rho)_{max}$ = 0.194 eÅ^{-3} $(\Delta\rho)_{min}$ = -0.188 eÅ^{-3}

Measurement: *X'calibur system – Oxford diffraction make,*

Programs system: SHELX 97, CRYSALIS RED

Structure determination: SHELX 97

CCDC deposition number: 824525

Both intra- and intermolecular hydrogen bonds are found in the crystal structures of the tautomers. The two tautomers are connected via intermolecular N-H…N, O-H…O, O-H…N and C-H….O hydrogen bonds.

Table 4.2 Selected bond lengths (Å), bond angles (^{o}) and torsion angles (^{o}) for non hydrogen atoms (e. s. d. 's are given in parentheses)

	Molecule I	**Molecule IIA**	**Molecule IIB**
N1-N2	1.382(1)	1.377(1)	1.384(1)
N2- C3	1.346(2)	1.326(2)	1.327(2)
C3-C4	1.366(2)	1.397(2)	1.399(2)
C4-C5	1.411(2)	1.368(2)	1.368(2)
N1- C5	1.387(2)	1.358(2)	1.352(2)
C5 -O5	1.261(2)	1.326(2)	1.325(2)
C3- N2- N1	108.4(1)	105.6(1)	104.7(1)
C5 -N1 -N2	108.6(1)	110.3(1)	110.8(1)
C5 -N1 -C9	130.0(1)	129.3(1)	127.0(1)
N2 -N1 -C9	119.6(1)	120.3(1)	121.1(1)
O5 -C5 -N1	122.4(1)	119.1(1)	118.8(1)
N1 -C5 -C4	105.5(1)	107.3(1)	107.4(1)
N2 -C3 -C4	108.9(1)	110.9(1)	111.5(1)
N2 -C3 -C6	119.1(1)	120.2(1)	121.2(1)
C5 -N1 - C9 -C10	-38.0(2)	49.2(2)	54.7(2)
N2 - N1 - C9 - C10	159.0(1)	-133.7(1)	-138.1(1)
N2 - N1 - C9 - C14	-19.8(2)	45.8(2)	42.8(2)
C4 - C3 - C6 - C7	-82.4(2)	75.0(2)	69.2(2)
N2 - C3 - C6 - C8	-142.3(2)	128.9(2)	125.4(2)

Despite the rich availability of aryl rings, there are no aromatic $\pi - \pi$ stacking interactions in the structure. However, C-H…π hydrogen bonds are present. Details of N-H…N, O-H…O, O-H…N, C-H….O and C-H…π hydrogen bonds are given in Table 4.3.

Table 4.3 Geometry of N-H...N, O-H…O, O-H...N, C-H…O, C-H…π hydrogen bonds. Cg1, Cg2, Cg3 represent the center of gravity of the pyrazole ring (molecule – IIA), pyrazole ring (molecule – IIB) and phenyl ring (molecules – IIB) respectively

D – H ....A	D – H (Å)	H...A (Å)	D...A(Å)	θ [D – H...A(Å)]
C10-H10...O5	0.98(2)	2.48(2)	3.003(2)	113(1)
O5B-H5B ... N2A	0.82	1.799(1)	2.617(2)	175.1(1)
O5A-H5A…O5	0.82	1.764(1)	2.544(2)	158.2(1)
N2-H2...N2B^{i}	0.88(2)	1.96(2)	2.836(2)	169(2)
C11A-H11A ...O5A^{ii}	0.95(2)	2.60(2)	3.539(2)	169(2)
C11-H11 ...O5^{iii}	0.99(2)	2.54(2)	3.471(2)	156(1)
C14-H14…Cg3^{iv}	0.93(2)	2.95(2)	3.720(2)	141(1)
C12-H12…Cg1^{v}	0.96(2)	2.79(2)	3.611(2)	145(1)
C8A-H81A…Cg2^{vi}	0.96	2.917	3.765(3)	148

Symmetry codes : (i) x+1, y+1, z (ii) 1-x, 1-y, 1-z (iii) 1-x, 2-y, -z (iv) -x, -y, 1-z (v) 1-x, -y, 1-z (vi) -x, 1-y, 1-z

This analysis was carried out by collaborators at Physics Department of University of Jammu and the detailed results were published elsewhere [36].

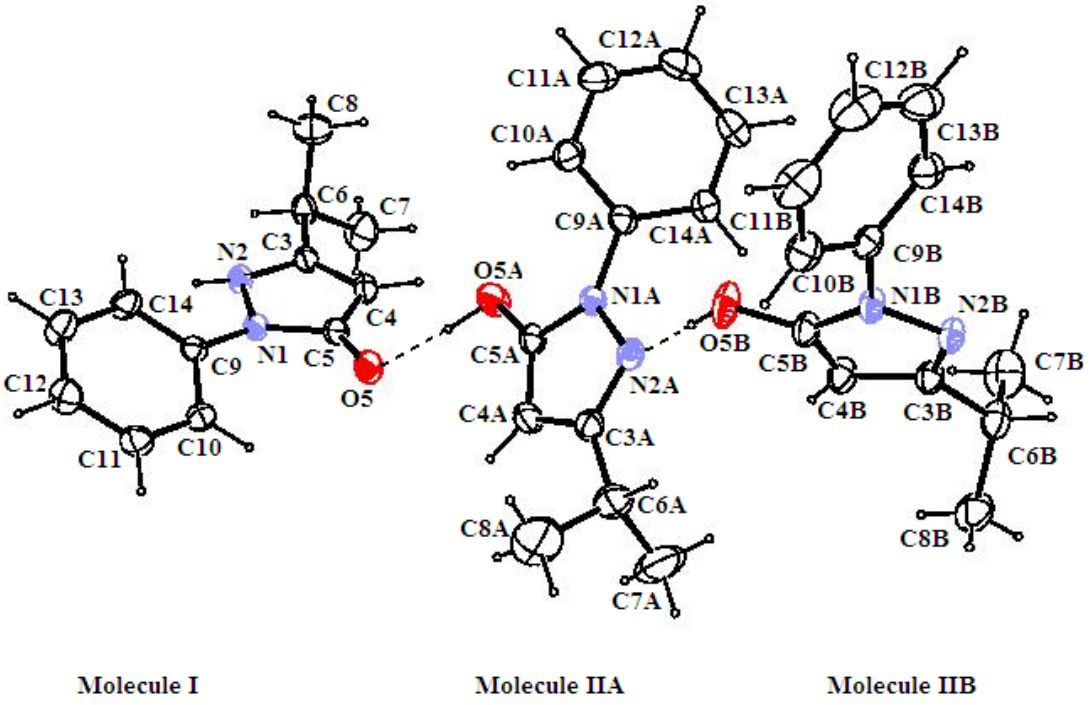

Figure 4.5 *ORTEP* view of the molecules, showing the atom-labeling scheme. Displacement ellipsoids are drawn at the 40% probability level and H atoms are shown as small spheres of arbitrary radii

4.5 Powder XRD of 1-phenyl-3-(propan-2-yl)-1*H*-pyrazol-5-ol crystals

The crystalline nature and the unit cell parameters of 1-phenyl-3-(propan-2-yl)-1*H*-pyrazol-5-ol crystals were studied by powder XRD in continuation of single crystal XRD studies [36]. Figure 4.6 exhibits the powder XRD pattern of 1-phenyl-3-(propan-2-yl)-1*H*-pyrazol-5-ol crystals. All major reflections in the XRD pattern were fitted and assigned the corresponding plane. The 1-phenyl-3-(propan-2-yl)-1*H*-pyrazol-5-ol crystals exhibited triclinic system with the estimated unit cell parameters as, a = 11.1593 Å, b = 11.2247 Å, c = 14.1140 Å, α = 73.333°, β = 88.286°, γ = 82.767°, which corresponds to the value reported in single crystal XRD.

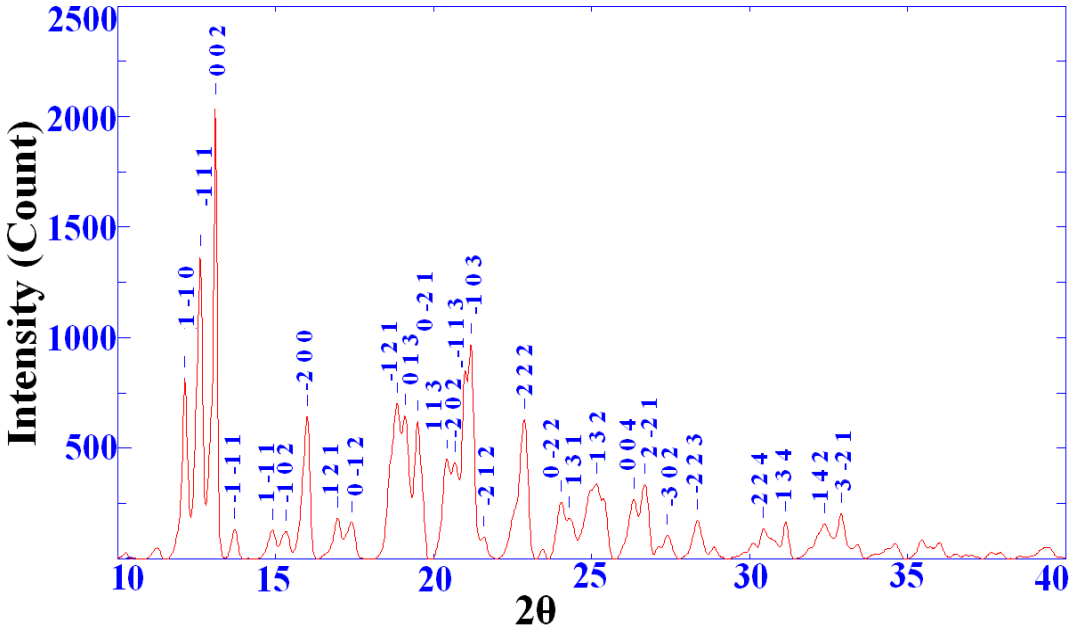

Figure 4.6 Powder XRD pattern of 1-phenyl-3-(propan-2-yl)-1*H*-pyrazol-5-ol crystal

4.6 FT – IR spectral study of 1-phenyl-3-(propan-2-yl)-1*H*-pyrazol-5-ol crystals

Most of the organic compounds show absorptions in the mid – infrared region extending from 400 cm^{-1} to 4000 cm^{-1}. Details of the FT-IR technique are previously discussed in section 2.4 of chapter II. Figure 4.7 shows the FT – IR spectrum of 1-phenyl-3-(propan-2-yl)-1*H*-pyrazol-5-ol crystals. The analysis of spectrum suggests that the absorptions occurring at 3130.3 cm^{-1} show C – H stretching. The absorption occurring at 2965.2 cm^{-1} is due to the C – H asymmetric stretching vibration of – CH_3. The absorptions taking place at 2877.1 cm^{-1} C – H symmetric stretching vibration of – CH_3. The absorption taking place at 1801.6 cm^{-1} is due to C = O stretching vibration of ester due to pyrazole. Whereas, the absorption taking place at 1534.0 cm^{-1} is due to C = C stretching due to aromatic ring skeleton.

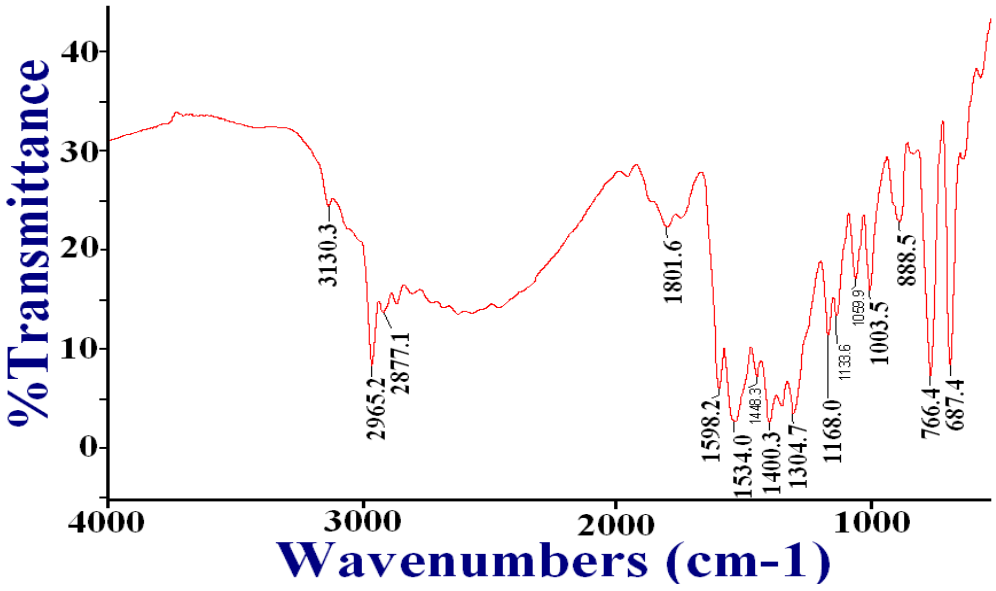

Figure 4.7 FT – IR spctrum of 1-phenyl-3-(propan-2-yl)-1*H*-pyrazol-5-ol crystal

The absorption at 1448.3 cm^{-1} is assigned to C – H in plane asymmetric bending. The absorption taking place at 1400.3 cm^{-1} is due to C – H out of plane symmetric bending. The absorption observed at 1133.6 cm^{-1} is due to = N – N – and the absorption observed at 1003.5 cm^{-1} is due to C – H in plane bending. The absorptions observed at 888.5 cm^{-1}, 766.4 cm^{-1} and 687.4 cm^{-1} are attributed to either out of plane bending vibrations or aromatic substitution.

4.7 Thermal Study of 1-phenyl-3-(propan-2-yl)-1*H*-pyrazol-5-ol crystals

The thermal studies, such as TGA, DTA and DSC, of powdered samples of 1-phenyl-3-(propan-2-yl)-1*H*-pyrazol-5-ol were carried out using Linseis Simultaneous Thermal Analyzer (STA) PT-1600, in the atmosphere of air from 25 °C to 900 °C at a heating rate of 15 °C/min using α-Al_2O_3 as standard reference. Details of the techniques used for the thermal study are elaborately discussed in section 2.7 of chapter II.

Thermal study of different pyrazole compounds have been reported by Paz *et al*. [33]. The thermal decomposition behavior of 1-phenyl-3-(propan-2-yl)-1*H*-pyrazol-5-ol was similar to the reported other pyrazole based compounds. Figure 4.8 shows the thermo-gram of 1-phenyl-3-(propan-2-yl)-1*H*-pyrazol-5-ol crystalline powder. The TG plot shows that the sample remains stable up to 160 ^{o}C and then it starts decomposing rapidly up to 280 ^{o}C and beyond that it decomposes slowly up to 610 ^{o}C, where complete decomposition is observed. The DTA plot indicates that the decomposition process of 1-phenyl-3-(propan-2-yl)-1*H*-pyrazol-5-ol occurs through an endothermic reaction at 105.2 ^{o}C and two exothermic peaks observed at 278.2 ^{o}C and 558.1 ^{o}C, respectively. From the DSC plot several thermodynamic parameters were calculated by using the software TA evaluation available with the set up. For the first endothermic reaction at 105.2 ^{o}C the enthalpy and the change in heat capacity are calculated and found to be -119964.9 J/kg and 866.9 J/kgK, respectively. This may be due to some phase change occurring without significant breaking of the bonds resulting into marginal weight loss, which may be due to melting of a sample. The melting point of 1-phenyl-3-(propan-2-yl)-1*H*-pyrazol-5-ol is 90 ^{o}C. After the endothermic reaction, minor exothermic reaction is observed at 278.2 ^{o}C and values of the enthalpy and the change in heat capacity are found to be 77457.6 J/kg and 1362.4 J/kgK, respectively. Similarly, the second exothermic reaction occurring at 558.1 ^{o}C may be due to complete decomposition of the sample into the gaseous phase and reaction within the products. For this reaction, values of the enthalpy and the change in heat capacity are found to be 2636717 J/kg, 10891.7 J/kgK, respectively.

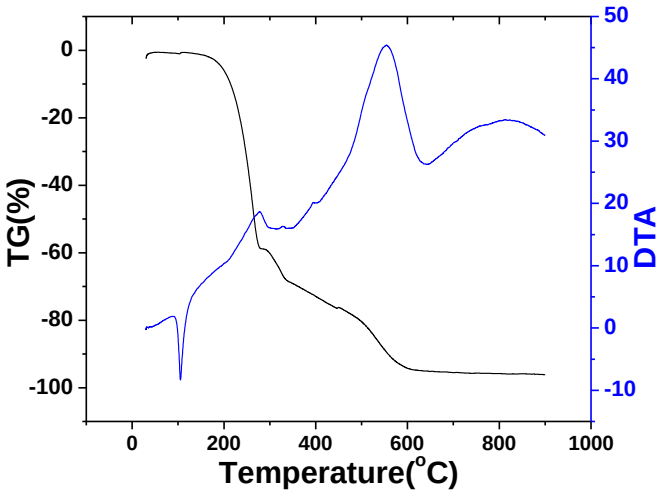

Figure 4.8 TG – DTA of 1-phenyl-3-(propan-2-yl)-1*H*-pyrazol-5-ol crystal

4.8 Kinetic Parameters of 1-phenyl-3-(propan-2-yl)-1*H*-pyrazol-5-ol Decomposition

The kinetic parameters of 1-phenyl-3-(propan-2-yl)-1*H*-pyrazol-5-ol were evaluated at 200°C from the TG curve by applying Coats and Redfern relation [37] as discussed in chapter III. Figure 4.9 illustrate the Coats and Redfern plot.

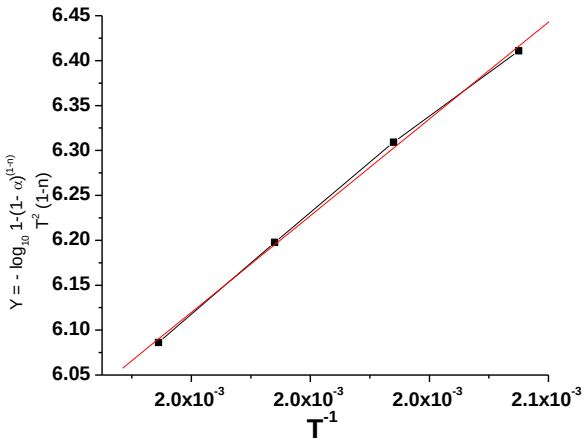

Figure 4.9 Coats and Redfern plot with linear fit

Table 4.4 Kinetic parameters of 1-phenyl-3-(propan-2-yl)-1*H*-pyrazol-5-ol crystal

Sample	Kinetic Parameters
1-phenyl-3-(propan-2-yl)-1*H*-pyrazol-5-ol crystals	Order of reaction (n) = 0
	Activation Energy (E) = 51.54 $kJK^{-1}Mol^{-1}$
	Frequency factor (A) = 9.36×10^{18}

4.9 Thermodynamic Parameters of 1-phenyl-3-(propan-2-yl)-1*H*-pyrazol-5-ol Decomposition

Various thermodynamic parameters such as standard entropy of activation, $\Delta^{\#}S°$, standard enthalpy of activation, $\Delta^{\#}H°$, standard Gibbs energy of activation, $\Delta^{\#}G°$ and standard internal energy of activation, $\Delta^{\#}U°$ were calculated by applying well known formulae, as described in detail by Laidler [38] and already mentioned in chapter III. Table 4.5 gives the values of thermodynamic parameters of decomposition at 200 ^{o}C.

Table 4.5 Thermodynamic parameters of 1-phenyl-3-(propan-2-yl)-1*H*-pyrazol-5-ol crystal

Sample	Thermodynamic Parameters
1-phenyl-3-(propan-2-yl)-1*H*-pyrazol-5-ol crystals	Standard Entropy $\Delta^{\#} S° = 114.10\ Jkmol^{-1}$
	Standard Enthalpy $\Delta^{\#} H° = 43.34\ kJmol^{-1}$
	Standard Gibbs free energy $\Delta^{\#} G° = -12.90\ kJmol^{-1}$
	Standard change in internal energy $\Delta^{\#} U° = 47.44 kJmol^{-1}$

For spontaneous process, $\Delta^{\#} S°$ is positive and $\Delta^{\#} G°$ is negative. The positive values of $\Delta^{\#} S°$ and $\Delta^{\#} H°$ indicates spontaneous reaction at high

temperature [39]. Table 4.5 indicates further that the nature of reaction is spontaneous at high temperature.

4.10 Dielectric Study

Every material has a unique set of electrical characteristics which are dependent on its dielectric properties. The dielectric constant of a material is associated with the energy storage capability in the electric field in the material and the loss factor is associated with the energy dissipation, conversion of electric energy to heat energy in the material. The experimental technique used for the dielectric study is already described in section 2.8 of the chapter II. The dielectric constants, dielectric loss, a.c. conductivity *(σ_{ac})* and a.c. resistivity *(ρ_{ac})* were evaluated with the frequency of applied field at room temperature using well known formulae as depicted in chapter II.

Dielectric study of Active Pharmaceutical Ingredients (API), amino acids and carbohydrates has been reported [40]. The dielectric study of amorphous pharmaceutical drugs has been reported in correlation with molecular mobility and isothermal crystallization kinetics [41]. A broadband dielectric spectroscopic study of Verapamil Hydrochloride (VH), a calcium channel blocker was carried out to understand its molecular dynamics by Adrjanowicz *et al.* [42]. Figure 4.10 shows the variation of dielectric constant κ with frequency of applied field. The dielectric constant decreases rapidly as frequency increases. The nature of the plot in the figure 4.10 suggests that the space-charge polarization is active in low frequency region, which is reflected in terms of rapid decrease in the value of dielectric constant with increase in frequency. This also further suggests that the dipoles can not

comply with the varying field and hence the decreasing nature is exhibited. The same type of nature is observed for the variation of dielectric loss (*tan δ*) with the frequency of applied field as shown in the figure 4.11.

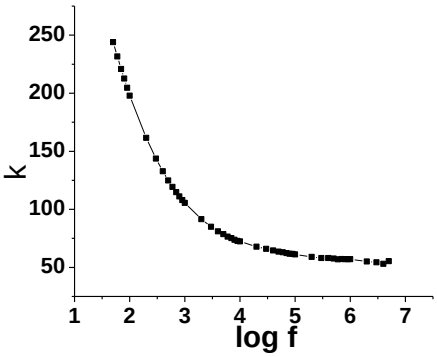

Figure 4.10 Plot of *κ* versus log f

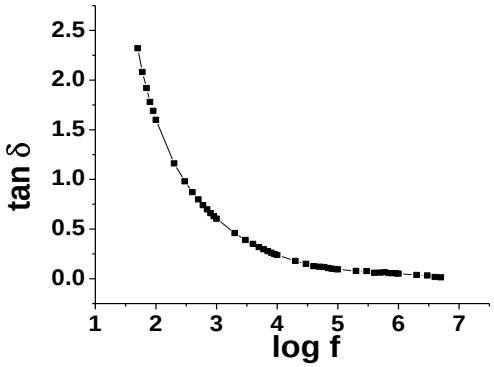

Figure 4.11 Plot of *tan δ* versus *log f*

Usually, typical current carriers in organic solids are through *π*-conjugated systems and the electrons can move via *π*-electron cloud, especially, by hopping, tunneling and other related mechanisms. Figure 4.12 shows that the a. c. conductivity σ_{ac} increases as the frequency increases and the opposite nature is observed for a. c. resistivity.

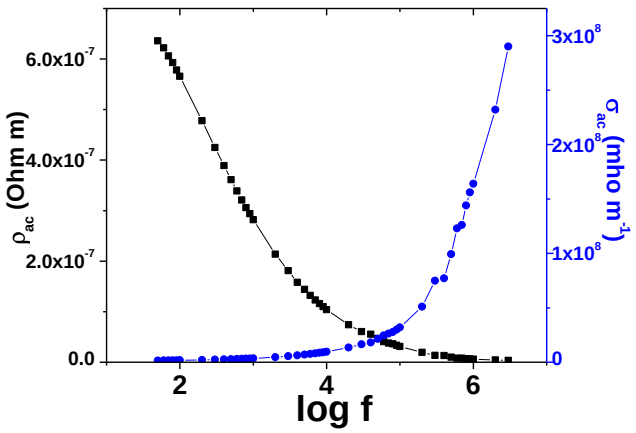

Figure 4.12 plots of a.c. conductivity and a.c. resistivity versus log f

Electrical conductivity of solid electrolytes as a function of frequency can generally be described as frequency independent, dc conductivity σ_{dc}, and a strongly frequency dependent, ac conductivity σ_{ac}, components. A typical frequency dependence of conductivity spectrum is shown in the figure 4.13, which exhibits three distinguished regions: (a) low frequency dispersion, (b) an intermediate frequency plateau and (c) an extended dispersion at high frequency [43-47]. The variation of conductivity in the low frequency region is attributed to the polarization effects at the electrode and electrolyte interface.

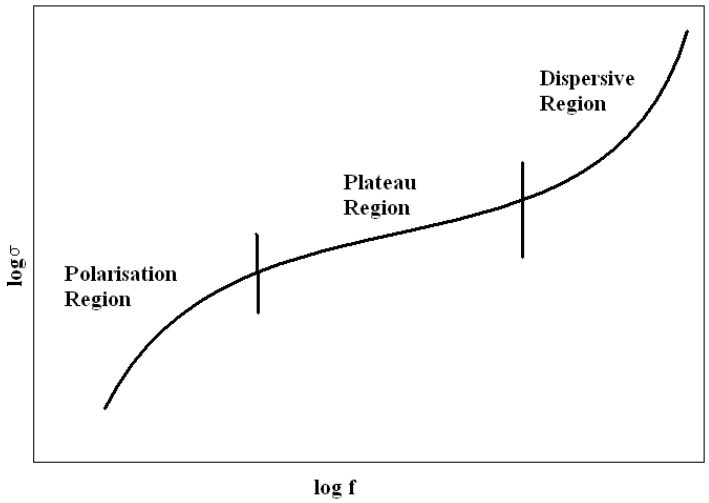

Figure 4.13 schematic representation of log conductivity versus frequency

As the frequency reduces, more and more, charge accumulation occurs at the electrode and electrolyte interface and hence, drop in conductivity. In the intermediate frequency plateau region, conductivity is almost found to be frequency independent and is equal to dc conductivity σ_{dc}. In the high frequency region, the conductivity increases with the frequency. The frequency dependant of conductivity or so – called universal dynamic response of ionic conductivity is related by a simple expression given by Jonscher's power law [45]

$\sigma_\omega = \sigma_0 + A\ \omega'$ .... (4.1)

where, σ_ω is the ac conductivity, σ_0 is the limiting zero frequency conductivity or σ_{dc}, A is a pre – exponential constant, $\omega = 2\pi f$ is the angular frequency.

When the conductivity is measured with an AC technique of frequency $\omega = 2\pi v$, the response that characterizes a great variety of materials with diverse chemical compositions, either the crystalline or amorphous, can be written as follows by slightly modifying (4.1),

$\sigma(\omega,T) = \sigma_{dc}(T) + a(T)\omega^n$ …. (4.2)

Where, σ_{dc} (T) is the 'direct current' (or static, ω=0) conductivity, a(T) is a factor that depends on temperature but not on ω ,and n is an exponent in the range $0.6 \leq n \leq 1$ [48].

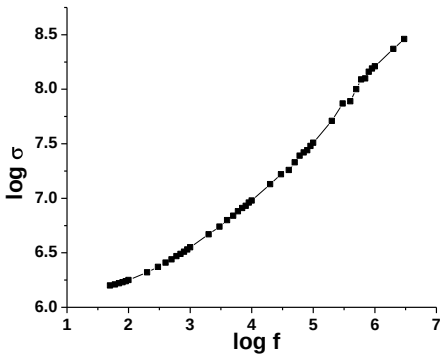

Figure 4.14 Plot of log of a.c. conductivity versus log f

Figure 4.14 shows plot of $log\sigma_{ac}$ versus $log\ f$ which exhibits that as the frequency increases the a.c. conductivity increases. The exponent n is calculated from the slope of the plot for room temperature, which is 0.6, from this one can conclude that the a. c. conductivity follows Jonscher's power law.

4.11Synthesis of 1-phenyl-3-(propan-2-yl)-1*H*-pyrazol-5-ol Nano particles

Nano particles of 1-phenyl-3-(propan-2-yl)-1*H*-pyrazol-5-ol were synthesized by using water/oil (w/o) microemulsion technique. Importance of microemulsion technique in the synthesis of nano particles of pharmaceutically important materials and the hypothesis of synthesis of nano particles in micro emulsion technique are already discussed in detail in chapter III.

4.11.1 Synthesis of nano particles

1-phenyl-3-(propan-2-yl)-1*H*-pyrazol-5-ol crystalline material was used for the synthesis of nano particles. The mixture of Triton X – 100/water/n-heptane was used for the synthesis of nano particles. Single phase region was identified for the mixture of all this three solutions. Amount of surfactant was decided as the molar ratio R = 6. A detail of single phase diagram has been discussed in chapter III. The solution of 1-phenyl-3-(propan-2-yl)-1*H*-pyrazol-5-ol made in chloroform was added into this mixture in drop – wise manner with continuous stirring. After 15 – 20 min. of constant stirring nano particles were formed at the liquid – liquid interface of the solution, which were filtered out by using Whatman filter paper no. 42. The yield of synthesized nano particles was around 65%.

4.12 Powder XRD Study of 1-phenyl-3-(propan-2-yl)-1*H*-pyrazol-5-ol Nano particles

Figure 4.15 shows the powder XRD pattern of 1-phenyl-3-(propan-2-yl)-1*H*-pyrazol-5-ol nano particles. The peak broadening shows that the formed material is nano in nature. 1-phenyl-3-(propan-2-yl)-1*H*-pyrazol-5-ol

nano particles showed triclinic system with estimated unit cell parameters as, *a* = 11.1593 Å, *b* = 11. 2247 Å, *c* = 14. 1140 Å, *α* = 73. 333^{o}, *β* = 88. 286^{o} and *γ* = 82.767^{o}, which corresponds to the bulk crystalline sample unit cell parameters.

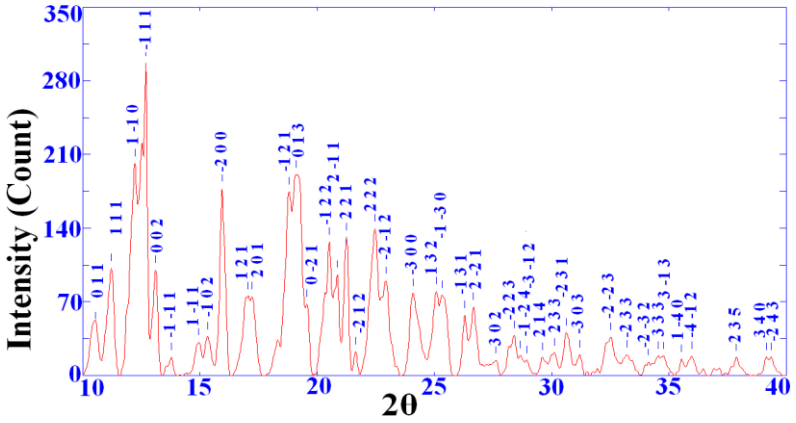

Figure 4.15 Powder XRD pattern of 1-phenyl-3-(propan-2-yl)-1*H*-pyrazol-5-ol nano particles

The average particle size of 1-phenyl-3-(propan-2-yl)-1*H*-pyrazol-5-ol nano particles was determined from the powder XRD pattern by employing the Scherrer's formula. From the Scherrer's formula the average particle size of 1-phenyl-3-(propan-2-yl)-1*H*-pyrazol-5-ol nano particles was found to be 33 nm.

4.13 TEM Study of 1-phenyl-3-(propan-2-yl)-1*H*-pyrazol-5-ol Nano particles

The TEM study was carried out to determine the exact size and morphology of the synthesized 1-phenyl-3-(propan-2-yl)-1*H*-pyrazol-5-ol nano crystalline particles. The TEM images of different size nano particles are shown in figures 4.16 (a), 4.16 (b) and 4.16 (c), which indicate nano particles of 41.14 nm, 29.13 nm and 11.28 nm, respectively. TEM results suggested

that the particles were having nearly spherical morphology and their sizes varied from 11 nm – 42 nm. From the images, one can find that the large size particles in figure 4.16 (a) are having more precise spherical type morphology with comparison to figures 4.16 (b) and 4.16 (c). As the particle size decreases agglomerated nanoparticles are formed. The possible explanation for this has been discussed in earlier chapter III.

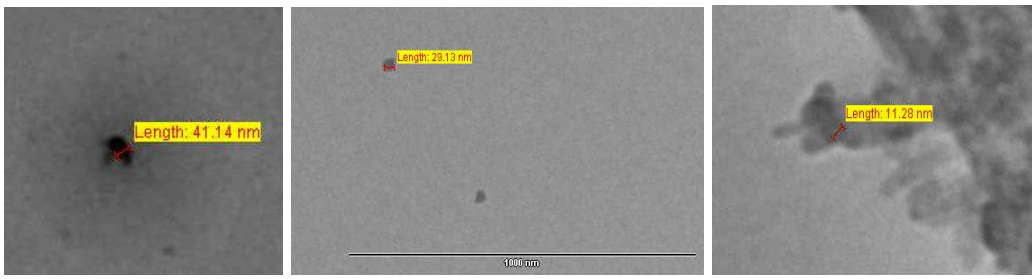

(a) (b) (c)

Figure 4.16 TEM images of 1-phenyl-3-(propan-2-yl)-1*H*-pyrazol-5-ol nano particles

4.14 FT – IR spectral study of 1-phenyl-3-(propan-2-yl)-1*H*-pyrazol-5-ol Nano particles

FT – IR spectrum of 1-phenyl-3-(propan-2-yl)-1*H*-pyrazol-5-ol nanocrystalline particles is shown in figure 4.17. The analysis of spectrum suggests that the absorptions occurring at 3129.6 cm^{-1} show C – H stretching. The absorption occurring at 2961.7 cm^{-1} is due to the C – H asymmetric stretching vibration of – CH_3. The absorptions taking place at 2872.2 cm^{-1} C – H symmetric stretching vibration of – CH_3. The absorption taking place at 1789.3 cm^{-1} is due to C = O stretching vibration of ester due to pyrazole. Whereas, the absorption taking place at 1533.2 cm^{-1} is due to C = C stretching due to aromatic ring skeleton. The absorption at 1453.0 cm^{-1} is assigned to C – H in plane asymmetric bending. The absorption taking place

at 1400.1 cm^{-1} is due to C – H out of plane symmetric bending. The absorption observed at 1126.6 cm^{-1} is due to = N – N – and the absorption observed at 1001.6 cm^{-1} C – H in plane bending. The absorption observed at 887.0 cm^{-1},827.8 cm^{-1}, 761.9 cm^{-1}, 686.7 cm^{-1}, 491.3 cm^{-1} and 446.8 cm^{-1} are attributed to either out of plane bending vibrations or aromatic substitution.

Comparing the FT – IR spectra of 1-phenyl-3-(propan-2-yl)-1*H*-pyrazol-5-ol Crystalline sample and nano crystalline sample, it can be noticed that no major changes are observed. Very small changes are observed in 890 cm^{-1} to 440 cm^{-1} range. However, they cannot be firmly attributed to the nano crystalline nature.

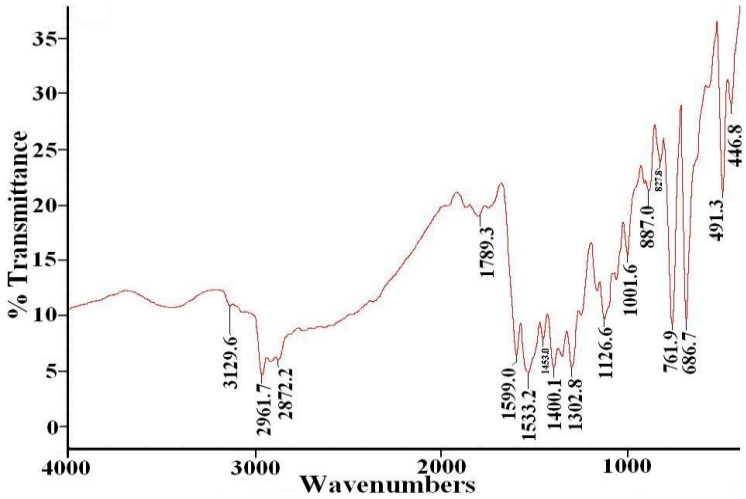

Figure 4.17 FT – IR spectrum of 1-phenyl-3-(propan-2-yl)-1*H*-pyrazol-5-ol nano particles

4.15 Thermal study of 1-phenyl-3-(propan-2-yl)-1*H*-pyrazol-5-ol nano particles

Thermal studies like TG, DTA and DSC were carried out on 1-phenyl-3-(propan-2-yl)-1*H*-pyrazol-5-ol nano particles. Figure 4.18 shows the TG – DTA curves of 1-phenyl-3-(propan-2-yl)-1*H*-pyrazol-5-ol nano particles. The TG plot shows that the nano particles remain stable up to 168.6 ^{o}C and then it

starts decomposing rapidly up to 271.4 ^{o}C and beyond that they decompose slowly up to 621.4 ^{o}C, where complete decomposition is observed. The DTA plot indicates that the decomposition process of 1-phenyl-3-(propan-2-yl)-1*H*-pyrazol-5-ol nano particles occurs through two endothermic reaction at 104.5 ^{o}C and 333.8 ^{o}C and three exothermic peaks observed at 268.7 ^{o}C, 302.1 ^{o}C and 586.4 ^{o}C, respectively. From the DSC plot several thermodynamic parameters were calculated by using the software TA evaluation available with the set up. For the first endothermic reaction at 104.5 ^{o}C the enthalpy and the change in heat capacity are calculated and found to be -57310.5J/kg and 829.3 J/kgK, respectively. This may be due to some phase change occurring without significant breaking of the bonds resulting into marginal weight loss, which may be due to melting of a sample. The melting point of 1-phenyl-3-(propan-2-yl)-1*H*-pyrazol-5-ol is 90 ^{o}C. Another endothermic reaction found at 333.8 ^{o}C the enthalpy and the change in heat capacity are calculated and found to be -36728.9 J/kg and 546.2 J/kgK, respectively. In between these two endothermic reactions, two minor exothermic reactions are observed at 268.7 ^{o}C and 302.1 ^{o}C. The values of enthalpy and change in heat capacity for 268.7 ^{o}C are found to be 24572.3 J/kg and 2186.3 J/kgK, respectively, and for another exothermic reaction at 302.1 ^{o}C the values of enthalpy and change in heat capacity are found to be 44352.1 J/kg and 822.9 J/kgK, respectively. Similarly, the third exothermic reaction occurring at 586.4 ^{o}C may be due to complete decomposition of the sample into the gaseous phase and reaction within the products. For this reaction, values of the enthalpy and the change in heat capacity are found to be 5016337 J/kg, 22521.7 J/kgK, respectively.

By comparing the TG plot of nano particles of 1-phenyl-3-(propan-2-yl)-1*H*-pyrazol-5-ol with the TG plot of crystalline material one observes that the nano particles are little more thermally stable than the crystalline material. This may be due to higher surface to volume ratio and higher surface energy giving slightly more thermal stability.

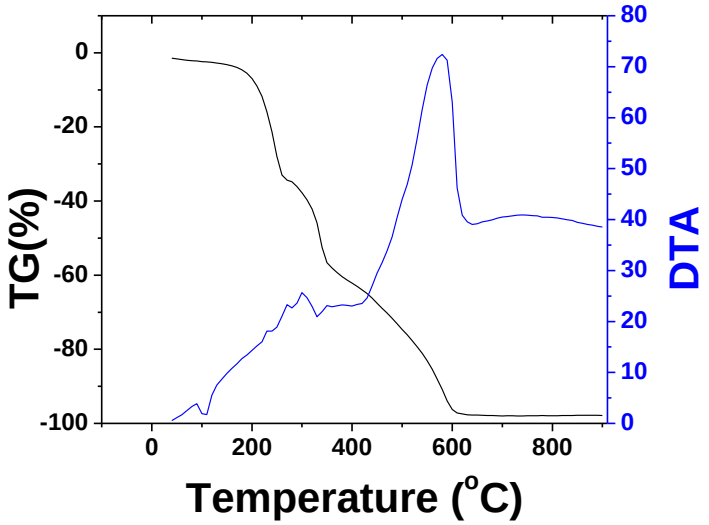

Figure 4.18 TG – DTA of 1-phenyl-3-(propan-2-yl)-1*H*-pyrazol-5-ol nano particles

4.16 Kinetic parameters of 1-phenyl-3-(propan-2-yl)-1*H*-pyrazol-5-ol Nano – particles

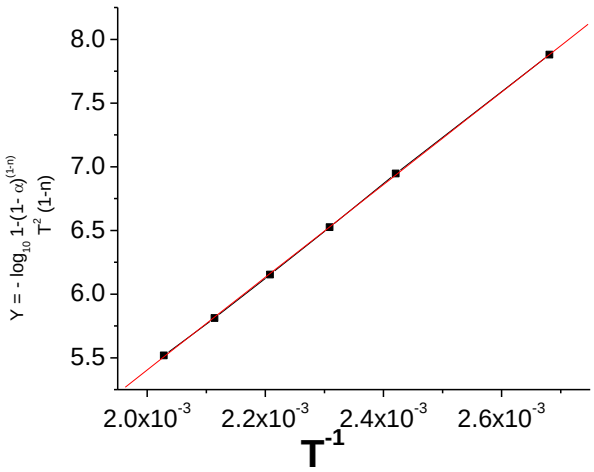

Figure 4.19 Coats and Redfern plot with linear fit

Kinetic parameters of decomposition of 1-phenyl-3-(propan-2-yl)-1*H*-pyrazol-5-ol nano particles were calculated using Coats – Redfern relation [37] as discussed in chapter III . Figure 4.19 shows the Coats – Redfern plot.

Table 4.6 Kinetic parameters of 1-phenyl-3-(propan-2-yl)-1*H*-pyrazol-5-ol nano particles

Sample	Kinetic Parameters
1-phenyl-3-(propan-2-yl)-1*H*-pyrazol-5-ol nano particles	Order of reaction (n) = 0
	Activation energy (E) = 82.25 $kJK^{-1}Mol^{-1}$
	Frequency factor (A) = 2.36×10^{21}

Table 4.6 shows the values of kinetic parameters of 1-phenyl-3-(propan-2-yl)-1*H*-pyrazol-5-ol nano particles calculated from the plot. As the activation energy is considered as a barrier to be surmounted to form reaction products [49], the higher value of activation energy for nano particles suggests slower reaction rate and hence more stability.

4.17 Thermodynamic parameters of 1-phenyl-3-(propan-2-yl)-1*H*-pyrazol-5-ol Nano – particles

Various thermodynamic parameters such as standard entropy of activation $\Delta^{\#}S°$, standard enthalpy of activation $\Delta^{\#}H°$, standard Gibbs energy of activation $\Delta^{\#}G°$ and standard internal energy of activation $\Delta^{\#}U°$ were calculated by applying well known formulae, as described in detail by Laidler [38]. Table 4.7 gives the values of various thermodynamic parameters calculated for 1-phenyl-3-(propan-2-yl)-1*H*-pyrazol-5-ol nano particles at 200 ^{o}C.

Table 4.7 Thermodynamic parameters of 1-phenyl-3-(propan-2-yl)-1*H*-pyrazol-5-ol nano particles

Sample	Thermodynamic Parameters
1-phenyl-3-(propan-2-yl)-1*H*-pyrazol-5-ol nano particles	Standard Entropy $\Delta^{\#} S^{\circ}$ = 190.95 $Jkmol^{-1}$
	Standard Enthalpy $\Delta^{\#} H^{\circ}$ = 67.34 $kJmol^{-1}$
	Standard Gibbs free energy $\Delta^{\#} G^{\circ}$= - 30.60 $kJmol^{-1}$
	Standard change in internal energy $\Delta^{\#} U^{\circ}$ = 77.06 $kJmol^{-1}$

The positive value of $\Delta^{\#} S^{\circ}$ and negative value of $\Delta^{\#} G^{\circ}$ indicates spontaneous process. Moreover, the positive values of $\Delta^{\#} S^{\circ}$ and $\Delta^{\#} H^{\circ}$ further suggests the spontaneous reaction at high temperature as it has been observed for crystalline bulk samples.

By comparing various thermal parameters of crystalline 1-phenyl-3-(propan-2-yl)-1*H*-pyrazol-5-ol and nano particle of 1-phenyl-3-(propan-2-yl)-1*H*-pyrazol-5-ol samples of tables 4.5 and 4.7, one finds that the values of thermal parameters are higher for the nano particle sample than the bulk crystalline sample. This further confirms higher stability of nano particle sample.

4.18 Dielectric Study

Dielectric study could not be performed because the nano particles sample could not be pelletized in a conventional way to carry out dielectric study. Any organic popular binder like alcohols or acetone could not be used because of high solubility of nano particle samples and water made it highly dispersed colloidal paste and the sample could not be pelletized without using

any binder, therefore, the dielectric study was not performed on nano particle of 1-phenyl-3-(propan-2-yl)-1*H*-pyrazol-5-ol.

4.19 Conclusions

(1) 1-phenyl-3-(propan-2-yl)-1*H*-pyrazol-5-ol material was synthesized by using the mixture of methyl isobutyl acetate and phenyl hydrazine prepared in methanol in presence of few drops of acetic acid as a catalyst.

(2) Single crystals of 1-phenyl-3-(propan-2-yl)-1*H*-pyrazol-5-ol were grown by using slow solvent evaporation technique. Pale yellowish, transparent crystals having maximum size 5mm × 4 mm were obtained.

(3) Single Crystal XRD of 1-phenyl-3-(propan-2-yl)-1*H*-pyrazol-5-ol confirmed two different tautomeric forms (keto and enol) of the same molecule co-crystallized in a 1 : 2 ratio.

(4) Single Crystal XRD suggested that 1-phenyl-3-(propan-2-yl)-1*H*-pyrazol-5-ol was having triclinic crystal system with the unit cell parameter as, a = 11. 1593 Å, b = 11.2247 Å, c = 14.1140 Å, α = 73.333°, β = 88.286°and γ = 82.767°.

(5) The powder XRD confirmed the structural identity with the unit cell parameters obtained by the Single Crystal XRD of the grown single crystals.

(6) FT-IR spectrum of the 1-phenyl-3-(propan-2-yl)-1*H*-pyrazol-5-ol crystals revealed the presence of functional groups and confirmed the presence of C – H stretching, C = O stretching, C = C aromatic ring skeleton, = N – N stretching and aromatic ring substitution.

(7) From TGA curve it was found that the crystalline material remained stable up to 160 ^{o}C, thereafter, it started decomposing slowly up to 280 ^{o}C and then it decomposed completely into gaseous products up to 610 ^{o}C. DTA plot showed an endothermic reaction at 105.2 ^{o}C and two exothermic reactions at 278.2 ^{o}C and 558.1 ^{o}C. Various thermal parameters were calculated from DSC.

(8) By applying the Coats and Redfern relation to the decomposition stage, the value of kinetic parameters were calculated at 220 ^{o}C. The value of order of reaction(*n*), activation energy (*E)* and frequency factor (*A)* were found to be 0, 51.54 kJ $K^{-1}Mol^{-1}$ and 9.36 x 10^{18}, respectively.

(9) The thermodynamic parameters for the decomposition process were also evaluated at 200 ^{o}C. The value of standard entropy, standard enthalpy, standard Gibbs energy and standard change in internal energy of activation were found to be, 114.10 $Jkmol^{-1}$, 43. 34 $kJmol^{-1}$, - 12.90 $kJmol^{-1}$ and 47.44 $kJmol^{-1}$, respectively. The positive values of standard entropy and standard enthalpy suggested spontaneous reaction at higher temperature.

(10) The dielectric constant and the dielectric loss decreased as the frequency increased. Moreover, as the frequency increased the a. c. conductivity increased while a. c. resistivity decreased.

(11) The nano particles of 1-phenyl-3-(propan-2-yl)-1*H*-pyrazol-5-ol were synthesized by using w/o microemulsion technique with the mixture of water/ triton X – 100/ n – heptane. Ternary phase diagram was constructed by varying the proportion of all the three solutions.

(12) The characteristic broadening of the Powder XRD pattern confirmed nano structured nature of the material. 1-phenyl-3-(propan-2-yl)-1*H*-pyrazol-5-ol nano particles showed triclinic crystal system with unit cell parameters as, *a* = 11. 1593 Å, *b* = 11.2247 Å, *c* = 14.1140 Å, *α* = 73.333°, *β* = 88.286°and *γ* = 82.767°, which were identical to the bulk one.

(13) The average particle size of the 1-phenyl-3-(propan-2-yl)-1*H*-pyrazol-5-ol nanoparticles was calculated by using Scherrer's formula to a particular reflection in powder XRD pattern and it was found around 33 nm.

(13) From TEM study it was found that the 1-phenyl-3-(propan-2-yl)-1*H*-pyrazol-5-ol nano particles were having nearly spherical morphology with sizes varied from 11 nm – 42 nm.

(14) FT – IR spectrum of the 1-phenyl-3-(propan-2-yl)-1*H*-pyrazol-5-ol nano particles showed the same absorptions as shown in crystalline material. This showed there was no inclusion or presence of any extra bonding. No conclusive effect was noted in FT – IR spectrum due to the nano structured nature.

(15) TG of 1-phenyl-3-(propan-2-yl)-1*H*-pyrazol-5-ol nanoparticles showed that the sample remained almost stable up to 168 ^{o}C, thereafter, it decomposed rapidly and up to 621 ^{o}C the complete decomposition took place. DTA showed two endothermal absorptions taking place at 104.5 ^{o}C and 333.8 ^{o}C and three exothermic reactions occurring at 268.7 ^{o}C, 302.1 ^{o}C and 586.4 ^{o}C. DSC gave the entropy and heat change of these endothermic and exothermic reactions.

(16) Kinetic parameters of decomposition of the 1-phenyl-3-(propan-2-yl)-1*H*-pyrazol-5-ol nanoparticles were calculated by Coats – Redfern formula. The order of reaction (n), activation energy (E) and frequency factor (A) were estimated as, 0, 82.25 kJ $K^{-1}Mol^{-1}$ and 2.36 x 10^{21}, respectively. With comparison to the crystalline sample the higher value of activation energy suggested that the nano particle sample was thermally little more stable than crystalline sample.

(17) The thermodynamic parameters for the decomposition process were also evaluated at 200 ^{o}C. The values of standard entropy, standard enthalpy, standard Gibbs free energy and standard change in internal energy of activation were found to be, 158.14 $Jkmol^{-1}$, 71.90 $kJmol^{-1}$, - 26.63 $kJmol^{-1}$ and 77.06 $kJmol^{-1}$, respectively. These values were higher than those for the crystalline sample, which indicated the stable nature of nano particles with compare to crystalline material. Also, it confirmed the spontaneous reaction at higher temperature.

References

[1] T. Eicher, S. Hauptmann, *The Chemistry of Heterocycles: Structure, Reactions, Syntheses, and Applications*, 2nd Edition, Wiley – VCH. Weinheim, Germany (2003).

[2] A. Chauhan, P. K. Sharma, N. Kaushik, *Int. J. of Chemtech Res.*, **3** (2011) 11.

[3] T. K. Li, H. Theorell, *Acta Chemica Scandinavia*, **22** (1969) 892.

[4] H. B. Oza, D. G. Joshi, H. H. Parekh, *Heterocycl. Commun.*, **3** (1997) 239.

[5] G. Dannhardt, W. Kiefer, G. Kramer, S. Maehrlein, U. Nowe, B. Fiebich, *Eur. J. Med. Chem.*, **35** (2000) 499.

[6] A. Tanitame, Y. Oyamada, K. Ofuji, M. Fujimoto, N. Iwai, Y. Hiyama, K. Suzuki, H. Ito, H. Terauchi, M. Kawasaki, K. Nagai, M. Wachi, J. Yamagishi, *J. Med. Chem.*, **47** (2004) 3693.

[7] A. L. Gill, M. Frederickson, A. Cleasby, S. J. Woodhead, M. G. Carr, A. J. Woodhead, M. T. Walker, M. S. Congreve, L. A. Devine, D. Tisi, M. O'Reilly, L. C. A. Seavers, D. J. Davis, J. Curry, R. Anthony, A. Padova, C. W. Murray, R. A. E. Carr, H. Jhoti, *J. Med. Chem.*, **48** (2005) 414.

[8] F. Chimenti, A. Bolasco, F. Manna, D. Secci, P. Chimenti, O. Befani, P. Turini, V. Giovannini, B. Mondovi, R. Cirilli, F. La Torre, *J. Med. Chem.,* **47** (2004) 2071.

[9] T. Singh, S. Sharma, V. K. Srivastava, A. Kumar, *Archiv der Pharma,* **339** (2006) 24.

[10] Y. Kando, T. Kiji, M. Noguchi, Y. Manade, *Jpn. Kokai Tokkyo Koho JP* 08, 311, 036.

[11] I. Bouabdallah, L. A. M'Barek, A. Zyad, A. Ramdani, I. Zidane, A. Melhaoui, *Nat Prod Res.*, **20** (2006) 1024.

[12] D. Berta, E. Felder, A. Vulpetti, M. Villa, PCT Int. Appl. WO 02 62804 (Cl. CO7D498/04).

[13] J. J. Vora, D. R. Patel, A. R. Patel, Y. S. Patel, *Asian J. of Biochem. and Pharm. Res*., **1** (2011) 108.

[14] S. D. Bharadwaj, V. S. Jolly, *Orient J. Chem.*, **12** (1996) 185.

[15] H. G. McFadden, J. L. Huppatz, M. Couzens, C. H. L. Kennard, D. E. Lynch, *Pesticide Sci.*, **36** (1997) 247.

[16] T. L. Siddall, Z. L. benko, G. M. Garvin, J. L. Jackson, J. M. Jackson, J. M. McQuinsto, D. G. Ouse, T. D. Thibault, J. A. Turner, J. C. Van Heertum; PCT Int. Appl. WO 98, 52,926.

[17] A. A. Bekhit, H. M. Ashour, Ael – D Bekhit, S. A. Bekhit, *Med Chem.*, **5** (2009) 103.

[18] A. Kumar, R. S. Verma, B. P. Jagu, *J. Ind. Chem. Soc.*, **67** (1990) 120.

[19] K. N. Sarma, M. C. S. Subha, K. C. Rao, *Eur. J. of Chem.*, **7** (2010) 745.

[20] J. Panda, S. V. Srinivas, M. E. Rao, *J. Ind. Chem. Soc.*, **79** (2002) 770.

[21] M. T. Di Parsia, C. Suárez, M. J. Vítolo, V. E. Márquez, B. Beyer, C. Urbina, I. Hurtado, *J. Med Chem.*, **24** (1981) 117.

[22] B. Roman, *Pharmazie*, **45** (1990) 214.

[23] R. Soliman, *J. Med. Chem.*, **22** (1979) 321.

[24] H. G. Garg, P. P. Singh, *J. Chem. Soc.*, **2** (1936) 1141.

[25] M. M. Mohy El-Din, A. M. Senbel, A. A. Bistawroos, A. El-Mallah, N. A. Nour El-Din, A. A. Bekhit, H. A. Abd El Razik, *Basic Clin Pharmacol Toxicol.*, **108** (2011) 263.

[26] H. Yamashita, M. Odate, h. Iizuka, H. Kawazura, Y. Shiga, H. Namekawa, Eur. Pat. Appl. Ep 295695 (1988) (Cl. C07D 401/6).

[27] P. T. Chovatia, J. D. Akabari, P. K. Kachhadia, P. D. Zaalavadia, H. S. Joshi, *J. Serb. Chem. Soc.*, **71** (2007) 713.

[28] K. Zalgislaw, A. Seffan, *Acta. Pol. Pharm.*, **36** (1979) 645

[29] J. Lertvorachon, J. P. Kim, D. V. Soldatov, J. Boyd, G. Roman, S. J. Cho, T. Popek, Y. S. Jung, P. C. K. Lau, Y. Konishi, *Bioorg. Med. Chem.*, **13** (2005) 4627.

[30] R. Lan, Q. Liu, P. Fan, S. Lin, S. R. Fernando, D. McCallion, R. Pertwee, A. Makriyannis, *J. Med. Chem.*, **42** (1999) 769.

[31] M. B. Smith, J. March, *Advanced Organic Chemistry*, Wiley Interscience, New York, USA (2001).

[32] A. R. Katritzky, J. Elguero, *The Tautomerism of Heterocycles,* Academic Press, New York, USA (1976).

[33] J. L. G. de Paz, J. Elguero, C. Foces-Foces, A. L. Llamas-Saiz, F. Aguilar-Parrilla, O. Klein, H. H. Limbach, *J. Chem. Soc., Perkin Trans.,* **2** (1997) 101.

[34] G. M. Sheldrick, *Acta Cryst.,* **A64** (2008) 112.

[35] L. J. Farrugia, *J. Appl. Cryst*., **30** (1997) 565.

[36] K. Kapoor, V. K. Gupta, Rajnikant, P. M. Vyas, M. J. Joshi, S. D. Tada, S. M. Sorathia, H. S. Joshi, *X – Ray Str. Anal. Online*, **27** (2011) 59.

[37] A. W. Coats and J. P. Redfern, *Nature*, **201** (1964) 68.

[38] K. J. Laidler, *"Chemical Kinetics",* 3rd Ed., Harper and Row, New York, USA (1987).

[39] A. G. Whittaker, A. R. Mount, M. R. Hill, *Physical Chemistry,* Viva, New Delhi, India (2001).

[40] D. R. Mantheni, M. P. K. Maheswaran, H. F. Sobhi, N. I. Perea, A. T. Riga, M. E. Matthews, and K. Alexander, J. Term. Anal. Calorim., DOI: 10.1007/s10973-011-1423-y.

[41] J. Menegotto, J. Alie, C. Lacabanne, and M. Bauer, *Dielectric News Lett.* **19** (2004) 1.

[42] K. Adrjanowicz, K. Kaminski, M. Paluch, P. Wlodarczyk, K. Grzybowska, Z. Wojnarowska, L. Hawelek, W. Sawicki, P. Lepek, and R. Lunio, *J. of Pharma. Sci.,* **99** (2010) 828.

[43] L. L. Hensch, J. K. West, *Principles of Electronic Ceramics,* John Wiley & Sons, Singapore (1990).

[44] A. K. Johncher, *Phys. Thin Films,* **11** (1980) 23.

[45] A. K. Johncher, *Nature,* **256** (1977) 673.

[46] A. K. Johncher, *J. Mater. Sci.,* **16** (1981) 2037.

[47] M. D. Ingram, *Phys. Chem. Glasses,* **28** (1987) 215.

[48] J. O. López, R. G. Aguilar, *Rev. Mex. Fis.,* **49** (2003) 529.

[49] R. S. Boikess and E. Edelson, Chemical Principles, Harper & Row, New York, USA (1978).

Chapter – V

Synthesis and Characterization of Cholesterol Crystals and Nano Particles

5.1 Introduction

Cholesterol (Cholest – 5 – en – 3β – ol), is a sterol (a combination of steroid and alcohol) and a lipid found in the cell membranes of all body tissues and transported in the blood plasma of all animals. Lesser amount of cholesterol is also found in plant membranes. A cholesterol name originates from the Greek *chole* – (bile) *stereos* – (solid) and the chemical suffix – *ol* for an alcohol. It is highly fat soluble but slightly soluble in water, which is less than 0.001% [1,2]. Cholesterol present in the diet is slowly absorbed by the gastro intestinal tract in to the intestinal lymph.

De la Salle (1770) and de Fourcroy (1789) were the first to describe, after isolating white easily crystallizable compound from alcohol and ether extracts of human gall stones. Chevreul later identified the compound as the major component of gallstones and in 1816 named the substance *cholesterine.* Cholesterine was renamed as “cholesterol” soon after Berthelot demonstrated in 1859 that cholesterine was in fact an alcohol [3].

Figure 5.1 (a) & (b) show the 2 – D and 3 – D images of cholesterol structure, which consists of a tetracyclic cyclopenta[a]phenanthrene structure with an iso – octyl side chain. The four rings (A, B, C, D) have *trans* ring junctions, and the side chain and two methyl groups are at an angle to the rings above the plane with β stereochemistry. Cholesterol has one hydroxyl group at C_3 and a double bond between C_5 and C_6. An 8 carbon aliphatic side

chains is attached to $C_{17.}$ Cholesterol also contains a total 5 methyl groups. Due to the presence an – OH group, cholesterol is weakly amphiphilic. Cholesterol is yellowish crystalline solid. The crystals, under the microscope, exhibit a notched (⌐¬) appearance. It is almost insoluble in water but soluble in organic solvents such as chloroform, benzene, ether, etc. [4].

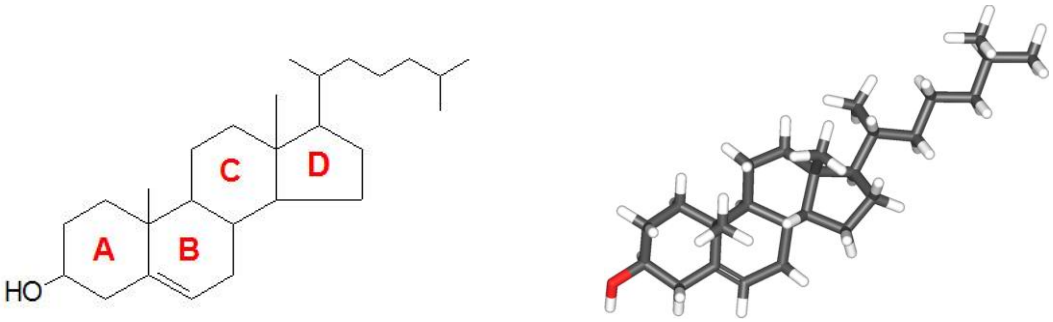

(a) (b)

Figure 5.1 Cholesterol Structure (a) 2- dimensional (b) 3 – dimensional

5.2 Importance of Cholesterol

Looking at the importance of cholesterol in human life a brief review of cholesterol is attempted hereby.

Biosynthesis of cholesterol involves highly complex series of atleast thirty different enzymatic reactions, which were proposed K. Bloch and F. Lynen, and both of them received Nobel Prize in 1964. Cholesterol is synthesized in liver through a very long and energetically costly pathway. Nineteen sterol intermediates are involved in the conversion of acetyl – CoA to cholesterol. Such a complicated and energetically unfavorable process is adopted to generate a single specific sterol – cholesterol, which is the strong evidence of its vital function within the cell [5,6].

About 20 – 25% of total daily production of cholesterol occurs in the liver, nevertheless, the other sites of higher synthesis rates are intestines, adrenal glands and reproductive organs. For a person with an average weight of 68 kg, the total body content of cholesterol is about 35 gm. Typical daily internal production is about 1 gm and typical dietary intake is 200 to 300 mg. Out of 1200 to 1300 mg input to the intestines about 50% is reabsorbed into the blood stream.

It is worth – while to summarize of cholesterol on cell membranes [3]:

(1) Cholesterol is known to influence the physical properties of membranes. Depending on temperature, cholesterol can either make a membrane more or less fluid. The change in fluidity is arises due to the rigidity of steroid rings. Being conformationally inflexible, when it is placed into a membrane, it restricts the motion of hydro-carbon chains on adjacent phospholipids molecules. As a matter of fact, the phospholipids molecules exist in either a gel or liquid state, which is determined by gelation temperature. If the prevailing temperature is greater than the gelation temperature then the phospholipids remain in the liquid state. In this case, the addition of cholesterol decreases the fluidity of the membrane by restricting the liquid motion of the phospholipids hydrocarbon chains. Thus, the addition of cholesterol increases the fluidity of the membrane by interfacing with the packing (into a gel) of hydrocarbon chains.

(2) Cholesterol is known to exhibit specific and direct interactions with membrane proteins. The cholesterol affects the activities of enzymes that act adjacent to, but not within, membranes. The ability of cholesterol to stimulate

or inhibit enzyme activity is due to direct interaction between cholesterol and enzyme.

It has been found that cholesterol may acts as an antioxidant [7]. Cholesterol also aids in the manufacture of bile (which helps digest fats), and is also important for the metabolism of fat soluble vitamins, including vitamin A, D, E and K. It is the major precursor of vitamin D and of the various steroid hormones, including the sex hormones.

By far the most abundant use of cholesterol in the body is to form cholic acid in the liver. Almost 80% of the cholesterol is converted into cholic acid. It is conjugated with other substances to form bile salts, which promotes digestion and absorption of fats. A small quantity of cholesterol is used by (a) the adrenal glands to form *adrenocortical hormones*, (b) the ovaries to form progesterone (c) estrogen and the testes to form testosterone. The female sex hormones, the *estrogens,* decrease the blood cholesterol, where as the male sex hormones, the *androgens,* increase blood cholesterol. Unfortunately the mechanisms of these effects are unknown, but the sex effects are very important because the higher cholesterol in the male is associated with a higher incidence of heart attacks [8].

Moreover, a large amount of cholesterol is precipitated in the corneum of the skin. This, along with other lipids, makes the skin highly resistant to the absorption of water – soluble substances and also to the action of many chemical agents. Also, these lipid substances help to prevent water evaporation from the skin; without this protection the amount of evaporation is as much as 5 to 10 liters per day instead of the usual 300 to 400 ml [8].

Inborn errors of cholesterol synthesis are associated with multiple systematic abnormalities including skeleton malformations. The Smith – Lemli – Opitz Syndrome (SLOZ) is characterized by multiple malfunctions such as nervous system and skeletal mal functions [9].

As noted earlier, cholesterol is almost insoluble in pure water, but the bile salts and lecithin in bile combine physically with the cholesterol to form ultramicroscopic *micelles* that are soluble. Bile salts have propensity to form micelles, which are small spherical globules about 3 to 4 nanometers in diameter composed of 20 to 40 molecules of bile salts. Thus the nature has adopted nanotechnology, for the absorption of cholesterol! When the bile becomes concentrated in the gallbladder, the bile salts and the lecithin become concentrated along with cholesterol which keeps it in the solution. Under abnormal conditions the cholesterol may precipitate, resulting in the formation of *gallstones*. The different conditions that can cause cholesterol precipitation are (i) too much absorption of cholesterol from the bile, (ii) too much absorption of bile salts and lecithin from the bile, (iii) too much secretion of cholesterol in bile and (iv) inflammation of the epithelium of the gallbladder [5]. The crystallization pathways of cholesterol in ternary systems of cholesterol – lecithin – water [10] and ternary and quaternary aqueous systems containing bile salt, lecithin and cholesterol [11], which is reviewed by Jirsa and Groen [12]. This has been described in figure 5.2.

Atherosclerosis is a disease of the arteries in which fatty lesions called *atheromatous plaques* develop in the inside arterial wall. These plaques start by deposition of minute crystal of cholesterol in the intima and sub-lying smooth muscle with time, the crystals grow larger and coalesce to form very

large mat-like crystals. Later on, calcium salts often precipitate with the cholesterol and other lipids of the plaques, leading to bony-hard calcifications thus make the arteries completely rigid [8].

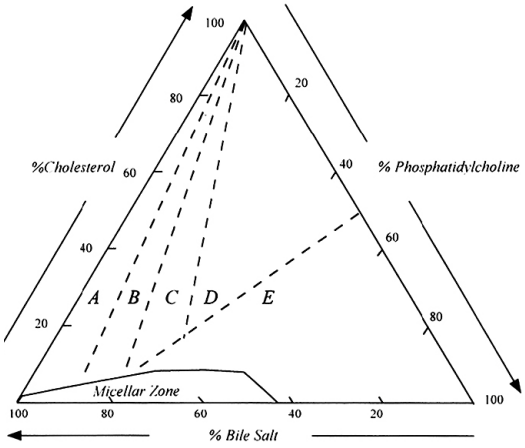

Figure 5.2 A quaternary phase diagram showing relative concentrations for which various crystallization pathways occur [12,13]

Earlier, the 1970s, Donald Small [14] evaluated cholesterol crystals and their potential role in arthrosclerosis. However, the concept of plaque rupture as the underlying cause of acute cardiovascular events had not been elucidated at that time and hence the connection between cholesterol crystals and plaque rupture was unrecognized. Abela and Aziz [15.16] demonstrated that when cholesterol crystallizes from a liquid to a solid state, it expands in volume. Moreover, it has already been shown that cholesterol is present in a liquid state in the arterial wall [17]. Therefore, expansion within the confined space of the necrotic core of atheromatous plaques can lead to disruption of the plaque cap and overlying intima, leading to arterial thrombosis [18].

The mammalian nervous system contains disproportionate cholesterol content. In brain, its content is nearly 10 fold greater than any organ [19].

Development of the capacity to synthesize and store such a large amount of cholesterol indicates that there is a close link between the evolution of the nervous system and specific role of cholesterol. Notwithstanding, within the brain nearly 70% of cholesterol is present in mylin, where it performs important role. The need for efficient signaling despite a small transverse diameter of axons is a key selective pressure driving the accretion of cholesterol in mammalian brain [20]

Moreover, the nervous system operates by exchanging electrical signals between nerve cells which are transmitted via highly specialized contact sites, the so-called synapses. The availability of cholesterol in the brain also determines the degree of synapse formation [21,22]. Nerve cells seem to be able to produce enough cholesterol on their own in order to survive and develop but too little to furnish a sufficient number of synaptic contacts. Therefore, they have to rely on it being supplied from an external source. Unlike all other organs, the brain cannot use the supply in blood since the so-called lipoproteins, which regulate the transport of cholesterol and other lipid-soluble materials, are too large to cross the blood-brain barrier. Therefore, the brain has to ensure its own supply of cholesterol. These new results show that glial cells produce excess cholesterol and supply nerve cells with enough of it to allow them to form synapses. This relationship highlights a completely new role for glial cells [23].

It has been found that disturbances in cholesterol metabolism are associated with the development of various neurological conditions. Defects in cholesterol metabolism (Cerebrotendinuous Xanthamatosis) and intracellular transport (Niemann Pick syndrome) lead to neurological disease. The genetic

connections between neurological disorders and cholesterol metabolism are discussed by Björkhem *et al.* [24].

Cholesterol is also known as *Jekyll and Hyde molecule* because it plays both good as well as bad roles in a body. As it has been noted earlier, it is connected with the heart diseases. Heart disease is the number one killer in India and world. Globally around 60% of people are suffering from cardio vascular diseases. There are two types of cholesterols: the good cholesterol and the bad cholesterol. Basically cholesterol is the same but the lipoproteins which transport it give this label. The Low Density Lipoprotein (LDL – a bad cholesterol) transports cholesterol and triglyceride from liver and small intestine to cells and tissues. This LDL high concentration level causes atherosclerosis, heart attack, stroke and peripheral diseases. The High Density Lipoprotein (HDL – a good cholesterol) removes cholesterol from atheroma within arteries and transport it back to the liver for excretion or re-utilization. HDL contains highest proportion of protein. About one-third to a quarter of blood cholesterol is carried by HDL.

Arthritis is again serious diseases and large numbers of peoples in the world are suffering from arthritis. There are several crystals such as monosodium urate monohydrate, calcium pyrophosphate dihydrate and hydroxyapatite play important role, which has been discussed extensively by Parekh [25]. Nevertheless, cholesterol crystals are formed in the synovial fluid in arthritis diseases in 0.1 – 0.3 % cases. Two type of cholesterol crystals grow in the synovial fluid during inflammations, which are (1) flat planar plates of square, rectangular or rhomboid shape and (2) thin needle type. Optical properties of cholesterol crystals in human synovial fluid are studied by

Zakharova *et al.* [26]. Cholesterol crystals are also found in shoulder synovial fluid [27] and bursal fluid [28].

Cholesterol was crystallized from different solvents under various conditions and the effect of different solvents on the crystal structure was studied earlier by Garti *et al.* [29,30]. Cholesterol crystal formation and growth was reported in bile solution [31]. Different morphologies of gel grown cholesterol crystals, for instance, fibrous, needle type, dendritic type and platelet type, were reported by Elizabeth *et al.* [32]using acetone, ethanol and methanol as solvents for cholesterol. Galloway *et al.* [33] have recently reported seven new solvates of cholesterol using solvents of varying carbon chain length and overall size from propanol through to phenyl ethanol. While micro topographical study of cholesterol crystals was also reported. They also observed crystallogrphically oriented etch pits. The gel growth of cholesterol crystals was earlier reported [32,34]. The epitaxial growth of cholesterol crystal from the well characterized bile solution on calcite substrates and the nucleation and epitaxial growth of cholesterol monohydrate was demonstrated in real time by AFM [35].

There are certain compounds which acts as cholesterol crystallization inhibitors, promotors and pro – nucleating as well as anti – nucleating factors, which are elaborately discussed by Jirsa and Groen [12]. It has been found that apolipoprotein A – I both increase the cholesterol crystal occurence in time and reduce the rate of crystal growth [36]. The inhibitory effect of I_gA on cholesterol crystal growth is also reported [37]. On the other hand, Pattinson and Willis [38] identified a pronase – resistant C – like phospholipase activity as high cholesterol crystallization promoting one.

Looking at the vast activities of research briefly reviewed hereby in the *in vivo* growth of cholesterol crystals and the factors affecting the growth, the present author has felt deem fit to conduct the cholesterol crystal growth experiments by using gel technique and characterize them by various techniques.

5.3 Growth of Cholesterol Crystals

The single diffusion gel growth technique was used to grow cholesterol crystals. Distilled water and analytical reagent (AR) grade chemicals were used to grow the cholesterol crystals. All test tubes and glassware were cleaned as well as autoclaved at 120 °C for 15 min before use. The whole experiment was conducted at the room temperature and process was carried out in the aseptic medium in a laminar flow hood to avoid microbial contaminations.

5.3.1 Preparation of Sodium – Meta Silicate Stock Solution

In the present investigation, sodium meta-silicate (SMS) - {$Na_2SiO_3.9H_2O$} powder was used for preparation of the gel medium. First of all 200 g SMS powder was added in one liter of double distilled water in a beaker. The mixture was stirred vigorously for 2 h for uniform mixing up using a magnetic stirrer. Thus, a dense milky solution of sodium meta-silicate was formed. It was then kept in undisturbed condition for 24 h to allow sedimentation so that heavy insoluble impurities could accumulate at the bottom of a beaker. This was decanted into another beaker and filtered twice with Whatman qualitative filter paper of 11 µm pore size and 12.5 cm diameter (Cat No 1001 125) for high-purity filtration. Then the solution was centrifuged on MSE high-speed

centrifuge unit for about half an hour at 10000 revolutions per minute. Practically the solution got rid off all suspended impurities and as a result, transparent, slightly golden colored solution of SMS was obtained. Then, the filtered solution was stored in a light protected glass container with air tight cork so that the solution may not be affected by oxygen and carbon dioxide (usually to avoid absorption of carbon dioxide) in air and light. This is known as stock SMS solution, which could be preserved for quite a long time period.

5.3.2 Preparation of SMS Solution with Definite specific Gravity

The specific gravity (SG) of the stock SMS solution can be determined by pyknometer, i.e. specific gravity bottle, which is usually made of glass, with a close-fitting ground glass stopper having a capillary tube through it, so that air bubbles may escape from the apparatus. The SMS solution of desired SG was prepared by adding double distilled water of appropriate volume. The SG of each of the SMS solutions was determined by the following formula,

$$\textit{Specific Gravity (SG)} = \frac{W_S - W_0}{W_W - W_0} \qquad \text{....(5.1)}$$

Where, W_0 = Weight of the empty dry bottle, W_S = Weight of the bottle filled with SMS solution and W_W = Weight of the bottle filled with distilled water.

In the present study, the SG of SMS solutions was selected 1.05 for the growth of cholesterol crystal growth.

5.3.3 Preparation of Gel

1 N Aqueous solution of Acetic Acid {CH_3COOH} was mixed with the SMS solution of definite SG in appropriate amount so that the desired value of

the pH could be set for the mixture. Here, during the procedure of adjusting the definite value of pH of the mixture, the SMS solution was added in a drop by drop manner to the Acetic Acid solution, with constant stirring to avoid excessive ion concentrations which otherwise cause premature local gelling and make the final medium inhomogeneous. The gel solution of 20 mL was transferred into the test tubes of 140 mm length and 25 mm diameter. In the present study, the pH value of the mixture was kept at 5.0 for cholesterol crystal growth. It has been noted in chapter I that as polymerization process in the silica hydro gel is pH sensitive, the pore size distribution and hence the gel density varies with pH. It was observed that the time required for gelation was very sensitive to pH. Moreover, it was also noticed that gels of insufficient density took a long time to form and were mechanically unstable. Within 2 days, good quality gels were set in the test tubes for the above selected pH value. Here, the silica gel was chosen as it remains stable and does not react with the supernatant solution. Here, the role of silica hydro gel was to give support to the growth of cholesterol crystals and provide proper surface for the growth of crystals. There was no direct role of silica hydro gel in the growth of cholesterol crystals as cholesterol is insoluble in water.

5.3.4 Pouring of Supernatant Solution

After the gelation took place, 20 ml supernatant solutions (SS) of cholesterol prepared in acetone with 1 wt. % concentration was gently poured on the set gels in test tubes by using pipette without damaging the gel surface. Moreover, in order to avoid damage, the supernatant solution was added drop wise with a pipette in such a way that the drops were allowed to

fall on to the side of the test tube wall. Then the test tubes were capped with airtight stopples and kept undisturbed.

5.3.5 Growth of cholesterol crystals

The complete crystal growth of cholesterol took place within 12 days of the pouring supernatant solution over the SMS gel. As cholesterol is having very low solubility in water and the top portion of silica hydro-gel provides the sites for nucleation, the growth of crystals took place majority in the supernatant solution. Figure 5.3 (a) shows the cholesterol crystal growth in the supernatant solution. Figure 5.3 (b) shows the harvested crystals, which are very thin, transparent, platelets having size 35 mm × 5 mm. As it can be notices from the figure that the crystals are so thin and transparent that it is difficult to identify the crystals on the graph paper clearly.

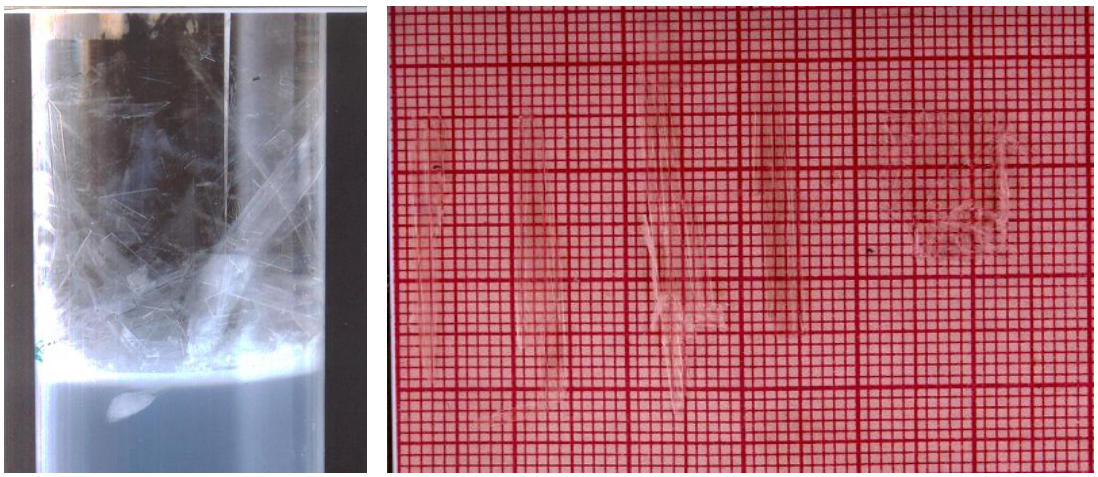

(a) (b)

Figure 5.3 (a) Cholesterol crystals grown in supernatant solution (b) harvested crystals

5.4 Powder XRD study of Cholesterol Crystals

Powder XRD was carried out to study the crystalline nature and determine the unit cell parameters of cholesterol. Figure 5.4 shows the powder XRD pattern of cholesterol crystals. Anhydrous cholesterols are known to crystallize in triclinic structure with lattice parameters, a = 14.10 Å, b= 33.74 Å, c = 10.46 Å, α = 94.60^o, β = 90.00^o and γ = 95.72^o [39], similarly, the cholesterol monohydrate is also known to crystallize in triclinic crystal structure with the lattice parameters; a = 12.39 Å, b= 34.46 Å, c = 12.41 Å, α = 91.90^o, β = 98.1^o and γ = 100.80^o [40]. In the present work all peaks were indexed and the latice parameters were found to be a = 14.234 Å b= 34.086 Å, c = 10.481 Å, α = 94.70^o, β = 90.00^o, γ = 95.72^o and they are also in good agreement with ASTM data (07 - 0714). These unit cell parameters also correspond to those observed by Ammal *et al.* [41] for anhydrous cholesterol.

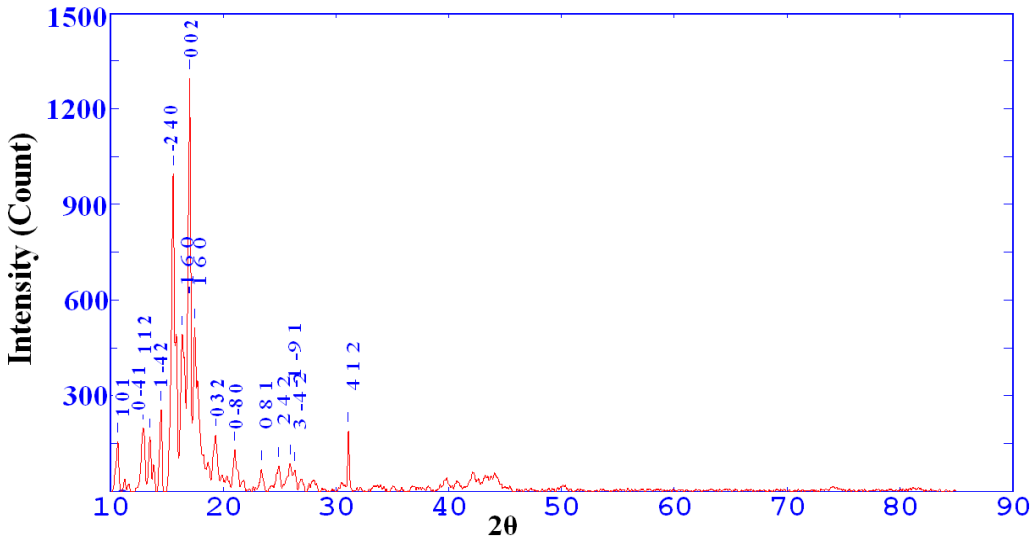

Figure 5.4 Powder XRD pattern of cholesterol crystals

5.5 Surface morphological study of Cholesterol crystals

Surface morphology study of cholesterol crystals was carried out by using Scanning Electron Microscopy (SEM) and Atomic Force Microscopy (AFM).

5.5.1 SEM micrograph of Cholesterol crystal

Figure 5.5 (a) shows the SEM image of the grown cholesterol crystal at 1.24kX magnification which suggests the presence of steps on the crystal surface. However, at higher magnification of 2.47kX bunching of several steps is observed in figure 5.5 (b), which is expected to give contribution in the growth of crystal. This suggests that the growth of cholesterol crystals occurs in the step – wise manner.

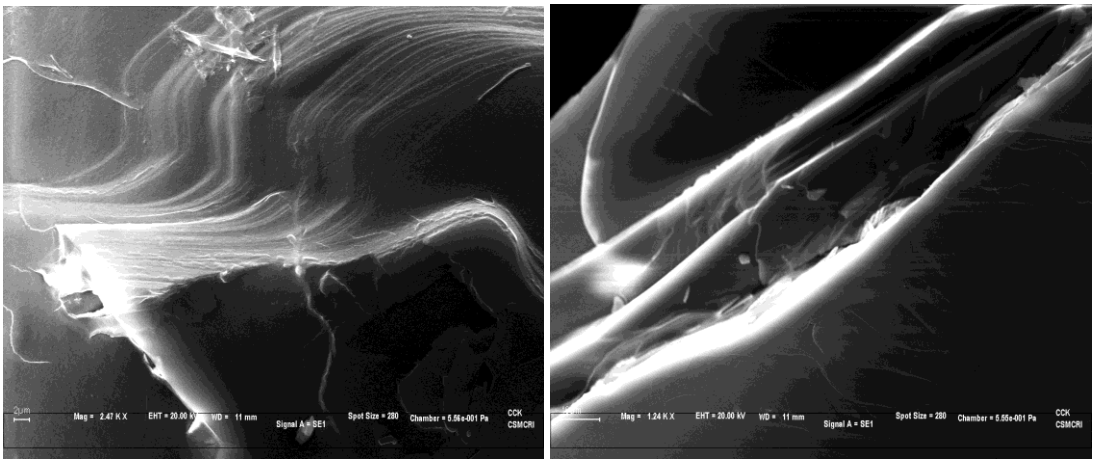

(a) (b)

Figure 5.5 SEM images at (a) 2.47 KX (b) 1.24 KX resolution for cholesterol crystal

5.5.2 AFM of Cholesterol Crystal

The surface characterization of cholesterol monohydrate single crystal was reported by Abendan and Swift [42] using chemical force microscopy to

establish the prominent plate face as either hydrophobic (001) or hydrophilic (002). They recorded AFM images under different conditions as in contact tapping mode, both in air and *in situ*. The platelet type cholesterol crystal having the largest face (001) was selected for the micro topographical study. As it has been observed from SEM images, the cholesterol crystals are grown in stepwise manner. Atomic Force Microscopy (AFM) images are taken on (001) as grown face of platelet type cholesterol crystals. Figures 5.6 (a) and (b) show the AFM image of steps observed on the surface of the crystal. Figure 5.6 (c) shows the depth profile of the same region. The step size was measured to be 2.66 nm. The area roughness of this region was 266.64 pm and line roughness was 77.49 pm. The step is not smooth and straight one, but it is uneven, probably, with some kinks. According to the well established model for crystal growth, the steps with kinks play important role in growth [43]. Figures 5.7 (a, b) show the AFM images of the step, which show that the main step is splitting in to two as one large step and the other small step, the depth profile is shown in figure 5.7 (c) indicating the height of large step as 14.83 nm and the small step as 10.84 nm.

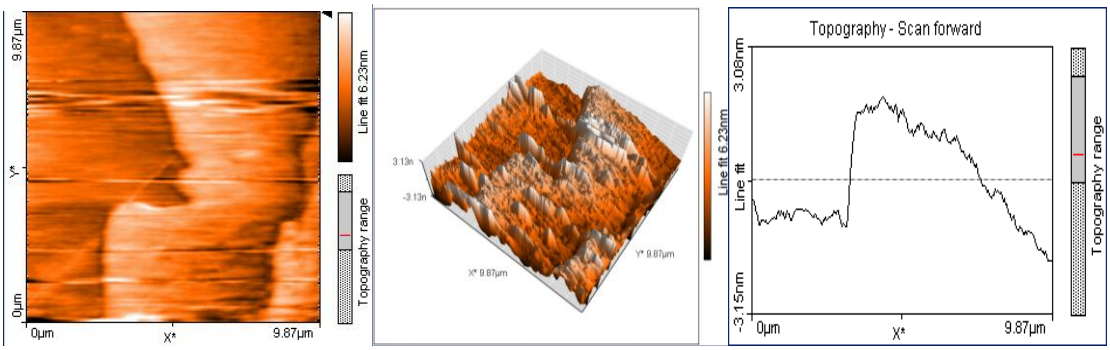

(a) (b) (c)

Figure 5.6 AFM image of the choesterol crystal step

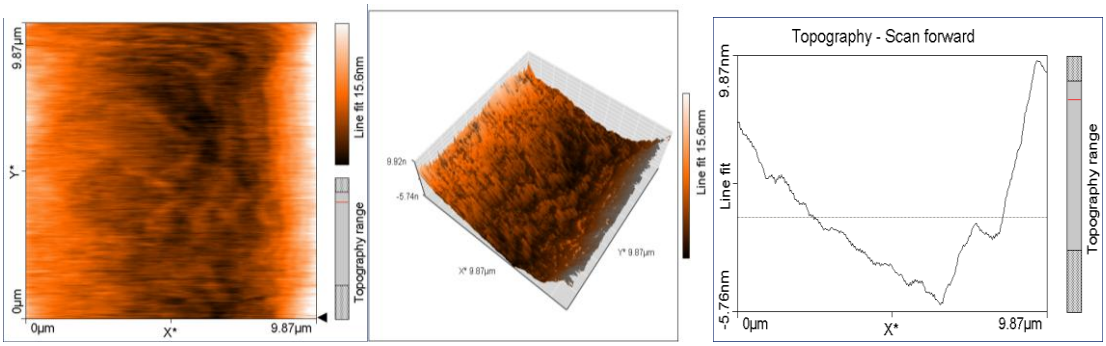

(a) (b) (c)

Figure 5.7 AFM image of observed well in cholesterol crystal

Figures 5.7 (a, b) shows a flat region or valley region between two steps. The depth profiling indicated the depth of the valley region as -11.25 nm. Most crystal surfaces have several large regions that are relatively flat over several micrometers and also display molecular level layer and step feature. Surface features correspond to the bi-layer step height and suggests the gross surface reconstructions [42].

5.6 FT – IR Spectrum of Cholesterol crystals

Most of organic compound shows absorptions in mid – infrared region, which extends from 400 cm^{-1} to 4000 cm^{-1}. Details of the FT-IR technique are previously discussed in chapter II.

Figure 5.8 shows the FT – IR spectrum of cholesterol crystals. The absorption occurring at 3430.5 cm^{-1} is due to O – H stretching, the absorption at 2939.9 cm^{-1} is due to C – H stretching, the absorptions at 1462.1 cm^{-1} and 1373.1 cm^{-1} are assigned to C – H bending vibration and the absorptions at 1187.7 cm^{-1}, 1123.0 cm^{-1} and 1054.5 cm^{-1} are due to C – O stretching vibrations of esters

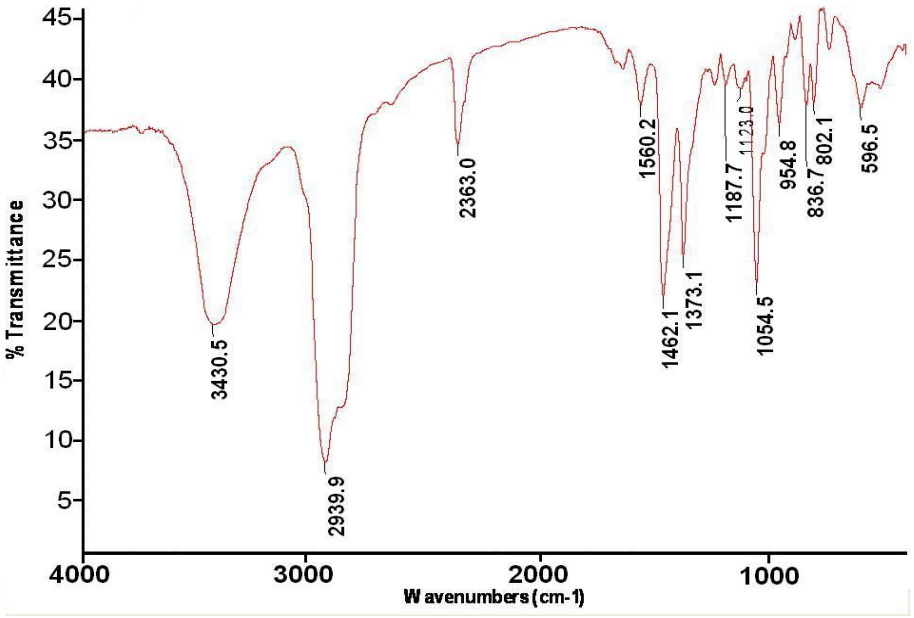

Figure 5.8 FT – IR spectrum of cholesterol crystals

and the absorptions occurring at 954.8 cm^{-1}, 836.7 cm^{-1}, 802.1 cm^{-1} and 596.5 cm^{-1} are attributed to aromatic substitution The observed wavenumbers and proposed assignments are found in good agreement with reported [44,45].

5.7 Thermal Study of Cholesterol Crystals

The thermal studies, such as TGA, DTA and DSC of powdered samples of cholesterol was carried out using Linseis Simultaneous Thermal Analyzer (STA) PT-1600, in the atmosphere of air from 25 °C to 900 °C at a heating rate of 15 °C/min using α-Al_2O_3 as standard reference. Details of the techniques used for the thermal study are elaborately discussed in chapter II.

Figure 5.9 shows the TG – DTA of cholesterol crystals grown from acetone solution. A minor weight loss occurs around 140 ^oC which is similar to that of observed by Kalkura and Devanarayana [34] . This is also confirmed from the DTA curve in terms of a minor endothermic peak at 143.3 ^oC,

corresponding to the melting of the cholesterol. The melting point of cholesterol is 148.5 ^{o}C [46]. From the DSC curve different thermodynamic parameters are calculated. For the endothermic peak at 143.3 ^{o}C, the enthalpy, the heat capacity and the heat change are -42.6546 J/g, 0.6408 J/gK and -43.8304 µVs/mg , respectively. From the TG curves one finds that Cholesterol starts decomposing from 240 ^{o}C onwards. The DTA curve indicates another endothermic peak observed at 401.4 ^{o}C, which corresponds to complete decomposition of the substance. The values thermodynamic parameter obtained from DSC curve for this endothermic peak are enthalpy -1131.197 J/g, heat capacity 0.2118 J/gK and heat change -395.1908 µVs/mg. After the decomposition, two exothermic reactions are observed at 480 ^{o}C and 532.9 ^{o}C, respectively, which may be due to reaction between two gaseous products.

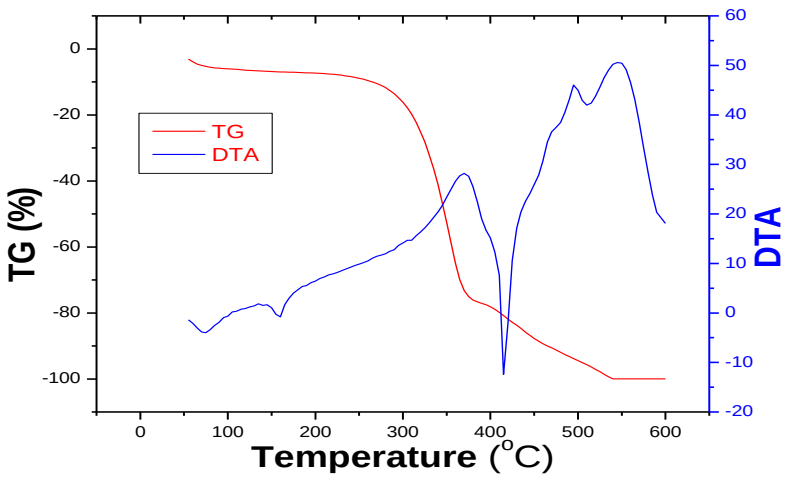

Figure 5.9 TG – DTA of cholesterol crystals

The thermodynamic parameters from DSC are also calculated for these reactions, which are enthalpy 68.7289 J/g, heat capacity 1.7218 J/gK and heat change 38.2542 µVs/mg and enthalpy 1616.013 J/g, heat capacity

24.5955 J/gK and heat change 422.6913 μVs/mg, respectively. These reults correspond to the results obtained by Kalkura and Devanarayana [34].

5.8 Kinetic Parameters of Cholesterol Crystal Decomposition

The kinetic parameters of cholesterol crystal were evaluated from the TG curve by applying Coats and Redfern relation [47] as already discussed in chapter III. Figure 5.10 illustrate the Coats and Redfern plot. Table 5.1 shows the calculated Kinetic parameters of cholesterol crystal.

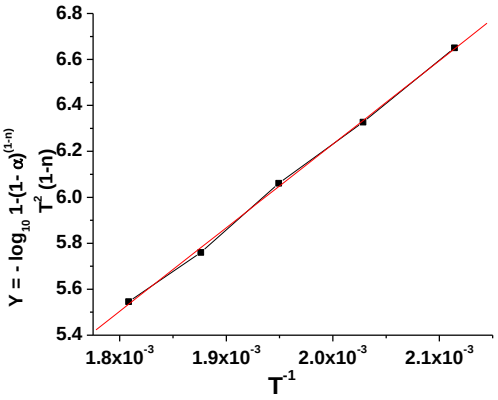

Figure 5.10 Plot of Coats – Redfern relation for cholesterol crystal

Table 5.1 Kinetic parameters of cholesterol crystal

Sample	Kinetic Parameters
Cholesterol crystals	Order of reaction (n) = 0
	Activation energy (E) = 69.59 $kJK^{-1}Mol^{-1}$
	Frequency factor (A) = 1.23×10^{20}

5.9 Thermodynamic Parameters of Cholesterol Crystal

Various thermodynamic parameters such as standard entropy of activation $\Delta^{\#}S°$, standard enthalpy of activation $\Delta^{\#}H°$, standard Gibbs energy

of activation $\Delta^{\#}G°$ and standard internal energy of activation $\Delta^{\#}U°$ were calculated by applying well known formulae, as described in detail by Laidler [48] and mentioned in chapter III. Table 5.2 gives the values of thermodynamic parameters of decomposition.

Table 5.2 Thermodynamic Parameters of Cholesterol Crystal

Sample	Thermodynamic Parameters
Cholesterol crystals	Standard Entropy $\Delta^{\#} S° = 135.25\ Jkmol^{-1}$
	Standard Enthalpy $\Delta^{\#} H° = 61.06\ kJmol^{-1}$
	Standard Gibbs free energy $\Delta^{\#} G° = -69.32\ kJmol^{-1}$
	Standard change in internal energy $\Delta^{\#} U° = 65.33\ kJmol^{-1}$

The positive values of $\Delta^{\#} S°$ and $\Delta^{\#} H°$ and negative values of $\Delta^{\#} G°$ suggest spontaneous nature at high temperature of the reaction taking place.

5.10 Dielectric Study

The dielectric response of biomolecules is a property of fundamental importance in biochemistry and biophysics. The dielectric constant inversely scales the strength of electrostatic interactions that play a crucial role in the formation, stability and function of nucleic acid, proteins, peptides, biological membranes and lipid bilayers [49]. Cholesterol is a poor conductor of heat and electricity, since it has high dielectric constant. It is present in abundance in nervous tissues. It appears that cholesterol function as an insulating cover for the transmission of electrical impulses in the nervous tissue; therefore, an attempt is made to study the dielectric properties at different frequency of applied field. Cholesterol has one hydroxyl group at C_3 and double bond between C_5 and C_6. An 8 carbon aliphatic side chain is attached to C_{17}.

Cholesterol contains total 5 methyl groups. Due to the presence of an – OH group, cholesterol is weakly amphiphilic. As a structural component of plasma membranes, cholesterol is an important determinant of membrane permeability properties. Cholesterol performs several other biochemical functions which include its role in membrane structure and function, in the synthesis of bile acids, hormones and vitamin D. [4]. Therefore, an attempt is made to study the dielectric properties of cholesterol.

The dielectric studies of pelletized cholesterol was carried out in the 50 Hz – 5 MHz frequency range. Figure 5.11 shows the variation of dielectric constant with frequency. The value of dielectric constant decreases as frequency increases. The high value dielectric constant in the low frequency region may be due to the contributions from all four polarizations namely, electronic, ionic, orientational and space charge polarizations [50].

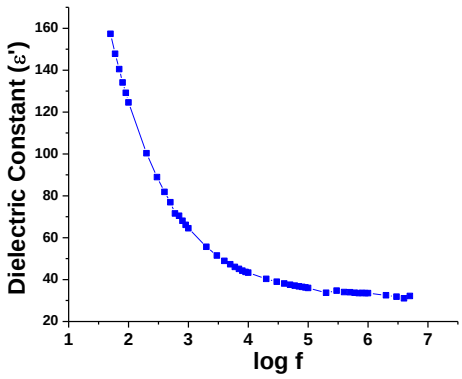

Figure 5.11 Plot of Dielectric constant versus log f

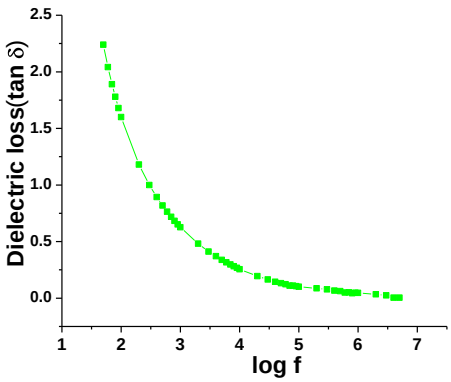

Figure 5.12 Plot of Dielectric loss versus log f

The electronic exchange of the number of ions in the crystals gives local displacement of electron in the direction of the applied field, which inturn gives rise to polarization. As the frequency of applied field increases a point

will be reached where the space charge can not sustain and comply with the external varying field and hence exhibiting the diminishing values of dielectric constant.

Continuous and gradual decrease in dielectric constant suggests that cholesterol crystals like any normal dielectric may possess domains of different size and varying relaxation times [51]. Figure 5.12 shows the variation of dielectric loss with frequency of applied field. The behaviour of variation is similar to that of dielectric constant with frequency. The dielectric loss is a measure of energy absorbed by material. The variation of a. c. conductivity σ_{ac} with frequency shows that it increases as the frequency increases and the opposite nature is observed for a. c. resistivity as shown in figure 5.13. Recently, a.c. conductivity and dielectric measurements of bulk pyronine G (Y) is reported by Yaghmour [52], the author observed that the dielectric constant and the dielectric loss decreased by increasing frequency and the a.c. conductivity was due to the correlated barrier hopping. Usually, typical current carriers in organic solids are through π – conjugated systems and the electrons can move via π – electron cloud, especially, by hopping, tunneling and other related mechanisms.

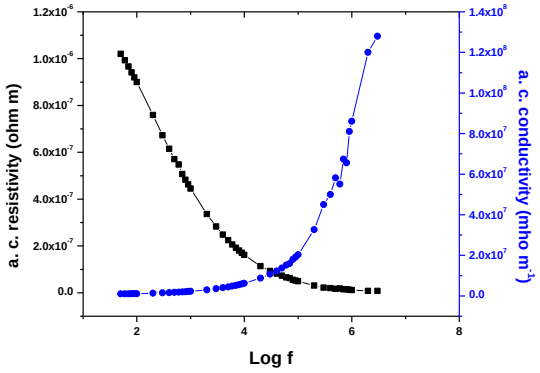

Figure 5.13 Pot of a.c.resistivity and a.c.conductivity versus log f

5.11 Synthesis of Cholesterol nano particles

Low Density Lipoprotein (LDL) is the main carrier of cholesterol in the plasma. Novel approaches have been proposed for cancer treatment based on lipid emulsions (LDE) [53] and nano emulsions [54]. The nano emulsion is composed of a core of cholesterol esters and residual amounts of triglycerides surrounded by a monolayer of phosphatidylcholine with free cholesterol. The LDE and nano emulsions are expected to bind to the LDL receptor. As LDL receptors are up – regulated in cancer cells [55], the association of chemotherapeutic agent with LDE and nano emulsion would concentrate the agent in the neoplastic tissue after the intravenous injection of the complex. In this manner, the delivery of drug to the tumor could be increased while the tissues and organs would be less damaged by the chemotherapy [54-56]. The nano-emulsion thus can serve as a vehicle to direct chemotherapeutic agents against tumors and decrease the toxicity and increase the anti-tumoral action of the drugs [56], for example, in breast carcinoma the nano emulsion concentrates roughly five times more in tumor than in normal contralateral mammary tissues [57] and in the case of ovarian caricinomas it is eight times [58]. As noted earlier in section 5.2 of this chapter, the emulsion formed by bile salts and the micelles play important role in cholesterol absorption, it is appropriate to investigate this in detail by selecting suitable micro emulsion systems.

Earlier organic nano particles such as cholesterol, rhovanile and rhodiarome were synthesized by different micro emulsions, such as AOT/Heptane/Water; Triton/Decanol/Water; CTAB/Hexanol/Water [59,60]. Altogether, a hypothesis of formation of nano particles in water/oil micro

emulsion has been proposed by Debuigne *et al.* [59]. In the micro emulsion, the effect of various parameters on the synthesis of organic nano – particles has also been discussed by the same authors, which are summarized as follows:

(1) The influence of factor R = [H_2O/AOT]

(2) The influence of concentration of organic compound.

(3) The influence of volume of solution and vessel geometry.

(4) The influence of mixture of two micro emulsions.

(5) The influence of addition of organic compound.

(6) The influence of time after injection of organic solution in the micro emulsion.

(7) The influence of equipments used for stirring the solution.

(8) The influence of quantity of organic compound in the micro emulsion without phase separation.

However, no attempt was made by earlier workers to characterize cholesterol nano particles and compare their properties with bulk crystalline material. Looking at various therapeutic applications, the present author has synthesized cholesterol nano particles by triton – 100/water/ n – butyl alcohol microemulsion and characterized by various techniques.

5.12 Synthesis of nano particles

The mixture of Triton X – 100/water/n- butyl alcohol was used for the synthesis of nano particles of cholesterol. Single phase region was identified by the mixture of all this three solutions in an appropriate manner. Amount of surfactant was decided as the molar ratio R remains six. Details of single

phase region in the phase diagram have been discussed in chapter I. The solution of Cholesterol made in chloroform was added into this mixture in drop – wise manner with continuous stirring. After 15 – 20 min. nano particles were formed at the liquid – liquid interface of the solution, which was filtered out by using Whatman filter paper no. 42. The yield of synthesized nano particles was around 60%.

5.13 Powder XRD study

Figure 5.14 shows the powder XRD pattern of cholesterol nano particles. The peak broadening in the powder XRD pattern confirms that the synthesized particles were nano structured in nature. Cholesterol nano particles show triclinic crystal system with estimated unit cell parameters as, a = 14.234 Å, b = 34.209 Å, c = 10.481 Å, α = 94. 60°, β = 90.00° and γ = 95.72°, which corresponds to the bulk crystalline one.

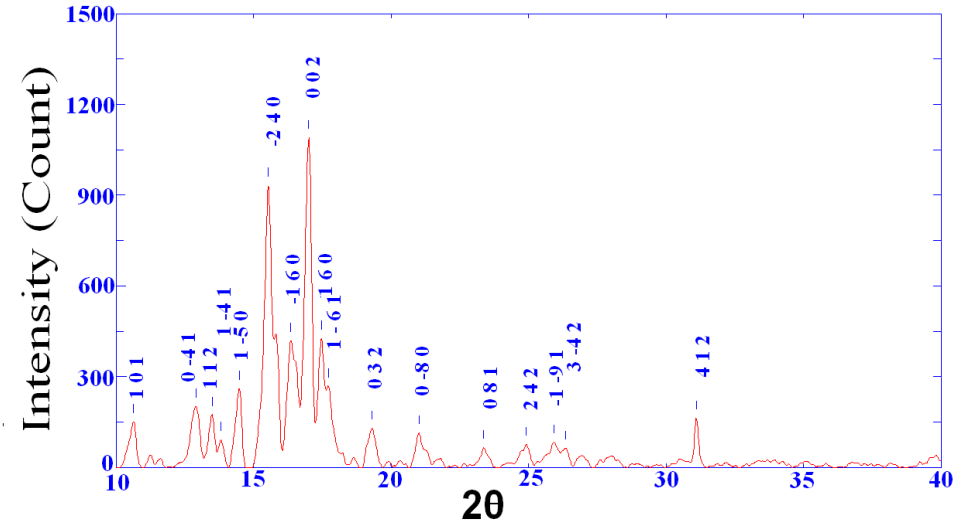

Figure 5.14 Powder XRD pattern of cholesterol nano particles

The average particle size of cholesterol nano particles was determined from the powder XRD pattern by employing the Scherrer's formula as discuss in chapter III. From the Scherrer's formula, the average particle size of cholesterol nano particles was found to be 22 nm.

5.14 TEM study of cholesterol nano particles

The TEM study was carried out to determine the size and morphology of the synthesized cholesterol nano – particles. The TEM images of the cholesterol nano particles are shown in figure 5.15. TEM images suggest that the agglomerated cholesterol nano particles were having nearly spherical morphology and the size varied from 15 – 31 nm. The possible mechanism for obtaining different size of nano particles is discussed hereby. The micro emulsion is expected to tolerate a minimum quantity of cholesterol molecules in order to form nano particles without phase separation. At initial stage the microemulsion is expected to remain thermodynamically stable. If the number of cholesterol molecules per aqueous core increases then the interaction with surfactant molecules increases at the interface. Therefore, the number of cholesterol molecules per aqueous core is larger and the interaction between these and surfactant molecules are also larger at the water – alcohol interface. The optimal radius of curvature is then disturbed and the phase separation occurs more readily for specific molar ratio (R) factor. As the cholesterol molecules come into contact with aqueous core, the nuclei formation takes place due to the insolubility of cholesterol in water. Then the nano particles later on grow to a certain favored size and stabilized in the same manner with surfactants in spite of their presence in both immiscible

phases. The stirring of the micro-emulsion during synthesis also plays important role.

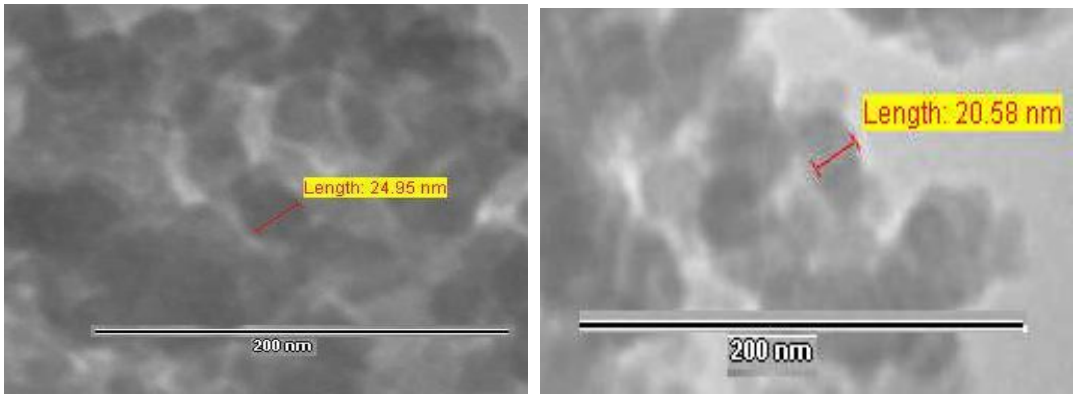

(a) (b)

Figure 5.15 TEM micrographs of cholesterol nano particles

Different parameters have been calculated for the formation of cholesterol nano particles by using the approach proposed by Destree *et al* [61].

The volume of the water core has been calculated by using the following formula,

$$V_{wc} = \frac{4}{3}\pi r_{wc}^{3} \quad \text{..... (5.2)}$$

Where, r_{wc} = Radius of water core in nm [63], which is estimated as

$$r_{wc} = 0.18\,R + 0.45 \quad \text{…. (5.3)}$$

Where, R = Molar Ratio

In the present study, for the value of R = 4, and the radius of water core was found to be 1.17 nm and the volume of the water core was estimated to be 6.54 nm^3.

The Number of water cores is obtained from the following expression,

$$N_{wc} = \frac{V_t}{V_{wc}} \quad \text{.... (5.4)}$$

Where, V_t = total amount of water; V_{wc} = Volume of the water core,

In this calculation, the amount of water in the organic phase and in the surfactant layer is neglected.

The volume of nanoparticle calculated from the TEM data is,

$$V_{np} = \frac{4}{3}\pi r_{np}^3 \quad \text{.... (5.5)}$$

Considering the average value of radius of nano-particles as 23 nm, the volume of nano particles was found to be 50939.17nm^3.

If it is assumed that the density of nanoparticles is equivalent to that of macroscopic material, the mass of single nanoparticle of cholesterol is calculated as follows,

$$m_{np} = V_{np} d \quad \text{.... (5.6)}$$

Where, d = density of the cholesterol

The mass of single nano particle was estimated to be 5.34×10^{-24} g.

The number of nanoparticles is given by,

$$N_{np} = \frac{m_t}{m_{np}} \quad . \quad \ldots (5.7)$$

Where m_t = total mass of the active principle introduced in to microemulsion.

The number of nanoparticles per water core can be calculated by,

$$N_{np/wc} = \frac{N_{np}}{N_{wc}} \quad . \quad \ldots (5.8)$$

The calculation suggests that the number of cholesterol nanoparticles per water core is 0.22. It also suggests that certain water cores might be empty. As per earlier estimation for the number of cholesterol nanoparticles per water core is 0.05 [61].

5.15 Dynamic Light Scattering (DLS) study of Cholesterol nano particles

Cholesterol nano particles were dispersed in double distilled water and DLS study was carried out. Figure 5.16 shows the histogram of the particle size distribution and Table 5.3 shows the percentile value of each nanoparticle.

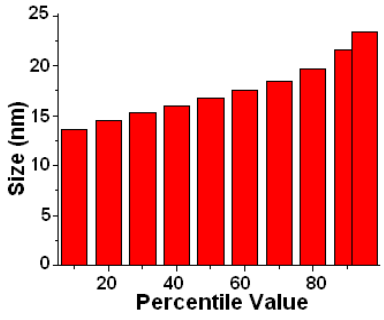

Figure 5.16 Histogram of particle size distribution by DLS particle size measurement

Table 5.3 Particle Size distribution by DLS study

Percentile (%)	Size (nm)
10.00	13.61
20.00	14.49
30.00	15.26
40.00	15.99
50.00	16.73
60.00	17.53
70.00	18.47
80.00	19.69
90.00	21.56
95.00	23.40

The DLS study results correspond to the results of particle size obtained by TEM and powder XRD studies.

5.16 FT – IR Spectral study of Cholesterol Nano particles

FT – IR spectrum of cholesterol nano particles are shown in figure 5.17. The analysis of spectrum suggests that the absorption occurring at 3432.4 cm^{-1} is due to O – H stretching vibrations, the absorptions occurring at 2933.6 cm^{-1} and 2866.7 cm^{-1} are due to C – H stretching vibrations, the absorptions at 1466.1 cm^{-1} and 1372.5 cm^{-1} are assigned to C – H bending vibration

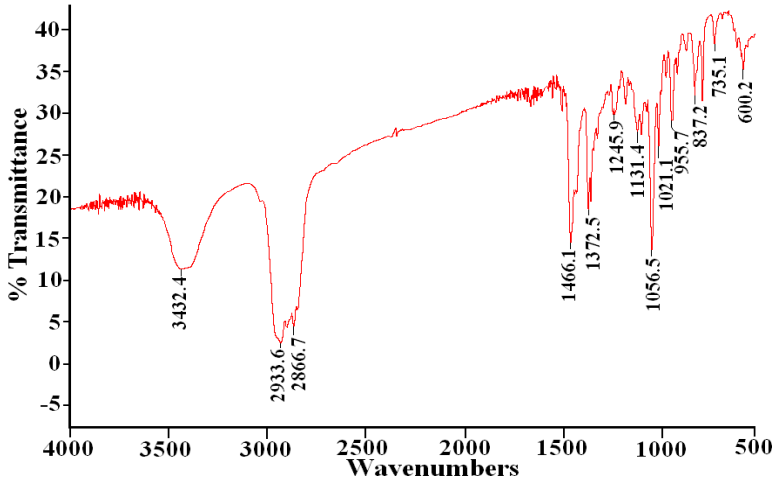

Figure 5.17 FT – IR Spectra of cholesterol nano particles

and the absorptions at 1245.9 cm^{-1}, 1131.4 cm^{-1}, 1056.5 cm^{-1} and 1021.1 cm^{-1} are due to C – O stretching vibrations of esters and the absorptions at 955.7 cm^{-1} , 837.2 cm^{-1}, 735.1 cm^{-1} and 600.2 cm^{-1} are attributed to aromatic substitution.

By comparing the FT – IR spectra of cholesterol crystals with nano particles, it can be noticed that no major changes are observed. Very small changes are observed from 1200 cm^{-1} to 590 cm^{-1}. However, they cannot firmly be attributed to the nano structured nature.

5.17 Thermal Study

Thermal studies like TG, DTA and DSC were carried out on cholesterol nano particles. Figure 5.18 shows the TG – DTA curves of cholesterol nano particles. The TG plot shows that nano particles remain stable up to 260.5 ^{o}C and then it starts decomposing rapidly up to 389.4 ^{o}C and beyond that they decompose slowly up to 580.1 ^{o}C, where almost complete decomposition is observed. The DTA plot indicates that the decomposition process of cholesterol nano particles occurs through two endothermic reactions at 146.4 ^{o}C and at 393.1 ^{o}C, respectively. From the DSC plot several thermodynamic parameters were calculated by using software TA available with the set up. For the endothermic reaction at 146.4 ^{o}C the enthalpy and the change in heat capacity are calculated and found to be -51772.4 J/kg and 663.0 J/kgK, respectively. This may be due to some phase change occurring without significant breaking of the bonds resulting into marginal weight loss, which may be due to melting of the sample.

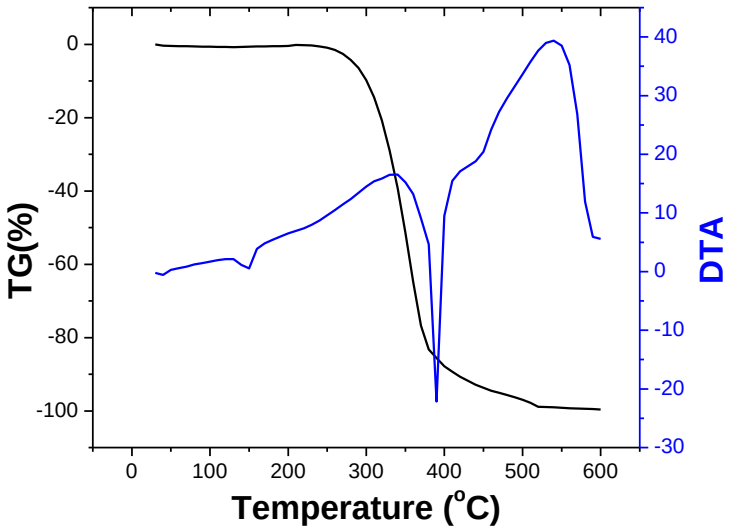

Figure 5.18 TG – DTA of cholesterol nano particles

The melting point of cholesterol is 148.5 ^{o}C [46]. Another endothermic reaction occurring at 393.1 ^{o}C, values of the enthalpy and the change in heat capacity are found to be - 1138699 J/kg and 640.8 J/kgK, respectively.

By comparing the TG plot of nano particles of cholesterol with the TG plot of crystalline material, one observes that the nano particles are little more thermally stable than the crystalline material. This may be due to the higher surface to volume ratio and higher surface energy giving slightly more thermal stability.

5.18 Kinetic Parameters of Cholesterol Nano Particles

Kinetic parameters of decomposition of cholesterol nano particles were calculated by using Coats – Redfern relation [47] as discussed in chapter III. Figure 5.19 shows the Coats – Redfern plot and table 5.4 shows the values of kinetic parameters calculated from the plot for cholesterol nano particles.

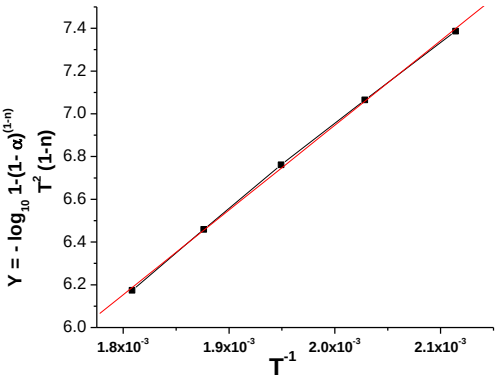

Figure 5.19 Coats – Redfern plot of cholesterol nano particles

As the activation energy (E) is considered as a barrier to be surmounted to form reaction products [63], the higher value of activation energy for nano particles suggest slower reaction rate for thermal decomposition and hence more thermal stability.

Table 5.4 Kinetic parameters of cholesterol nano particles

Sample	Kinetic Parameters
Cholesterol nano particles	Order of reaction (n) = 0
	Activation Energy (E) = 75.87 $kJK^{-1}Mol^{-1}$
	Frequency factor (A) = 1.00×10^{23}

5.19 Thermodynamic Parameters of Cholesterol Nano Particles

Various thermodynamic parameters such as standard entropy of activation $\Delta^{\#}S°$, standard enthalpy of activation $\Delta^{\#}H°$, standard Gibbs energy of activation $\Delta^{\#}G°$ and standard internal energy of activation $\Delta^{\#}U°$ were calculated by applying well known formulae, as described in detail by Laidler

[48]. Table 5.5 gives the value of various thermodynamic parameters calculated for cholesterol nano particles at 300 ^{o}C.

The positive value of $\Delta^{\#}$ S° and negative value of $\Delta^{\#}$ G° indicates spontaneous reaction at higher temperature. By comparing the various kinetic and thermodynamic parameters of crystalline cholesterol and nano particles of cholesterol of tables 5.2 and 5.5, one finds that the values of these parameters are higher for the nano particles than the crystalline sample, which also confirms that the nano particles are higher in thermal stability than bulk crystalline cholesterol samples.

Table 5.5 Thermodynamic parameters of cholesterol nano particles

Sample	Thermodynamic Parameters
Cholesterol nano particles	Standard Entropy $\Delta^{\#}$ S° = 190.95 Jkmol^{-1}
	Standard Enthalpy $\Delta^{\#}$ H° = 67.35 kJmol $^{-1}$
	Standard Gibbs free energy $\Delta^{\#}$ G°= - 30.61 kJmol $^{-1}$
	Standard change in internal energy $\Delta^{\#}$ U° = 71.61 kJmol $^{-1}$

5.20 Dielectric Study

Dielectric study could not be performed because the nano particles sample could not be pelletized in a conventional way to carry out dielectric study. Any organic popular binder, like alcohols or acetone, could not be used because of nano particle samples were having high solubility and water made it highly dispersed colloidal paste. The sample could not be pelletized without using any binder; therefore, the dielectric study was not performed on cholesterol nano particles.

5.21 Conclusions

(1) Cholesterol crystals were grown by using single diffusion gel growth technique.

(2) The grown cholesterol crystals were very thin and had stepped surface with maximum dimension of 35 mm × 5 mm.

(3) The powder XRD studies confirmed the structural identity of the grown cholesterol crystals. Cholesterol crystallized in triclinic system with unit cell parameters as, a = 14.234 Å b= 34.086 Å, c = 10.481 Å, α = 94.70^{o}, β = 90.00^{o}, γ = 95.72^{o}.

(4) The SEM image of cholesterol crystals suggest the presence of steps on the surface of crystals and this steps were expected to play a major role in the growth of crystals.

(5) The AFM images were taken on (0 0 1) face of platelet type of crystal, to measure the height and roughness of the steps. AFM images showed that the steps were not smooth but with some roughness might be due to the presence of kinks. The kinks and steps were assumed to be important for growth as per the Kossel's model for crystal growth. The valley region between two steps was identified.

(6) FT – IR spectrum of cholesterol crystals revealed the presence of functional groups and confirmed the presence of O – H stretching, C – H stretching, C – H bending, C – O stretching and aromatic ring substitution.

(7) From TG curve it was found that the crystalline sample remained stable up to 240 ^{o}C. DTA plot showed two endothermc reactions at 143.3 ^{o}C and 401.4

^{o}C and two exothermic reactions at 480 ^{o}C and 532.9 ^{o}C. Various thermal parameters were calculated from the DSC curve.

(8) By applying the Coats and Redfern relation to the decomposition stage the value of kinetic parameters were calculated at 300 ^{o}C. The values of order of reaction *(n)*, activation energy *(E)* and frequency factor *(A)* were found to be 0, 69.59 $kJK^{-1}Mol^{-1}$ and 1.23×10^{20}, respectively.

(9) The thermodynamic parameters for the decomposition process were also evaluated at 300 ^{o}C. The value of standard entropy, standard enthalpy, standard Gibbs energy and standard change in internal energy of activation were found to be, 135. 25 $Jkmol^{-1}$, 61. 06 $kJmol^{-1}$, - 69.32 $kJmol^{-1}$ and 65.33 $kJmol^{-1}$, respectively. The positive values of standard entropy and standard enthalpy and the negative value of standard Gibbs free energy suggested the spontaneous reaction at higher temperature.

(10) The dielectric constant and the dielectric loss decreased as the frequency increased. As the frequency increased the a. c. conductivity increased while a. c. resistivity decreased.

(11) The nano particles of cholesterol were synthesized by using w/o microemulsion technique with the mixture of water/ triton X – 100/ n – butanol.

(12) Broadening in the Powder XRD pattern confirmed nano structured nature of the material. Cholesterol nano particles showed Triclinic crystal system with unit cell parameters as, a = 14.234 Å, b = 34.209 Å, c = 10.481 Å, α = 94. 60°, β = 90.00°and γ = 95.72°, which were identical to the crystalline cholesterol.

(13) The average particle size of the cholesterol nanoparticles was calculated by using Scherrer's formula to a particular reflection in powder XRD pattern and it was found around 22 nm.

(13) From TEM it was found that the cholesterol nano particles were having nearly spherical morphology with sizes varied from 15 nm – 31 nm. From the calculation it was found that 0.22 cholesterol nano particle per water core was available, which indicated there were some empty water cores also.

(14) Dynamic Light Scattering (DLS) study gave the particle size distribution from 13 nm – 23 nm.

(15) The FT – IR spectrum of cholesterol nano particles showed the same absorptions as shown in crystalline material. There was no inclusion or presence of any extra bonding in terms of presence of adsorbed surfactant or oil phase. No conclusive effect was noted in FT – IR spectrum due to the nano structured nature.

(16) TG of cholesterol nano particles suggested that the sample remained almost stable up to 260.5 ^{o}C, thereafter, it decomposed rapidly and up to 580.1 ^{o}C the complete decomposition took place. DTA showed two endothermal reactions taking place at 146.4 ^{o}C and 393.1 ^{o}C. DSC gave the entropy and heat capacity change of these endothermic and exothermic reactions.

(16) Kinetic parameters of the cholesterol nanoparticles were calculated by Coats – Redfern formula. It was found that the order of reaction *(n)*, activation energy *(E)* and frequency factor *(A)* were estimated as 0, 75.87 kJK^{-1}Mol^{-1}and

1.00×10^{23}, respectively. With comparison to the crystalline sample the higher value of activation energy suggested that the nano particle sample was thermally little more stable than the crystalline sample.

(17) The thermodynamic parameters for the decomposition process were also evaluated at 300 ^{o}C. The values of standard entropy, standard enthalpy, standard Gibbs free energy and standard change in internal energy of activation were found to be, 190.95 Jkmol^{-1}, 67.35 kJmol $^{-1}$, - 30.61kJmol $^{-1}$ and 71.61 kJmol $^{-1}$, respectively. These values were higher than those for the crystalline sample, which indicated the stable nature of nano particles with comparison to crystalline material. Also, it confirmed the spontaneous reaction at higher temperature.

References

[1] F. Bischoff, R. E. Katherman, *Am. J. Physiol.,* **152** (1948) 189.

[2] P. Ehwall, M. Mandell, *Acta Chem. Scand.,* **15** (1961) 1404.

[3] S. P. Wrenn, *Engineering Approaches to Cholesterol – linked Diseases*, Chemical Engineering, (2001).

[4] U. Satyanarayana, U. Chakrapani, *Biochemistry,* Books & Allied, Kolkata, (2000).

[5] H. R. Waterham, *FEBS Letts.,* **580** (2006) 5442.

[6] O. G. Mouritsen, M. J. Zukermann, *Lipids,* **39** (2004) 1103.

[7] L. L. Smith, *Free. Radic. Biol. Med.*, **11** (1991) 47.

[8] A. C. Guyton, *Textbook of Medical Physiology*, W. B. Saunders Co., USA (1981).

[9] S. Wu, F. De Luca, *The J. of Bio. Chem.*, **279** (2004) 4642.

[10] M. Bourges, D. M. Small, D. M. Dervichian, *Biochem. Biophys. Acta*, **137** (1967) 157.

[11] D. M. Small, M. Bourges, D. G. Dervichian, *Nature*, **211** (1966) 816.

[12] M. Jirsa, A. K. Groen, *Frontiers in Biosci.*, **6** (2001) e154.

[13] F. M. Konikoff, J. M. Donovan, *Cholesterol Crystallization in Bile. In: Gall Bladder and Biliary Tract Diseases*. Eds: N. A. Afdhal, Marcel Dekker, New York, USA (2000).

[14] D. M. Small, *Arterioscler Thromb Vasc. Biol.*, **8** (1988) 103.

[15] G. S. Abela, K. Aziz, *Clin. Cardiol.*, **28** (2005) 413.

[16] G. S. Abela, K. Aziz, *Scanning*, **28** (2006) 1.

[17] B. Lundber, *Atherosclerosis*, **56** (1985) 93.

[18] G. S. Abela, *J. of Clin. Lipid.*, **4** (2010) 156.

[19] J. M. Dietschy, S. D. Turly, *J. Lipid Res.*, **45** (2004) 1375.

[20] G Snipe, U. Suter, *Cholesterol and Myelin, in Sub-cellular Biochemistry,* **28.** Ed. Plenum Press, New York, USA (1997).

[21] D. H. Mauch, K. Nägler, S. Schumacher, C. Göritz, E. C. Müller, A. Otto and F. W. Pfrieger, *Science*, **294** (2001) 1354.

[22] F. W. Pfrieger, *Biochim Biophys Acta.*, **10**, (2003) 271.

[23] http://www.mdc-berlin.de/en/news/archive/2001

[24] I. Björkhem, V. Leoni, S. Meaney, *J. Lipid Res.,* **51** (2010) 2889.

[25] B. B. Parekh, *Ph. D. Thesis,* Saurashtra University, Rajkot (2005).

[26] M. M. Zakharova, V. A. Nasonova, A. F. Konstantinova, V. S. Chudakov, R. V. Gainutdinov, *Crystallogr. Rep.*, **54** (2009) 509.

[27] J. W. Riordan, P. A. Dieppe, *Rheumatology*, **26** (1987) 430.

[28] M. B. Lazarevic , J. L. Skosey, J. Vitic, V. Mladenovic, B. L. Myones, J. Popovic, W. I. Swedler, *Semin Arthritis Rheum.,* **23** (1993) 99.

[29] N. Garti, L. Karpuj, S. Sarig, *Thermochim. Acta.*, **35** (1980) 343.

[30] N. Garti, L. Karpuj, S. Sarig, *J. Lipid Res.*, **22** (1981) 785.

[31] M. J. Whiting, J McK Watts, *J. Lipid Res.*, **24** (1983) 861.

[32] A. Elizabeth, C. Joseph, M. A. Ittyachen, *Bull. Mater. Sci.*, **24** (2001) 43.

[33] R. J. Galloway, S. A. Raza, R. D. Young, I. D. H. Oswald, *Cryst. Grow. & Des.*, **12** (2012) 231.

[34] S. N. Kalkura and S. Devanarayanan, *J. Mat. Sci. Lett.*, **5** (1986) 741.

[35] M. C. Frincu, S . D. Fleming, A. L. Rohl, J. A. Swift, *J. Am. Chem.Soc.*,**126**, (2004) 7915.

[36] N. Busch, N. Matiuck, S. Sahlin, S. P. Pillay, R. T. Holzbach, *J. Lipid. Res.,* **32** (1991) 695.

[37] N. Busch, F. Lammert, H. U. Marschall, S. Matern, *J. Clin. Invest.*, **96** (1995) 3015.

[38] N. R. Pattinson, K. E. Willis, *Gastroenterology*, **99** (1990) 1798.

[39] H. S. Sheih, L. G. Hoard, C. F. Nordman, *Act. Cryst. B*, **37** (1978) 1538.

[40] B. M. Craven, *Acta Crysta*, **B 35** (1979) 1123.

[41] M. S. Ammal, K. V. George, I. Jayakumari, *Cryst. Res. Technol.*, **42**, (2007) 876.

[42] R. S. Abendan, J. A. Swift, *Langmuir*, **18**, (2002) 4847.

[43] A. R. Verma, *Crystal Growth and Dislocations*, Butterworths, London, UK (1953)

[44] S. N. Kalkura, V. Ramakrishnan**,** S. Devanarayanan, *Infrared Phy.*, **27**, (1987) 335.

[45] N. T. Saraswathi, F. D. Gnonam, *J. Cryst. Growth*, **179**, (1997) 611.

[46] D. R. Lide, *CRC Handbook of Chemistry and Physics,* Taylor and Francis, Boca Raton, USA (2009)

[47] A. W. Coats, J. P. Redfern, *Nature*, **201** (1964) 68.

[48] K. J. Laidler, *Chemical Kinetics*, Harper and Row, New York, USA(1987).

[49] L. Yang, C. V. Valdeavella, H. D. Blatt and B. M. Pettitt, *Biophy. J.*, **71** (1996) 3022.

[50] N. V. Prasad, G. Prasad, T. Bhimasankaran, S. V. Suryanarayana, G. S. Kumar, *Ind. J. Pure Appl. Phy.*, **34** (1996) 639.

[51] K. D. Parikh, D. J. Dave, B. B. Parekh, M. J. Joshi, *Cryst. Res. Technol.*, **45** (2010) 603.

[52] S. J. Yaghmour, *Eur. Phys. J. Appl. Phys.*, **49** (2010) 10402.

[53] R. C. Maranhao, E. L. Garicochea Silva, P. Dorlhiac – Liacer, S. M. S. Cadena, I. J. C. Coelha, J. C. Meneghetti, F. J. C. Pileggi, D. A. F. Chamone, *Cancer. Res.,* **54** (1994) 4660.

[54] L. A. Pires, R. Hegg, C. J. Valduga, S. R. Graziani, D. G. Rodrigues, R. C. Maranhao, *Cancer Chemother. Pharmacol.,* **63** (2009) 281.

[55] Y. K. Ho, R. G. Smith, M. S. Brown, J. L. Goldstein*, Blood,* **52** (1978) 1099.

[56] R. C. Maranhao, S. R. Graziani, N. Yamaguchi, R. F. Melo, M. C. Latrilha, D. G. Rodrigues, R. D. Couto, S. Schreier, A. C. Buzaid, *Cancer Chemother. Pharmacol.,* **49** (2002) 487.

[57] S. R. Graziani, F. A. F. Igreja, R. Hegg, C. Meneghetti ,L. I. Brandizzi, R. Bardoza, R. F. Amancio, J. A. Pinotti, R. C. Maranhao, *Gynecol. Oncol*., **85** (2002) 493.

[58] A. Ades , J. P. Carvalho, S. R. Graziani, R. F. Amancio, J. S. Souen, J. A. Pinotti, R. C. Maranhao, *Gynecol. Oncol.,* **82** (2001) 25.

[59] F. Debuigne, L. Jeunieau, M. Wiame, J. B. Nagy, *Langmuir*, **16** (2000) 7605.

[60] C. Detsree, J. B. Nagy, *Adv. In Coll. And Intf. Sci.*, **123 – 126** (2006) 353.

[61] C. Destree, J. Ghijsen and J. B. Nagy, *Langmuir,* **23** (2007) 1965.

[62] J. Eastoe, B. H. Robinson, A. J. W. G. Visser, D. C. Steatler, *J. Chem. Soc.,* **67** (1991) 1899.

[63] R. S. Boikess and E. Edelson, Chemical Principles, Harper & Row, New York, USA (1978).

Chapter – VI

Growth Inhibition Study of Cholesterol Crystals

6.1. Introduction

The atherosclerotic plaques, as already discussed in chapter – V principally consist of lipids such as cholesterol, cholesteryl esters, phospholipids and triglycerides along with calcifications. Chemical analysis of advanced plaques has shown the presence of considerable amounts of free cholesterol, identified as cholesterol crystals. Cholesterol and its esters are important steroids, which are responsible for atherosclerosis and gallstones in human body. Cholesterol is an essential constituent of all animal cells, without it the cells of animals, humans too, will not function properly and the organism will die. This fatty substance is a life giving, life sustaining force. As potent as it is in maintaining the life, when it is in proper balance; on the other hand, it is equally threatening to life, when it is out of balance.

Cholesterol forms an integral part of the call membranes. As already noted in chapter – V the molecular structure of cholesterol is ideally suited to the cellular surroundings, as it consists of a hydroxyl group, that interact with the polar head group of the phospholipid, and a tetracyclic steroid body bonded to an eight carbon alkyl chain that interacts with the hydrophobic fatty acid chains of the phospholipids bilayer of the cell membrane. Once oriented within the membrane, one of the roles of cholesterol is to alter the physicochemical properties of the cell membrane by subtly altering the interactions of the surrounding fatty acid chains. Pure lipid layers posses a gel/liquid – crystal transition at elevated temperatures whereby the chains

"melt" and become less ordered. The addition of > 40 mol% cholesterol causes the disappearance of this phase transition, resulting in an "intermediary" structure that posse a bilayer thickness between that of the gel and liquid – crystal states [1,2]. Moreover, a study by carried out by Lund – Katz *et al.* [3].

Figures from the W.H.O. suggest that 4 billion people, or nearly 70 percent of the world's population, are users of herbal medicine for some purpose of primary health care. Medicinal herbs have always been in usage in some form or the other in indigenous systems of medicines including Ayurveda, Sidha and Unani in India. Expectations for the global market of the herbal medicine value was set to exceed US$ 26 Billion by 2011, in comparison to the 2006 total of US$ 19 Billion [4].

Medicinal plants and natural products have provided many serendipitous bedside observations. Research in genomics, proteomics and metabolomics has stimulated discovery of many new entities, which are yet to be pursued for their drug like activites. A new trans-disciplinary endeavor called Reverse Pharmacology (RP) has recently emerged and addresses both these needs [5]. RP is the science of integrating documented clinical/ experimental hits into leads by transdisciplinary exploratory studies and further developing these into drug candidates by experimental and clinical research [6]. RP designed as an academic discipline to reduce three major bottlenecks of costs, time and toxicity.

In the present chapter the growth inhibition of cholesterol crystals in the presence of extracts of *Fagonia Cretica* is discussed. In the growth Inhibition

study the growth of cholesterol crystals is carried out in the presence of inhibitors. In human body also the nutrients are constantly supplied for growth of crystals and inhibition of crystals growth is aimed to be achieved by providing suitable conditions due to inhibitors.

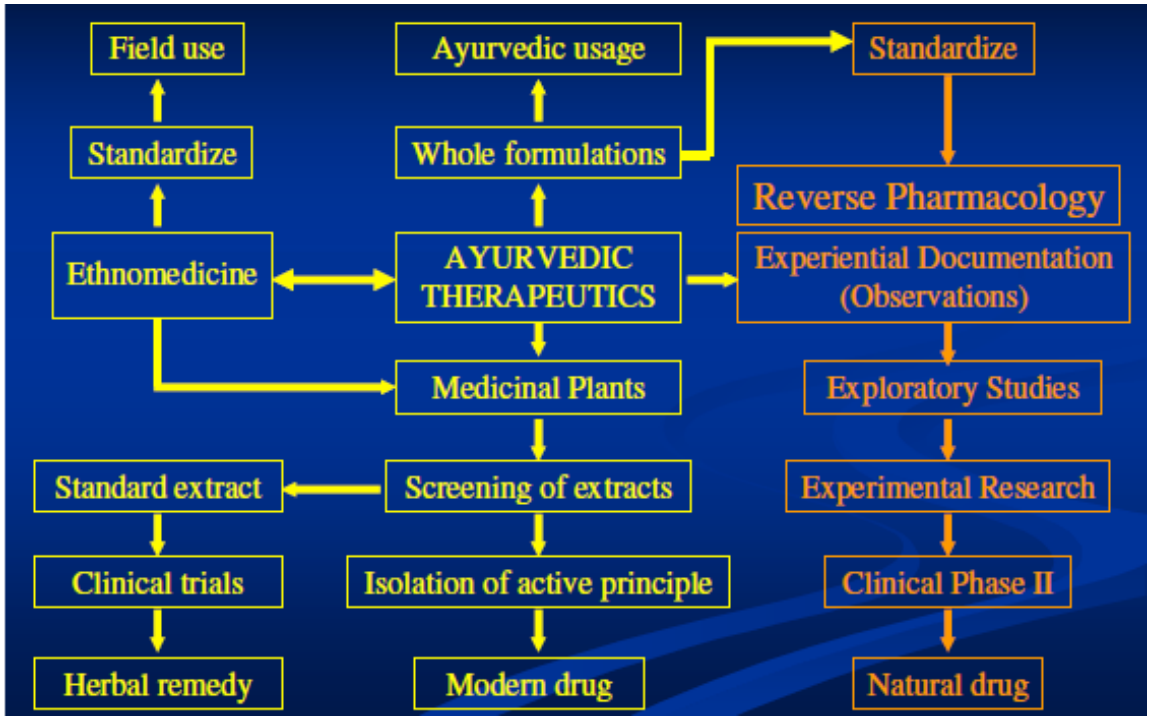

Figure 6.1 R & D paths for medicinal plants [7]

This differs largely from the gross dissolution where the crystal is placed in the solution and the dissolution is studied. The gel growth can mimic the growth occurring in body conditions and has been found to be the most suitable for *in vitro* growth inhibition studies [8]. The present growth inhibition study may prove to be an important mile stone in the path way of reverse pharmacology in terms of its contribution in screening of extracts, experimental studies, exploratory studies and experimental research as shown in chart of figure 6.1. The reason behind selecting *Fagonia cretica* for growth inhibition studies of cholesterol crystals is due to, apart from its

excellent phytochemical properties, its natural availability on the university campus of the present author.

6.2 Growth Inhibition Study

There are three types of compounds play important role in crystal formation, viz., inhibitors, promoters and complexers [9]. The presence of inhibitors inhibits the growth of crystals, whereas the promoters enhance the growth. But the complexers in general do not alter the growth. The action of compound depends on many factors such as type of crystalline substance, the crystalline plane under consideration, chemical reactivity, molecular fitting etc. However, certain substances form soluble complexes with the lattice ions of specific crystals and decrease the free ion activity of that ion and effectively decrease the state of saturation for that ion system.

Many studies, have focused on the role of inhibitors of crystal formation i.e. nucleation, crystal growth and aggregation. There are evidences to show that recurrent urinary stone formers may have deficiency of naturally occurring biliary inhibitors of crystal formation or will be having more promoters for the crystal growth [10 – 12]. In the early 1980s the evidence was given by several workers [13 - 15] that biliary proteins play important role in cholesterol crystallization. By combining lectin affinity and crystal growth assay [16] in a systematic study, various glycoprotein mixtures were separated from normal human bile, some of which primarily promote and others primarily inhibit crystallization [17,18]. The factors affecting cholesterol monohydrate crystal nucleation time in model systems of supersaturated bile are studied by Kibe *et al.* [19]. It has been found that the subgroup of lectin – bound biliary proteins

bind to cholesterol crystals, modify its morphology and inhibits the crystallization [20].

There are many reports that ayurvedic drugs (ingredients medicinal plants) are used for hypercholesterolaemia. *Allium sativum* (Garlic) possesses significant hypocholesterolemic and hypolipidaemic effects which are well proved in experimental and clinical trials [21]. Hypocholesterolemic action of *Acorus calamus* (Sweet Sedge), *Piper longum* (Pipali), *Zingiber officinale* (Ginger) along with *Piper retropractum* (Genus) and *Plumbago zeylanica* (Chitrak) has been well-proved experimentally [22].

Blood cholesterol can also be lowered by diet or drug therapy. Lipid lowering drug therapy is usually fully effective only when combined with dietary therapy [23]. If substances which raise the level of inhibitors could be introduced into the diets of the patients, the risk of future gall stone formation might be reduced. Dietary factors do play some role in gallstone formation but the evidence is not really strong enough to make specific recommendations [24].

In order to obtain experimental evidence of such inhibitors, experiments have been carried out to study the effect of some Indian medicinal plants on the crystallization of cholesterol in silica gel medium by solubility reduction technique. Ammal *et al.* [25] studied the effect of *Cassia fistua Linn* extract on the growth of cholesterol crystals. The change in cholesterol crystal morphology from plate like to needle like and wool like gave indication of inhibition of the crystals by some phyto-active compounds in the *Cassia fistua Linn.* Earlier study of growth inhibition of cholesterol

crystals by several medicinal plants was reported by Saraswathi and Gnanam [26].

Dietary guidelines for optimal health call for reducing the intake of cholesterol. One strategy for doing so involves plant sterols found in almost all the medicinal plants. Despite their structure similarity to cholesterol, minor isomeric difference and/or the presence of methyl and ethyl group in the side chain of the substance result in their poor absorption by the intestinal walls. Interestingly, although the plant sterols are not effectively absorbed by the body, they nonetheless are highly effective in blocking the absorption of cholesterol itself as reported by Garret *et al.* [27]

India has a very long history of safe and continuous usage of many herbal drugs in the officially recognized alternative system of heath viz., Ayurveda, Yoga Unani, Siddha, Homeopathy and Naturopathy. This has been reviewed by Vaidya and Devsagayam [28]. There are several books available on herbal medicinal plants [29 - 31]. Looking at the wealth of information available in literature on herbal medicinal plants, in the present author's laboratory, several predecessors have carried out extensive work on *in vitro* growth inhibition of various bio – mineral crystals and bio – crystals using various herbal extracts and fruit juices. These studies carried out by predecessors contributed significantly in identifying potent *in vitro* formulations, which are important miles stones in RP. The growth inhibition studies of urinary type crystals such as calcium oxalate monohydrate [32], calcium hydrogen phosphate dihydrate (CHPD - brushite) [33 – 35], struvite [36 – 38], crystals responsible for arthropathies such as hydroxyapatite [39],

monosodium urate monohydrate [40] and calcium pyrophosphate [41] have been carried out by using gel based technique.

6.3 Importance of *Fagonia Cretica L.*

6.3.1 Nomenclature and Plant Description

Fagonia Cretica L. also known as *Fagonia Arabica L.,* a member of the family *zygophyllaceae,* is a small spiny under shrub with stiff, more or less prostrate branches found in north-west India and Deccan.

Figure 6.2 *Fagonia Cretica L.* plant and flowers

Synonyms

Language	Name
Sanskrit	Duhsparśā, Durālambhā, Dhanvyāsakah, Virupā, Durālabhā, Utrabhaksyā
Bengali	Duralabha
English	Khorasan thorn
Gujarati	Dhamaaso
Hindi	Damahan, Dhamaasa, Hinguaa, Dhanhare
Malyalam	Kodittuva
Marathi	Dhamaasaa
Punjabi	Dama, Dhamah, Dhamaha
Tamil	Tulganari
Telugu	Chittigava, Gilaregati

This much – branched spiny undershrub is covered with glandular haird, 1,3 – foliolate leaves (opposite) having pairs of sharp stipular spines (often longer than leaves), leaflets linear sessile, the middle longest and small rose coloured flowers (petals double the number of sepals). The fruits are glandular, pubescent pyramidal 5- partite schizocarps enclosing flat compressed ovoid seeds. It is commonly found in dry places [42].

6.3.2 Chemical Composition

The upper part of this plant contains at least six saponins. Saponin A & B are based on nahagenin, saponin C based on 21 α, 22 β – dihydroxy nahagenin; two saponins on hederagenin and the last on oleanolic acid. Also present are diterpens fagonon, 16 – O – acetyl fagonone and 7β – fagonone, chinovic acid, ceryl alcohol, β – sitosterol, fagonin, fagogenin, betulin, oleanolic acid, compesterol, β – sitosterol, stigmasterol and alkaloid harmine. Flavonoids present are ternatin, herbacetin, gossypetin, 5,7,4 – trihydroxy 3,8,3 – trimethoxy flavones, kaempferol, 4 – ome kaempferol and isorhamnetin. Also present are phenolic acids such as p – hydroxybenzoic, vanillic syringic, p – coumaric, ferulic acids and other alkaloids [43 – 45]. Formulations of saponins obtained from *Fagonia cretica L.* are suggested as follows [46], where R = H and R = β – D – Glc depending upon the type of saponins.

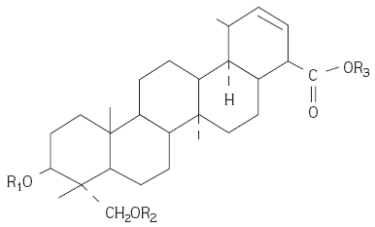

Figure 6.3 Structre of Saponin

6.3.3 Medicine Properties

The aqueous decoction of leaves and young twigs is a popular remedy for the treatment of skin lesions particularly amongst children. It is reputed in the indigenous system of medicine as a tonic, febrifuge and prophylactic against small pox [47]. *Fagonia cretica* alcoholic extracts found to have anti – cancer [48], anti – fungal [49] anti – inflammatory, analgesic and anti – microbial activity [50]. It is astringent, febrifuge and prophylactic against small – pox. The plant is bitter and used for the treatment of fever, thirst, vomiting, dysentery, asthma, urinary discharges, liver troubles, typhoid, toothache, stomach troubles and skin diseases [51]. It also shows good cytotoxic and antitumor potential [52].

6.4 Crystal Growth

Earlier attempts were made to grow cholesterol crystals by single diffusion gel growth technique by solubility reduction [25,26,53].

The single diffusion gel growth technique was used to study the growth and inhibition behavior of cholesterol crystals in the presence of *Fagonia* cretica *L.* extract. Sodium Metasilicate (SMS)-{$Na_2SiO_3.9H_2O$} solution of specific gravity 1.05 was used to prepare the gel. An aqueous solution of acetic acid of 1N concentration was mixed with the SMS solution in appropriate amount so that the pH value 5.0 could be set for the mixture. The gel solution of 20 mL was transferred into the test tubes of 140 mm length and 25 mm diameter. All test tubes and other glassware were autoclaved at 120°C for 15 min. Here, the silica gel was chosen because it remains stable and does not react with the reacting solutions or with the product crystal formed.

After the gelation took place, 20 mL supernatant solutions (SS) containing 1wt% cholesterol solution prepared in ethanol (i.e. control solution, without inhibitor) and 1 wt% cholesterol solution prepared in 1.0 % concentrations of herbal extract were gently poured on the set gel in the respective test tubes. This was done in the aseptic medium in a laminar flow hood to avoid microbial contaminations. After pouring SS, the test tubes were capped with airtight stopples. The experiment was conducted at the room temperature.

The apparent lengths of growing cholesterol crystals in each of the test tubes were measured by using a traveling microscope of least count 0.001 cm at regular time interval and photographed with the digital camera of 14 mega pixel. The apparent lengths of growing cholesterol crystals were measured and the mean length of crystals was calculated. The statistical analysis of the single factor ANOVA was carried out.

6.5 Preparation of Herbal Extract

The plant material was collected from the Saurashtra University Campus and also from Mangrol (Ghed) (Longitude – 70.14; Latitude – 21.18) in Saurashtra Region. The botanical identity of this plant was confirmed by Prof. Dr. Vrinda Thaker, Department of Biosciences, Saurashtra University, Rajkot.

The whole plant material was dried and a coarse powder was prepared. It was soaked in ethanol and kept for 48 hours with continuous shaking. After 48 hours it was filtered and the solvent was evaporated to get the concentrated extract. The ethanolic extract was syrupy in consistency and greenish in color.

6.6 Growth and Inhibition Study

There are several studies carried out focusing on the growth inhibition of cholesterol by herbal medicine or herbal extracts *in vitro.* Saraswathi and Gnanam [26] studied *in vitro* growth inhibition of cholesterol crystals using silica gel based growth technique and tested sevral Indian medicinal plants. They evaluated the growth inhibition in terms of number of grown crystals and size. They classified the inhibitory effect of medicinal plants as *Commiphora mughul* > *Aegle marmeleos* > *Cynoden dactylon* > *Musa paradisica* > *Polygalia javana* > *Alphinia officinarum* > *Solanum trilobatum* > *Enicostemma lyssopi folium.*

Das and Verma [54] used *Portulaca oleracea* (Kulfa), *Trianthema monogyha* (Pathri), *Lycoperiscon esculantum* (tomato) and *Vitis vinifera* (Grape) for dissolution of cholesterol in alcoholic solution of ursodeoxy cholic acid and chenodeoxy cholic acid and found that tomato was most effective for *in vitro* dissolution of cholesterol.

Altogether, using the same silica gel based growth technique, Ammal *et al.* [25] verified the growth inhibition of choelsterol crystals, in terms of average size and number of grown crystals, using ethanolic solution of *Cassia fistua linn.*

Moreover, a herb *Larrea tridentata,* used for traditional treatment of gallstones in Mexico, is effectively tested on cholesterol gall stones by Arteaga *et al.* [55]. Also, the effect of common dietry *Fenu greek* (Methi) seeds on biliary proteins that influence nucleation of cholesterol crystals in bile was studied [56].

As mentioned in section 6.4 that the growth inhibition of cholesterol crystals by alcoholic extract of *Fagonia cretica Linn* was carried out and the growth of crystals in the presence of extract and control solution was observed continuously. The dimensions of crystals were recorded and photographed at regular time intervals. From the series of photogrpahs of figure 6.4 one can observe clearly that the alcoholic extarct of *Fagonia cretica* inhibits the growth of crystals. The growth of cholesterol crystals occurs on the gel in the supernatant solution as cholesterol is insoluble in water and does not grow in the silica hydrogel. The silica gel medium provides concentration lowering, which is already discussed in chapter – I. The alcoholic extarcts are preffered over the aqueous extracts because the solubility of cholesterol is very less in water, the use of water would bring large scale precipitation of cholesterol. To maintain the same condition in control and extract test tubes,the alcoholic extracts are used.

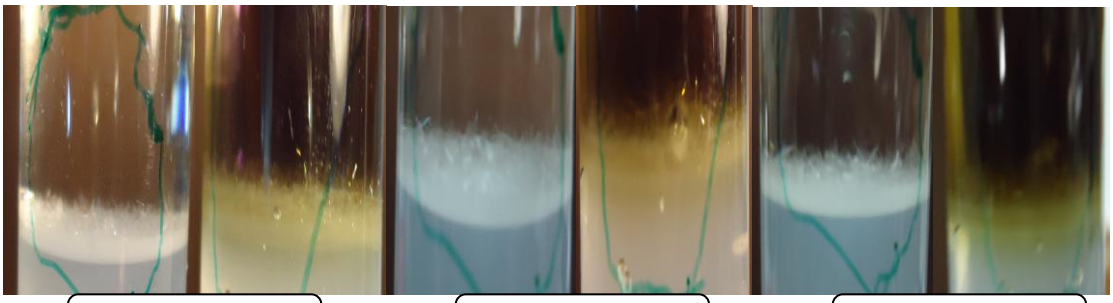

C **2 HOUR** F C **3 HOUR** F C **4 HOUR** F

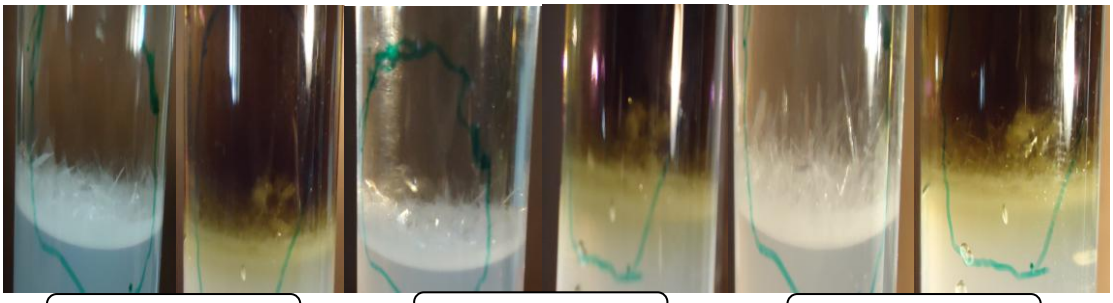

C **5 HOUR** F C **6 HOUR** F C **7 HOUR** F

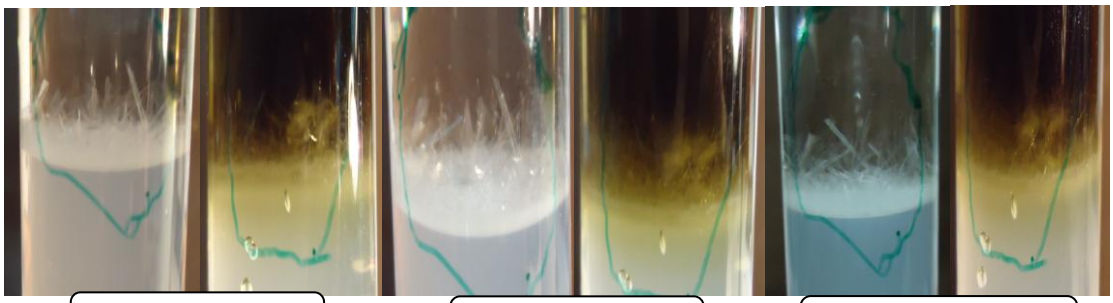

C **8 HOUR** F C **9 HOUR** F C **10 HOUR** F

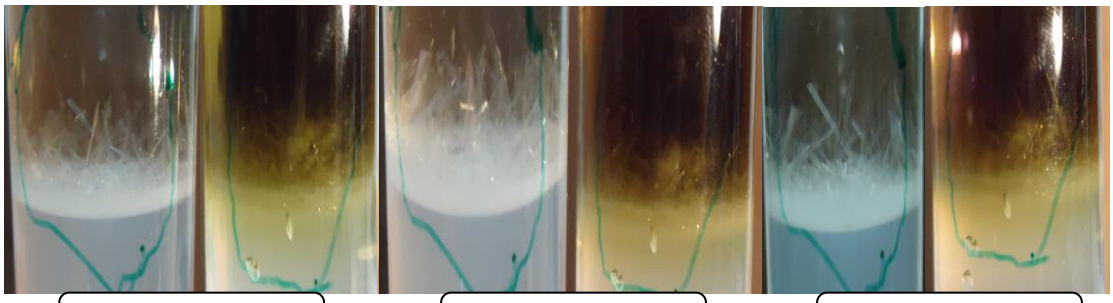

C **11 HOUR** F C **12 HOUR** F C **13 HOUR** F

C **14 HOUR** F C **15 HOUR** F C **16 HOUR** F

C **17 HOUR** F C **18 HOUR** F C **19 HOUR** F

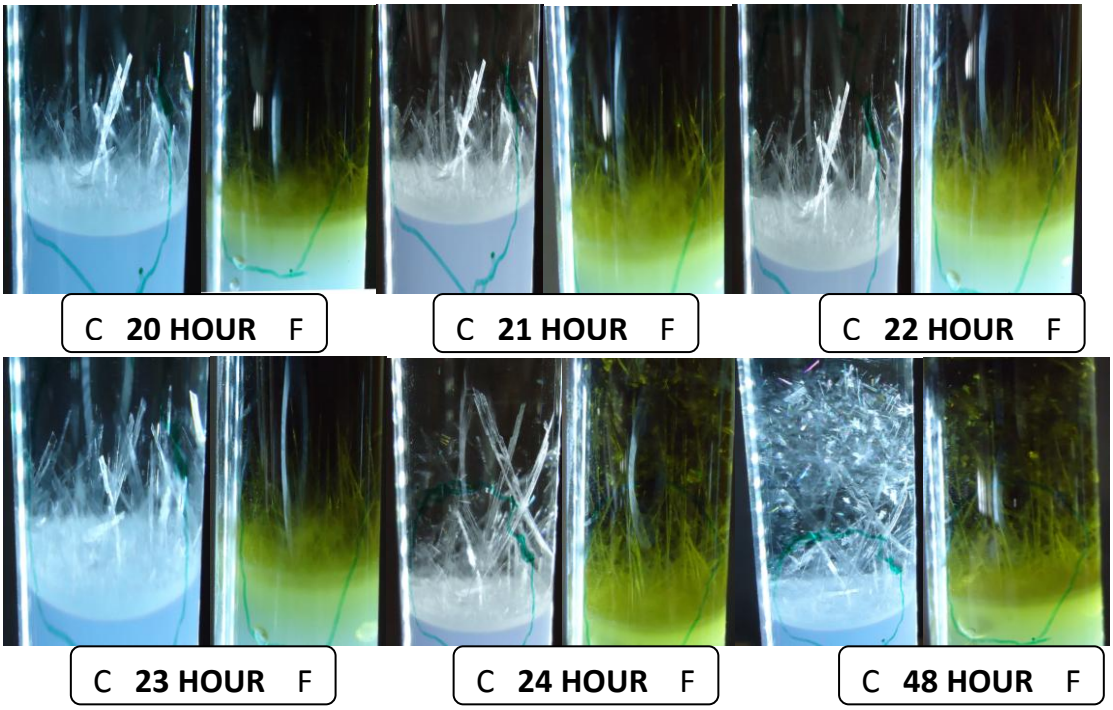

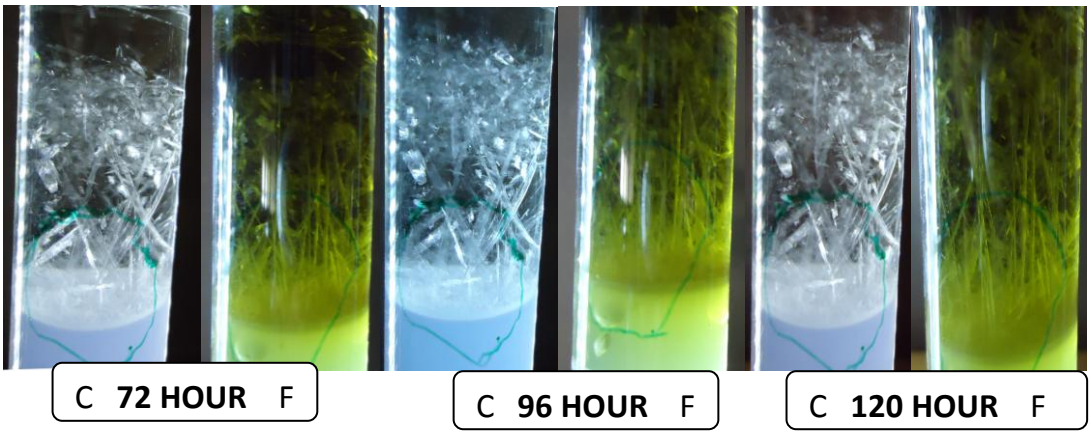

Figure 6.4 Cholesterol Crystals grown in control (C) and Extract of *Fagonnia Cretica* (F)

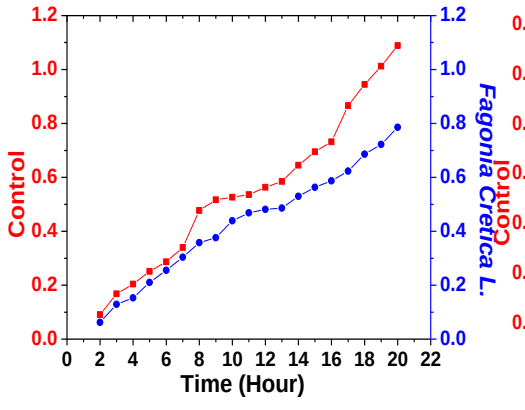

Figure 6.5 Length of the Crystals (1 to 20 hrs)

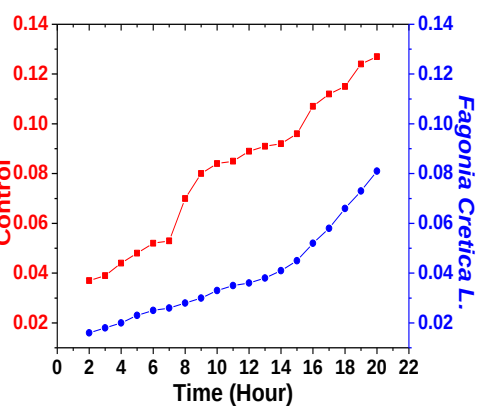

Figure 6.6 Breadth of the Crystals (1 to 20 hrs)

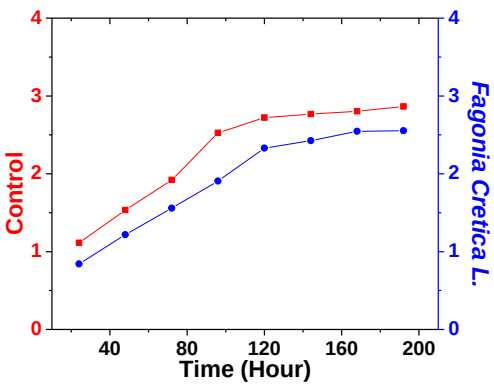

Figure 6.7 Length of the Crystals

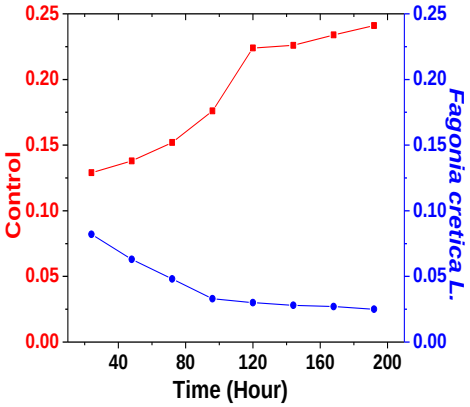

Figure 6.8 Breadth of the Crystals

Figures 6.5 and 6.6 show the plots of average length and breadth of the grown crystals, respectively, for 1 to 20 hours, where as figures 6.7 and 6.8 show the plots of average length and breadth of the grown crystals up to 8 days.

These figures show clearly the inhibitions of cholesterol crystals due to herbal extract of *Fagonia cretica Linn.* Also, it can be marked that the inhibition is experienced comparatively more on breadth than length.

6.7 Statistical Analysis

The single factor analysis of variance (ANOVA) was carried out using MS excel to check the comparison of values of apparent length and breadth of cholesterol crystal in the control and extract solution groups. ANOVA statistical analysis confirmed that the variations in the average length and the average breadth of cholesterol crystals with herbal extracts were highly significant at 0.05 level. From this *in vitro* growth inhibition study, it can be concluded that the investigated herbal extract *Fagonia Cretica L.* is found to be a potent inhibitor for cholesterol crystals.

6.8 Mechanism of Inhibition

Inhibition of crystal growth is widely studied subject and hence a collection of research papers has been edited by Amjad [51] and published in a book form. Inhibition is a complex interplay where the crystal structure, the nature and types of bonds exposed on plane considered, the adsorption on the crystalline face, the chemical potentials and chemical reactivity, the impeding the motion of growing steps on crystalline face, the formation of a complex of cations required for growth in solutions etc. have their important influence.

Considering brushite crystal as a good model, Skitric *et al*. [52] summarized following points for interaction of additives with crystal.

(1) The importance of molecular size and structure of the additive, i.e., small or macromolecules, number of functional groups in the molecule and its overall charge in the growth of crystals. This may be useful in the selection of inhibiting molecule. For example, glutamate and aspartate ions have only one overall negative charge, which produce no significant effect on CHPD (brushite) crystal faces, which can be increased by attaching more negative groups like OH^{-}.

(2) The importance of structural fit between the organic molecule and the ionic structure of a particular crystal face. This decides the order of inhibition or reaction at particular crystalline face. This may differently affect various crystalline faces depending upon the crystalline face exposed to the solution and as a result may change the morphology of the growing crystal. Small molecules with negatively charged groups, such as citrate ions do interact

with the lateral faces of brushite crystals and slowing down the crystallization and inviting changes in the crystal morphology.

(3) The influence of the hydration layer exposed on the surface of the crystals. For polyaspartic acid and brushite crystals, such structural fit exists between distances of neighboring calcium ions from two adjacent layers constitute Ca - HPO_4 bi layer lying beneath hydrated layer parallel to the (0 1 0) plane.

Madsen and Pederson [57] have found for brushite that most of the foreign metal ions are inhibitors, the only exception being Mg^{2+}, which has no significant effect and Pb^{2+}, which is a promoter. They have explained the inhibition and promotion mechanism as follows:

(1) Inhibition of crystal growth is due to adsorption of the inhibitor and so it is the inhibition of nucleation. The inhibitor is adsorbed to minute nuclei and preventing their further development.

(2) Promotion involves most likely the nucleation stage only, this stage being facilitated by the possibility of forming less soluble compound than that formed in the absence of additive. For example, the promotive effect of Pb^{2+} on both crystallization and hydrolysis of brushite may be due to nucleation of less soluble hydroxypyromorphite $\{Pb_5OH(PO_4)_3\}$.

(3) Reduction of average crystal size in comparison with the blank may be caused by promotion of nucleation, inhibition of crystal growth, or both. Growth inhibition is usually accompanied by irregular growth, because adsorption is not uniform, or growth rate fluctuates in space and time. If the

degree of adsorption is different for different faces of crystal then habit modification occurs.

There are also growth inhibition studies reported for hydroxyapatite by aspartic acid [58], heme crystals by antimalarials [59], COM crystals from human kidney tissue culture medium [60], calcium pyrophosphate crystals [61]. There are several models and mechanisms discussed by many authors, for instance, a model on complete crystal growth inhibition based on thermodynamics of interfaces [62] and computation by numerical solutions to modified fully transient 2D continuum model of crystal growth for arrest by an adsorption – inhibition mechanism [63].

Looking at figures 6.5 to 6.8, one can find that for the length of platelet type cholesterol crystals the inhibition is comparatively less than for the width. This is crystal morphology sensitive and hence depends on the crystallographic planes. According to the Kossel's model [64], which is described at length by Verma [65], the crystalline surface is having kinks in a step and adsorption of molecules of the same type at these kinks from solution contributes to the advancement of the step, this has been shown in figure 1.2 (a) and (b). Now adsorption of any molecular species, having similar but not exactly the same molecular structure of the molecular building block of the crystal, in the step at crystalline surface will block further arrival and adsorption of right molecular species needed to grow the crystal in stepwise manner. The step height, the molecular fit and the chemical bonds exposed are dependent on the crystallographic plane and hence the morphology of the crystal. If adsorption of any molecule on the step, impeding the step progress, is effective on one crystallographic plane may not exhibit the same nature for

the other crystallographic plane. Any molecular adsorption inhibits or retards the motion of steps on crystalline face needed for growth is known as inhibitor and the phenomenon can be called as poisoning. The adsorption of inhibitor molecule in steps may cause bunching of steps. This has been demonstrated by De Yoreo *et al.* [66] using AFM for citrate inhibition on COM (Calcium Oxalate Monohydrate) crystal.

In the present study, the author believe that phytochemicals like saponins present in herbal extracts are having molecular structure, as shown in figure 6.3, likely to get adsorbed on steps on the crystalline face and inhibit their motion. As the molecular fit depends on the crystallographic plane, this effect is more prominent on the width than the length of growing crystals. As it has been already mentioned in chapter – V that the growth of cholesterol crystals occurs in a stepwise manner, which has been revealed by SEM and AFM study, the growth inhibition of cholesterol crystal is mainly due to phytochemical adsorption on steps at crystalline face.

6.9 Conclusion

1. In comparison to pure cholesterol crystal growth (control), the cholesterol crystal growth in the presence of *Fagonia cretica L.* alcoholic extract exhibited significant growth inhibition.

2. The growth inhibition of cholesterol was more effective to the width of the growing crystals than the length.

3. The inhibition of growth of cholesterol crystals was due to various phytochemicals adsorptions at growth steps on crystalline faces blocking further the addition of cholesterol molecules needed for growth.

References

[1] P. R. Maulik, G. G. Shipley, *Biophys. J.,* **70** (1996) 2256.

[2] W. I. Calhoun, G. G. Shipley, *Biochemistry,* **18** (1979) 1712.

[3] S. Lund – Katz, H. M. Laboba, L. R. McLean, M. C. Phillips, *Biochemistry,* **27** (1988) 3416.

[4] A. Sharma, C. Shankar, L. K. Tyagi, M. Singh. C. V. Rao, *Acad. J. of Plant. Sci.,* **1** (2008) 26.

[5] B. Patwardhan, A. D. B. Vaidya, M. Chorghade, S. P. Joshi, *Current Bioactive Compounds*, **4** (2008) 201.

[6] A. D. B. Vaidya, *Ayurveda in Transition*, **1** (2010) 27.

[7] A. D. B. Vaidya, *International Arogya,* New Delhi, India (2007).

[8] K. C. Joseph, B. B. Parekh, M. J. Joshi, *Curr., Sci.,* **85** (2005) 1232.

[9] D. Barrett, B. Parulkar, S. Kramer, *Urology,* **42** (1993) 431.

[10] D. Hirsh, R. Azoury, S. Sarig, *J. Crystal Growth*, **104** (1990) 759.

[11] R. Ross, *Nature*, **362** (1993) 801.

[12] M.J. Whiting, J. M. Watts, *Clin. Sci.*, **68** (1985) 589.

[13] R. T. Holzbach, A. Kibe, E. Thiel, J. H. Howell, M. Marsh, R. E. Hermann, *J. Clin. Invest.,* **73** (1984) 35.

[14] A. Kibe, R. T. Holzbach, N. F. LaRusso, S. J. T. Mao, *Science,* **225** (1984) 514.

[15] S. Gallinger, P. R. C. Harvey, C. N. Petrunka, R. G. Ilson, S. M. Strasberg, *Gastroentrology,* **92** (1987) 867.

[16] N. Busch, H. Takumo, R. T. Holzbach, *J. Lipid Res.,* **31** (1990) 1903.

[17] N. Busch, N. Matiuck, S. Sahlin, S. P. Pillay, R. T. Holzbach, *J. Lipid. Res.,* **32** (1991) 695.

[18] N. Busch, F. Lammert, H. U. Marschall, S. Mattern, *J. Clin. Invest.,* **96** (1995) 3009.

[19] A. Kibe, M. A. Dudley, Z. Halpern, M. P. Lynn, A. C. Breuer, R .T. Holzbach, *J. Lipid Res.,* **26** (1985) 1102.

[20] N. Busch, F. Lammert, H. U. Marschall, S. Mattern, *J. Clin. Irest.,* **96** (1995) 3009.

[21] S. K. Banerjee, S. K. Maulik, *Nutr. J.*, **1** (2002) 4.

[22] A. K. Awasthi, K. Kothari, R. K. Sharma, *J. Sci. Res. Plants Med. XV-2*, **XVI-1** (1994-1995) 58.

[23] P. N. Durrington, *Post Grad. Med. J.*, **68** (1992) 867.

[24] M.C. Bateson, *The Darlington Postgrad.,* **10** (1991) 46.

[25] M. S. Ammal, K. V. George, I. Jayakumari, *Cryst. Res. Technol.*, **42** (2007) 876.

[26] N. T. Saraswathi, F. T. Gnanam, *J. Cryst. Growth,* **179** (1997) 611.

[27] R. H. Garret, C. M. Grisham, *Biochemistry,* Brooks/Cole Cenage Learning, Boston, USA (2010).

[28] A. D. B. Vaidya, T. P. A. Devasagayam, *J. Clin. Biochem. Nutr.,* **41** (2007) 1.

[29] V. M. Gogte, *Medicinal Plants I – II,* Bharatiya Vidya Bhavan, Mumbai, India (2002).

[30] S. S. Handa, *Indian Herbal Pharmacopeia,* **Vol I & II**, IDMA, Mumbai, India (1998).

[31] Ayurvedic Pharmacopeia of India, Govt. of India, Ministry of Health and Family Welfare, New Delhi.

[32] V. S. Joshi, B. B. Parekh, M. J. Joshi, A. B. Vaidya, *J. Cryst. Growth,* **275** (2005) e1403.

[33] V. S. Joshi, B. B. Parekh, M. J. Joshi, A. B. Vaidya, *Urol. Res.,* **33** (2005) 80.

[34] K. C. Joseph, B. B. Parekh, M. J. Joshi, *Curr. Sci.,* **88** (2005) 1232.

[35] B. B. Parekh, M. J. Joshi, *Ind. J. Pure and Appl. Phy.,* **43** (2005) 675.

[36] C. K. Chauhan, M. J. Joshi, A. D. B. Vaidya, *Am. J. Inf. Dise.*, **5** (2009) 170.

[37] C. K. Chauhan, M. J. Joshi, A. D. B. Vaidya, *J. Mater. Sci.: Mater. Med.,* **20** (2009) 85.

[38] C. K. Chauhan, M. J. Joshi, A. D. B. Vaidya, *Ind. J. Biochem. and Biophys.,* **48** (2011) 202.

[39] B. B. Parekh, M. J. Joshi, A. B. Vaidya, *J. Cryst. Growth,* **310** (2008) 1749.

[40] B. B. Parekh, S. R. Vasant, K. P. Tank, A. Raut, A. D. B. Vaidya, M. J. Joshi, *Am. J. Inf. Dise.,* **5** (2009) 232.

[41] B. B. Parekh, *Ph. D. Thesis,* Saurashtra University, Rajkot (2005).

[42] M. Daniel, *Medicinal Plants: Chemistry and Physics*, Science Publishers, New Hampshire, USA (2006).

[43] M. S. Abdel-Kader, A. A. Omar, N. A. Abdel-Salam, F. R. Stermitz, *Phytochem*, **36** (1994)1431.

[44] A. A. Ansari, l. Kenne, Atta – ur Rehman, T. Wehler, *Phytochem*, **26** (1987) 1487.

[45] A. A. ansari, l. Kenne, Atta – ur Rehman, T. Wehler, *Phytochem*, **27** (1988) 3979.

[46] M. A. Saeed, Z. Khan, A. W. Sabir, *Tr. J. of Biol.,* **23** (1999) 187.

[47] V. Singh, R. P. Pandey, *Ethnobotany of Rajasthan,* Pawan kumar Scientific Publishers, India (1998).

[48] A. L. Soomro, N. A. Jaffary, *J. Pak. Med. Assoc.*, **53** (2003) 6.

[49] Q. Mandeel, A. Taha, *Pharm. Bio.*, **43** (2005) 164.

[50] S. Sharma, L. Joseph, M. George, V. Gupta, *Pharmacology Online*, **3** (2009) 623.

[51] Z. Amjad (Ed.), *"Advances in Crystal Growth Inhibition Technologies"*, Kluwer Academic Publishers, New York (2002).

[52] M. Skitric, S. Sarig, H. Füredi-Milhofer, *Prog. Colloid Polym. Sci.*, **110** (1998) 300.

[53] S. N. Kalkura, S. Devanarayana, *J. Mater. Sci. Lett.,* **5** (1986) 741.

[54] I. Das, S. Verma, *J. of Sci. & Ind. Res.,* **67** (2008) 291.

[55] S. Arteaga, A. Carmona, J. Luis, A. Andrade – Cetto, R. R. Cardenas, *J. Phrm. Pharmacol.,* **57** (2005) 1.

[56] R. R. Reddy, K. Srinivasan, *Steroids,* **76** (2011) 455.

[57] H. E. Lundager Madsen, Jo Bech Pedersen, *"Influence of Foreign Metal Ions on Crystal Morphology and Transformation of Brushite"*, In *"Advances in Crystal Growth Inhibition Technologies"*, Z. Amjad (Ed.), Kluwer Academic Publishers, New York (2002).

[58] S. P. Huang, K. C. Zhou, Z. Y. Li, *Trans. Nonferrous Met. Soc. China*, **17** (2007) 612.

[59] C. R. Chong, D. J. Sullivan Jr., *Biochem Pharmacol*., **66** (2003) 2201.

[60] Y. Nakagawa, H. C. Margolis, S. Yokoyama, F. J. Kezdy, E. T. Kaiser, F. L. Coe, *J. Biological Chem*., **256** (1981) 3936.

[61] J. D. Sallis, A. Wierzbicki, H. S. Cheung, *"Calcium Pyrophosphate Crystal Salt Forms and the Influence of Phosphocitrate"*, In *"Advances in Crystal Growth Inhibition Technologies"*, Z. Amjad (Ed.), Kluwer Academic Publishers, New York (2002).

[62] M. R. Anklam, A. Firoozabadi, *J. Chem. Phys.*, **123** (2005) 144708.

[63] L. N. Brush, E. Le, *Cryst. Growth Des.*, **6** (2006) 643.

[64] W. Kossel, *Nachr. Ges. Wiss.,* Göttingen, (1927) 135.

[65] A. R. Verma, *Crystal Growth and Dislocations,* Butterworth, London, UK (1953).

[66] J. J. De Yoreo, S. R. Qiu, J. R. Hoyer, *Am. J. Physiol. And Renal Physiol.,* **291** (2006) F1123.

Chapter - VII

Synthesis and Characterization of Curcumin Nano particles

7.1 Introduction

Curcumin is the main curcuminoid of the popular Indian spice turmeric (*curcuma longa*), which is a member of the ginger family (*zingiberaceae*). Turmeric, a common Indian curry spice, has also earned synonyms like *"Holy Powder"* and *"Indian Solid Gold"*. Turmeric has shown wide range of therapeutic applications in the traditional Indian medicine [1-2], such as treating wounds, infections and other health problems.

Turmeric also possesses two other curcuminoids, which are desmethoxy curcumin and bisdemethoxy curcumin. The curcuminoids are natural phenols and responsible for the yellow color of turmeric. Curcumin can exist in several tautomeric forms, including a 1,3 – diketo form and two equivalent enol forms. However, the enol form is more energetically stable in the solid phase and also in solution [3]. Curcumin (1,7-bis(4-hydroxy-3-methoxyphenyl)1,6-heptadiene-3,5-dione) is also bright yellow in color and find common application is food coloring.

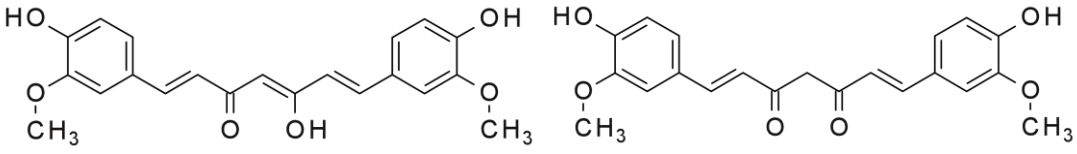

(a) (b)

Figure 7.1 Curcumin Molecular Structure (a) Enol form (b) Keto form [4]

(a) (b) (c)

Figure 7.2 (a) Turmeric plant (b) turmeric (c) turmeric powder [5]

Curcumin incorporates several functional groups. The aromatic ring systems, which are poly-phenols, are connected by two α, β – unsaturated carbonyl groups. The diketones form stable enols or are easily protonated and form enolates, while the α, β – unsaturated carboyl is a good Michel acceptor (a nuclophilic addition of a carbon-ion or other nucleophile to an α, β – unsaturated carbonyl compound) and undergoes nucleophilic addition. It is worth noting here that all molecules or ions with free pair of electrons or atleast one π – bond can act as nucleophiles. Curcumin structure was first identified in 1910 by J. Milobedzka *et al.* [6]

7.2 Applications of Curcumin

Ongoing research and clinical trials provide ample evidence that this natural phenolic compound curcumin possesses diverse pharmacological properties, for instance, anti-inflammatory, anti-carcinogenic, anti-infectitious[7 - 10], anti-oxidant, anti-diabetic and anti-viral [11], the compound is also considered as a cancer chemo-preventive agent [12,13]. A number of derivatives of curcumin are also widely used as antibacterial, anti-protozoal,

anti-angiogenic and anti-cancer agents [14,15]. The interaction of curcumin with human serum albumin (HSA) and bovine serum albumin (BSA) has been investigated [16-20].

Curcumin shows good effect against malaria, cervical cancer, pancreatic cancer, colon cancer, psoriasis because of its antitumor effects and its potential utility as a cancer chemopreventive agent [21]. Curcumin has been shown to inhibit tumor formation in the skin, forestomach, duodenum and colon in mice [22], as well as the mammary glands, colon, tongue and sebaceous glands of rats [23]. The low molecular weight and polar structure of curcumin allows it to penetrate the blood – brain barrier effectively. Animal studies have indicated that curcumin can enhance the adult hippocampus neurogenesis process by increasing the number of newly generated cells in the dentate gyrus region of hippocampus [24]. In one of the recent studies, low doses of curcumin have shown to effectively disaggregate beta amyloid as well as prevent fibril and oligomer formation and thus found to be protective in treating Alzheimer's disease [25].

Antidepressant activity of curcumin has been reported in animal models of depression. Recently, research on exploring antidepressant properties of curcumin is exponentially increasing. The molecules is effective in forced swim test and chronic unpredictable stress [26,27]. Curcumin posses antidepressant activity through modulating release of serotonin and dopamine. Curcumin enhances the level of neurotrophic factors such as brain derived neurotrophic factor [28]. Another exciting use of curcumin is in the treatment of diabetic neuropathy. Curcumin enhanced the glucose lowering of insulin and protects against the onset of diabetic neuropathy [29,30].

Curcumin is found to be effective in preventing the inflammation induced increase in rat liver enzymes such as serum glutamic axaloacetic transamilase and serum glutamic pyruvic transamilase [31,32].

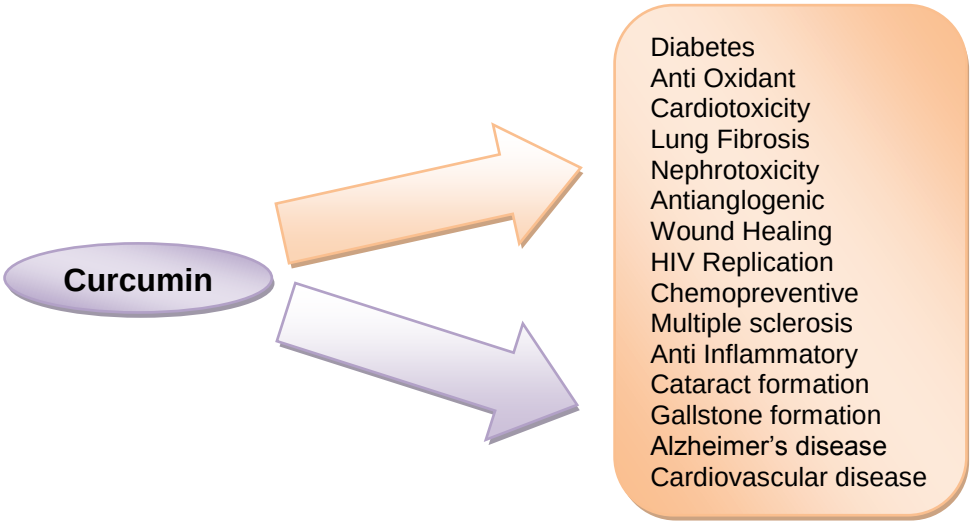

Figure 7.3 Medicinal properties of Curcumin [33]

Curcumin is effective in reducing the incidence of cholesterol gall stone formation and also in reducing the biliary cholesterol concentration induced by feeding a lithogenic diet in mice [34,35]. Curcumin can block HIV replication by inhibiting HIV integrase [36] and viral protease [37]. Curcumin also has modulatory effects in diseases besides all these diseases described over here in figure 7.3.

There are large number of review articles and book chapters available on curcumin and its applications [38-43].

7.3 Curcumin Nano – particles

As discussed in the previous section that curcumin finds wide range of applications, which has lead several authors to synthesize curcumin nano particles and functionalize them with other compounds for therapeutic and targeted drug delivery.

Bhawana *et al.* [44] synthesized curcumin nano particles by a wet – milling technique of the 2 - 40 nm range. The authors noted that unlike curcumin, the curcumin nano particles were freely dispersed in water even in the absence of any surfactant. It was found that the aqueous dispersion of nano curcumin was more effective than curcumin against *staphylococcus aureus*, *Bacillus subtilis*, *Escherichia coli*, *Pseudomonas aeruginosa*, *Penicillium notatum* and *Aspergillus niger.* The result demonstrated that the water solubility and antimicrobial activity of curcumin significantly improved by the particle size reduction up to the nano range. For the selected micro – organisms, notwithstanding, the activity of nano – curcumin was more pronounced against the Gram positive (Gram +Ve) bacteria then the Gram negative (Gram - Ve) ones. Its antibacterial activity was superior to the antifungal activity. The authors used TEM for nano curcumin study.

Ovarian cancer is the most lethal of the gynecological cancers and the fifth most common cause of cancer mortality in women in USA. Curcumin can make ovarian cancer cells more vulnerable to chemotherapy and radiation. However, curcumin is poorly adsorbed by the body, which puts limit on its effectiveness. A nano particle formulation was developed by Yallapa *et al.* [45] to provide increased bioavailability as well as targeted delivery of curcumin to tumors. Moreover, recently Yallapa *et al.* [46] have reviewed curcumin nano-formulation as a future medicine for cancer. They have focused the discussion on the design and development of nano – particles, self – assemblies, nano – gels, liposomes and complex fabrication for sustained and efficient curcumin delivery.

As noted earlier, curcumin has many diverse applications, but its optimum potential is limited by its lack of solubility in aqueous solvents and poor bioavailability. Anand *et al.* [47] used a polymer based nano particles to improve bioavailability. Here, curcumin was encapsulated with 97.5% efficacy in biodegradable nano-particulate formation of polylactide coglycolide (PLGA) and a stabilizer polyethylene glycol (PEG - 5000). Apart from this, Anitha *et al.* [48] studied biologically curcumin loaded dextron – sulphate – chitosan nanoparticles and characterized them by DLS, XRD, FTIR, AFM, SEM and DTA. Polymeric nanoparticle encapsulation of curcumin is termed as a novel strategy for human cancer therapy by Bisht *et al.* [21]. The interaction of gold – curcumin nano particles with human peripheral blood lymphocytes is reported by Sindhu *et al.* [49]. The surface modification of solid – lipid curcumin nanoparticles for oral delivery is carried out [50]. Recently, micro-fluidic fabrication of cationic curcumin nano particles of less than 50 nm is used as an anti cancer agent [51], not only for the cancer, curcumin nano particles encapsulated by PLGA has been used for Alzheimer's disease and termed as a gateway for multifaceted approach by Mathew *et al.* [52].

Micro – emulsion technique finds many applications as those have been briefly reviewed in earlier chapter – I, particularly, in drug delivery it finds predominant attention. Lin *et al.* [53] investigated terpene micro emulsions for transdermal curcumin delivery in terms of effect of terpenes and co-surfactants. Jing *et al.* [54] reported preparation and characterization of curcumin micro emulsion. The self micro-emulsifying drug delivery system is found to improve curcumin dissolution and its bioavailability [55]. To study this various oils, surfactants and co-surfactants were selected to optimize the

formulation. Pseudo-ternary phase diagrams were constructed and orthogonal design was used to compare the oil – in – water micro emulsion forming capacity of different oils/surfactants/co-surfactant. The solubility of curcumin in various oils and co-surfactants was determined to find the suitable ingredients with good solubilizing capacity. Droplet size was measured to obtain the concentration of oil, surfactant and co-surfactant for forming stable micro emulsion. The authors [55], further, tested the quality and bioavailability in mice.

Looking at various applications of curcumin bulk and nano particles the present author has chosen to synthesize curcumin nano – particles by micro emulsion technique and characterize them.

7.4 Synthesis of Nano particles

The mixture of Triton X – 100/water/n- hexane was used for the synthesis of nano particles of cholesterol. Single phase region was identified by the mixture of all this three solutions. Amount of surfactant was decided as the molar ratio R remains six. Detailed single phase description was discussed in chapter 3. The solution of curcumin (obtained from Himedia with 99%purity) made in chloroform was added into this mixture in drop – wise manner with continuous stirring. After 15 – 20 min. nano particles were formed at the liquid – liquid interface of the solution which was filtered out by using Whatman filter paper no. 42. The yield of synthesized nano particles was around 65%.

7.5 Powder XRD Study of Curcumin Nano particles

The single crystal XRD study was reported for mono-carbonyl analogues of Curcumin [56]. Recently, new polymorphs of curcumin are reported by Samphui *et al.* [57]. They have identified three polymorphs of curcumin crystals as monoclinic with space group $P_{2/n}$ with unit cell parameters *a*=12.5676 Å, *b*= 7.6425 Å, *c*= 19.9582 Å; orthorhombic with space group $P_{ca}2_1$ having unit cell dimensions *a*=35.417 Å, *b*= 7.7792 Å, *c*= 12.6482 Å and

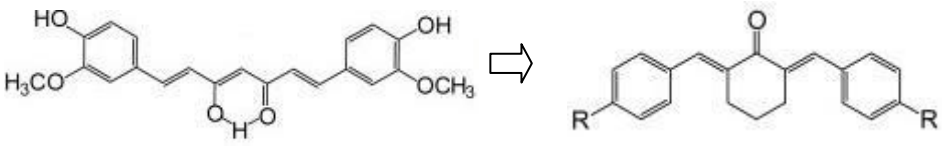

(a) (b)

Figure 7.4 (a) enol form (b) keto form

orthorhombic with space group Pb_{ca} having unit cell parameters as *a*= 12.536 Å, *b*= 7.9916 Å, *c*= 34.462 Å. Moreover, crystal structure of curcumin analogues have been reported [58]. Chemical structure of curcumin shows tautomerism, where the α, β – unsaturated β – diketone (heptadine - divne) moiety undergoes keto – enol tautomerism and forms a hydrogen bond containing 6 – membered ring [58]. The crystal structure was determined for heterocyclic derivative of curcumin: 3,5 – bis [β – (4-acetoxy-3-methoxy phenyl) ethyl] pyrazole benzene by Lozada *et al.* [59] Figure 7.5 shows the powder XRD pattern of curcumin nano particles. The characteristic peak broadening shows that the formed particles were nano in nature. The

curcumin nano particles exhibited orthorhombic symmetry and the unit cell parameters were estimated as, *a*=35.256 Å, *b*=7.7712 Å, *c*=12.6743 Å.

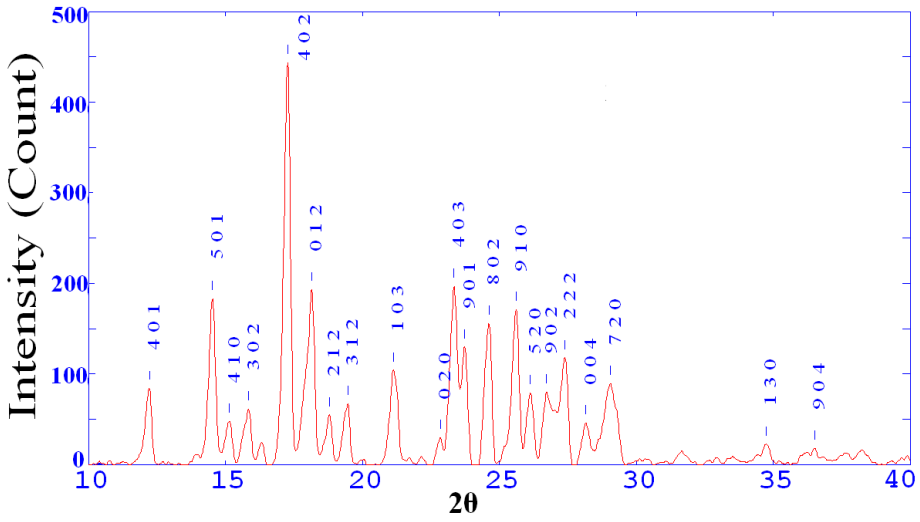

Figure 7.5 Powder XRD pattern of Curcumin nano particles

The average particle size of curcumin nano particles was determined from the powder XRD pattern by employing the Scherrer's formula to maximum intensity peak as discuss in chapter III. From the Scherrer's formula the average particle size of curcumin nano particles was found to be 24 nm.

7.6 TEM study of Curcumin Nano – particles

The TEM study was carried out to determine the size and morphology of the synthesized curcumin nano – particles. The TEM images of the curcumin nano particles are shown in figures 7.6 (a) and (b). TEM images suggest that the agglomerated curcumin nano particles were having nearly spherical morphology and size varied from 20 – 35 nm. The possible mechanism for obtaining different size of nano particles is already discussed in chapter III.

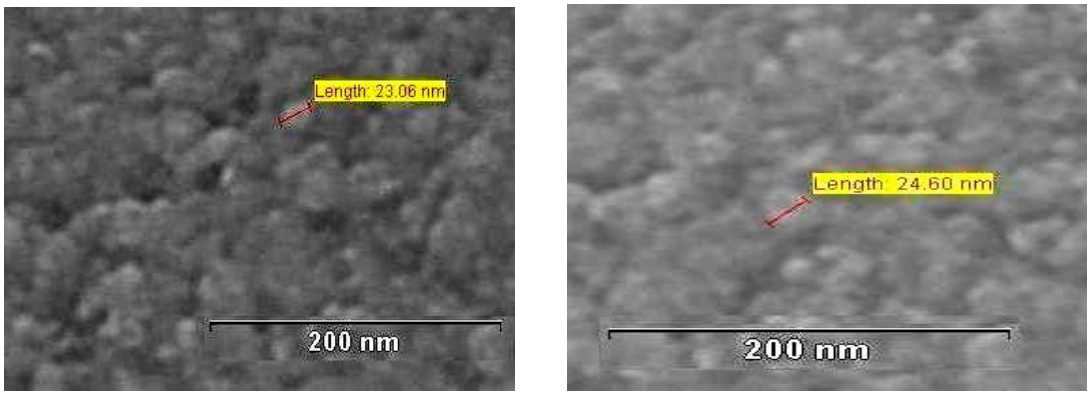

(a) (b)

Figure 7.6 TEM micrograph of curcumin nano particles

7.7 FT – IR Spectral study of Curcumin Nano particles

Yadav *et al.* [60] have reported important absorptions in FTIR spectrum of curcumin as follows: (1) 3595 cm^{-1} to phenolic (- OH) vibrations; (2) 3075 cm^{-1} to aromatic C – H stretching vibrations; (3) 1600 cm^{-1} to the stretching vibration of benzene ring skeleton; (4) 1510 cm^{-1} to mixed (C = O) and (C = C) vibration; (5) 1425 cm^{-1} to the olifinic C – H in plane bending vibration (δ_{C-H}); (6) 1280 cm^{-1} to Ar-O stretching. FT – IR spectrum of curcumin nano particles are shown in figure 7.7. The FT – IR spectrum of curcumin nanoparticles was

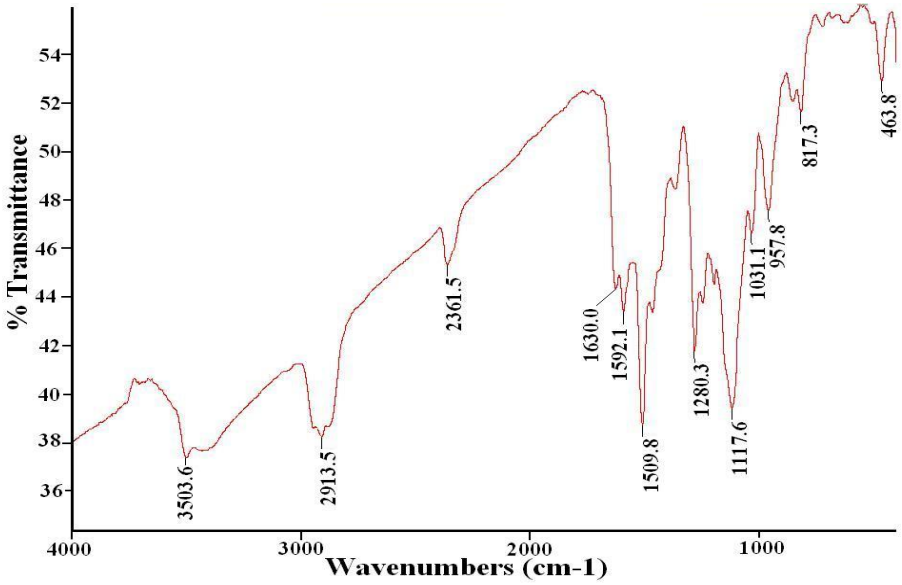

Figure 7.7 FT – IR Spectrum of curcumin nano particles

reported by Bisht et al [21]. The absorption occurring at 3503.6 cm^{-1} is due to O – H stretching vibrations, the absorption occurring at 2913.5 cm^{-1} is due to C – H stretching vibrations of CH_3 stretching asymmetrically, the absorption at 1630 cm^{-1} is due to C=O stretching vibration, there is little bit shifting in the C = O stretching, which may due to conjugation of the C = O [61]. The absorptions observed at 1592.1 cm^{-1} and 1509.8 cm^{-1} are due to C=C stretching observed due to CH-C=O stretching, the absorptions at 1208.3 cm^{-1}, 1117.6 cm^{-1} and 1031.1 cm^{-1} are due to C – O stretching vibrations and the absorptions at 957.8 cm^{-1} , 817.3 cm^{-1} and 463.8 cm^{-1} are attributed to aromatic substitution.

7.8 Thermal Study of Curcumin Nano particles

Thermal studies like TG, DTA and DSC was carried out on curcumin nano particles. Figure 7.8 shows the TG – DTA of curcumin nano particles. The TG plot shows minor decomposition up to 260 ^oC and beyond that it decomposes rapidly up to 590 ^oC, where complete decomposition is observed. The DTA plot indicates that the decomposition process of curcumin nano particles occurs through an endothermic reaction at 181.4 ^oC and an exothermic peak observed at 596.2 ^oC. From the DSC plot several thermodynamic parameters were calculated by using the software TA evaluation available with the set up. For an endothermic reaction at 181.4 ^oC, the enthalpy and the change in heat capacity are calculated and found to be -11428.47J/kg and 936.2 J/kgK, respectively. This may be due to some phase change occurring without significant breaking of the bonds resulting into marginal weight loss, which may be due to melting of a sample. The melting point of curcumin is 183 ^oC [62]. An exothermic reaction observed at 596.2 ^oC,

may be due to complete decomposition of the sample into the gaseous phase and reaction within the products. For this reaction the values of the enthalpy and the change in heat capacity are found to be 9362765 J/kg, 20256.2 J/kgK, respectively.

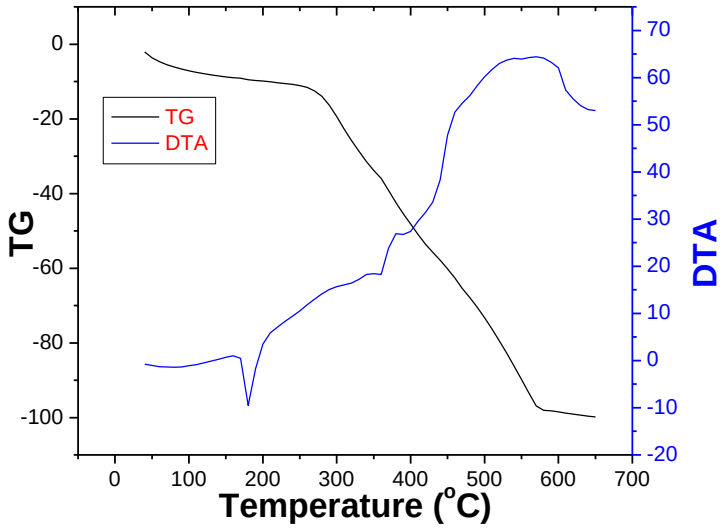

Figure 7.8 TG – DTA of curcumin nano particles

7.9 Kinetic Parameters of Curcumin Nano particles

Kinetic parameters of decomposition for curcumin nano particles were calculated using Coats – Redfern relation [63] as discussed in chapter III. Figure 7.9 shows the Coats – Redfern plot. Table 1 shows the Kinetic parameters of curcumin nano particles.

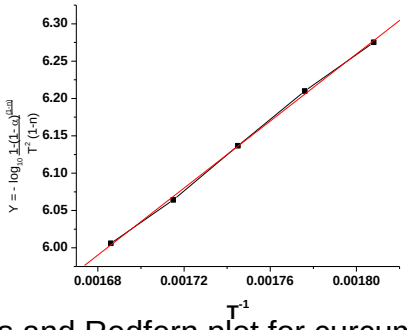

Figure 7.9 Coats and Redfern plot for curcumin nano particles

Table 7.1 Kinetic parameters of curcumin nano particles

Sample	Kinetic Parameters
Curcumin nano particles	Order of reaction (n) = 2
	Activation energy (E) = 42.97 $kJK^{-1}Mol^{-1}$
	Frequency factor (A) = 6.50×10^{17}

As the activation energy is considered as a barrier to be surmounted to form reaction products [64], the higher value of activation energy for nano particles suggests slower reaction rate and hence more stability.

7.10 Thermodynamic Parameters of Curcumin Nano particles

Various thermodynamic parameters such as standard entropy of activation $\Delta^{\#}S°$, standard enthalpy of activation $\Delta^{\#}H°$, standard Gibbs energy of activation $\Delta^{\#}G°$ and standard internal energy of activation $\Delta^{\#}U°$ were calculated by applying well known formulae, as described in detail by Laidler [65]. Table 7.2 gives the value of various thermodynamic parameters calculated for curcumin nano particles at 300 ^{o}C.

Table 7.2 Thermodynamic parameters of curcumin nano particles

Sample	Thermodynamic Parameters
Curcumin nano particles	Standard Entropy $\Delta^{\#} S° = 90.57\ Jkmol^{-1}$
	Standard Enthalpy $\Delta^{\#} H° = 33.44\ kJmol^{-1}$
	Standard Gibbs free energy $\Delta^{\#} G° = -18.44\ kJmol^{-1}$
	Standard change in internal energy $\Delta^{\#} U° = 38.20\ kJmol^{-1}$

The positive value of standard entropy and negative value of Gibbs free energy indicates spontaneous process.

7.11 Conclusions

(1) The nano particles of curcumin were synthesized by using w/o microemulsion technique with the mixture of water/ triton X – 100/ n – hexane.

(2) Broadening in the Powder XRD pattern confirmed nano structured nature of the material. Curcumin nano particles showed orthorhombic crystal system with unit cell parameters as, *a*=35.256 Å, *b*=7.7712 Å, *c*=12.6743 Å.

(3) The average particle size of the curcumin nanoparticles was calculated by using Scherrer's formula to a particular reflection in powder XRD pattern and it was found around 24 nm.

(4) TEM study was carried out to evaluate the exact particle size and morphology of the sample. From TEM it was found that the curcumin nano particles were having nearly spherical morphology with sizes varied from 20 nm – 35 nm.

(5) FT – IR spectrum of the curcumin nano particles confirmed the presence of O – H, C – H, C = O, C – O and aromatic ring substitution.

(6) TG of curcumin nanoparticles showed that the sample remained almost stable up to 260 ^{o}C, thereafter, it decomposed rapidly and at 590 ^{o}C a complete decomposition took place. DTA showed an endothermal absorption taking place at 181.4 ^{o}C and an exothermic reaction observed at 596.2 ^{o}C. DSC gave the entropy and heat change of these endothermic and exothermic reaction.

(7) Kinetic parameters of decomposition for the curcumin nanoparticles were calculated by Coats – Redfern formula. It was found that the order of reaction

(n), activation energy (E) and frequency factor (A) were, 2, 42.97 $kJK^{-1}Mol^{-1}$ and 6.50 x 10^{17}, respectively.

(8) The thermodynamic parameters for the decomposition process were also evaluated. The values of standard entropy, standard enthalpy, standard Gibbs free energy and standard change in internal energy of activation were found to be, 90.57 $Jkmol^{-1}$, 33.44 $kJmol^{-1}$, - 18.44 $kJmol^{-1}$ and 38.20 $kJmol^{-1}$, respectively.

References

[1] http://www.natural/news.com/curcumin.html

[2] B. B. Aggarwal, C. Sundaram, N. Malani, H. Ichikawa, *Curcumin: The Indian Solid Gold,* Ch.1, Charak International (2006).

[3] T. M. Kolev, E. A. Velcheva, B. A. Stamboliyska, M. Spiteller, *Int. J. Quant. Chem.,* **102** (2005) 1069.

[4] http://en.wikipedia.org/wiki/Curcumin

[5]http://pakagri.blogspot.in/2008/01/haldi-turmeric-cultivation-needs-boost.html

[6] J. Milobedzka, S. Kostanecki, W. Lampe, *Berichte der deutschen chemischen gesellschaft,* **43** (1910) 2163.

[7] R. Kuttan, P. Bhanumathy, K. Nirmala, M. C. George, *Cancer Lett.*, **29** (1985) 197.

[8] O. P. Sharma, *Biochem. Pharmacol.*, **25** (1976) 1811

[9] M. L. Kuo, T. S. Huang, J. K. Lin, *Biochem. Biophys. Acta*, **1317** (1996) 95.

[10] S. Bhaumik, R. Anjum, N. Rangaraj, B. V. V. Pardhasaradhi, A. Khar, *FEBS Lett.*, **456** (1999) 311.

[11] V. S. Govindarajan, *CRC Crit. Rev. Food Sci. Nutr.*, **12** (1980) 199.

[12] B. B. Aggarwal, A. Kumar, A. C. Bharti, *Anticancer Res.*, **23** (2003) 363.

[13] D. P. Chauhan, *Curr. Pharm. Des.*, **8** (2002) 1695.

[14] C. V. Rao, A. Rivenson, B. Simi, B. S. Reddy, *Cancer Res.*, **55** (1995) 259.

[15] J. L. Arbiser, N. Klauber, R. Rohn, R. V. Leeuwen, M. T. Huang, C. Fisher, E. Flynn, H. R. Byers, *Mol. Med.*, **4** (1998) 376.

[16] A. Barik, K. I. Priyadarsini, H. Mohan, *Photochem. Photobiol.*, **77** (2003) 597.

[17] A. C. Pulla Reddy, E. Sudharshan, A. G. Appu Rao, B. R. Lokesh, *Lipids*, **34** (1999) 1025.

[18] F. Zsila, Z. Bikádi, M. Simonyi, *Biochem. Biophys. Res. Commun.*, **301** (2003) 776.

[19] A. Barik, B. Mishra, A. Kunwar, K. I. Priyadarsini, *Chem. Phys. Lett.*, **436** (2007) 239.

[20] A. Kunwar, A. Barik, R. Pandey, K. I. Priyadarsini, *Biochim. Biophys. Acta*, **1760** (2006)1513.

[21] S. Bisht, G. Feldmann, S. Soni, R. Ravi, C. Karikar, A. Maitra, *J. of Nanobiotech.*, **5** (2007) 1.

[22] R. A. Sharma, C. R. Ireson, R. D. Verschoyle, K. A. Hill, M. L. Williams, C. Leuratti, M. M. Manson, L. J. Marnett, W. P. Steward, A. Gescher, *Clin. Cancer Res.*, **7** (2001) 1452.

[23] Y. Jiao, J. Wilkinson IV, E. Christine Pietsch, J. L. Buss, W. Wang, R. Planalp, F. M. Torti, S. V. Torti, *Free Red. Biol. and Med.*, **40** (2006) 1152.

[24] S. J. Kim, T. G. Son, H. R. Park, M. Park, M. S. Kim, H. S. Kim, H. Y. Chung, M. P. Mattson, J. Lee, *J. Biol. Chem.,* **283** (2008) 14497.

[25] S. Kulkarni, A. Dhir, K. K. Akula, *Sci. World J.*, **9** (2009) 1233.

[26] M. K. Bhutani, M. Bishnoi, S. K. Kulkarni, *Pharmacol Biochem Behav,* **92** (2009) 39.

[27] S. K. Kulkarni, M. K. Bhutani, M. Bishnoi, *Psycopharmacology,* **201** (2008) 435.

[28] R. Wang, Y. B. Li, Y. H. Li, Y. Xu, H. L. Wu, X. J. Li, *Brain Res*, **1210** (2008) 84.

[29] S. Sharma, K. Chopra, S. K. Kulkarni, *Phytother Res*, **21** (2007) 278

[30] S. K. Kulakarni, A. Dhir, *Ind. J. Pharm. Sci.*, **72** (2010) 149.

[31] R. C. Srimal, N. Dhawan, J. Pharm. Pharmcol., **25** (1973) 447.

[32] M. Susan, M. N. Rao, *Arzneim Forsch*, **42** (1992) 962.

[33] B. B. Aggarwal, A. Kumar, *Herb. And Trad. Med.: Mol. Asp. of Heal.,* (2004) 781.

[34] M. S. Hussain, N. Chandrasekara, *Ind. J. Med. Res.*, **96** (1992) 288

[35] K. K. Soudamini, M. C. Unnikrishnan, K. B. Soni, R. Kuttan, *Ind. J Physiol Pharmacol*, **36** (1992) 239.

[36] A. Mazumder, K. Raghavan, J. Weinstein, K. W. Kohn, Y. Pommier, *Biochem. Pharm.*, **49** (1995) 1165.

[37] Z. Sui, R. Salto, J. Li, C. Craik, P. R. Ortiz de Montellano, *Bioorg Med Chem,* **1** (1993) 415.

[38]http://www.mccormickscienceinstitute.com/assets/Aggarwal_BioandMedicinal.pdf

[39] http://www.crcnetbase.com/doi/abs/10.1201/9780203025901.ch36

[40] B. B. Aggarwal, B, Sung, *Trends in Pharmacological Sci,* **32** (2008) 85.

[41] R. K. Maheshwari, A. K. Singh, J. Giddipati, R. C. Srimal, *Life Sci.,* **78** (2006) 2081.

[42] S. K. Kulkarni, A. Dhir, *Ind. J. Pharma. Sci.*, (2010) 149.

[43] E. Sikora, G. Scapagnini, M. Barbagallo, *Immunity & Aging,* **7** (2010) 1.

[44] Bhawana, R. K. Basniwal, H. S. Buttar, V. K. Jain, N. Jain, *J. Agri, Food Chem.,* **59** (2011) 2056.

[45] M. M. Yallapa, D. M. Maher, V. Sundaram, M. C. Bell, M. Jaggi, S. C. Chauhan, *J. of Ovr. Res.,* **3** (2010) 1.

[46] M. M. Yallapa, M .Jaggi, S. C. Chauhan, *Drug Dis. Today,* **17** (2012) 71.

[47] P. Anand, H. B. Nair, B. Sung, A. B. Kunnumakkara, V. R. Yadav, R. R. Tekmal, B. B. Aggarwal, *Biochem. Pharmacol.,* **79** (2010) 330.

[48] A. Anitha, V. G. Deepagan, V. V. Divya Rani, D. Menon, S. V. Nair, R. Jayakumar, *Carbohydrate polymer,* **84** (2011) 1158.

[49] K. Sindhu, K. J. Sreeram, R. Rajaram, *J. Biomed. Nanotechnol,* **7** (2011) 56.

[50] P. Mistry, *Master's Thesis*, Creighton University, USA (2010).

[51] S. Devi, P. Prabhakaran, L. Filgueica, K. S. Iyer, C. L. Raston, *Nanoscale,* **4** (2012) 2575.

[52] A. Mathew, A. Arvind, T. Fukuda, T. Hasumura, Y. Nagaoka, Y. Yoshida, T. Mekawa, K. Venugopal, D. S. Kumar, *Nanotechnology,* IEEE – Nano, 15 – 16th August (2011) 833.

[53] C. H. Lin, F. Y. Chang, D. K. Hung, *Colloids Surf. B Biointerfaces,* **82** (2011) 63.

[54] C. Jing, Z. G. Xi, L. H. Xiang, *Ch. Pharmaceut. J.,* **39** (2005) 1877.

[55] X. Wu, J. Xu, X. Huang, C. Wen, *Drug Develop. & Ind. Pharm.,* **37** (2011) 15.

[56] W.Jianzhang, W. Cong, C. Yuepiao, Y. Shulin, Z. Xiaoyong, Q. Peihong, P. Jing, W. Xiaoping, L. Guang, L. Xiaokun, *Chin. J. of Org. Chem.*, **30** (2010) 884.

[57] P. Smaphui, N. R. Goud, U. B. R. Khandavilli, S. Bhanoth, A. Nangia, *ESI for Chem. Commun.* (2011) 51.

[58] G. Jiang, S. Yang, H. Zhou, L. Shao, K. Huang, J. Xiao, Z. Huang, X. Li, *Eur. J. Med. Chem.,* **44** (2009) 915.

[59] M. C. Lozada, R. G. Enriquez, B. Ortiz, M. S. Garcia, *Anal. Sci.: X – Ray Str. Anal. Online*, **24** (2008) XI.

[60] V. R. Yadav, S. Suresh, K. Devi, S. Yadav, *AAPS Pharma Sci Tech,* **10** (2009) 752.

[61] S. Jagmohan, *Organic Spectroscopy: Principles and Applications,* CRC Press, Boca Raton, Florida, USA (2000).

[62] D. R. Lide, *CRC Handbook of Chemistry and Physics,* CRC Press, (2008).

[63] A. W. Coats, J. P. Redfern, *Nature*, **201** (1964) 68.

[64] R. S. Boikess, E. Edelson, *Chemical Principles*, Harper & Row, New York, 178, 561.

[65] K. J. Laidler, *"Chemical Kinetics",* 3rd Ed.,Harper and Row, New York (1987).

Chapter – VIII

General Conclusion

The recent advances in science and technology have brought a great demand of various crystals with numerous applications. A multidisciplinary nature field in science and technology has been emerged in more than last fifty years, known as crystal growth, which deals with the crystal growth methods, crystals characterizations and crystal growth theories. Bio – crystallizations and bio – mineralizations are very important phenomena in which crystal growth of specific bio – material compounds occur in a body of living organism. This phenomenon is observed in the animal and plants there are many theories and reasons proposed for this.

These bio-crystallizations are not welcomed and the aim is always to suppress them. Studies show that the heart diseases are number one killer in the world and also in India. It was predicted by W.H.O. (World health Organization) that by 2010 the population of India would suffer approximately 60% of the world's heart disease. Globally around 60 million people suffer from Cardio Vascular Disease (CVD) annually. As per W.H.O. survey up to 2030 almost 23.6 million people will die from the CVD. Cholesterol is supposed to be the causative agent of coronary heart diseases like atherosclerosis and gall stones [1]. These bio – crystallizations and bio – mineralizations have deep social as well as economic impact. A large number of people are suffering from different ailments related to the bio – mineralization and bio – crystallization phenomenon. Occurrence of a bio – mineralization crystal in to a living tissue causes severe inflammation and

pain. The ailment can be dealt with by considering the three main aspects, i. e. prevention, relief and cure. In this direction the herbal medicine and Ayurveda give good hopes. People prefer herbal medicine as they in majority give less side effects as compared to the traditional allopathic medicines. In this direction the Reverse Pharmacology has to play important role.

Nanotechnology plays an important role in advanced biology and medical research particularly in the development of potential site specific delivery systems with lower drug toxicities and greater efficiencies [2]. The era of nanotechnology has allowed novel research strategies to flourish in the field of drug delivery.

Nanotechnology offers great visions of improved, personalized treatment of disease. The hope is that personalized medicine will make it possible to develop and administer the appropriate drug, at the appropriate dose, at the appropriate time to the appropriate patient. The benefits of this approach are accuracy, efficacy, safety and speed. Some techniques are only imagined, while others are at various stages of testing, or actually being used today. While some researchers use the term nanomedicine to refer to applications of nanoparticles currently under development, other researchers reserve the term nanomedicine to refer to longer range research that involves the use of manufactured nano-robots to make repairs at the cellular level. While nanomedicine potentially offers promising new value propositions and revenue streams, it also could completely displace certain classes of drugs. For example, currently-employed chemotherapeutic agents are being substituted with novel nanoparticle reformulations. Today, commercial nanomedicine is at a nascent stage of development and its full potential years

or decades away. Currently, the most advanced area of nanomedicine is the development and use of nanoparticles for drug delivery [3]

One treatment involves targeted chemotherapy that delivers a tumor-killing agent called tumor necrosis factor alpha (TNF) to cancer tumors. TNF is attached to a gold nanoparticle along with Thiol-derivatized polyethylene glycol (PEG-THIOL), which hides the TNF bearing nanoparticle from the immune system. This allows the nanoparticle to flow through the blood stream without being attacked. This targeted chemotherapy method to deliver TNF and other chemotherapy drug to cancer tumours is developed by CytImmune company [4].

Iron (III) oxide nanoparticles can be used to improve MRI images of cancer tumors. The nanoparticle is coated with a peptide that binds to a cancer tumor. Once the nanoparticles are attached to the tumor, the magnetic property of the iron oxide enhances the images from the Magnetic Resonance Imagining scan. Magnetic nanoparticles that attach to cancer cells in the blood stream may allow the cancer cells to be removed before they establish new tumors [5].

Nano – particle formations by super para magnetic iron oxide, gadolinium, perflurocarbon and special polymers will enhance *in vivo* imaging capability of detection of tumors, plaques, genetic defects and other diseases at much earlier stages with lower, safer concentration of injected compounds. The demand for non diagnostic product was 8.4 billion US$ and will be 12 billion US$ in 2016. Besides pharmaceutical and diagnostic products, several medical supplies and devices have emerged as key application to nano

technology. Nano materials are getting demand as active ingredients of burn dressing, bone cement, bone substitute and dental products. In 2016 demand of medical supplies and devices based at least partially on nano materials will be 16.2 billon US$ [6,7].

Way back in 2006, Wagner *et al.* [8] has reviewed nano medicine product in market based on health care application, composition, *in vivo* imaging, *in vitro* diagnostics, bio materials and nano crystalline drug products by giving composition, indication and company (manufacturer) details. For example nano crystal drugs like Megasterol acetate is used for apatite stimulant (Trade Name: MEGACE®ES) marketed by PAR Pharmaceuticals. In the fray of developing drugs based on nano crystalline products, the giants like MERCK, ABBOTT, WYETH, NOVATIS etc. have entered. A good review articles are available discussing nano technology in medicine and pharmaceutical science [3,9,10].

The present author has grown bulk crystals of APIs and synthesized the nano particles of the same, looking at various drug applications of nano crystalline APIs bio-materials; the author has summarized the salient features and conclusions as follows.

1. The two compounds of Active Pharmaceutical Ingredient (API) crystals, n-Butyl 4 - (3,4-dimethoxyphenyl) – 6 – methyl – 2 – thioxo – 1,2,3,4 tetrahydropyrimidine – 5 – carboxylate and 1-phenyl-3-(propan-2-yl)-1*H*-pyrazol-5-ol,are grown by slow non-aqueous solvent evaporation technique and characterized by various techniques. The unit cell parameter

determination by using powder X – Ray Diffraction, FTIR study, thermal study, dielectric study, thermodynamic and kinetic parameter study, etc.

2. The two API compounds nano particles are synthesized by micro-emulsion techniques using water/ n – butanol/ triton X – 100 and water/ triton X – 100/ n – heptane system for n-Butyl 4 - (3,4-dimethoxyphenyl) – 6 – methyl – 2 – thioxo – 1,2,3,4 tetrahydropyrimidine – 5 – carboxylate and 1-phenyl-3-(propan-2-yl)-1*H*-pyrazol-5-ol, respectively. Nano particles nature was confirmed by TEM and Powder XRD. The FTIR, thermal and dielectric studies as well as thermodynamic and kinetic parameters studies were carried out

3. It was found that there was no change in FTIR spectra of the APIs as the particle size reduces from crystal to nano. The powder XRD patterns exhibited the same crystalline system as the bulk crystalline, but with characteristic peak broadening. TG curves of both the APIs showed that the nano particles were having more thermal stability then that of crystalline API materials. As the particle size reduces surface to volume ratio increases so more number of molecules comes on the surface and they can sustain more thermal energy than that of micro crystals may be due to higher surface energy. As far as pharmaceutical ingredients are concerned, it is advantageous because the higher thermal stability brings less possibility of thermal degradation at preservation temperature, which increases the shelf life and no need to preserve at cool places- like refrigerators. The value of Activation Energy is higher than that of crystal substance, which means that he nano particles are more stable then crystals. The same was confirmed from the thermodynamic parameters.

4. Cholesterol crystals were grown by using single diffusion gel growth technique; grown crystals were characterized by Powder XRD, FT-IR, SEM, AFM, Thermal study, Kinetic and Thermodynamic parameters and dielectric study. Cholesterol nano particles were synthesized by micro-emulsion techniques using water/ n – butanol/ triton X – 100. Synthesized nano particles were characterized by TEM, Powder XRD, DLS, Thermal, Thermodynamic and Kinetic parameters. The nano particles of cholesterol showed higher thermal stability than that of nano particles, which is probably the reason that the nano cholesterol is used as coating for the drugs used for ovarian cancer. The value of activation energy was also high for nano particles of cholesterols indicating high thermal stability. By using the data of DLS study, it was found that 0.22 cholesterol nano particle per water core was available, which indicated there were some empty water cores also.

5. SEM and AFM study of cholesterol crystals exhibited steps on the surface of the crystal, which was significant in cholesterol crystal growth.

6. In the *in vitro* growth inhibition studies of cholesterol crystals by *Fagonia cretica L.* extract, the growth rate of crystals in pure and *Fagonia cretica L* extract containing test tubes were recorded up to 8 days. From the periodic measurements of the length and breadth of growing crystals, the growth inhibition due to *Fagonia cretica L* extract was proved. This has important therapeutic implication.

7. Turmeric (*Curcuma longa*), a common Indian dietary pigment and spice, possesses a wide range of therapeutic utilities in the traditional Indian medicine. The active component of turmeric, identified as Curcumin, which is

found in the rhizome of *Curcuma longa.* The nano – particles of Curcumin were synthesized by using w/o microemulsion technique with mixture of water/ Triton X – 100/n - hexane. Synthesized nano particles were characterized by Powder XRD, TEM, FTIR, Thermal Study, Thermodynamic and Kinetic parameters. Curcumin shows two tautomers having two crystal systems monoclinic and orthorhombic. In the present study curcumin showed orthorhombic crystal system with unit cell parameters: *a*=35.256 Å, *b*=7.7712 Å, *c*=12.6743 Å. FTIR confirmed the presence of O – H, C – H, C = O, C – O and aromatic ring substitution. Thermogravimetry indicated thermal stability up to 260^0C.

References

[1] I. Thabrew, R. M. Ayling, C. Wicks, *Biochemistry for Clinical Medicine,* Greenwich, Medical Media, London, UK (2001).

[2] R. Ramachandran, P. Shanmughavel, *Ind. J. Biochem. Biophys.,* **47** (2010) 56.

[3] N. Haque, R. R. Khalel, N. Parvez, S. Yadav, N. Hwisa, M. S. Al-Sharif, B. Z. Awen, K. Molvi, *J.Chem. Pharm. Res.,* **2** (2010) 161.

[4] www.cytimmune.com

[5] http://www.physorg.com/news65705979.html

[6] http://www.fredonoiagroup.com; *Nanotechnology in health care U S Industry study with forecast 2011, 2016 & 2021 study # 2168, Feb 2007.*

[7] http://www.ema.europa.en; *1st International Workshop on Nanomedicine 2010, European medicines agency.*

[8] V. Wagner, A. Dullaart, A. K. Bock, A. Zweek, *Nature Biotech.,* **24** (2006) 1211.

[9] M. Patel, A. Shah, N. M. Patel, M. R. Patel, K. R. Patel, *J. Pharm. Sci. and Bioscie. Res.,* **1** (2011) 1

[10] E. A. Martis, R. B. Badve, M. D. Degwekar, *Chronical of Young Scientist*, **3** (2012) 68.

Suggestion for future work

1. To find out the Biological activity of bulk API and nano API of the studied systems and compare it.

2. To Study other well known API systems for both bulk materials and nano particles by taking various emulsion systems.

3. By comparing mechanical properties of bulk materials and nano materials, the effect of particle size can be studied. For nano-materials the nano-indentation technique can be used.

4. To study the growth and inhibition of cholesterol crystals by taking *Allium sativum* (garlic), Terminalia Arjuna (arjuna) and other herbal extracts.

5. Taking AFM of control and herbal extract grown crystals for the comparison.

6. Encapsulation of nanoparticles of APIs in suitable coating material.

7. Study of various micro-emulsion systems which are non toxic for direct application and delivery of nanoparticles in a body.

Research Paper Publication

1. "*Thermal, FT – IR and Dielectric Studies of Gel grown Sodium Oxalate Crystals*"

B. B. Parekh, **P. M. Vyas**, Sonal R. Vasant and M. J. Joshi

Bull. Mater. Sci, **31** (2008) 143 – 148.

2. "*Synthesis of nano – particle of Calcium Pyrophosphate Dihydrate*"

S. R. Vasant, K. P. Tank, **P. M. Vyas**, K. B. Mehta, B. B. Parekh and M. J. Joshi

Med. J. D. Y. Patil Uni., **2** (2009) 166 – 170.

3. **"*Growth and characterization of Bis Thiourea Strontium Chloride Single Crystals*"**

R. R. Hajiyani, D. J. Dave, C. K. Chauhan, **P. M. Vyas** and M. J. Joshi

Modern Phys. Lett. B, **24** (2010) 735 -747.

4. **"*Synthesis and Characterization of n-Butyl 4-(3, 4-dimethoxyphenyl) – 6–methyl–2– thioxo– 1,2,3,4 tetrahydropyrimidine – 5 – carboxylate crystals*"**

P. M. Vyas, A. M. Pansuriya, Y. T. Naliyapara and M. J. Joshi

Proceedings of the National Symposium on Growth of Detector Grade Single Crystals (NSGDSC - 09), Bhabha Atomic Research Centre (BARC), (2009), Mumbai, p.118 -121.

5. "*Synthesis and Characterization of Cholesterol nanoparticles by using w/o microemulsion technique*"

P. M. Vyas, S. R. Vasant, R. R. Hajiyani and M. J. Joshi

AIP Conference Proceedings, **1276** (2010) 198 – 209.

6. "*Growth and characterization of Struvite-K crystals"*

C. K. Chauhan, **P. M. Vyas** and M. J. Joshi

Cryst. Res. and Technol., **46** (2011) 187 – 194.

7. **"*Synthesis and Characterization of N-butyl 4-(3,4 - dimethoxyphenyl)– 6 – ethyl – 2 – thioxo –1,2,3,4 tetrahydropyrimidine – 5 – carboxylate nanocrystalline particles by w/o microemulsion method*"**

   P. M. Vyas, M. J. Joshi, A. M. Pansuriya and Y. T. Naliapara

   Int. J. of Nanosci. , **10** (2011)1237 – 1244.

8. **"*Co-crystallization of Two Tautomers: 1-Phenyl-3-(propan-2-yl)-1,2-dihydropyrazol- 5-one and 1-Phenyl-3-(propan-2-yl)-1H-pyrazol-5-ol*"**

   K. Kapoor, V. K. Gupta, Rajnikant, **P. M. Vyas**, M. J. Joshi, S. D. Tada, S. M. Sorathia, H. S. Joshi

   X-ray Structure Analysis Online, **27** (2011) 59 – 60.

9. ***"(E)-N_-{7-Methoxyspiro[chromeno[4,3-d]thiazole-4,1_-cyclohexan]-2-yl}-N,N-dimethylacetimidamide"***

   K. Kapoor, V. K. Gupta, Rajnikant, **P. M. Vyas**, M. J. Joshi, K. M. Menpara and K. D. Ladva

   Acta Crystal. E, **67** (2011) o2855 – o2856.

10. **"*Synthesis and Characterization of 1-phenyl-3-(propan-2-yl)-1H-pyrazol-5-ol single crystals*"**

    P. M. Vyas, J. D. Akbari, S. D. Tada, H. S. Joshi and M. J. Joshi

    Cryst. Res. and Technol., **47** (2012) 763 – 770.

11. ***"Growth and Characterization of L – Arginine doped ADP crystals"***

    R. R. Gohel, **P. M. Vyas**, D. J. Dave, K. D. Parikh and M. J. Joshi

    Recent Trends in Func. Mater. Res., Proceeding of National Workshop on Functional Oxides, Nanomaterials and Devices, (2012), 27 – 28.

Research Papers Presented at International, National and State level Conferences

➢ International Conferences

1. ***"Synthesis of nanocrystalline Hydroxyapatite by wet chemical process and in vitro dissolution study"***

K. P. Tank, **P. M. Vyas**, Bharat B. Parekh and M. J. Joshi

10^{th} International Conference on Advanced Materials, 8^{th} – 10^{th} October, 2007, Bangalore.

2. ***"Synthesis of nanoparticles of Calcium Pyrophosphate Dihydrate"***

S. R. Vasant, K. P. Tank, **P. M. Vyas**, K. B. Mehta, B. B. Parekh and M. J. Joshi

International Conference on Biomedical engineering and nanotechnology, 21^{st} – 23^{rd} October, 2008, D. Y. Patil University, Kolhapur.

3. ***"Synthesis and Characterization of Cholesterol nano particles by using w/o microemulsion technique"***

P. M. Vyas, S. R. Vasant, R. R. Hajiyani and M. J. Joshi

International Conference on Advanced in Nanoscience and Nanotechnology, 9^{th} – 11^{th} December, 2009, IIT – Guwahati, Guwahati.

4. ***"Thermal and Dielectric studies of n-Butyl 4-(3, 4-dimethoxyphenyl) – 6–methyl– 2– thioxo– 1,2,3,4 tetrahydropyrimidine – 5 – carboxylate Crystals"***

P. M. Vyas, A. M. Pansuriya, Y. T. Naliapara, B. B. Parekh and M. J. Joshi

9^{th} International Workshop on Crystal Growth of Organic Materials, 4^{th} – 7^{th} August, 2010 Nanyang Technological University, Singapore.

5. ***"Study of L – arginine Doped Ammonium Dihydrogen Phosphate Crystals"***

   M. J. Joshi, R. R. Gohel, **P. M. Vyas**, D. J. Dave, K. D. Parikh, B. B. Parekh

   16th International Conference on Crystal Growth, 8th – 13th August, 2010, Beijing, China.

6. ***"Growth and Characterization of Potassium Magnesium Phosphate Crystals"***

   C. K. Chauhan, **P. M. Vyas**, M. J. Joshi

   16th International Conference on Crystal Growth, 8th – 13th August, 2010, Beijing, China.

7. ***"Growth and Characterization of Pure and Dye Doped Calcium Levo-Tartrate Single Crystals using Silica Gel Column"***

   J. A. Shah, **P. M. Vyas**, S. R. Vasant, V. S. Joshi and M. J. Joshi

   International Conference on Materials for Advanced technologies – 2011, 26th June – 1st July, 2011, Singapore.

8. ***"Synthesis and Characterization of n-Butyl 4- (3, 4 - dimethoxyphenyl) – 6 – methyl – 2 – thioxo – 1,2,3,4 tetrahydropyrimidine – 5 – Carboxylate nanoparticles using w/o microemulsion technique"***

   P. M. Vyas, A. M. Pansuriya, Y. T. Naliapara, C. K. Chauhan and M. J. Joshi

   15th International Conference of Indian Society of Biologist and Chemist, 4th – 7th February, 2011, Saurashtra University, Rajkot.

9. ***"Synthesis and characterization of 5-isopropyl-2-phenyl-2,4-dihydro-3H- pyrazole- 3- one nano particles by using w/o microemulsion technique"***

   P. M. Vyas, S. R. Vasant, J. D. Akbari, H. S. Joshi and M. J. Joshi

15th International Conference of Indian Society of Biologist and Chemist, 4th – 7th February, 2011, Saurashtra University, Rajkot.

10. "***Growth and characterization of Curcumin nano particles by using w/o microemulsion technique"***

P. M. Vyas, M. J. Joshi and A. B. Vaidya

International Conference on Advanced Materials, 12th – 16 th December, 2011, PSG College of Technology, Coimbatore.

11. ***"Effect of Fagonia crettica Linn in the in vitro inhibition of Cholesterol Crystals"***

P. M. Vyas, L. D. Chariya, V. B. Mandaliya, V. S. Thaker and M. J. Joshi

6th National Convention of Society of Pharmacognosy and International Symposium on Herbal and traditional Medicine, 9th – 11th March, 2012, Department of Pharmaceutical Sciences, Saurashtra University, Rajkot.

➢ National Conferences

1. ***"Growth and Characterization of Sodium Oxalate Crystals"***

B. B. Parekh, **P. M. Vyas** and M. J. Joshi

11th National Seminar on Crystal Growth, 7th – 9th December, 2006, SSN Nagar, Kalavakkam, Chennai.

2. ***"Growth Inhibition of Struvite crystals in the presence of citrus medica linn"***

C. K. Chauhan, L. K. Maniar, R. M. Vaisnav, **P. M. Vyas**, K. P. Tank, D. D. Khunti and M. J. Joshi

11th National Seminar on Crystal Growth, 7th – 9th December, 2006, SSN Nagar, Kalavakkam, Chennai.

3. ***"Dielectric Study of Mn^{++} doped ADP Crystals"***

P. M. Vyas, P. Kurani, B. B. Parekh, K. D. Parikh and M. J. Joshi

One Day National Seminar on Recent Trends in Material Science, 25th March, 2007, Department Of Physics, Saurashtra University, Rajkot

4. ***"Growth and Characterization of gel grown Calcium Pyrophosphate Crystals"***

B. B. Parekh, **P. M. Vyas** and M. J. Joshi

One Day National Seminar on Recent Trends in Material Science, 25th March, 2007, Department Of Physics, Saurashtra University, Rajkot

5. ***"Growth and Characterization of 4 – (2 – hydroxyl – phenylamino) – Pent – 3 en – 2 – one crystals"***

B. B. Parekh, H. S. Joshi, **P. M. Vyas** and M. J. Joshi

12th National Seminar on Crystal Growth, 21st – 23rd December, 2007, SSN Nagar, Kalavakkam, Chennai.

6. ***"Etching L – Histidine, DL – Methionine and L – threonine doped KDP crystals"***

D. J. Dave, K. D. Parikh, **P. M. Vyas**, R. R. Hajiyani, K. B. Mehta, R. R. Gohel and M. J. Joshi

12th National Seminar on Crystal Growth, 21st – 23rd December, 2007, SSN Nagar, Kalavakkam, Chennai.

7. ***"Growth and Thermal and Kinetic parameters of 4 – (2 – hydroxyl – phenylamino) – pent – 3 en – 2 – one crystals"***

B. B. Parekh, **P. M. Vyas,** D. J. Dave**,** R. R. Hajiyani and M. J. Joshi

Seminar on Advances in Material Research, 15th February, 2008, Department of Physics, Saurashtra University, Rajkot

8. ***"Synthesis and Characterization of n-Butyl 4-(3, 4-dimethoxyphenyl) – 6–methyl– 2– thioxo– 1,2,3,4 tetrahydropyrimidine – 5 – carboxylate crystals"***

P. M. Vyas, A. M. Pansuriya, Y. T. Naliapara and M. J. Joshi

National Symposium on Growth of Detector Grade Single Crystals, 23rd – 26th November, 2009, Bhabha Atomic Research Centre, Mumbai

9. ***"Growth and Single Crystal XRD study of 4 - (2 - hydroxyphenylamino) –pent–3-en–2-one crystals"***

P. M. Vyas, B. B. Parekh, D. H. Purohit, H. S. Joshi and M. J. Joshi

National Workshop on X – Ray Diffraction Studies, 17th – 19th March 2010, Department of Physics, Saurashtra University, Rajkot

10. ***"Growth, Powder XRD, Thermal and Dielectric studies of Cholesterol Crystals"***

P. M. Vyas, S. R. Vasant, C. K. Chauhan, H. S. Joshi and M. J. Joshi

39th National Seminar on Crystallography, 25th – 27th October, 2010, Department of Physics and Electronics, University of Jammu, Jammu

11. ***"Growth, Powder XRD and FT – IR spectroscopy studies of KNO_3 added KDP Crystals"***

R. G. Mansuriya, **P. M. Vyas**, B. B. Parekh, K. D. Parikh, D. J. Dave and M. J. Joshi

39th National Seminar on Crystallography, 25th – 27th October, 2010, Department of Physics and Electronics, University of Jammu, Jammu

12. ***"Growth, FT-IR Spectroscopy, Thermogravimetry and Chemical Etching Studies of Potassium Pentaborate Crystals"***

H. S. Jani, **P. M. Vyas**, S. R. Vasant, K. P. Tank, C. K. Chauhan, B. B. Parekh and M. J. Joshi

XV National Seminar on Crystal Growth, 23rd - 25th February, 2011, PSN College of Engineering and Technology, Tirunnelveli

13. ***"Growth and Characterization of L – arginine Doped ADP Crystals"***

R. R. Gohel, **P. M. Vyas,** D. J. Dave**,** K. D. Parikh and M. J. Joshi

National Workshop on Function Oxides, Nano materials and Device

Application, 1st – 2nd March, 2012Department of Physics, Saurashtra University, Rajkot

14. ***"Surface Micro Topographical and Dielectric studies of Cholesterol crystals"***

P. M. Vyas and M. J. Joshi

5th National Conference on Condensed Matter and Materials Physics, 3rd – 5th March, 2012, Department of Physics, Vallabbh Vidyanagar

15. ***"Growth and Characterization of Cholesterol Crystals by Using Various Solvents"***

A. Zinzuvadia, K. S. Ravaliya, N. B. Pujara and **P. M. Vyas**

5th National Level Science Symposium on Recent Trends in Science and Technology, 18th March, 2012, Christ College, Rajkot.

16. ***"Growth of Struvite Crystals by Using Various Beverages"***

M. Solanki, D. Solanki, N. Sodahatar and **P. M. Vyas**

5th National Level Science Symposium on Recent Trends in Science and Technology, 18th March, 2012, Christ College, Rajkot.

17. ***"Characterization of Struvite Crystals Grown by using Various Beverages"***

P. Y. Raval, R. N. Purohit, B. H. Raja and **P. M. Vyas**

5th National Level Science Symposium on Recent Trends in Science and Technology, Christ College, Rajkot, 18th March, 2012.

- **State Level Conferences**

1. ***"Growth of Cholesterol Crystals"***

P. M. Vyas, B. B. Parekh and M. J. Joshi

21st Gujarat Science Congress, 11th March, 2007, Hemchandracharya North Gujarat University, Patan

2. *"Synthesis and Characterization of Zn doped nanohydroxyapatite"*

K. P. Tank, S. R. Vasant, B. B. Parekh, **P. M. Vyas**, R. R. Gohel and M. J. Joshi

23rd Gujarat Science Congress, 15th February, 2009, Veer Narmad South Gujarat University, Surat

❖ **AWARDS**

1. **Best oral Presentation** in 12th National Seminar on Crystal Growth, SSN Nagar, Chennai.
2. **First Prize - Oral Presentation** in Physics Section at 23rd Gujarat Science Congress, Veer Narmad South Gujarat University, Surat.
3. **Best Oral Presentation** in 5th National Conference on Condensed Matter and Materials Physics, Department of Physics, Sardar Patel University, Vallabh Vidyanagar.
4. **Second Prize - Poster Presentation** in 5th National Level Science Symposium on Recent Trends in Science and Technology, Christ College, Rajkot.

Bull. Mater. Sci., Vol. 31, No. 2, April 2008, pp. 143–147. © Indian Academy of Sciences.

Thermal, FT–IR and dielectric studies of gel grown sodium oxalate single crystals

B B PAREKH[†], P M VYAS, SONAL R VASANT and M J JOSHI*

Physics Department, Saurashtra University, Rajkot 360 005, India

[†]Institute of Diploma Studies, Nirma University of Science and Technology, Ahmedabad 384 481, India

MS received 29 October 2007; revised 25 January 2008

Abstract. **Oxalic acid metabolism is important in humans, animals and plants. The effect of oxalic acid sodium salt is widely studied in living body. The growth of sodium oxalate single crystals by gel growth is reported, which can be used to mimic the growth of crystals *in vivo*. The grown single crystals are colourless, transparent and prismatic. The crystals have been characterized by thermogravimetric analysis, FT–IR spectroscopy and dielectric response at various frequencies of applied field. The crystals become anhydrous at 129·3°C. Coats and Redfern relation is applied to evaluate the kinetic and thermodynamic parameters of dehydration. The dielectric study suggests very less variation of dielectric constant with frequency of applied field in the range of 1 kHz–1 MHz. The nature of variation of imaginary part of complex permittivity, dielectric loss and a.c. resistivity with applied frequency has been reported.**

Keywords. **Gel growth; FT–IR; TGA; dielectric study; kinetic parameters; thermodynamic parameters.**

1. Introduction

Oxalic acid and its salts play an important role in human body, animals, plants and micro-organisms. Oxalic acid is produced naturally in body when ascorbic acid and glycine are metabolized. Oxalic acid metabolisms in man (Hodgkinson and Zarembski 1968) and in oxalate accumulating plants (Yang and Loewus 1975; Caliskan 2000) have been explained. Oxalic acid metabolism responsible for increased mean plasma oxalic acid level leading to renal failure is studied (Balcke 1985). Increased plasma oxalic acid levels may be important for calcium oxalate deposits in uraemia (clinical syndrome due to renal failure). Sodium salt of oxalic acid, sodium oxalate, is highly toxic through all routes of exposure, having industrial applications such as in metal cleaning, leather tanning, electroplating bath, etc. The effect of sodium oxalate on living body has been widely reported. When rat received 10 mg of sodium oxalate for 30 days, the presence of renal tubular dilation with oxalate deposits (or stenosis) was found (Ono and Kikawa 1989). Oxalate crystals in rat kidneys by intraperitoneal (within peritoneal cavity) administration of sodium oxalate have been reported (Tawashi *et al* 1980). On the other hand, temporary paralysis of vagus mechanism in turtle heart by sodium citrate and sodium oxalate is reported (Shaefer 1936). Also, sodium oxalate toxicity has been discussed in terms of acute renal failure following its ingestion (Hamilton *et al* 1999).

Slow diffusion of reactants in the gel medium can be considered to mimic the growth of crystals in a body (Joseph *et al* 2005). Various roles of sodium oxalate crystals have prompted the present authors to study the growth of sodium oxalate crystals by gel method and characterize them by different techniques, viz. thermogravimetry, FT–IR and dielectric study.

2. Experimental

2.1 *Crystal growth*

The growth of sodium oxalate crystals has been carried out using single diffusion gel growth technique. Glass test tubes of 25 mm diameter and 150 mm length were used as crystal growth apparatus. Sodium metasilicate solution of 1·05 specific gravity was acidified by 3N acetic acid in such a manner that pH 5 could be set for the mixture. This was transferred into different test tubes and allowed to set into the gel form. Thereafter, 1·5 M oxalic acid solution was poured onto the set gel. After a few days good quality, colourless, transparent, prismatic, single crystals of sodium oxalate were grown, which is shown in figure 1.

When sodium metasilicate goes into solution, monosilicic acid is expected to be produced (Henisch 1996) according to the following reaction

*Author for correspondence (mshilp24@rediffmail.com)

$$Na_2SiO_3 + 3H_2O = H_4SiO_4 + 2NaOH.$$

This sodium hydroxide is expected to react with oxalic acid diffusing in a gel from the supernatant solution and forming sodium oxalate by the following reaction

$$2NaOH + H_2C_2O_4 = Na_2C_2O_4 + 4H_2O.$$

2.2 *Characterization technique*

The crystals were characterized by three different techniques. The FT–IR spectrum was recorded on BRUCKER IFS 66V FT–IR spectrometer in the range from 400–4000 cm^{-1} in KBr medium. The thermogravimetry analysis (TGA) was carried out using NETZSCH Geratebau GmbH from room temperature to 1000°C at a heating rate of 28°C/min. The dielectric measurements were carried out on powdered sample pellets at room temperature by using LCR meter model Agilent 4284-A, in the frequency range from 500 Hz–1 MHz.

3. Results and discussion

The presence of oxalates of metals is wide spread. Many times these minerals are formed as a result of expulsion of heavy metals from fungi, lichens and plants (Frey-Wyssling 1981; Arnott and Webb 1983; Chisholm *et al* 1987). Many oxalates exist in nature, for example, copper oxalate or moolooite (Chisholm *et al* 1987; Clarke and Williams 1986), ferrous oxalate or humboldtine (Manasse 1911; Rezek *et al* 1988), sodium oxalate or natroxalate and ammonium oxalate or oxammite (Winchell and Benoit 1951).

Figure 1. Growth of sodium oxalate monohydrate crystals in silica hydro-gel.

The crystal structure of sodium oxalate has been determined (Jeffrey and Parry 1954) with unit cell parameters obtained as $a = 10{\cdot}35 \pm 0{\cdot}02$ Å, $b = 5{\cdot}26 \pm 0{\cdot}02$ Å, $c = 3{\cdot}46 \pm 0{\cdot}02$ Å and $\beta = 92°54' \pm 6'$. Altogether, neutron diffraction study of sodium oxalate monohydrate crystal is reported at 123°K (Pederson and Kvick 1989). Mostly the growth of sodium oxalate is reported by aqueous solution method. The growth of sodium oxalate by aqueous solution slow evaporation technique and structural refinement is carried out (Reed and Ohnstead 1981). In another study, the growth from aqueous solution and *in situ* optical microscopic and atomic force microscopic observations are reported (Lowe *et al* 2002). The growth of single crystals has been monitored by optical microscopy on {001} and {200} faces. The {001} and {200} faces have been imaged at low supersaturation and room temperature display steps spreading with some apparent nucleation.

Thermal studies of certain oxalates of metals have been reported. Calcium oxalate monohydrate (Girija *et al* 1998) and humboldtine–ferrous oxalate (Frost and Weier 2004) have been investigated by conducting thermal analysis. In the present study, TGA of sodium oxalate was carried out up to 1000°C at a heating rate of 28°C/min. The thermogram is shown in figure 2. From the thermogram one can observe that the sample lost its water molecules at 129·3°C and became anhydrous. In the second stage, at 259·7°C the loss of 2CO is observed and in the following stage the $\frac{1}{2}O_2$ is lost at 556·9°C. However, one water molecule was found to be associated with sodium oxalate crystals. Table 1 represents the decomposition process of sodium oxalate crystals.

Usually, the pyrolysis occurs through many stepped mechanisms. Various kinetic parameters such as the order of reaction, the frequency factor and the activation energy can be calculated from the thermogram. The authors have applied the Coats and Redfern relation (Coats and Redfern 1964) to evaluate the kinetic parameters for dehydration process from the thermogram. The Coats and Redfern relation is as follows, which has been discussed in detail elsewhere (Parekh and Joshi 2007)

$$\log_{10}[\{1 - (1 - \alpha)^{1-n}\}/\{T^2(1 - n)\}] = \{\log_{10}[AR/\alpha E]\cdot[1 - 2RT/E]\} - \{E/2{\cdot}3RT\}, \quad (1)$$

where a is the fraction of the original substance decomposed at time t, $a = (W_0 - W)/(W_0 - W_f)$, W_0 the initial weight, W the weight at time t, W_f the final weight, n the order of reaction, A the frequency factor, E the activation energy, R a gas constant and a the heating rate in deg min^{-1}. Figure 3 is the best linear fitted plot for Coats and Redfern relation for $n = 0$. The values of activation energy and frequency factors were calculated from the plot, which are given in table 2. Thermodynamic parameters were also calculated using standard formulae reported elsewhere (Parekh and Joshi 2007). Table 2 shows the values of these parameters. The standard enthalpy,

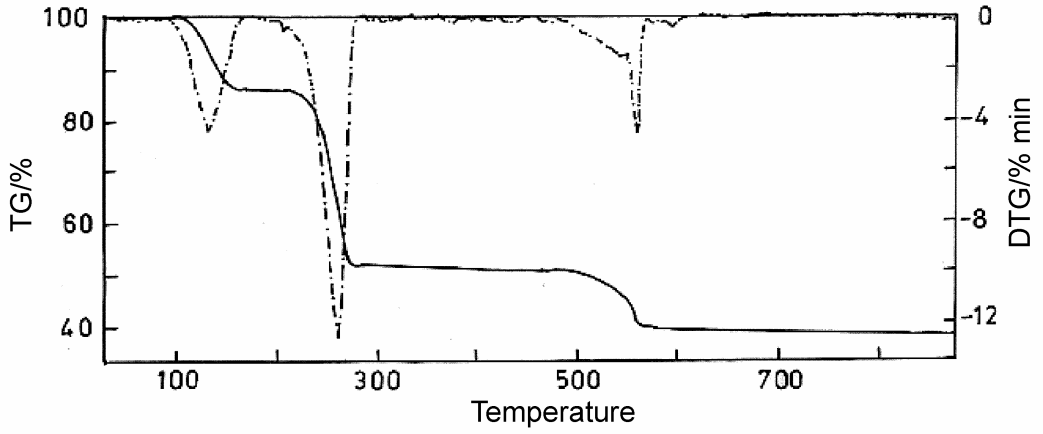

Figure 2. Thermogram of sodium oxalate monohydrate.

Table 1. Decomposition process of sodium oxalate monohydrate crystals and TG results.

Temperature (°C)	Substance	Theoretical weight (%) (calculated)	Practical weight (%) (from graph)
Room temperature	$Na_2C_2O_4{\cdot}1{\cdot}21H_2O$	100	100
129·3°C	$Na_2C_2O_4$	85·99	85·99
259·7°C	Na_2O_2	50·19	51·62
556·9°C	Na_2O	39·88	39·95

Table 2. Kinetic and thermodynamic parameters of dehydration of sodium oxalate monohydrate.

Kinetic parameters	Thermodynamic parameters
Order of reaction (n) = 0	Standard entropy $\Delta^{\#}S^{o}$ = 82·1696 J mol^{-1}
Activation energy (E) = 62·414 kJ mol^{-1}	Standard enthalpy $\Delta^{\#}H^{o}$ = 53·708 kJ mol^{-1}
Frequency factor (A) = 2·141 × 10^{17}	Standard Gibbs free energy $\Delta^{\#}G^{o}$ = 10·684 kJ mol^{-1}
	Standard change in internal energy $\Delta^{\#}U^{o}$ = 58·0616 mol^{-1}

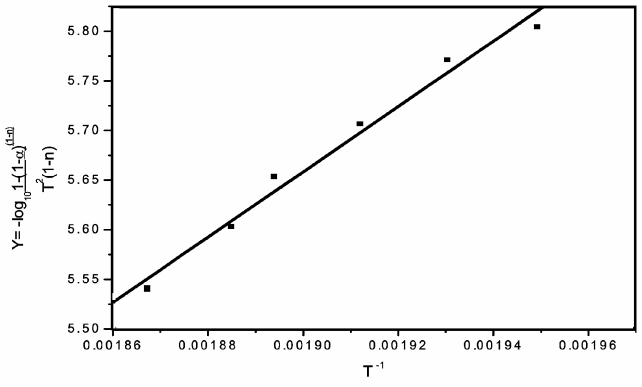

Figure 3. Plot of Coats and Redfern relation for sodium oxalate crystals.

$\Delta^{\#}H^{o}$, is positive, which indicates that the reaction is endothermic. The positive value of standard change in entropy, $\Delta^{\#}S^{o}$, indicates spontaneous type process. Also, the positive value of standard change in Gibbs free energy, $\Delta^{\#}G^{o}$, suggests spontaneous reaction.

The FT–IR spectroscopic studies of humboldtine ($FeC_2O_42H_2O$) (Frost and Weier 2004) and calcium oxalate monohydrate (Joshi 2001) have been reported. The FT–IR spectrum of sodium oxalate monohydrate is shown in figure 4. The absorptions between 418 cm^{-1} and 600 cm^{-1} show the presence of oxygen metal bonds. Broad absorptions at 1741·6 cm^{-1} and 1613·3 cm^{-1} indicate the presence of more than one C=O bond, while absorptions at 885·3 cm^{-1}, 1029·6 cm^{-1} and 1236·3 cm^{-1} are due to C–C stretching vibrations. The presence of water of hydration is primarily confirmed by the presence of a sharp dip at 3407 cm^{-1}, which is due to O–H stretching.

Dielectric study of hydrated barium oxalate and cadmium oxalate crystals have been reported (Dharmaprakash and Rao 1989). The nature of variation of dielectric constant with frequency indicated that the higher space charge polarizability was present in the lower frequency region. The variation of dielectric constant with frequency is

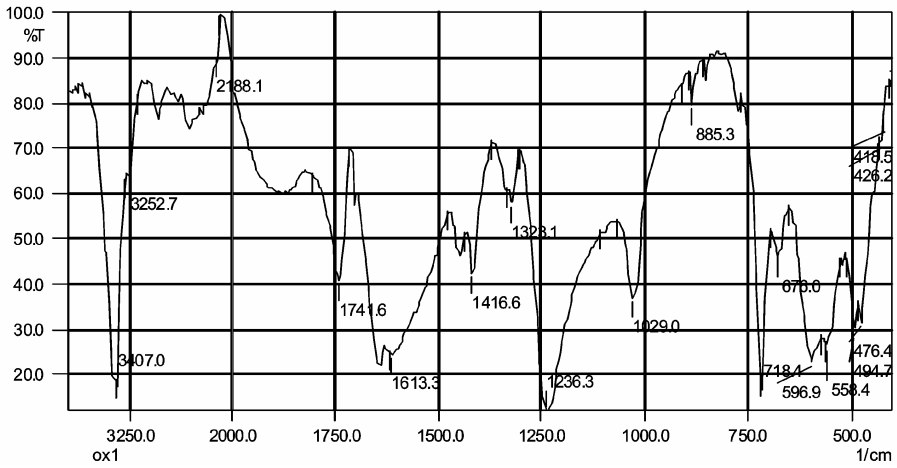

Figure 4. FT–IR spectrum of sodium oxalate crystals.

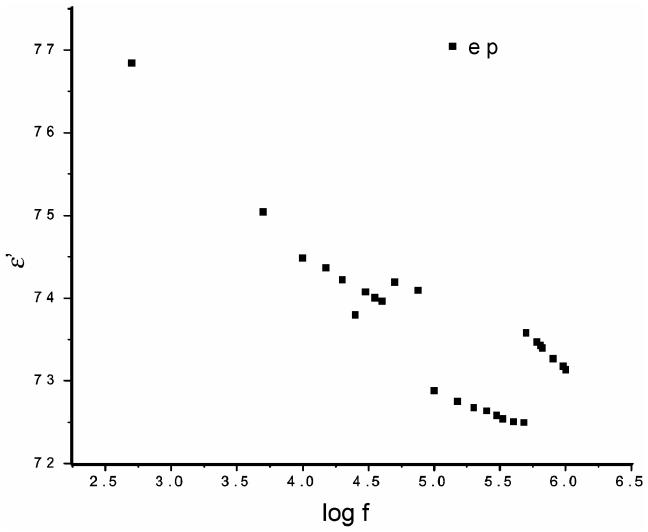

Figure 5. Plot of dielectric constant vs frequency of applied field.

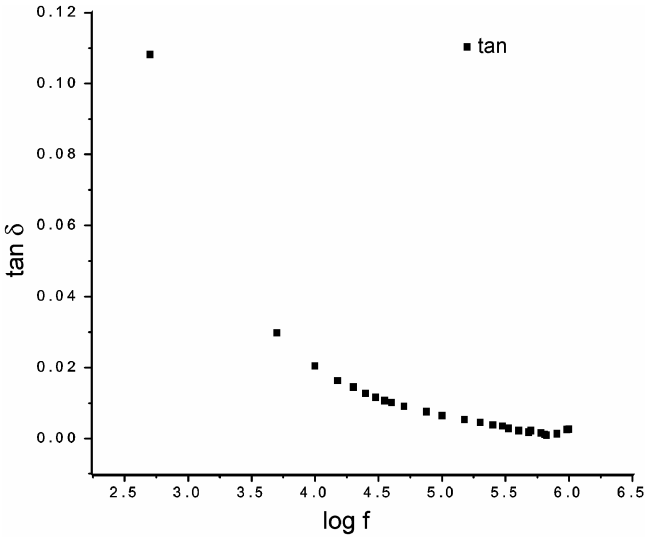

Figure 6. Plot of dielectric loss vs frequency of applied field.

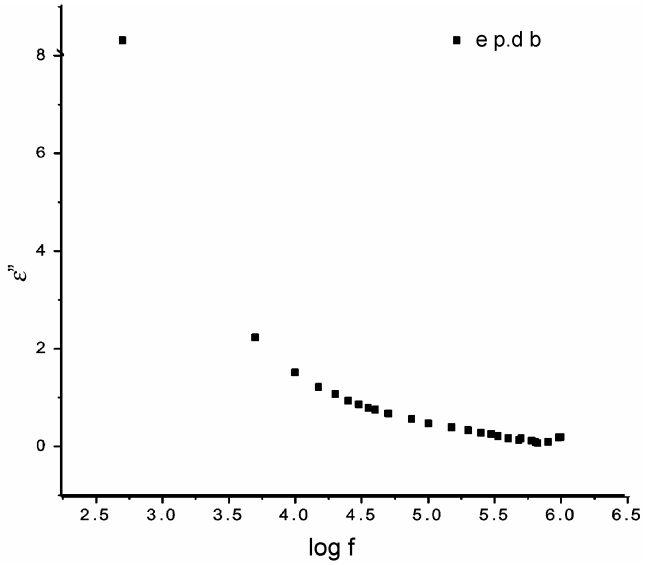

Figure 7. Plot of imaginary part of the complex permittivity vs frequency of applied field.

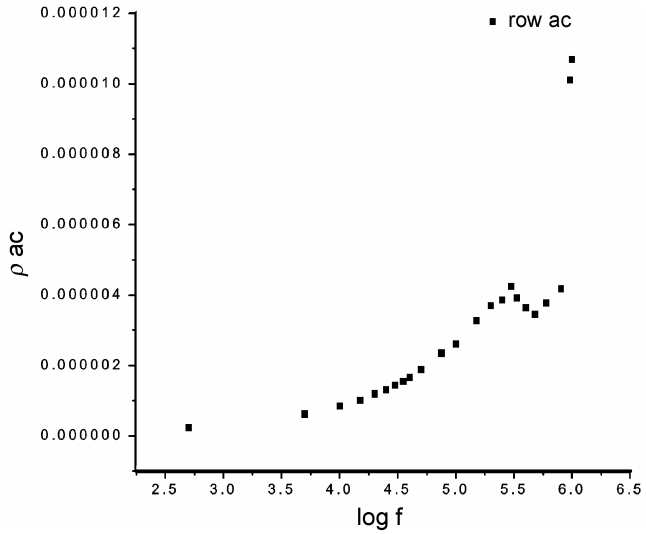

Figure 8. Plot of a.c. resistivity vs frequency of applied field.

shown in figure 5. The plots suggest that as the frequency of applied field increases the dielectric constant decreases with some variations. However, the variation in the dielectric constant is very less, i.e. 76·84 maximum and 72·50 minimum, in the range of frequency of applied field.

Recently, the variation of dielectric constant, dielectric loss and a.c. conductivity with frequency of applied field was reported (Parekh and Joshi 2007) for calcium pyrophosphate tetrahydrate crystals. The variation of dielectric loss, tan δ, with applied field is shown in figure 6, which suggests that the dielectric loss decreases as the frequency increases. The response of normal materials to external fields depends on the frequency of the applied field. In fact, polarization of material does not respond instantaneously to an applied field. For this reason the permittivity is often treated as a complex function of frequency of the applied field. The variation of imaginary part of the complex permittivity with frequency of applied field is shown in figure 7. This indicates that as the frequency increases the value of the imaginary part of the permittivity decreases. The nature of variation of a.c. resistivity with frequency of applied field is shown in figure 8. This indicates that as the frequency of the applied field increases the a.c. resistivity increases rapidly.

4. Conclusions

Growth of sodium oxalate crystals was carried out by single diffusion gel growth technique. Good quality, transparent, prismatic, single crystals were harvested. The crystal is thermally unstable and decomposes through three stages into sodium oxide form at 556·9°C. One water molecule was found to be associated with the crystal. The kinetic parameters of dehydration were calculated by applying Coats and Redfern relation to thermogram. Thermodynamic parameters were also evaluated which suggest the spontaneous type nature of reaction. The FT–IR spectrum indicated the presence of C=O bond, C–C bond and O–H bond. As the frequency of the applied field increases the dielectric constant decreases, however, the response was found to be very poor. The dielectric loss (tan δ) and the imaginary part of the complex permittivity decreased as the frequency of the field increased. However, the a.c. resistivity increased rapidly as the frequency of the applied field increased.

Acknowledgements

The authors are thankful to UGC, New Delhi, for the SAP and Profs K N Iyer and H H Joshi for keen interest. One of the authors (BBP) is thankful to DBT, New Delhi, for JRF and SRF and the authority of Nirma University, Ahmedabad, for encouragement.

References

Arnott H J and Webb M A 1983 *Scann. Electron Microsc.* **4** 1
Balcke P 1985 *Wien Klin Wochenschr. Suppl.* **160** 1
Caliskan M 2000 *Turk. J. Zool.* **24** 103
Chisholm J E, Jones G C and Purvis O W 1987 *Miner. Mag.* **51** 715
Clarke R M and Williams I R 1986 *Miner. Mag.* **50** 295
Coats A W and Redfern J P 1964 *Nature* **201** 68
Dharmaprakash S M and Mohan Rao P 1989 *J. Mater. Sci. Lett.* **8** 1167
Frey-Wyssling A 1981 *Am. J. Bot.* **68** 130
Frost R L and Weier M L 2004 *Thermal Analysis and Calorimetry* **75** 277
Girija E K, Charistic Latha S, Kalkura S N, Subramanian C and Ramasamy P 1998 *Mater. Chem. & Phys.* **52** 253
Hamilton S E, Pielage P J and Fassett R G 1999 *Emergency Medicine Australasia* **11** 35
Henisch H K 1996 *Crystal growth in gels* (New York: Dover)
Hodgkinson A and Zarembski P M 1968 *Calcified Tissue Int.* **2** 115
Jeffrey G A and Parry G S 1954 *J. Am. Chem. Soc.* **76** 5283
Joseph K C, Parekh B B and Joshi M J 2005 *Curr. Sci.* **88** 1232
Joshi V S 2001 *Crystal growth and characterization of some urinary crystals*, Ph.D. Thesis, Saurashtra University, Rajkot
Lowe J, Ogden M, Mckinnon A and Parkinson G 2002 *J. Cryst. Growth* **237–239** 408
Manasse E 1911 *Rend. Acad. Lincei* **19** 138
Ono K and Kikawa K 1989 *ASAIO Trans.* **35** 629
Pederson B F and Kvick Å 1989 *Acta Crystallogr.* **C45** 1724
Parekh B B and Joshi M J 2007 *Cryst. Res. & Technol.* **42** 127
Reed D A and Ohnstead M M 1981 *Acta Crystallogr.* **B37** 938
Rezek K, Sevcu J, Civiš S and Novotný J 1988 *Pro Mineralogii a Geologii Casopis* **33** 419
Shaefer G D 1936 *J. Pharmacol. & Exptl. Therapeut.* **58** 264
Tawashi R, Cousineau M and Sharkawi M 1980 *Invest. Urol.* **18** 90
Winchell H and Benoit R J 1951 *Am. Mineral.* **36** 590
Yang J C and Loewus F A 1975 *Plant Physiol.* **56** 283

Modern Physics Letters B, Vol. 24, No. 8 (2010) 735–747

DOI: 10.1142/S0217984910022810

World Scientific
www.worldscientific.com

GROWTH AND CHARACTERIZATION OF BIS-THIOUREA STRONTIUM CHLORIDE SINGLE CRYSTALS

R. R. HAJIYANI*, D. J. DAVE, C. K. CHAUHAN, P. M. VYAS and M. J. JOSHI†

Crystal Growth Laboratory, Department of Physics,
Saurashtra University, Rajkot 360 005, India
**hajiyanirakesh@gmail.com*
†*mshilp24@rediffmail.com*

Received 5 June 2009
Revised 12 July 2009

Bis-thiourea strontium chloride was synthesized and single crystals were grown by the slow solvent evaporation technique using aqueous solvent. The solubility curve was obtained and the determination of the induction period as well as the evaluation of kinetic parameters of nucleation was carried out. The powder XRD analysis suggested orthorhombic crystal structure. The FT-IR spectrum confirmed the presence of various functional groups. The thermo-gravimetry analysis was carried out and the crystals were found to be stable up to 170°C. Applying Coats and Redferm relation to the thermogram, the kinetic and thermodynamic parameters of dehydration were calculated. The dielectric study was carried out in the frequency range of applied field from 500 Hz to 1 MHz. The variations of dielectric constant, dielectric loss, AC resistivity and AC conductivity were studied with frequency. It was found that the dielectric constant and the dielectric loss decreased as the frequency of applied field increased, whereas the AC resistivity increased as the frequency increased.

Keywords: Bis-thiourea strontium chloride; induction period; nucleation parameters; powder XRD; TGA; dielectric study.

1. Introduction

Nonlinear Optical (NLO) materials crystals are in great demand because of their various applications in science and technology, such as different harmonic generators, sum and difference generators and parametric oscillators.[1,2] There are inorganic and organic class of NLO materials available with different merits and demerits,[3,4] however, another class of NLO materials are the semi-organic materials, which possess the properties of both organic and inorganic NLO materials[5–7] such as a wide range of electronic characteristics, mechanical hardness, and thermal stability and, on the other hand, structural variety, large polarizability, and easy processing of the organic molecules. Metal complexes of urea and urea analogs have been explored.[7] Bis-thiourea cadmium chloride[8] and bis-thiourea zinc chloride[9] crystals have been synthesized, grown and characterized, which exhibit good NLO properties. Bis-thiourea cadmium chloride exhibits the highest laser-induced

damage threshold values compared with other similar crystals.[10] Recently, a few more urea-based semi-organic NLO crystals are reported, for instance, tertrakis thiourea nickel chloride,[11] bis-thiourea bismuth chloride,[12] and zinc tris-thiourea sulphate.[13] As other thiourea compounds are expected to show NLO properties the present authors have attempted to synthesize bis-thiourea strontium chloride (BTSC) and grow single crystals by the slow solvent evaporation method, which is for the first time reported in the present communication as per the current knowledge of the authors. The induction period was measured and various nucleation parameters were studied. The grown crystals were characterized by powder XRD, FT-IR, TGA and dielectric study. However, at present, the study of NLO properties was not carried out.

2. Experimental Technique

Pure BTSC salt was synthesized by the slow solvent evaporation method using AR grade stoichiometric incorporation of thiourea and strontium chloride in double-distilled water. The expected chemical reaction is as shown in Eq. (1).

$$\mathrm{SrCl_2} + 2\mathrm{CS(NH_2)} \rightarrow \mathrm{Sr[CS(NH_2)_2]_2Cl_2}(1)\,. \tag{1}$$

The synthesized salt was purified by several re-crystallizations. BTSC single crystals were grown by the slow evaporation technique at room temperature, i.e. at 301 K. In the present study, a seed crystal was dipped in saturated solution at the desired constant temperature. The growth vessel was closed and through a small opening slow evaporation was allowed. A constant temperature water bath with $\pm 0.1^{\circ}$C accuracy was used to maintain a constant temperature. Crystal growth was completed in about 10 days. The grown crystals were characterized by various techniques. Figure 1 shows the distorted hexagonal, transparent, platelet-type BTSC crystals.

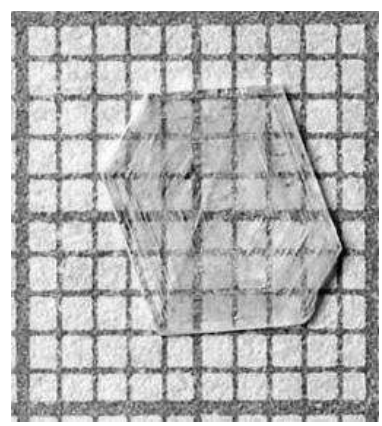

Fig. 1. Grown BTSC crystal.

The crystals were characterized by several techniques. The powder XRD study was carried on PW1710 BASED TYPE set-up using Cu-K_α radiation. The data were analyzed by the software powder X. The FTIR spectroscopic study was carried in the range from 400 cm^{-1} to 4000 cm^{-1} using SIMADZU 8400 FTIR in KBr medium. The dielectric study was carried out using Solartron-Impedance Gain Phase Analyzer SI-1260 set up at different frequencies of applied field from 500 Hz to 1 MHz. A specially designed sample holder was used. The TGA was carried out on NETZSCH Geratebau GmbH from room temperature to 900°C in the atmosphere of nitrogen.

3. Results and Discussion

Several researchers have reported the growth of different complexes of thiourea. The first structural study of bis-thiourea zinc chloride (BTZC) was reported by Kuncher *et al.*[14] and later on the preliminary Second Harmonic Generation (SHG) studies were carried out on solution-grown BTZC crystals by Oussaid *et al.*[15] The influence of pH on the growth habit[16] and hardness[17] of solution-grown BTZC crystals is reported. The BTSC crystals are characterized by various techniques, which are discussed hereby.

3.1. *Solubility determination and solubility curves*

For crystal growth by solution technique, it is important to determine the solubility of the solute in a suitable solvent at different temperatures. The nature of the solubility curve provides important information on the solubility of solute at different temperatures and the conditions required to be maintained to grow crystals. The solubility of the synthesized BTSC was determined gravimetrically at different temperatures and the solubility curve was drawn, which is shown in Fig. 2. The solubility of BTSC increases with temperature.

3.2. *Nucleation and induction period study*

Non-steady state nucleation and steady state nucleation processes are related by the induction period which is also related to the size and complexity of the critical nucleus and it can be affected by external influences. However, the induction period has been frequently used as a measure of the nucleation rate. In the present study, the induction period (τ) was measured at different super-saturation (S) by the visual observation method. The values of energy of formation (ΔG) for nuclei of radius (r) in equilibrium with solution have been calculated for different values of super-saturation (S) by using standard formulations.[18]

The interfacial tension (γ) can be calculated from

$$\gamma = RT\left[\frac{3m}{16\pi v^2 N}\right]^{\frac{1}{3}}, \tag{2}$$

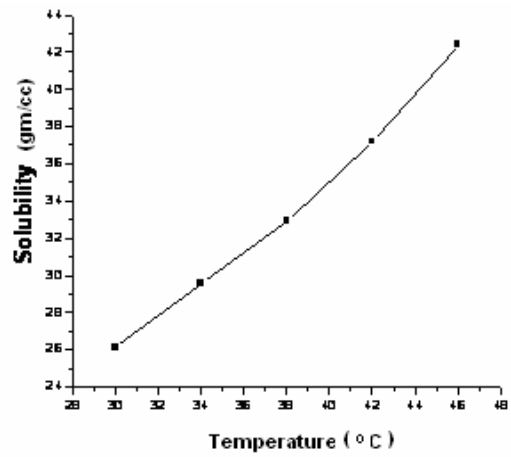

Fig. 2. Solubility curve for BTSC crystals.

Table 1. Induction periods and nucleation parameters of BTSC.

Super-saturation	Induction period (s)	ΔG (kJ/mol)	R (nm)
1.025	835	643.27	12.300
1.050	778	323.02	6.210
1.075	725	217.98	4.185
1.100	680	165.36	3.175

where R is the gas constant, v is the molar volume, N is Avogadro's number and m is the slope of the line $\ln \tau$ *against* $1/\ln S^2$. The energy of formation of a critical nucleus can be calculated from the experimental data as

$$\Delta G = \frac{RTm}{\ln S^2}. \tag{3}$$

The radius of the nucleus in equilibrium with its solution can be computed as

$$r = \frac{2\gamma v}{RT \ln S}. \tag{4}$$

The values of ΔG and r for different values of super-saturation (S) are given in Table 1. The interfacial tension (γ) of the solid relative to its solution can be calculated from the slope of the line $\ln \tau$ *against* $1/\ln S^2$ by using standard formulations,[18] which is found to be 1.36 mJm^{-2}. From Table 1, one can notice that as the super-saturation increases, the values of induction period, ΔG and r decrease. This means that the kinetic parameters are influenced by the super-saturation.

The nucleation kinetics were studied on potential semi-organic NLO crystal bis-thiourea cadmium acetate (BTCA).[19] The interfacial tension was measured from

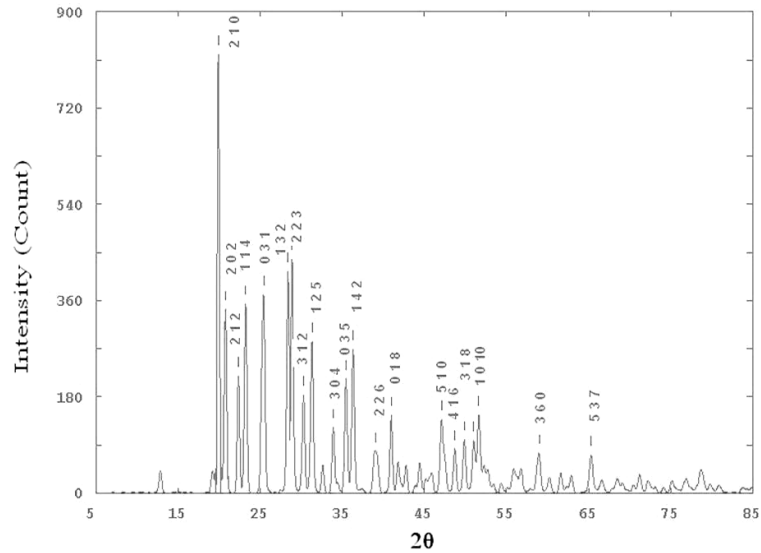

Fig. 3. Powder X-ray diffractogram of BTSC.

the plot drawn for $\ln \tau$ versus $1/\ln S^2$ relation and was estimated to be 2.10 mJ/m^2. It was also further reported that the interfacial tension of BTCA increased with the increasing super-saturation.

3.3. *Powder XRD*

Using Powder-X computer software, the h, k, and l parameters as well as d and 2θ values were generated in such a way that these values match with the powder X-ray diffraction pattern. The estimated values of unit cell parameters of BTSC crystals are $a = 9.800$ Å, $b = 10.700$ Å, $c = 18.000$ Å and $\alpha = \beta = \gamma = 90°$, which shows the orthorhombic crystal structure. Figure 3 shows the powder XRD pattern of BTSC crystals. Earlier works reported the powder XRD study and estimated the unit cell parameters of bis-thiourea zinc chloride (BTZC).[20] Orthorhombic form of BTCA was reported earlier.[19]

3.4. *FT-IR study*

The FT-IR spectrum of bis-thiourea zinc chloride[20] and zinc tris-thiourea sulphate[13] have been reported. Figure 4 shows the FTIR spectrum of BTSC. The C–S stretching vibrations occur at 3271 cm^{-1}, while the C–S bending occurs at 1047 cm^{-1} and 1082 cm^{-1}. The C–N stretching vibrations occur at 1026 cm^{-1}, whereas the N–H bending vibrations occur at 924 cm^{-1}. The NH_2 stretching vibrations occur at 1466 cm^{-1}. The vibrations occurring below 900 cm^{-1} may be due to metal and halogen bonding vibrations.

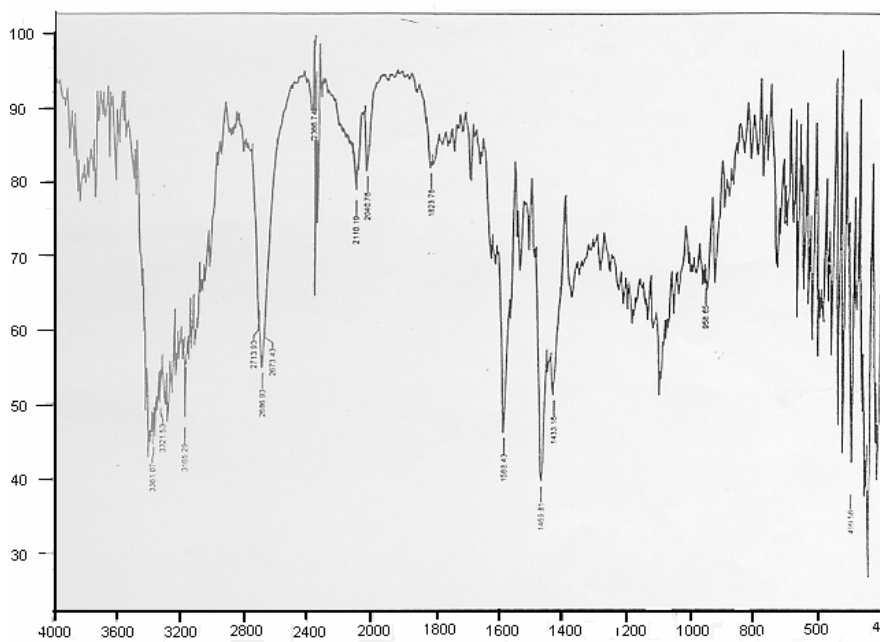

Fig. 4. FT-IR spectrum of BTSC crystals (transmittance % versus wavenumber cm^{-1}).

3.5. *TGA study*

Figure 5 shows the thermo-gram of BTSC, which indicates that the compound is stable up to 170°C and then the decomposition starts precipitously and thereafter remains stable from 300°C to 400°C. Above this temperature, the mass loss occurs through a slow decomposition process and is followed by a stable state from 580°C to the end of the analysis where the loss is 91% of the original mass. The possible mechanism of decomposition and the expected products are summarized in Table 2 along with the theoretically calculated and experimentally obtained weight losses. The end product of the pyrolysis is expected as the metallic residue of strontium. Thermogram of bis-thiourea zinc chloride (BTZC) was studied and it was found that the crystal remains stable up to 232°C.[20] In comparison to BTZC, the BTSC crystals are more stable.

3.5.1. *Kinetic and thermodynamic study of dehydration*

The use of thermo-gravimetric data to evaluate the kinetic parameters of solid-state reactions involving weight loss has been investigated by many workers.[13,22–24]. If the pyrolysis occurs through a many-stepped mechanism, usually, the shape of the curve can be determined by the kinetic parameters of pyrolysis, such as order of reaction, frequency factor and energy of activation. Kotru *et al.*[25] reported the kinetics of solid-state decomposition of neodymium tartrate. They also calculated various

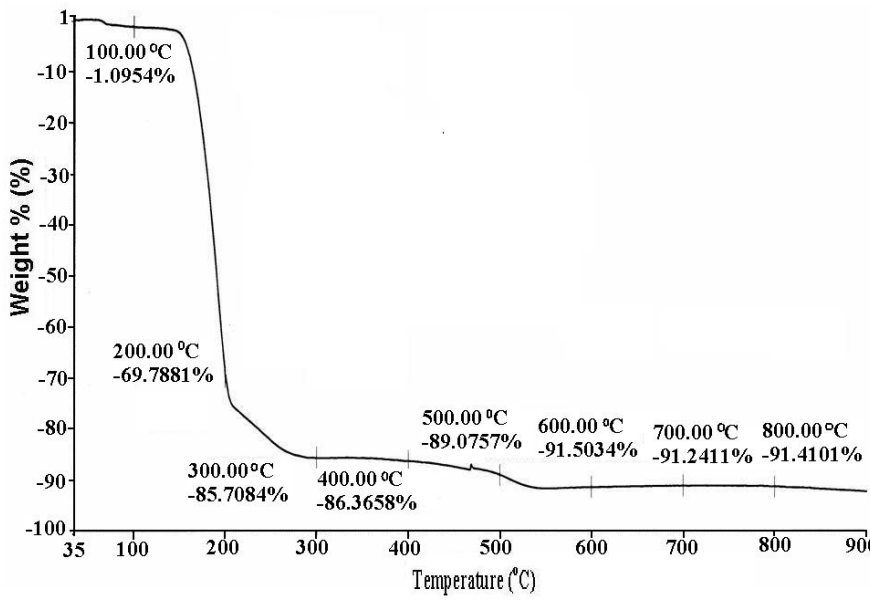

Fig. 5. Thermogram of the BTSC crystals.

Table 2. The decomposition behavior of BTSC.

Possible substance	Temperature (°C)	Theoretically calculated weight (%)	Experimentally obtained weight (%)
BTSC	Room temp.	100	100
SrH_2	200°C	28.85	30.21
Sr	800°C	9.4	8.59

kinetic parameters and suggested that the decomposition process took place according to cylindrical kinetic model. Recently, the kinetics of dehydration of gypsum,[26] lithium sulphate monohydrate single crystals[27] as well as the kinetic and thermodynamic parameters of decomposition of chromate in different gas atmosphere[28] and L-arginine doped KDP crystals[29] has been evaluated.

Usually, the kinetic parameters can be evaluated from the TG curves by applying several equations,[21−24] which are proposed by different authors on the basis of different assumptions to the kinetics of the reaction and the Arrhenius law. These equations are (i) the Coats and Redfern Relation, (ii) the Horowitz and Metzger Relation and (iii) the Freeman and Carroll Relation. However, in the present investigation, the Coats and Redfern relation is discussed in detail because it facilitates not only to evaluate the activation energy and order of reaction but also the frequency factor. Thus, it helps evaluate the thermodynamic parameters further.

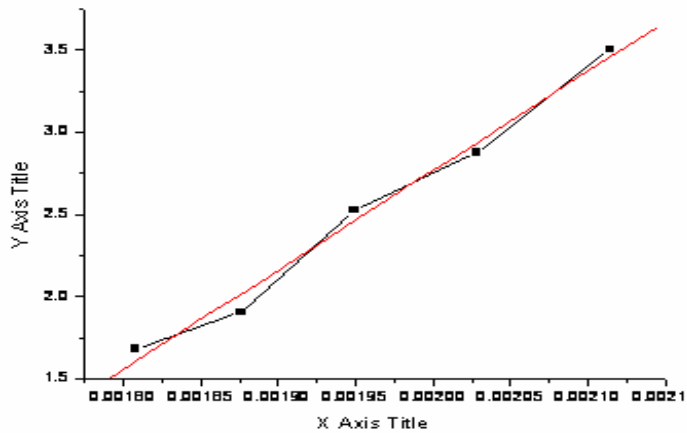

Fig. 6. Coats and Redfern plot for BTSC crystals, $X = (1/T)$ and $Y = -\log_{10}[\{1-(1-\alpha)^{1-n}\}/\{T^2(1-n)\}]$.

3.5.2. *Coats and Redfern (C-R) Relation*

Coats and Redfern[21] derived the following equation to determine the values of activation energy and order of reaction:

$$\log_{10}\left(\frac{1-(1-\alpha)^{1-n}}{T^2(1-n)}\right) = \left\{\log_{10}\left(\frac{AR}{aE}\right)\left(1-\frac{2RT}{E}\right)\right\} - \left\{\frac{E}{2.3RT}\right\}, \qquad (5)$$

where E is the activation energy of the reaction, A is the frequency factor, α is the fraction of decomposed material at time t, n is the order of reaction and T is the absolute temperature. The plots of $Y = -\log_{10}[\{1-(1-\alpha)^{1-n}\}/\{T^2(1-n)\}]$ versus $X = 1/T$ were straight lines for different values of n, however, the best linear fit plot gives the correct value of n. The value of activation energy is obtained from the slope of the best linear fit plot. The activation energy can be calculated from the slope of the plot. The frequency factor can be calculated for a particular temperature using relation (5). The Coats and Redfern relation was solved for various values of n. The statistical regression analysis was applied to different values of n and the highest values of co-relation co-efficient indicated the best linear fit curve. This was found for $n = 5$. Figure 6 shows the plot drawn for the Coats and Redfern relation.

The values of activation energy, frequency factor and the order of reaction are found for the first major decomposition stage occurring between 170°C to 300°C. Table 3 gives the values of different kinetic parameters obtained from the Coats and Redfern relation.

Table 3. The values of different kinetic parameters of BTSC obtained from the Coats and Redfern relation.

Order of reaction (n)	Activation energy (E) kJ mol^{-1}	Frequency factor (A)
5	115.887	1.079×10^{24}

3.5.3. *Thermodynamic parameters*

The thermodynamic parameters have been evaluated for the first major decomposition stage from the thermo-gram of BTSC crystals. Different thermodynamic parameters such as the standard entropy of activation ($\Delta^{\#}S^{\circ}$), standard enthalpy ($\Delta^{\#}H^{\circ}$), standard Gibbs free energy ($\Delta^{\#}G^{\circ}$) and standard change in internal energy ($\Delta^{\#}U^{\circ}$) were calculated by applying well known formulas, as described in detail by Laidler[30] The thermodynamic parameters for dehydration of gel-grown iron (II) tartrate have been estimated by Joseph *et al.*[31] Dabhi and Joshi[32,33] and Parikh *et al.*[29] have reported the thermodynamic parameters for dehydration of various gel grown metal-tartrate crystals.

Table 4 summarizes the values of different thermodynamic parameters obtained for the decomposition of the BTSC crystalline sample. Positive values of $\Delta^{\#}S^{\circ}$ and $\Delta^{\#}H^{\circ}$ and the negative value of $\Delta^{\#}G^{\circ}$ suggest that the process is spontaneous at high temperatures.

Table 4. The values of different thermodynamic parameters of BTSC crystals.

Standard entropy $\Delta^{\#}S^{\circ}$ kJ mol^{-1}	Standard enthalpy $\Delta^{\#}H^{\circ}$ kJ mol^{-1}	Standard Gibbs free energy $\Delta^{\#}G^{\circ}$ kJ mol^{-1}	Standard change in internal energy $\Delta^{\#}U^{\circ}$ kJ mol^{-1}
210.690	107.357	−0.7272	111.62

3.6. *Dielectric study*

The dielectric study of zinc tris-thiourea sulphate[34] has been reported. In the present investigation, the values of dielectric constant were calculated from the measured values of capacitance at room temperature within frequency range from 500 Hz to 1 MHz. The variation of dielectric constant with frequency is displayed in Fig. 7. From this plot, one can observe that as the frequency increases the dielectric constant initially decreases very rapidly and then slowly as the frequency increases.

This type of variation suggests higher space charge polarizability at the lower frequency region. This type of behavior is due to the electronic exchange of the number of ions in the crystal giving local displacement of electrons in the direction of applied field, which gives the polarization. As the frequency increases, a point is reached where the space charge cannot sustain and comply with the external field. Therefore, the polarization decreases and exhibits the reduction in the values of dielectric constant as the frequency increases. This behavior is similar to those of observed by Lopez *et al.*[35] and Dabhi *et al.*[36] for zinc tartrate and Arora *et al.*[37] for strontium tartrate.

Figure 8 represents the plot of $\tan\delta$ (dielectric loss) versus $\log f$ at room temperature. The nature of the plot is similar to that of the variation of dielectric constant with frequency.

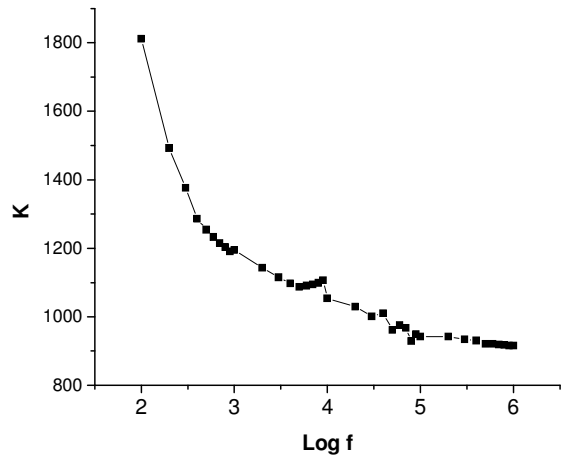

Fig. 7. Plot of dielectric constant versus $\log f$ for BTSC.

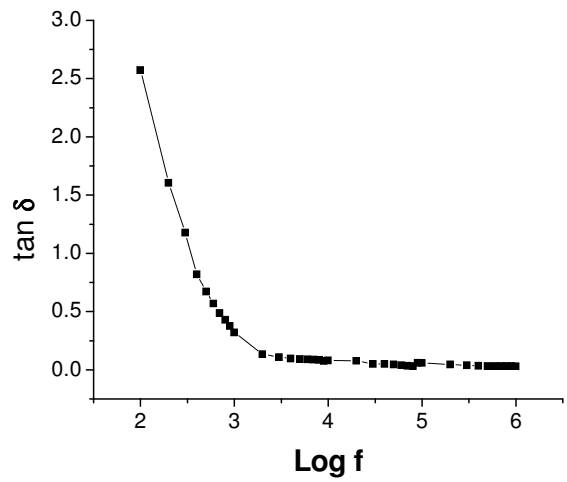

Fig. 8. Plot of $\tan\delta$ versus $\log f$ for BTSC.

The AC conductivity ($\sigma_{\rm ac}$) and AC resistivity ($\rho_{\rm ac}$) were calculated from the following formula:

$$\sigma_{\rm ac} = \frac{2\pi f C D t}{A}\,, \tag{6}$$

where C is the capacitance, D is the dissipation factor, A is the area, t is the thickness and f is the frequency.

$$\rho_{\rm ac} = \frac{1}{\sigma_{\rm ac}}\,. \tag{7}$$

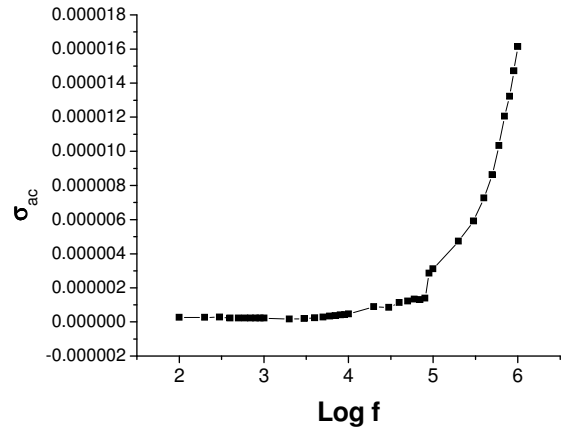

Fig. 9. Plot of AC conductivity (σ_{ac}) versus $\log f$ for BTSC.

Figure 9 represents the plots of the AC conductivity versus $\log f$. From this figure, one can easily notice that as the frequency increases, the AC conductivity increases and obviously the AC resistivity decreases.

4. Conclusion

Distorted hexagonal, transparent, platelet-type BTSC crystals were grown by slow solvent evaporation technique. The solubility of BTSC increased with temperature. The value of interfacial tension was found to be 1.36 mJm^{-2}. The estimated values of unit cell parameters of BTSC crystals were found to be $a = 9.800$ Å, $b = 10.700$ Å, $c = 18.000$ Å and $\alpha = \beta = \gamma = 90°$, which confirmed the orthorhombic crystal structure. The FT-IR spectrum verified the presence of C–S bond, C–N bond, N–H bond. The thermo-gram of BTSC indicated that the compound was stable up to 170°C and then precipitous decomposition occurred followed by a stable state from 300°C to 400°C and above this temperature, the mass loss occurred through a slow decomposition process, which was followed by stable state from 580°C to the end of the analysis, exhibiting 9% of the original weight. Kinetic and thermodynamic parameters of the first precipitous stage of decomposition were evaluated, suggesting a spontaneous process. The variation of the dielectric constant with frequency suggested that as the frequency of the applied field increased, the dielectric constant and dielectric loss decreased. This indicated higher space charge polarizability at a low frequency region and the space charge failed to sustain and comply with the frequency of external field in the higher frequency region. The AC conductivity increases with the increase in frequency and the AC resistivity decreases with the increase in frequency.

Further work is under progress to study the NLO properties and the optical properties of BTSC crystals.

Acknowledgment

The authors are thankful to Prof. K. N. Iyer and Prof. H. H. Joshi for their keen interest and Dr K. B. Modi for dielectric measurements. The authors are thankful to UCG, New Delhi, for financial assistance under DRS-SAP and Government of Gujarat for development of experimental facility under special assistance for Nanoscience and Nanotechnology and Environmental Physics. The authors (R. R. Hajiyani and C. K. Chauhan) are thankful to the Department of Education, Government of Gujarat, Smt. Jayanti S. Ravi, Commissioner of Higher Education and Joint Director, CHE, Gandhinagar, Dr R. A. Agarwal, Principal, H. and H. B. Kotak Institute of Science, Rajkot, for their encouragement.

References

1. V. G. Dimitriev, G. G. Gurzadyan and D. N. Nikogosyan, *Handbook of Nonlinear Optical Crystals* Springer Series in Optical Science, Vol. 64 (1991).
2. D. Eimerl, S. Velsko, L. Davis and F. Wang, in *Crystal Growth and Characterization of Materials*, ed. J. B. Mullin, Vol. 20, p. 59.
3. X. Wang, J. Zhang, D. Xu, M. Lu, D. Yuan, S. Xu, J. Huang, G. Zhang, S. Guo, S. Wang, X. Duan, Q. Ren and G. Lu, *J. Cryst. Growth* **235** (2002) 340.
4. D. Chemla and J. Zyss, *Nonlinear Optical Properties of Organic Molecules and Crystals*, Vols. 1–2 (Academic Press, Orlando, 1987).
5. D. Xu, M. Jiang and Z. Tan, *Acta Chem. Sinica* **41** (1983) 570.
6. A. Petrosyan, R. Sukiasyan, H. Karapetyan, S. Terzyan and R. Feigelson, *J. Cryst. Growth* **213** (2000) 103.
7. P. R. Newman, L. F. Warren, P. Cunningham, T. Y. Chang, D. E. Copper, G. L. Burdge, P. Dingels and C. K. Lowe-Ma, Semi-organics, a new class of NLO materials in *Advances in Organic Solid State Materials — Materials Research Society Symposium Proceedings*, Vol. 173, eds. C. Y. Chiang, P. M. Chaikan and D. O. Cowan (1990), p. 557.
8. S. Selvakumar, J. P. Julius, S. Rajasekar, A. Ramanand and P. Sagayaraj, *Mater. Chem. Phys.* **89** (2004) 243.
9. P. A. Mary and S. Dhanuskodi, *Cryst. Res. Technol.* **36** (2001) 1231.
10. G. Xing, M. Jiang, Z. Sao and D. Xu, *Chin. J. Lasers* **14** (1987) 302.
11. A. Bhaskaran, C. Raghavan, R. Sankar, R. M. Kumar and R. Jayavel, *Cryst. Res. & Technol.* **42** (2007) 477.
12. R. Sankar, C. Raghavan and R. Jayavel, *Cryst. Growth & Design* **7** (2007) 501.
13. C. Krishnan, P. Selvarajan and T. Freeda, *Mater. & Manuf. Process.* **23** (2008) 800.
14. N. Kuncher, R. Mary and S. Truter, *J. Chem. Soc.* **504** (1958) 3478.
15. N. Oussaid, P. Becker, M. Kemiche and C. Carabatos, *Phys. Status. Sol. B* **207** (1998) 103.
16. A. A. Mary and S. Dhanushkodi, *Cryst. Res. & Technol.* **36** (2001) 1231.
17. R. Rajasenkaran, R. MohanKumar, R. Jayavel and P. Ramasamy, *J. Cryst. Growth* **252** (2003) 317.
18. S. A. Rajasekar, Ph.D. Thesis, Madras University, Madras (2004).
19. R. Sankar, C. Raghavan and R. Jayavel, *Cryst. Res. & Technol.* **419** (2006) 919.
20. A. Anuradha, Ph.D. Thesis (Madras University, Madras, 2007).
21. A. W. Coats and J. P. Redfern, *Nature* **201** (1964) 68.
22. H. Horowitz and G. Metzger, *Anal. Chem.* **35** (1963) 1464.

23. E. S. Freeman and B. Carroll, *J. Phys. Chem.* **62** (1958) 394.
24. D. Van Krevelan, C. Van Hardeen and F. Huntlens, *Fuel* **30** (1951) 253.
25. P. N. Kotru, K. K. Raina and M. L. Koul, *Indian J. Pure & Appl. Phys.* **25** (1987) 220.
26. D. Fatu, *J. Therm. Anal. & Calorimetry* **65** (2001) 205.
27. A. N. Modestov, P. V. Poplankhin and N. Z. Lyakhov, *J. Therm. Anal. & Calorimetry* **65** (2001) 103.
28. S. Halawy, N. Fouad, M. Mohamed and M. Zaki, *J. Therm. Anal. & Calorimetry* **65** (2001) 153.
29. K. D. Parikh, D. J. Dave and M. J. Joshi, *Bull. Mater. Sci.* **30** (2007) 105.
30. K. J. Laidler, *Chemical Kinetics*, 3rd edn. (Harper and Row, New York, 1987).
31. S. Joseph and M. J. Joshi, *Indian J. Phys.* **71A** (1997) 183.
32. R. M. Dabhi and M. J. Joshi, *Indian J. Phys.* **76A** (2003) 481.
33. R. M. Dabhi and M. J. Joshi, *Indian J. Phys.* **76A** (2002) 211.
34. S. Moitra, S. Bhattachrya, T. Kar and A. Ghosh, *Phys. B Conden. Matt.* **403** (2008) 3244.
35. T. Lopez, J. Stockel, J. Peraza, M. E. Torres and A. C. Yanes, *Cryst. Res. & Technol.* **30** (1995) 677.
36. R. M. Dabhi, B. B. Parekh and M. J. Joshi, *Indian J. Phys.* **79** (2005) 503.
37. S. K. Arora, V. Patel, B. Amin and A. Kothari, *Bull. Mater. Sci.* **27** (2004) 141.

Synthesis and Characterization of Cholesterol Nano Particles by Using w/o Microemulsion Technique

Poorvesh M. Vyas[a], Sonal R. Vasant[a], Rakesh R. Hajiyani[a] and Mihir J. Joshi[a]

[a] *Crystal Growth Laboratory, Department of Physics, Saurashtra University, Rajkot – 360 005, Gujarat, India*

Abstract. Cholesterol is one of the most abundant and well known steroids in the animal kingdom. Cholesterol rich micro-emulsions and nano-emulsions are useful for the treatment of breast cancer and gynecologic cancers. The nano particles of cholesterol and other pharmaceutically important materials have been reported. In the present investigation, the nano particles of cholesterol were synthesized by direct precipitation technique using triton X – 100/water/n-butanol micro–emulsion. The average particle size of cholesterol nano particles was estimated by applying Scherrer's formula to the powder X – ray diffraction pattern, which was found to be 22 nm. The nanoparticles of cholesterol were observed by using TEM and the particle size was found within the range from 15nm – 31nm. The distribution of particle size was studied through DLS. The nanoparticles of cholesterol were characterized by using FT – IR spectroscopy and the force constant was also calculated for O – H, C – H and C – O bonds. The thermal response of nanoparticles of cholesterol was studied by TGA, which showed that the nanoparticles were stable up to 200^{o}C and then decomposed. Kinetic and thermodynamic parameters of decomposition process were also calculated by applying Coats and Redfern formula to thermo-gram.

Keywords: Emulsion, Lipids, TEM, X – Ray Diffraction, Nanocrystals, Thermal Stability.
PACS: 82.70Kj, 87.14Cc, 68.37Lp, 61.05Cp, 61.46Hk, 68.60Dv

INTRODUCTION

Cholesterol is the most abundant molecule in the mammalian plasma membrane [1].Cholesterol is the precursor of all steroids in the body such as corticosteroids, bile acid, sex hormone, vitamin D, etc. But its main role of pathologic processes is as a factor in the genesis of arthrosclerosis of vital blood vessels causing cerebro-vascular coronary and peripheral vascular diseases. Low Density lipoprotein (LDL) is the main carrier of cholesterol in the plasma. A novel approaches have been proposed for cancer treatment based on lipid emulsions (LDE) [2] and nano emulsions [3]. The nano emulsion is composed of a core of cholesterol esters and residual amounts of triglycerides surrounded by a monolayer of phosphatidylcholine with free cholesterol. The LDE and nanoemulsions are expected to bind to the LDL receptor. As LDL receptors are up – regulated in cancer cells [4], the association of chemotherapeutic

CP1276, *International Conference on Advanced Nanomaterials and Nanotechnology (ICANN-2009)*
edited by P. K. Giri, D. K. Goswami, A. Perumal, and A. Chattopadhyay

agent with LDE and nanoemulsion would concentrate the agent in the neoplastic tissue after the intravenous injection of the complex. In this manner, the delivery of drug to the tumor could be increased while the tissues and organs would be less damaged by the chemotherapy [3 – 5]. The nano-emulsion thus can serve as a vehicle to direct chemotherapeutic agents against tumors and decrease the toxicity and increase the anti-tumoral action of the drugs [5], for example, in breast carcinoma the nano-emulsion concentrates roughly five times more in tumor than in normal contralateral mammary tissues and [6] and in the case of ovarian caricinomas it is eight times [7].

Microemulsions are isotropic, transparent and thermodynamically stable systems composed of water, oil and surfactant, find large number of applications which are reviewed by Moulik et al [8, 9]. The internal structure and dynamics of micro – emulsions are having important properties, which are the focus of extensive investigations using a variety of methods [10, 11]. The microemulsion can be a potential system for drug delivery [12]. Moreover, the microemulsion is widely used in pharmaceutical applications because the total dose of the drug can be reduced when applied through the microemulsion route, therefore, the side effects can be minimized [9]. Nanomaterials exhibit novel properties, which largely diverge from the bulk properties of materials [13]. Micro – emulsion has attracted several researchers to synthesize and study different nano particles like ZnS[14], TiO_2[15], Simvastatin [16] Rhovanil, Rhodiarome [17] and Retinol[12].

Only a few authors have reported the synthesis of cholesterol nano-particles and reported TEM, UV – visible spectroscopy, ^2H NMR [17] and effect on size variation as changes the molar ratio by Dynamic Light Scattering and TEM [12] . In the present communication the authors report the synthesis of cholesterol nanoparticles by w/o micro-emulsion technique and characterization by powder XRD, TEM, DLS, FT-IR spectroscopy and TGA.

EXPERIMENTAL SECTION

Nano size cholesterol particles were synthesized by using water / oil micro – emulsion technique at room temperature. AR grade cholesterol, n – butanol, Triton X – 100 and chloroform were used. The Triton X – 100/ n – butanol/water ternary diagram was constructed by varying the concentration of all the three solutions in a stepwise manner in such a way that the total volume remained constant and it was found that the single phase existed in a large area. This phase diagram corresponds to the earlier reported one [18]. For the synthesis of cholesterol nanoparticles, appropriate amount of surfactant Triton X – 100 was added in water in such a manner that the molar ratio R = $[H_2O]$/surfactant was 4 and then the desired amount of n – butanol was added to obtain the resultant mixture in the single phase region of the ternary phase diagram. The mixture was stirred well for 15 min and thereafter the solution of cholesterol made in chloroform was added in a drop wise manner, followed by continuous stirring for another 30 min. The cholesterol nanoparticles were formed between liquid - liquid interface of the solution, which were filtered by using Whatman filter paper no. 42. The nano particles were air dried at room temperature.

The powder X-ray diffraction (XRD) was carried out on PHILIPS X'PERT MPD system using Cu K_α radiation and the data was analyzed by using Powder – x software. The TEM images were recorded on PHILIPS TECNAI using 200 kV EHT potentials and the size of the nano – particles was measured by the software ITEM available with the set – up. The thermo-gravimetric analysis (TGA) was carried out on NETZSCH Geratebau GmbH from room temperature to 800 ^oC at a heating rate of 15 ^oC / min in the atmosphere of nitrogen. The FT – IR spectrum was recorded by using Thermo Nicolet - 6700 set up in the range from 400 cm^{-1} to 4000 cm^{-1} in KBr medium. The size distribution of cholesterol nano-particle was measured using Thermo Nanotrac 250 dynamic light scattering (DLS) set up at room temperature. The concentrated nano-cholesterol formulations were diluted with milipore distilled water for DLS analysis. Each sample was analyzed 3 times and the average effective diameter was obtained.

Result & Discussion

Formation of Cholesterol Nano Particles

The formation of organic nano particles by using w/o microemulsion was discussed and the hypothesis for the formation of organic nano particles was given earlier [13 ,19]. As per the hypothesis, organic nano particles are formed through several stages. In the first stage, the Triton X – 100 (Surfactant) and n – butanol (Oil) were added in a specific amount in double distilled water one by one so that the formed aqueous cores were surrounded by surfactant and oil content. In the second stage, cholesterol dissolved in chloroform in proper proportion was added to the microemulsion by drop wise manner to allow it to diffuse into empty micelles during continuous stirring. In the third stage, cholesterol precipitated in the aqueous cores because of its very poor solubility in water. In the fourth stage, the deplacement of the solvent from micelles to the surrounding took place. In the fifth and the last stage the exchange of organic molecules between the aqueous cores occurred as a result of collision between different micelles. The growth of formed nuclei thus took place. Thereafter, the formed nanoparticles were stabilized by the surfactant. Finally the mixture was allowed to stabilize and then filtered to separate out the synthesized nano particles.

Powder XRD study

The powder XRD study was reported for cholesterol [20]. The JCPDS data on powder XRD of cholesterol are available [21]. However, no major attempt was made to analyze the powder XRD patterns and to estimate the unit cell parameters. The powder XRD study was carried out to confirm the crystalline nature of cholesterol nano particles and to determine the average particle size of cholesterol nano particles. The powder XRD pattern of cholesterol nano particles is shown in fig 1. In the present study, the nano particles of cholesterol were analyzed by considering the unit cell parameters of cholesterol crystals reported in JCPDS as standard.

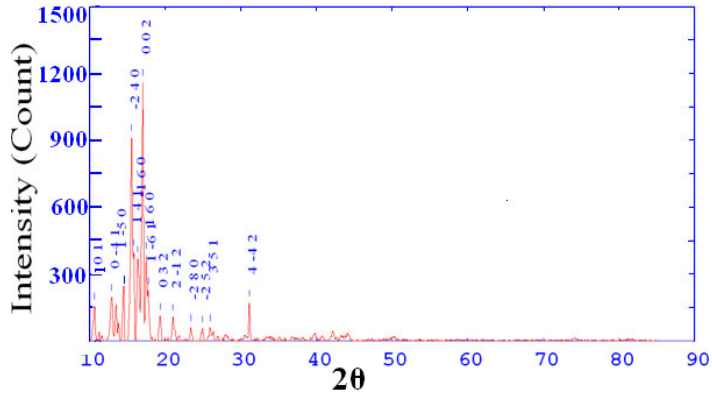

FIGURE1: Powder XRD pattern of cholesterol nanoparticles.

The cholesterol nano particles exhibited triclinic symmetry and the unit cell parameter were estimated as, a = 14.234 Å, b = 34.209 Å, c = 10.481 Å, α = 94. 60°, β = 90.00°, γ = 95.72°.

The average particle size of the cholesterol nano particles was determined from the powder XRD pattern by employing the Scherrer's formula as follows,

$$D = \frac{k\lambda}{\beta \cos\theta} \tag{1}$$

Where, D= Average diameter, K= Shape factor, λ = Wavelength of source used (For CuKα radiation is 1.54178Å), β = FWHM (Full Width Half Maximum) and θ= Angle of the peak for particular Bragg reflection. From the Scherrer's formula the average particle size of cholesterol nano particles was found to be of 22 nm.

Transmission Electron Microscopy (TEM)

The TEM study was carried out to determine the size and morphology of the synthesized cholesterol nano – particles. The TEM images of the cholesterol nano particles are shown in fig 2.

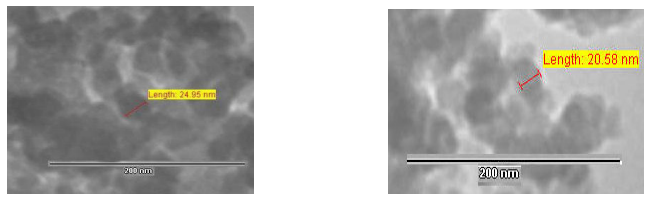

FIGURE2: TEM images of cholesterol nanoparticles.

TEM images suggest that the agglomerated cholesterol nano particles were having nearly spherical morphology and size varied from 15 – 31 nm. The possible

mechanism for obtaining different size of nano particles is discussed hereby. The microemulsion is expected to tolerate a minimum quantity of cholesterol molecules in order to form nano particles without phase separation. At initial stage the microemulsion is expected to remain thermodynamically stable. If the number of cholesterol molecules per aqueous core increases then the interaction with surfactant molecules increases at the interface. Therefore, the number of cholesterol molecules per aqueous core is larger and the interaction between these and surfactant molecules are also larger at the water – alcohol interface. The optimal radius of curvature is then disturbed and the phase separation occurs more readily for specific molar ratio (R) factor. As the cholesterol molecules come into contact with aqueous core, the nuclei formation takes place due to the insolubility of cholesterol in water. Then the nano particles later on grows to a certain favored size and stabilized in the same manner with surfactants in spite of their presence in both immiscible phases. The stirring of the micro-emulsion during synthesis also plays important role. Different parameters have been calculated for the formation of cholesterol nano particles by using the approach proposed by Destree et al [17].
The volume of the water core has been calculated by,

$$V_{wc} = \frac{4}{3}\pi r_{wc}^{3} \tag{2}$$

Where, r_{wc} = Radius of water core in nm [22], which is estimated as:

$$r_{wc} = 0.18\,R + 0.45 \tag{3}$$

Where R = Molar Ratio
In the present study, for the value of R = 4 nm, and the radius of water core was found to be 1.17 nm and the volume of the water core was estimated to be 6.54 nm^3.
The Number of water cores is obtained from:

$$N_{wc} = \frac{V_t}{V_{wc}} \tag{4}$$

Where, V_t = total amount of water; V_{wc} = Volume of the water core,
In this calculation, the amount of water in the organic phase in the surfactant layer is neglected.
The volume of nanoparticle calculated from the TEM data is,

$$V_{np} = \frac{4}{3}\pi r_{np}^{3} \tag{5}$$

Considering the average value of radius of nano-particles as 23 nm, the volume of nano particles was found to be 50939.17nm^3.
If it is assumed that the density of nanoparticles is equivalent to that of macroscopic material, the mass of single nanoparticle of cholesterol is calculated as follows,

$$m_{np} = V_{np}d \quad (6)$$

Where, d = density of the cholesterol
The mass of single nano particle was estimated to be 5.34×10^{-24} g.
The number of nanoparticles is given by,

$$N_{np} = \frac{m_t}{m_{np}} \quad (7)$$

Where m_t = total mass of the active principle introduced in to microemulsion.
The number of nanoparticles per water core can be calculated by,

$$N_{np/wc} = \frac{N_{np}}{N_{wc}} \quad (8)$$

The calculation suggests that the number of cholesterol nanoparticles per water core is 0.22. It also suggests that certain water cores might be empty. As per earlier estimation for the number of cholesterol nanoparticles per water core are 0.05 [17].

Size distribution of cholesterol nanoparticles by DLS study

Cholesterol nano particles were dispersed in double distilled water and DLS study was carried out. Fig. 3 shows the histogram of the particle size distribution and Table 1 shows the percentile value of each nanoparticles. The DLS study results correspond to the results of particle size obtained by TEM and powder XRD studies.

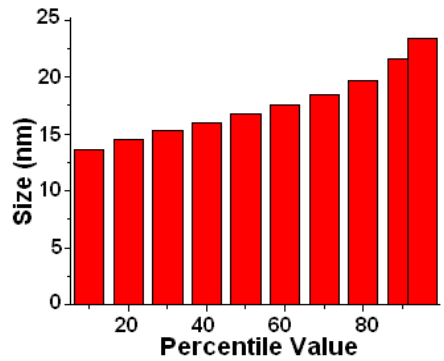

FIGURE3: Histogram of Particle size distribution by DLS particle size measurement

TABLE1: Particle size distribution by DLS Study

Percentile (%)	Size (nm)
10.00	13.61
20.00	14.49
30.00	15.26
40.00	15.99
50.00	16.73
60.00	17.53
70.00	18.47
80.00	19.69
90.00	21.56
95.00	23.40

Fourier Transform Infrared Spectroscopy (FT - IR)

The FT - IR spectral analysis was carried out to confirm the chemical bonding and functional groups present in the nano-material. The FT – IR spectrum of cholesterol crystals was reported by Kalkura et al [23]. FT – IR spectrum of cholesterol nano particles is shown in fig 4.

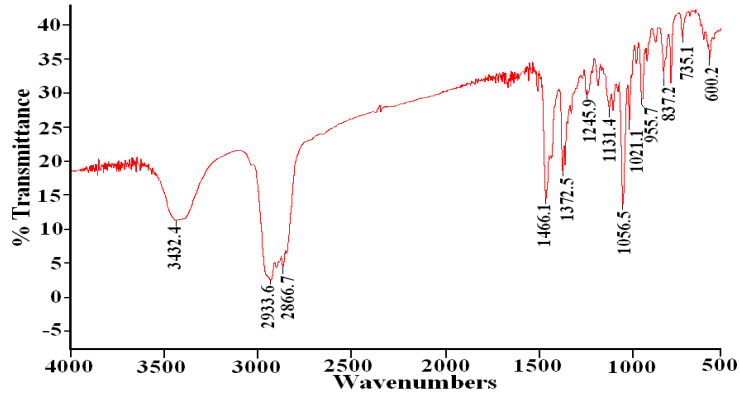

FIGURE 3: FT – IR spectrum of Cholesterol nanoparticles

The analysis of spectrum suggests that the absorption occurring at 3432.4 cm^{-1} is due to O – H stretching vibrations, the absorptions occurring at 2933.6 cm^{-1} and 2866.7 cm^{-1} are due to C – H stretching vibrations, the absorptions at 1466.1 cm^{-1} and 1372.5 cm^{-1} are assigned to C – H bending vibration and the absorptions at 1245.9 cm^{-1}, 1131.4 cm^{-1}, 1056.5 cm^{-1} and 1021.1 cm^{-1} are due to C – O stretching vibrations of esters and the absorptions at 955.7 cm^{-1} , 837.2 cm^{-1}, 735.1 cm^{-1} and 600.2 cm^{-1} are attributed to aromatic substitution. Considering a molecular model where the atoms are presented by point masses and the inter – atomic bonds are represented by mass less springs, which follows Hooke's law, and during the vibration the inter – nuclear distance changes sinusoidally but the center of gravity remains the same. Therefore, at any time during the vibration the atomic displacements are inversely proportional to

the masses. If masses are expressed in unified atomic mass unit (u) and force constant is expressed in milidynes per angstrom then the corresponding vibrations can be calculated by [24,25],

$$\upsilon = 1303\sqrt{F\left(\frac{1}{M_1}\right)+\left(\frac{1}{M_2}\right)} \tag{9}$$

Where υ = Wave number of particular absorption in the FT – IR spectra, F= Force Constant

The force constant values for different di-atomic vibrations are calculated by using relation (9) for FT-IR spectrum, which are given in Table 2. It can be noticed that the value of force constant increases as the stretching vibrations in wave numbers increases. The value of force constant is higher for di-atomic stretching vibration than the bending vibrations as comparatively less force is required to bend the bond than the stretch the bond.

TABLE2: FT – IR Assignments and Force constant

Assignments	**Absorption (cm^{-1})**	**Force Constant (mdyne/Å)**
O – H Stretching	3432.4	6.5294
C – H Stretching	2933.6	4.678
	2866.7	4.467
C – H bending vibration	1466.1	1.1688
	1372.5	1.2
C – O stretching	1245.9	6.2847
	1131.4	6.9575
	1056.5	4.5141
	1021.1	4.2199
Aromatic Substitution	955.7	0.497
	837.2	0.381
	735.1	0.308
	600.2	0.196

Thermal Study

Fig. 5 shows the thermogram of cholesterol nanoparticles. The sample remains stable almost up to 160^0C, thereafter, on further heating a minor weight loss taking place between 160^0C to 200^0C is observed, which is nearly 1weight percent of the original weight of the compound. Then a very sharp decomposition is observed and at 400^0C the sample is almost completely decomposed by liberating gaseous products.

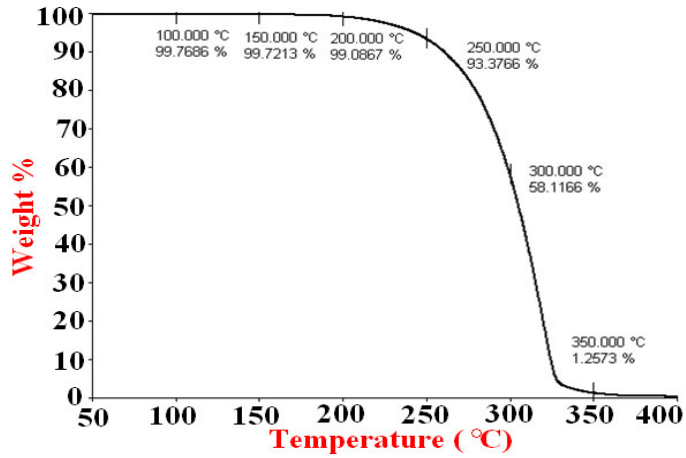

FIGURE5: Thermogram of Cholesterol nano particles

Thermodynamic and Kinetic Parameters

In the present study, the authors evaluated the thermodynamic and kinetic parameters for the decomposition of cholesterol nanoparticles at 240 ^{o}C by using the thermo-gram data of fig. (5). The kinetic parameters of decomposition process of cholesterol nanoparticles were calculated by using the Coats and Redfern relation [27] which has been discussed in detail elsewhere [28], the expression of Coats and Redfern relation is as follows:

$$\log_{10}\left(\frac{1-(1-\alpha)^{1-n}}{(1-n)T^2}\right) = \left[\log_{10}\left(\frac{AR}{\alpha E}\right)\left(1-\frac{2RT}{E}\right)-\left(\frac{E}{2.3RT}\right)\right] \qquad (10)$$

Where, $\alpha = \frac{(W_0 - W)}{(W_0 - W_f)}$ W_0 = Initial weight, W = Weight at time t, W_f = Final weight, n = Order of reaction, A = Frequency factor, E = Activation energy of the reaction, R =Gas constant and a = Heating rate.

To determine the kinetic parameters, a plot of $\log_{10}\left(\frac{1-(1-\alpha)^{1-n}}{(1-n)T^2}\right)$ versus $\frac{1}{T}$ is drawn for different values of order of reaction (n). The best linear fit gives the correct value of n and the value of activation energy can be calculated by using the slope of linear plot, which is shown in fig (6). Table 3 shows the values of different kinetic parameters, viz., order of reaction, frequency factor and activation energy.

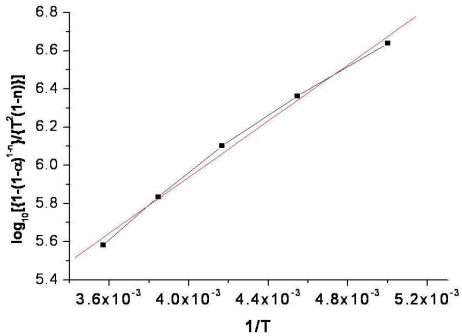

FIGURE 6: Linear fitted plot of Coats and Redfern relation for cholesterol nanoparticles

TABLE3: Kinetic parameters of Cholesterol Nano Particles

Kinetic Parameters	
Order of reaction (n)	0
Activation Energy (E)	75.87 $kJK^{-1}mol^{-1}$
Frequency factor (A)	1.00×10^{23}

The thermodynamic parameters of decomposition have been evaluated for the decomposition stage at 240 ^{0}C, the on set of precipitous decomposition process by using the standard formulae discussed by Laidler [29].

TABLE4: Thermodynamic Parameters of Cholesterol Nano Particles

Thermodynamic Parameters	
Standard change in Entropy ($\Delta^{\#}S^0$)	$190.95JK^{-1}mol^{-1}$
Standard change in Enthalpy ($\Delta^{\#}H^0$)	67.34 $kJmol^{-1}$
Standard change in Gibbs free energy ($\Delta^{\#}G^0$)	- 30.60 $kJmol^{-1}$

Table 4 shows the value of different thermodynamic parameters. The positive value of standard change in entropy ($\Delta^{\#}S^0$) and standard change in enthalpy ($\Delta^{\#}H^0$) as well as the negative value of standard change in Gibbs free energy ($\Delta^{\#}G^0$) suggest that the reaction will be spontaneous at higher temperatures [30].

CONCLUSION

Cholesterol nano – particles were synthesized by using w/o microemulsion. Broadening of the peaks of powder XRD pattern indicated the nano structured nature of the material and the average particle size was determined by using the Scherrer's formula, which was found to be 22 nm. From the Powder XRD data analysis the crystal structure of cholesterol nanoparticles was found to be triclinic and the unit cell parameters matched with those of the reported one. The particle size was also confirmed by TEM, which varied from 15 nm – 31 nm. The number of nanoparticle per water core was estimated to be 0.22. The particle size distribution was also confirmed by DLS particle size analyzer, which showed the maximum number of nano particles were of 23 nm size. The FT – IR study confirmed the presence of O – H,

C – H and C – O stretching as well as aromatic substitutions. Higher values of force constant for diatomic stretching vibrations than the bending vibrations were obtained. From the TGA it was found that the nanoparticles of cholesterol were stable up to 200^{o}C, then precipitous decomposition took place and at 400 ^{o}C cholesterol nano particles decomposed almost completely. The nature of the thermodynamic parameters suggested the spontaneous reaction at higher temperature.

ACKNOWLEDGMENTS

The authors are thankful to the Government of Gujarat for sanctioning the grants to develop experimental facilities under the project "Nanoscience & Technology and Environmental Physics" and Prof. K.N. Iyer for his keen interest. The authors (PMV & SRV) are thankful to UGC, New Delhi, for sanctioning the Fellowship under the Meritorious Research Student Fellowship scheme.

REFERENCES

1 L. Finegold, *Cholesterol in Membrane Models,* Boca Raton, Fl, USA : CRC Press, 1993.
2 R. C. Maranhao, E. L. Garicochea Silva, P. Dorlhiac – Liacer, S. M. S. Cadena, I. J. C. Coelha, J. C. Meneghetti, F. J. C. Pileggi, D. A. F. Chamone, *Cancer. Res.* **54**, 4660 - 4666 (1994).
3 L.A. Pires, R. Hegg, C. J. Valduga, S. R. Graziani, D. G. Rodrigues and R. C. Maranhao, *Cancer Chemother. Pharmacol.* **63**, 281 - 287 (2009).
4 Y. K. Ho, R. G. Smith, M. S. Brown and J. L. Goldstein*, Blood* **52**, 1099 - 1114 (1978).
5 R. C. Maranhao, S. R. Graziani, N. Yamaguchi, R. F. Melo, M. C. Latrilha, D. G. Rodrigues, R.D.Couto, S. Schreier and A.C. Buzaid, *Cancer Chemother. Pharmacol.* **49**, 487 - 498 (2002).
6 S. R. Graziani, F. A. F. Igreja, R. Hegg, C. Meneghetti ,L. I. Brandizzi, R. Bardoza, R. F. Amancio, J. A. Pinotti,R. C. Maranhao, *Gynecol. Oncol*. **85**, 493 - 497 (2002).
7 A. Ades , J. P. Carvalho, S. R. Graziani, R. F. Amancio, J. S. Souen, J. A. Pinotti, R. C. Maranhao, *Gynecol. Oncol.* **82**, 25 - 29(2001).
8 S. P. Moulik, L. G. Digout, W. M. Aylward and R. Palepu, *Langmuir* **16**, 3101 - 3106 (2000).
9 B. K. Pal and S. P. Moulik, *Current Science* **80**, 990 - 1001 (2001).
10 B. K. Pal, S. P. Moulik, *J. Dispersion Sci. Technol.* **18**, 301 - 367 (1997).
11 S. P. Moulik, B. K. Pal, *Adv. Collid. Inter. Sci.* **78**, 99 -195 (1998).
12 F. Debuigne, L. Jeunieau, M. Wiame and J. B. Nagy, *Langmuir* **16**, 7605 -7611 (2000).
13 Wanzhong Zhang , Xueliang Qiao, Jianguo Chena, *Materials Science and Engineering B* **142**, 1-15 (2007).
14 V. T. Liveri, M. Rossi, G. D. Arrigo, D. Manno and G. Micocci, *Appl. Phys. A* **69**, 369 – 373 (1999).
15 M. S. Lee, G. D. Lee, S. S. Park, S. S. Hong, *J. Ind. Eng. Chem.* **9**, 89 – 95 (2003).
16 K. M. Ghosen, S. Magdassi, *Nanomedicine* **5**, 274 -281 (2009).
17 C. Destree, J. Ghijsen and J. B. Nagy, *Langmuir* **23**, 1965 - 1973 (2007).
18 Y. Bayrak, M. Iscan, *J. of Surf. and Deter.* **7**, 363 - 366 (2004).
19 L. Jeunieau, F. Debuigne, J. B. Nagy, *J. Ed. Surfactant Science Series* **100**, 609 – 611 (2001)
20 M. Seethalakshmi Ammal, K. V. George, and I. Jayakumari, *Cryst. Res.Technol.* **42**, 876 - 880 (2007).
21 P. M. De Wolff, *X – ray powder Data File,* Card No. 07 – 0742, OR (P. M. De Wolff, JCPDS – ICDD, card No. -07 – 0742)
22 J. Eastoe, B. H. Robinson, A.J.W.G. Visser, D. C. Steatler, *J. Chem. Soc.* **67**, 1899 - 1903 (1991).
23 S. Narayana Kalkura, V. Ramakrishnan and S. Devanarayanan, *Infrared Phys.* **27**, 335 - 337 (1987).

24 N. B. Colthup, L. H. Daly and S. E. Wiberly, *"Introduction to infrared and raman spectroscopy"* 2nd edn.,New York: Academic Press, 1975.
25 V. S. Joshi, "Crystal growth and characterization of some urinary crystals", Ph. D. thesis, Saurashtra University, 2001.
26 S. Magdassi and M. Moshe, *Langmuir* **19**, 939 - 942 (2003).
27 A. W. Coats and J. P. Redfern, *Nature* **201**, 68 - 69 (1964).
28 K. D. Parikh, D. J. Dave, B. B. Parekh, M. J. Joshi, *Bull. of Mater. Sci.* **30**, 105 - 112 (2007).
29 K. J. Laidler, *Chemical Kinetics,*New York:Harper and Row, 1987.
30 A. G. Whittaker, A. R. Mount and M. R. Hill, *Physical Chemistry,* New Delhi: Viva, 2001.

Cryst. Res. Technol. **46**, No. 2, 187 – 194 (2011) / **DOI** 10.1002/crat.201000587

Growth and characterization of Struvite-K crystals

C. K. Chauhan*, P. M. Vyas, and M. J. Joshi

Crystal Growth Laboratory, Department of Physics, Saurashtra University, Rajkot - 360 005, Gujarat, India

Received 17 November 2010, revised 7 December 2010, accepted 14 December 2010
Published online 7 January 2011

Key words Struvite-K, Struvite, crystal growth, gel growth, FT-IR, thermal study.

Struvite-K is the natural potassium equivalent to Struvite. Struvite-K crystals were grown by single diffusion gel growth technique in silica hydro gel medium. Struvite-K crystals with different morphologies having transparent to translucent diaphaneity were grown with different growth parameters. The phenomenon of Liesegang rings was also observed with some particular growth parameters. The crystals were characterized by powder XRD, FT-IR, TGA and dielectric study. The powder XRD results of Struvite-K confirmed the orthorhombic crystal structure. The FT-IR spectrum proved the presence of water of hydration, metal – oxygen bond and P – O bond. The TGA, DSC and DTA were carried out simultaneously. It was found that crystals started dehydrating and decomposing from 75 °C and finally at 600 °C temperature it became 64.14% of the original weight and remained almost constant up to the end of analysis. From the thermo-gravimetry, the numbers of the water molecules associated with the crystal were calculated and found to be 5. The kinetic and thermodynamic parameters of dehydration / decomposition process were calculated. The variation of dielectric constant with frequency of applied field was studied in the range from 400 Hz to 100 kHz, which exhibited the decreasing nature of the dielectric constant as frequency increased. The dielectric study showed that a.c. conductivity increased and consequently the a.c. resistivity decreased with the increase in frequency.

1 Introduction

Potassium Magnesium Phosphate Hexahydrate [$KMgPO_4 \cdot 6H_2O$], also known as Struvite-K, is new inorganic phosphate mineral approved by the Commission on New Minerals and Mineral Names, International Mineralogical Association (CNMMN-IMA) in the year 2003 [1]. Struvite-K is the natural potassium equivalent to Struvite [$NH_4MgPO_4 \cdot 6H_2O$], since the crystals of Struvite-K are rich in potassium and similar to Struvite. Struvite type compound can be represented by $X^+Y^{2+}PO_4 \cdot nH_2O$, where n = 6 to 8. It contains one monovalent cation X^+ and one divalent cation Y^{2+}. Among phosphate containing biominerals, struvite has attracted considerable attention, because of its common occurrence in a wide variety of environments. A large number of Struvite type compounds and their structural relationships have been reported by Dickens and Brown in 1972 [2]. Their biological importance is dependent, in part, on their possible roles as precursors or nuclei of crystallization. Struvite-K is a well-defined potassium analogue of Struvite; where monovalent cation K^+ replaces the NH_4^+ ammonium cations. This ion replacement is possible, as the ionic radii of K^+ and NH_4^+ are almost identical [3]. Earlier, both the Struvite and Struvite-K were reported as iso-structural compounds [4,5]. Struvite-K was identified as a mineral at two different locations [6]: (1) at the famous sulphosalt locality of Lengenbach in Binntal, Switzerland, in a dolomitic rock of Triassic age, (2) at Rossblei, Austria, in an abandoned galena mine. The mineral occurs as pseudomorphous aggregates of dirty white colour reaching up to several millimeters in size. The aggregates represent close intergrowths of fine-grained struvite-K and newberyite [$Mg(PO_3OH) \cdot 7H_2O$]. Moreover, Struvite-K was also found as urinary calculi in the animals like dogs [7], goats [8] and buffalo calves [9] fed with the high-level cottonseed meal diet. In the present investigation, Struvite-K crystals were grown by single diffusion gel growth technique in silica hydro gel medium and characterized by Fourier transform infrared (FT-IR) spectroscopy, powder X-ray diffraction (XRD), and dielectric study. The thermal analysis of the Struvite-K was also carried out by using thermo gravimetric analysis (TGA), differential thermal analysis (DTA) and differential scanning calorimetry (DSC).

* Corresponding author: e-mail: ckc33@rediffmail.com
presently at: H. & H. B. Kotak Institute of Science, Dr Yagnik Road, Rajkot - 360 001, Gujarat, India

2 Experimental

Crystal growth The single diffusion gel growth technique was used to grow Struvite-K crystals. Distilled water and analytical reagent (AR) grade chemicals were used to grow the crystals. Sodium metasilicate (SMS) – [$Na_2SiO_3 \cdot 9H_2O$] solutions with different specific gravity were used to prepare the gel. To prepare the Silica hydro gel, SMS solution was first prepared by adding SMS powder to the distilled water and was stirred vigorously and continuously for 2 h for uniform mixing up. Then the solution was filtered. The density of the SMS solution was determined by specific gravity bottle method. Aqueous solutions of potassium dihydrogen phosphate (KDP) – [KH_2PO_4] with different concentrations were mixed with the SMS solutions in appropriate amount to set the gel at the specific pH values of the mixture, which was in 20 mL volume, transferred into the respective autoclaved test tubes of 140 mm length and 25 mm diameter. All test tubes and other glassware were autoclaved at 120 °C for 15 min. The time required to set the gel firmly was different for each set of mixture depending on pH value of the mixture. Within 2 days, good quality gels were set in the test tubes. After the gelation took place, 20 mL supernatant solutions of magnesium acetate [$Mg(CH_3COO)_2 \cdot 4H_2O$] were gently poured on the set gels in test tubes by using pipette. All the test tubes were capped with airtight stopples and kept undisturbed. Here, the silica hydro gel was chosen because it remains stable and does not react with the reactants present or with the product crystals grown. The whole process was carried out in the aseptic medium in laminar flow hood to avoid microbial contaminations. The experiment was conducted at the room temperature. Different growth parameters were used to grow Struvite-K crystals. Table 1 shows the growth parameters of the experiment. The following reaction is expected to occur in the gel between the two reactants

$$KH_2PO_4 + Mg(CH_3COO)_2 \cdot 4H_2O + 2H_2O \longrightarrow K Mg PO_4 \cdot 6H_2O + 2CH_3COOH\,. \quad (1)$$

The growth of crystals was started in the gel column below the gel-liquid interface within a day and completed within 20 days. The grown Struvite-K crystals were carefully removed from the gel medium using the forceps. The Struvite-K crystals which were sparingly soluble in water, quickly rinsed in distilled water and then dried on a filter paper. The grown crystals were kept in airtight bottles and used for further investigation.

Table 1 Different growth parameters used to grow Struvite-K crystals.

Set	Specific Gravity of SMS	Concentration of KDP (Reactant I) (M)	pH value of the Gel	Concentration of supernatant solution of magnesium acetate (Reactant II) (M)	Liesegang Rings observed having pH values
1	1.04	1.00	6.0 to 8.0	1.00	8.0
2	1.04	1.50	6.0 to 8.0	1.50	-
3	1.05	0.25	6.0 to 8.0	1.00	> 7.0
4	1.05	0.50	6.0 to 7.5	1.00	> 7.5
5	1.05	1.00	5.5 to 8.5	1.00	> 8.0
6	1.05	1.50	6.0 to 8.0	1.00	> 7.5
7	1.05	0.50	6.0 to 9.0	0.50	-
8	1.06	0.50	6.0 to 8.5	1.00	> 8.0
9	1.06	1.00	6.0 to 8.0	1.00	8.0
10	1.07	1.50	5.8 to 7.0	1.00	-

Characterization techniques The grown crystals in a fine powder form were analyzed by powder XRD using Philips X'Pert SW diffracto-meter system with monochromatic Cu Kα radiation. The powder XRD data were analyzed using Powder-X computer software. The FT-IR spectrum of powdered samples of the grown crystals was recorded on a Nicolet 6700 FT-IR spectrometer having optical resolution of 0.09 cm^{-1}, in the range from 400 cm^{-1} to 4000 cm^{-1} in KBr disc medium. The TGA, DTA and DSC were carried out to determine simultaneous changes of mass and caloric reactions on Linseis Simultaneous Thermal Analyzer (STA) PT-1600, in the atmosphere of air from 35 °C to 900 °C at a heating rate of 15 K/min. The dielectric study was carried out by measuring capacitance of the pressed pellets of samples of known dimension at room temperature on Agilent 4284 A precession Inductance, Capacitance and Resistance (LCR) meter using specially designed sample holder, within the frequency range from 400 Hz to 100 kHz. Dielectric constant was calculated by using standard formula.

3 Results and discussion

Crystal growth The gel growth technique was described in details by Henisch [10], Henisch et al. [11] as well as Patel and Rao [12]. The growth and characterization of the gel grown Struvite crystals was reported by

Chauhan et al [13]. Some of the Struvite-type compounds were grown by the gel growth technique [14,15]. Struvite analog $X^{+}Y^{2+}PO_4 \cdot nH_2O$ compounds with X = Rb and Tl and Y = Mg were obtained by means of the gelatine-gel diffusion technique by M. Weil [14]. Earlier needle type Struvite-K crystals were grown by gel diffusion technique by E. Banks et al. [15]. In the present study, Struvite-K crystals were grown by the single diffusion gel growth technique and the effects of various growth parameters on the growth and morphology of crystals were reported.

Figure 1a shows the photograph of Struvite-K crystals grown in the gel medium. Struvite-K crystals were grown by changing different growth parameters as mentioned in table 1. Crystals with different morphologies like prismatic type, star type, rectangular platelet type and dendritic type were grown in the gel. Figure 2 shows different type of morphology of grown Struvite-K crystals.

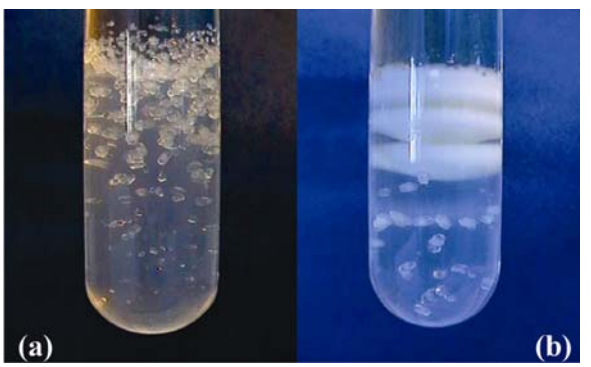

Fig. 1 (a) Struvite-K Crystals grown in gel medium, (b) Liesegang rings observed for 1.05 specific gravity of SMS solution, 0.25 M KDP solution, 7.0 pH value of the gel and supernatant solution of 1 M magnesium acetate.

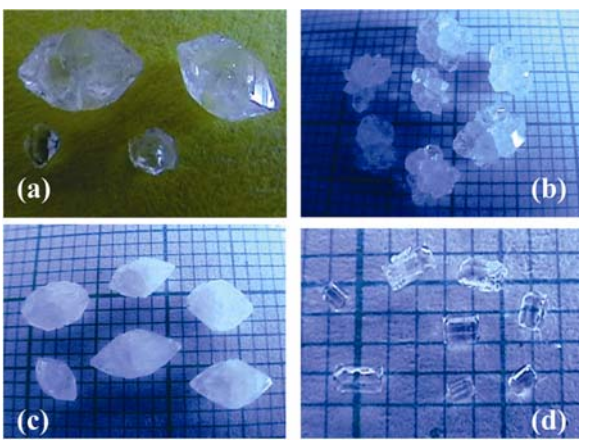

Fig. 2 Different morphology of Struvite-K crystals. (Online color for both figures at www.crt-journal.org)

Figure 1a shows that the prismatic type Struvite-K crystals were grown for the selected growth parameters as 1.05 specific gravity of SMS solution, 0.5 M KDP solution, 6.5 pH value of the gel and supernatant solution of 0.5 M magnesium acetate. Here, it was observed that number density, apparent size of the grown crystals decreased and the transparency increased with increase in the depth of gel column. In the case of the same growth parameters except for 7.0 pH of the gel, the prismatic type crystals were observed and its number density decreased but at the same time apparent crystal size increased. It was also observed that the number density of the grown crystals increased with the increasing concentrations of either the first reactant or the supernatant solution.

Figure 2a shows the transparent prismatic type Struvite-K crystals. As shown in figure 2b, the star type crystals were grown for SMS solution of specific gravity 1.05, 1.5 M KDP solution, 6.5 pH value of the gel and supernatant solution of 1 M magnesium acetate. However, only one star type crystal was observed for the SMS solution of specific gravity 1.04, 1 M KDP solution, 7 pH value of the gel and supernatant solution of 1 M magnesium acetate. The dendritic type growth was observed for the SMS solution of specific gravity 1.04, 1.5 M KDP solution, 6 pH value of the gel and 1.5 M magnesium acetate solution, which was due to the higher concentration of the reactants. As shown in figure 2c, comparatively large, opaque, prismatic type crystals having apparent size of 5 to 7 mm were observed for the growth parameters as 1.06 specific gravity of SMS solution, 1 M KDP solution, 7.5 pH value of the gel and 1 M magnesium acetate solution.

It was observed that pH values of the gel played an important role in the growth morphology of the crystals, for example, with the growth parameters having 1.05 specific gravity of SMS solution, 0.25 M KDP solution and 1 M magnesium acetate concentration of supernatant solution, the rectangular platelet type crystals were observed for 6.0 pH, the star type crystals were observed for 6.5 pH and prismatic type crystals were observed for 7.0 and 7.5 pH. It was also found that the higher the pH the gels were denser. It was noticed that comparatively dense gels produce poor crystals. The dense gels have small pore sizes and do not readily facilitate the movements of supernatant solution ions for the reaction and also the dense gel put constraints on the growth of crystals. This has been discussed in detail by Parikh et al. [16].

The grown Struvite-K crystals had transparent, translucent and opaque diaphaneity, depending upon the location and the growth conditions. It was observed that opaque crystals were grown at gel-liquid interface, whereas more transparent crystals were grown at the higher depth in the gel column. It was also noticed that as the pH value of the gel increased, the transparency of the grown crystals decreased. Moreover, transparency decreased with the increasing concentration of reactant solutions. Figure 2a and c show the transparent and opaque prismatic type crystals, respectively.

The Liesegang rings were also observed for 7.0 and higher pH values of the gel. Table 1 shows the cases for which Liesegang rings were observed. Figure 1b shows the formation of Liesegang rings in the test tube with the growth parameters 1.05 specific gravity of SMS solution, 0.25 M KDP solution, 7.0 pH value of the gel and supernatant solution of 1 M magnesium acetate. It was observed that as the pH of the gel increased, the number of Liesegang rings increased. The spacing between the Liesegang rings in the gel column increased with the depth. Moreover, the thickness of the Liesegang rings also increased with the depth. Joseph and Joshi [17] have discussed the effect of various parameters on the formation of Liesegang rings during the growth of calcium hydrogen phosphate dehydrate crystals. The crystals in the Liesegang rings are of the order of micrometer size. It is clear from the figure 1b that Struvite-K crystals were grown with prismatic morphology having apparent length of 3 to 5 mm; and they also formed a ring structure under the last Liesegang ring.

Powder XRD Figure 3 exhibits the powder XRD pattern of Struvite-K crystals. The crystal structure was found to be orthorhombic with cell parameters as, a = 6.893 Å, b = 6.141 Å, c = 11.222 Å and $\alpha = \beta = \gamma = 90°$. The values are closely matching with those reported by S. Graeser et al. [6].

FT-IR Study Many common minerals exhibit unique spectra in the mid-infrared range, which extends from 400 cm^{-1} to 4000 cm^{-1}. Often infrared spectroscopy is used to study these minerals in the urinary tracts and calculi [18-21]. Some studies have been undertaken on $MgHPO_4 \cdot 3H_2O$ [22,23].

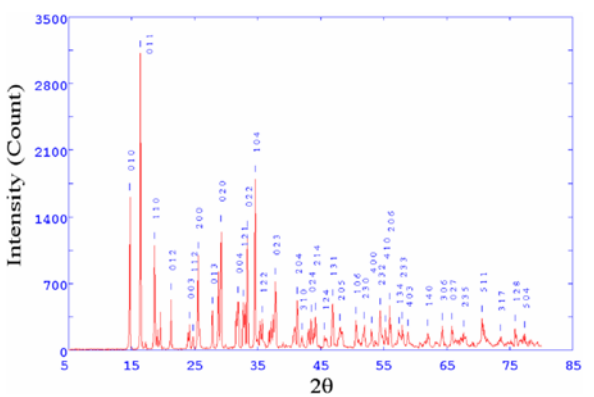

Fig. 3 XRD pattern of Struvite-K.

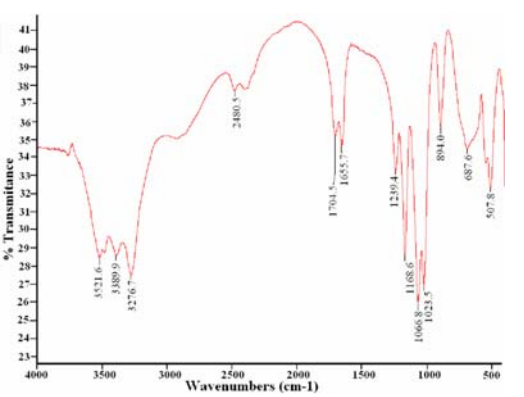

Fig. 4 FT-IR Spectrum of Struvite-K.

The FT-IR spectrum of the Struvite-K crystals is presented in figure 4 and the vibrational band assignments according to literature and experimental data are summarized in table 2. FT-IR spectroscopy provides a sensitive tool for the detection of H_2O molecules i.e. water of crystallization in minerals and their binding states in a crystal. The FT-IR technique investigates O–H vibrations, whose absorption bands appear at different frequencies depending on the cations directly linked to the hydroxyls. There are four regions found in the FT-IR spectrum depicting the absorptions due to water of crystallization in Struvite-K as shown in table 2, which closely matches to the previously reported peaks in several inorganic hydrated compounds [23-30]. Intense bands appeared at the 3276.7 cm^{-1}, 3389.9 cm^{-1} and 3521.6 cm^{-1} indicate H–O–H stretching vibrations of water of crystallization. The weak bands appeared at 2375 cm^{-1} and 2480.5 cm^{-1} in the spectrum can be assigned due to H–O–H stretching vibrations of cluster of water molecules of crystallization. The medium intense bands appeared at 1655.7 cm^{-1} and 1704.5 cm^{-1} in the spectrum indicate the H–O–H bending modes of vibrations suggesting the presence of water. A medium absorption band at 894 cm^{-1} indicates the wagging modes of vibration of the coordinated water and the Metal–Oxygen bond in the complex.

In the FT-IR spectrum, the ν_1 symmetric stretching vibration of PO_4 units was found to be at 1023.5 cm^{-1} in case of Struvite-K, which corresponds to the previously reported values for different minerals as 930 cm^{-1} (augelite), 940 cm^{-1} (wavellite), 970 cm^{-1} (rockbridgeite), 995 cm^{-1} (dufrenite) and 965 cm^{-1} (beraunite), 947 cm^{-1} (struvite) and 964 cm^{-1} (whitlockite) [31,32]. The position of the symmetric stretching vibrations is

mainly dependent on the type of mineral, the cation present and crystal structure. While, the positions of the asymmetric stretching vibrations ν_3 of PO_4 units in Struvite-K were 1066.8 cm^{-1}, 1168.6 cm^{-1} and 1239.4 cm^{-1}, which are in accordance with the values reported earlier [31]. The value of the symmetric bending vibrations ν_2 of PO_4 units was 421 cm^{-1}, which corresponds to the values reported for various phosphate minerals as 438 cm^{-1} (augelite), 452 cm^{-1} (wavellite), 440 cm^{-1} and 415 cm^{-1} (rockbridgeite), 455 cm^{-1}, 435 cm^{-1} and 415 cm^{-1} (dufrenite), 470 cm^{-1} and 450 cm^{-1} (beraunite), 404 cm^{-1} (struvite) and 431 cm^{-1} (whitlockite) [31]. Moreover, the position of the asymmetric bending vibrations ν_4 of PO_4 units in Struvite-K was 507.8 cm^{-1}. The absorption at 687.6 cm^{-1} indicates the presence of oxygen-metal bond.

Table 2 Assignments of different absorption bands in the FT-IR spectrum of Struvite-K.

Assignments		Reported infrared (IR) frequencies wavenumbers (cm^{-1})	Observed IR frequencies wavenumbers (cm^{-1})
Absorption peaks due to water of crystallization	H–O–H stretching vibrations of water crystallization	3280 to 3550	3276.7, 3389.9,3521.6
	H–O–H stretching vibrations of cluster of water molecules of crystallization	2060 to 2460	2375, 2480.5
	H–O–H bending modes of vibrations	1590 to 1650	1655.7, 1704.5
	Wagging modes of vibration of coordinated water	808	894
Absorption peaks due to PO_4 units	ν_1 symmetric stretching vibration of PO_4 units	930 to 995	1023.5
	ν_2 symmetric bending vibration of PO_4 units	404 to 470	421.8
	ν_3 asymmetric stretching vibration of PO_4 units	1017 to 1163	1066.8, 1168.6, 1239.4
	ν_4 asymmetric bending modes	509 to 554	507.8
Metal-Oxygen bonds	Metal-Oxygen bonds	400-650	687.6
	Deformation of OH linked to Mg^{2+}	847	894

TGA, DSC and DTA studies Joshi and Joshi [33,34] have reported thermal studies of calcium hydrogen phosphate dihydrate (brushite) crystals by conducting TGA. In the present study, the TGA, DSC and DTA were carried out simultaneously. TGA, DTA and DSC profiles obtained for the powdered Struvite-K are as shown by the curves (a), (b) and (c) respectively in figure 5. The graph of mass loss in mg on the Y-axis plotted versus temperature at a fixed rate of change of temperature in °C on the X-axis shows the thermo-gram, which was obtained as the curve (a) of figure 5. From the thermo-gram, it was found that the crystals started dehydrating and decomposing from 75 °C and finally at 600 °C it became 64.14% of the original weight and remained almost constant up to the end of analysis. Mass loss in a TGA analysis of sample at temperatures above 100 °C indicates association of water molecules with the Struvite-K chemical structure. A continuous loss of mass in the TGA curve can be attributed to the dehydration of the sample. The graph of DTA signal, i.e. differential thermocouple output in micro volts on the Y-axis plotted versus the sample temperature in °C on the X-axis gives the results of DTA. The transition temperatures were measured precisely using DTA curve. In the DTA curve an endothermic peak was observed at 180 °C, which might be due to release of crystalline water. Processes involving a loss of mass usually give rise to endothermic nature in DTA trace because of the work of expansion. On further heating at higher temperatures, anhydrate Struvite-K was obtained.

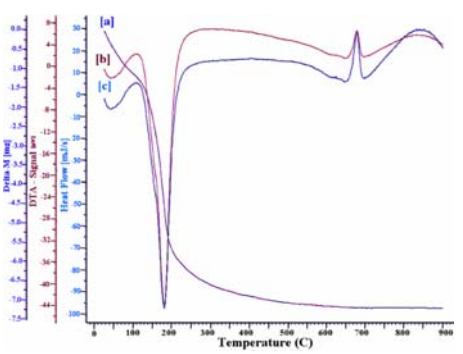

Fig. 5 TGA, DTA and DSC curve of Struvite-K.

From the thermo-gram, the number of water molecules associated with the crystal was estimated to be 5. In the temperature range 650–900 °C, no further weight loss occurred and the sample remained almost stable. In the DTA curve of Struvite-K crystals, two exothermic peaks were observed, one medium peak at 110 °C and the second strong one at 670 °C. Second exothermic peak might be due to high temperature phase transition. The

graph of heat flow in mJ/s on the Y-axis plotted versus temperature at a fixed rate of change of temperature in °C on the X-axis shows the output of the DSC, which was obtained as the curve (c) of figure 5. The DSC curve exhibited peaks at the same temperatures as peaks were obtained in DTA curve. In the thermogram, no remarkable change was observed for the peak which was noticed at 670 °C in DTA and DSC curves due to the possible phase transition, since no change took place in the mass of the specimen.

The kinetic and thermodynamic parameters for brushite [33], Struvite [13] crystals were calculated by applying Coats and Redfern relation [35] to the respective thermograms. In the present investigations, the kinetic parameters for dehydration of Struvite-K have been evaluated by applying the Coats and Redfern relation to the thermogram of figure 5.

The Coats and Redfern relation [35] is as follows;

$$\log_{10}\left(\frac{1-(1-\alpha)^{1-n}}{T^2(1-n)}\right)=\left\{\log_{10}\left(\frac{AR}{aE}\right)\left(1-\frac{2RT}{E}\right)\right\}-\left\{\frac{E}{2.3RT}\right\}, \quad (2)$$

where, E is the activation energy of the reaction, A is the frequency factor, α is the fraction of decomposed material at time t, a is the heating rate in K/min, R is the gas constant, n is the order of reaction and T is the absolute temperature.

The plots of $Y = -\log_{10}[\{1-(1-\alpha)^{1-n}\}/\{T^2(1-n)\}]$ versus $X = 1/T$ were straight lines for different values of n, however, the best linear fit plot gives the correct value of n. The value of activation energy is obtained from the slope of the best linear fit plot. The values of activation energy E, frequency factor A and the order of reaction n are 83.21 kJ Mol^{-1}, 4.64×10^{10} and 2, respectively.

Various thermodynamic parameters were calculated by applying well known formulae, as described in detail by Laidler [36]. Table 3 gives the values of different thermodynamic parameters. Here, negative value of $\Delta^{\ddagger}S°$ shows that the process is non-spontaneous, whereas the positive value of $\Delta^{\ddagger}H°$ shows that the enthalpy is increasing during the process and such process is an endothermic process. Positive value of $\Delta^{\ddagger}G°$ shows that the substance is thermodynamically unstable.

Table 3 The values of different thermodynamic parameters of Struvite-K.

Thermodynamic Parameter	Symbol	Value
Standard Entropy of activation	$\Delta^{\ddagger}S°$	-43.00 kJ Mol^{-1}
Standard Enthalpy of activation	$\Delta^{\ddagger}H°$	76.67 kJ Mol^{-1}
Standard Gibbs Energy of activation	$\Delta^{\ddagger}G°$	93.57 kJ Mol^{-1}
Standard Change in Internal Energy of activation	$\Delta^{\ddagger}U°$	79.94 kJ Mol^{-1}

Dielectric study Every material has a unique set of electrical characteristics that are dependent on its dielectric properties. The dielectric constant was calculated from the value of the capacitance of the sample using standard formula [37].

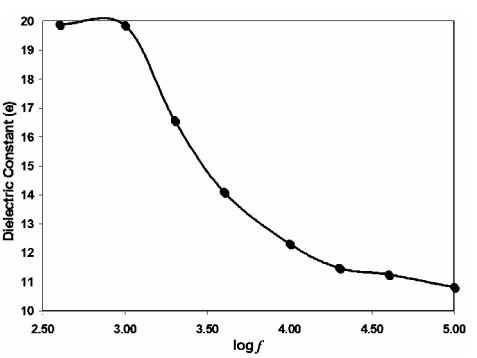

Fig. 6 Plot of dielectric constant versus log *f*.

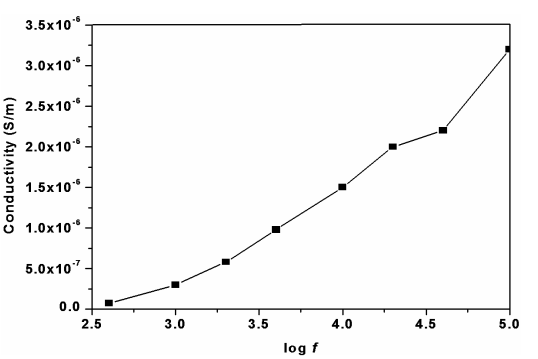

Fig. 7 a.c. conductivity versus log *f*.

Figure 6 shows the variation of dielectric constant with frequency of applied field. It was noticed for Struvite-K that the dielectric constant decreased with the increasing value of frequency of applied field. Initially, the dielectric constant remained almost constant up to 1 kHz frequency, there after it decreased rapidly with increasing frequency up to 20 kHz and then slowly decreased at higher frequency. This type of behavior indicates higher space charge polarizability of the material in the low frequency region. As the frequency increases, a point is reached where the space charge can not sustain and comply with the external field, and

hence the polarization decreases and exhibits the reduction in the values of dielectric constant as frequency increases. This has been discussed in detail elsewhere [37-39]. From the data of the variation of dielectric loss ($D = tan\ \delta$) with frequency of applied field at room temperature, it was observed that dielectric loss increased up to 2 kHz and followed by decreasing nature with higher frequency. Here, D is the dissipation factor (dielectric loss) which is equivalent to $tan\ \delta$. The angle δ is the complement of angle between the applied electric field and resultant current vector. The a.c. conductivity (σ_{ac}) and a.c. resistivity (ρ_{ac}) were calculated. Figure 7 shows the nature of variation of a.c. conductivity with frequency of applied field. It was found that a.c. conductivity increased whereas the a.c. resistivity decreased with the increasing value of frequency of applied field.

4 Conclusion

By changing the growth parameters, Struvite-K crystals having transparent to opaque diaphaneity with different morphologies like prismatic type, star type, rectangular platelet type and dendritic type were grown by single diffusion gel growth technique. Powder XRD confirmed the orthorhombic crystal structure with unit cell parameters as a = 6.893 Å, b = 6.141 Å, c = 11.222 Å and $\alpha = \beta = \gamma = 90°$. The estimated values of unit cell parameters were appreciably matching with the values reported in the literature. The absorption peaks obtained in FT-IR spectrum confirmed the water of crystallization, symmetric as well as asymmetric stretching and bending vibration of PO_4 units and metal-oxygen bonds in Struvite-K. The presence of water molecules was also confirmed by TGA and the numbers of the water molecules associated with the crystal were found to be 5. In the DTA and DSC curves the endothermic peak was observed at 180 °C due to process of dehydration and the exothermic peak was observed at 670 °C due to possible high temperature phase transition. TGA, DTA and DSC results show that the transformations were associated with the mass and temperature changes. The kinetic and thermodynamic parameters were calculated from the TGA curve. It was found that the process was endothermic, non-spontaneous and the substance was thermodynamically unstable. Dielectric study showed that the dielectric constant decreased with the increasing value of frequency. It was observed that the dielectric loss increased up to 2 kHz and then followed by a decreasing nature at higher frequency. The a.c. conductivity increased, whereas a.c. resistivity decreased, with the increasing value of frequency of applied field.

Acknowledgements The authors are thankful to the UGC, New Delhi, for the financial assistance under SAP and Prof. H. H. Joshi, Head, Physics Department, Saurashtra University, Rajkot, for his keen interest. The author (CKC) is thankful to the Dept. of Education, Govt. of Gujarat; Smt. Jayanti S. Ravi, Commissioner of Higher Education, CHE, Gandhinagar and Dr Ranjana Agarwal, Principal, H. & H. B. Kotak Institute of Science, Rajkot, for their encouragements.

References

[1] E. A. J. Burke and G. Ferraris, Am. Mineral. **89**, 1566 (2004).
[2] B. Dickens and W. E. Brown, Acta. Crystallogr. B **25**, 1159 (1972).
[3] J. E. Huheey, E. A. Keiter, and R. L. Keiter, Inorganic Chemistry, 4th Edition (Harper Collins, New York, 1993).
[4] M. Mathew and L. W. Schroeder, Acta Cryst. B **35**, 11 (1979).
[5] A. Whitaker and J. W. Jeffery, Acta Cryst. B **26**, 1429 (1970).
[6] S. Graeser, W. Postl, H. P. Bojar, P. Berlepsch, T. Armbruster, T. Raber, K. Ettinger, and F. Walter, Eur. J. Mineral. **20**, 629 (2008).
[7] J. Dunlevey and M. Laing, South Afr. J. Sci. **104**, 471 (2008).
[8] W. D. Sun, J. Y. Wang, K. C. Zhang, and X. L. Wang, Res. Vet. Sci. **88**, 461 (2010).
[9] X. Wang, K. Huang, J. Gao, X. Shen, C. Lin, and G. Zhang, Res. Vet. Sci. **62**, 275 (1997).
[10] H. K. Henisch, Crystal Growth in Gels (The Pennsylvania State Uni. Press, Pennsylvania, 1973).
[11] H. K. Henisch, J. Dennis, and J. I. Hanoka, J. Phys. Chem. Solids **26**, 493 (1965).
[12] A. R. Patel and A. V. Rao, Bull. Mater. Sci. **4**, 527 (1982).
[13] C. K. Chauhan, K. C. Joseph, B. B. Parekh, and M. J. Joshi, Indian J. Pure Appl. Phys. **46**, 507 (2008).
[14] M. Weil, Cryst. Res. Technol. **43**, 1286 (2008).
[15] E. Banks, R. Chianelli, and R. Korenstein, Inorg. Chem. **14**, 1634 (1975).
[16] K. D. Parikh, B. B. Parekh, D. J. Dave, and M. J. Joshi, Indian J. Phys. **80**, 719 (2006).
[17] K. C. Joseph and M. J. Joshi, Indian J. Phys. **76A**, 159 (2002).
[18] M. Daudon, M. F. Protat, R. J. Reveillaud, and H. Jaeschke-Boyer, Kidney Int. **23**, 842 (1983).
[19] B. Soptrajanov, G. Jovanovski, I. Kuzmanovski, and V. Stefov, Spectrosc. Lett. **31**, 1191 (1998).

[20] B. Soptrajanov, I. Kuzmanovski, V. Stefov, and G. Jovanovski, Spectrosc. Lett. **32**, 703 (1999).
[21] M. Volmer, J. C. M. De Vries, and H. M. J. Goldschmidt, Clin. Chem. **47**, 1287 (2001).
[22] F. A. Miller, G. L. Carlson, F. F. Bentley, and W. H. Jones, Spectrochim. Acta **16**, 135 (1960).
[23] F. A. Miller and C. H. Wilkins, Anal. Chem. **24**, 1253 (1952).
[24] Itaru Gamo, Bull. Chem. Soc. Jpn. **34**, 760 (1961).
[25] P. J. Lucchesi and W. A. Glasson, J. Am. Chem. Soc. **78**, 1347 (1956).
[26] J. Lecomte, J. Chim. Phys. **50**, C53 (1953).
[27] C. Duval, Anal. Chim. Acta **13**, 32 (1955).
[28] M. Dhandapani, L. Thyagu, P. A. Prakash, G. Amirthaganesan, M. A. Kandhaswamy, and V. Srinivasan, Cryst. Res. Technol. **41**, 328 (2006).
[29] V.C. Farmer, Monograph No. 4 Infrared spectra of minerals (Mineralogical Soc. Pub., United Kingdom, 1974).
[30] T. Kebede, K. V. Ramana, and M. S. Prasada Rao, Proc. Indian Acad. Sci. (Chem. Sci.) **113**, 275 (2001).
[31] R. L. Frost, M. L. Weier, W. N. Martens, D. A. Henry, and S. J. Mills, Spectrochim. Acta **62**, 181 (2005).
[32] S. K. H. Khalil and M. A. Azooz, J. Appl. Sci. Res. **3**, 387 (2007).
[33] V. S. Joshi and M. J. Joshi, Cryst. Res. Technol. **38**, 817 (2003).
[34] V. S. Joshi, Ph. D. Thesis (Saurashtra University, 2001).
[35] A. W. Coats and J. P. Redfern, Nature **201**, 68 (1964).
[36] K. J. Laidler, Chemical Kinetics, 3rd Edition (Harper and Row, New York, 1987).
[37] R. M. Dabhi, B. B. Parekh, and M. J. Joshi, Indian J. Phys. **79**, 503 (2005).
[38] S. K. Arora, V Patel, B Amin, and A Kothari, Bull. Mater. Sci. **27**, 141 (2004).
[39] F. M. Reicha, M. El-Hiti, A. Z. El-Sonabati, and M. A. Diab, J. Phys. D **24**, 369 (1991).

International Journal of Nanoscience
Vol. 10, No. 6 (2011) 1237−1244

DOI: 10.1142/S0219581X11008356

World Scientific
www.worldscientific.com

SYNTHESIS AND CHARACTERIZATION OF *n*-BUTYL 4-(3,4-DIMETHOXYPHENYL)-6-METHYL-2-THIOXO-1,2,3,4 TETRAHYDROPYRIMIDINE-5-CARBOXYLATE NANOCRYSTALLINE PARTICLES BY WATER/OIL MICROEMULSION METHOD

POORVESH M. VYAS*, MIHIR J. JOSHI*,‡, AKSHAY M. PANSURIYA† and YOGESH T. NALIAPARA†

*Department of Physics, Saurashtra University
Rajkot 360 005, Gujarat, India

†Department of Chemistry, Saurashtra University
Rajkot 360 005, Gujarat, India
‡mshilp24@rediffmail.com

Received 21 September 2010
Accepted 18 March 2011

Various pyrimidine derivatives are well known for their different pharmaceutical applications. The *n*-butyl 4-(3, 4-dimethoxyphenyl)-6-methyl-2-thioxo-1,2,3,4 tetrahydropyrimidine-5-carboxylate (*n*-butyl THPM) was synthesized by using *n*-butylacetoacetate. The *n*-butyl acetoacetate was obtained by transesterification of ethyl acetoacetate with *n*-butyl alcohol using Biginelli condensation. The synthesized powder was used to obtain the nanoparticles of *n*-butyl THPM by using water/oil microemulsion technique. The average particle size was calculated from the powder XRD pattern by applying Scherrer's formula. The nanoparticles of *n*-butyl THPM were observed by Transmission Electron Microscope (TEM). The diameter of the nanoparticles varied from 15 nm to 65 nm. The nanoparticles were also characterized by FT−IR spectroscopy, TG−DTA−DSC and mass spectroscopy. The *n*-butyl THPM nanoparticles were stable up to 280°C. Thermodynamic and kinetic parameters of decomposition were obtained by applying Coats and Redfern relation to the thermogram. The dielectric study was carried out in the frequency range of 50 Hz to 5 MHz. The dielectric constant, dielectric loss and ac conductivity decreased as the frequency of applied field increased.

Keywords: Microemulsion; powder XRD; TEM; FTIR; TGA.

1. Introduction

Pyrimidine derivatives possess wide range of biological properties such as antiviral, antitumor, antibacterial, anti-inflammatory[1]; antihypertensive[2]; anticardiovascular agents[3]; calcium channel blocking[4] and neuropeptide Y (NPY) antagonists.[5] Also, several marine alkaloids with interesting biological activities containing the dihydropyrimidine-5-carboxylate core have been isolated.[6−8] Recently, appropriately functionalized dihydropyrimidine

have emerged as orally active and hypertensive agents.[9–11] Other derivatives show interesting biological activities in several marine natural products, which contain the dihydropyrimidine-5-carboxylate core.[3] Monastrol, derivative of Tetrahydropyrimidine (THPM) is known as mitotic kinesin Eg5 inhibitor. Monastrol affects the cell division by a new mechanism. The discovery of a new class of proteins, the mitotic kinesins, offers a novel approach for cancer treatment. These proteins are exclusively involved in the formation and function of the bipolar mitotic spindle. Grover *et al.*[11] Dallinger *et al.*[12] and Saez *et al.*[13] established that monastrol blocks mitosis by specific and reversible inhibition of the mitotic kinesin Eg5. Looking at the applications of pyrimidine derivatives, present authors synthesized *n*-butyl 4-(3, 4-dimethoxyphenyl)-6-methyl-2-thioxo-1,2,3,4 tetrahydropyrimidine-5-carboxylate (*n*-butyl THPM) nanocrystalline particles for the first time, so far the knowledge of present authors is concerned, and characterized them by Transmission Electron Microscope (TEM), FT-IR spectroscopy, powder XRD, TG–DTA–DSC, mass spectroscopy and dielectric studies. However, The growth and characterization of *n*-butyl THPM crystals is already reported by present authors.[14,15]

2. Experimental Procedures

To obtain *n*-butyl THPM powder, *n*-butyl acetoacetate powder was synthesized first, which was obtained by transesterification of ethyl acetoacetate with *n*-butyl alcohol by using Biginelli condensation. The synthesized *n*-butyl acetoacetate (1.58 g, 10 mmol) powder was mixed with benzaldehyde (1.06 g, 10 mmol) and thiourea (1.14 g, 15 mmol) in absolute ethanol (20 ml) containing 2 to 3 drops of HCl as a catalyst. This mixture was refluxed for 15–18 h. The precipitates of THPM powder were obtained, filtered and washed with cold methanol in order to yield the pale yellowish powder. The yield of synthesized *n*-butyl THPM powder was 80%. Figure 1 shows the molecular structure of *n*-butyl THPM.

The *n*-butyl THPM nanocrystalline particles were synthesized by using water/oil (w/o) microemulsion technique. Microemulsions are isotropic, transparent and thermodynamically stable systems composed of water, oil and surfactant; which find applications in areas such as solubilization, reaction medium nanoparticle systems, corrosion inhibitors, cosmetics, etc.[16,17] The internal structure and

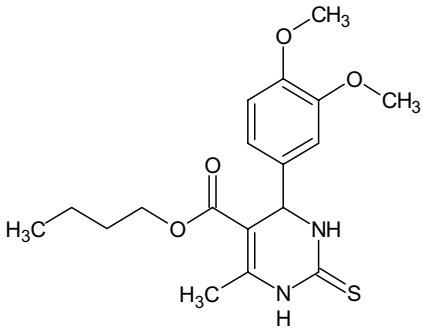

Fig. 1. Molecular structure of *n*-butyl 4-(3, 4-dimethoxyphenyl)-6-methyl-2-thioxo-1,2,3,4 tetrahydropyrimidine-5-carboxylate (*n*-butyl THPM).

dynamics of microemulsions are having important properties, which are the focus of extensive investigations using a variety of methods.[18,19]

The Triton X–100/*n*-Butanol/Water ternary diagram was constructed by varying the volume of the three liquids in a stepwise systematic manner in such a way that the total volume remained constant and it was found that the single phase existed in a large area. Triton X–100 was dissolved in appropriate amount of water in such a way that the molar ratio (R) = $[H_2O]$/surfactant was maintained at six, thereafter, the desired amount of *n*-butanol was added. This resulting mixture remained in the single phase region. The solution of *n*-butyl THPM made in suitable organic solvent (chloroform) was added in a drop-wise manner into this mixture with continuous stirring. Within 15–20 min *n*-butyl THPM nanocrystalline particles were formed between liquid–liquid interface of the solutions, which were filtered by using Whatman filter paper number 42 and air dried. The yield of synthesized nanoparticles was around 56%.

The powder X-ray Diffraction (XRD) was carried out on PHILIPS X'PERT MPD system using Cu K_α radiation and the data was analyzed by using powder-x software. The TEM images were recorded on PHILIPS TECNAI using EHT potentials of 200 kV and the sizes of the nanocrystalline particles were measured by the software ITEM attached with set-up. The TGA, DTA, DSC was carried out on LINSEIS STA PT — 1600 from room temperature to 900°C at a heating rate of 15°C/min. FT–IR spectrum was recorded by using Nicolet (Thermo Scientific) — 6700 set up in the range from 400 cm^{-1} to 4000 cm^{-1} in KBr medium. The mass spectrum was recorded using direct inlet probe on a GCMS–QP 2010 Shimadzu mass spectrometer and the approximate fragmentation of the compound was determined

by using ACD Chemsketch software. The dielectric measurements were carried out on pelletized nanocrystalline powder samples at room temperature by using HIOKI 3532 LCR HITESTER, in the frequency range from 50 Hz to 5 MHz.

3. Result and Discussion

3.1. *Formation of n-butyl THPM nanoparticles*

The synthesis of organic nanoparticles such as cholesterol and retinol by precipitating them directly in water cores through w/o microemulsion was discussed in detail elsewhere.[20,21] Debuigne *et al.* and Bayrak and Iscan [22,23] have proposed the hypothesis of the growth of nanoparticles by microemulsion technique. Mainly, there are three hypotheses proposed for the organic nanoparticles containing micelles,[19] which are; (i) the nanoparticles are in the organic phase and are in direct contact with the polar head of the surfactants, (ii) the nanoparticles are surrounded by water and (iii) the nanoparticle are surrounded by surfactant tails having their polar heads toward the water phase and the water is also in contact with a second layer of surfactant polar layers.

In the present hypothesis the formation of *n*-butyl THPM nanocrystalline particles is proposed through several stages. In the first stage, Triton X−100 and *n*-butanol were added one by one in a specific amount in double distilled water so that the aqueous cores were surrounded by oil and the surfactant. In the second stage, *n*-butyl THPM, dissolved in appropriate solvent was diffused into empty micelles during continuous stirring. In the third stage, the *n*-butyl THPM precipitated in the aqueous cores due to its insolubility in water. In the fourth stage, the displacement of the solvent from micelles to the surrounding took place, and in the fifth and last stage the exchange of organic molecules between the aqueous cores occurred as a result of collision between different droplets due to stirring.

3.2. *Powder XRD study*

The Powder X-ray Diffraction (XRD) study was used to confirm the crystalline nature of the sample and to determine the average particle size of the *n*-butyl THPM nanocrystalline particles. Figure 2 shows the powder XRD pattern of *n*-butyl THPM

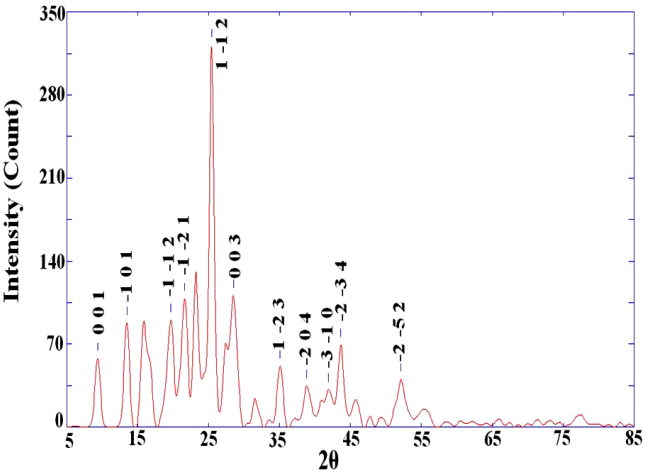

Fig. 2. Powder XRD pattern of *n*-butyl THPM nanoparticles.

nanocrystalline particles. The crystal structure of *n*-butyl THPM nanocrystalline particles was solved by considering the unit cell parameters of the nearest available compound dihydropyrimidine-5-carboxylate[24] from the literature as a reference and then the software powder-X was used to fit all peaks in the diffractogram and assigned the planes. The *n*-butyl THPM nanocrystals showed triclinic crystal system with estimated unit cell parameters as, $a = 7.1980$ Å, $b = 10.3378$ Å, $c = 10.2246$ Å, $\alpha = 103.78°$, $\beta = 107.56°$, $\gamma = 92.66°$.

3.3. *The average particle size determination*

The average particle size was determined from the powder XRD pattern of Fig. 2 by employing the Scherrer's formula given as follows:

$$D = \frac{K\lambda}{\beta \cos\theta}, \tag{1}$$

where, D is Average diameter, K is Shape factor (in our system K is 0.9), λ is Wavelength of source used, β is FWHM (full width half maximum) and θ is Angle of the peak for particular Bragg reflection. From the Scherrer's formula, the average particle size of *n*-butyl THPM nanoparticles was found to be 35 nm.

3.4. *Transmission electron microscopy*

The TEM study was carried out to determine the exact size and morphology of the synthesized *n*-butyl THPM nanocrystalline particles. The TEM images of different size nanoparticles are shown in

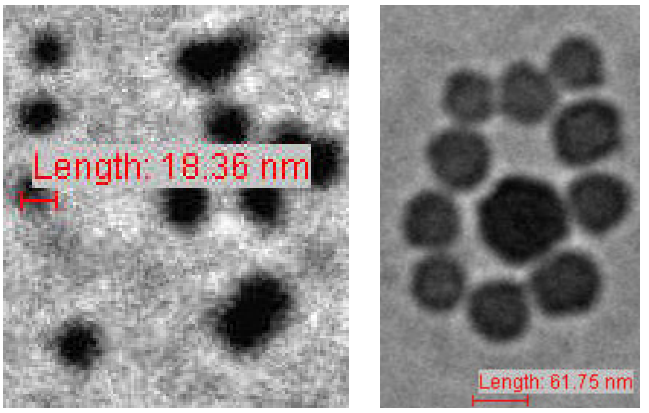

(a) (b)

Fig. 3. TEM images of *n*-butyl THPM.

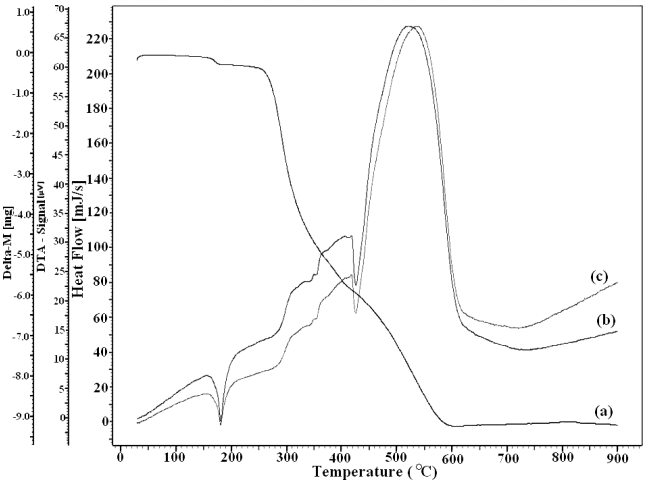

Fig. 4. (a) Thermogram (b) DTA (c) DSC of *n*-butyl THPM.

Figs. 3(a) and 3(b), which indicates nanoparticles of 18.36 nm, and 61.75 nm, respectively. TEM results suggested that the particles were having nearly spherical type morphology and their size varied from 15 nm to 65 nm. From the images of Figs. 3(a) and 3(b), one can find that the large-sized nanoparticles in Fig. 3(b) are having more precise spherical type morphology. In the present study, instead of monodispersed nanoparticles, different size of nanoparticles were obtained. The possible explanation for that could be given as follows. The microemulsion is expected to tolerate a limited quantity of organic molecules in order to form nanoparticles without phase separation. The initial microemulsion is expected to be thermodynamically stable. If the number of organic molecules per aqueous core increases then this interaction with surfactant molecules increases at the interface. The optimal radius of curvature is then disturbed and the phase separation occurs more readily for specific molar ratio (R) factor; as soon as the organic molecules come into contact with aqueous core, the nuclei formation takes place due to the insolubility of organic molecules in water. The nanoparticles later on grows to a certain favored size and are stabilized in the same manner with surfactants in spite of their presence in both immiscible phases. The magnetic stirring is expected to influence this and different sizes of nanoparticles are stabilized rather than the same size of nanoparticles.

3.5. *TG–DTA–DSC study*

Thermal studies of different pyrimidine compounds have been reported by several authors.[25,26] Thermal stability of *n*-butyl THPM nanocrystalline particles was assessed by employing the TGA, DTA and DSC as shown in Fig. 4. It can be noticed from the thermogram that a minor weight loss of the order of 0.2% of weight is observed within 160–180°C, which corresponds to a sharp endothermal peak at 177.5°C temperature with 102.62 J/g enthalpy. This suggests some minor phase change in the sample. The sample then remains almost stable up to around 280°C with 0.5% weight loss. Thereafter, it decomposes rapidly to a small stage around 400°C corresponding to a sharp endothermal peak indicating phase transition may be in terms of melting of the sample. The melting point of *n*-butyl THPM was measured by open capillary technique and was found to be 364°C.

Finally, it decomposes up to 620°C and the remaining is 9.3 wt.% of its original weight. This decomposition stage corresponds to a broad exothermic peak, which may be due to the combustion of organic chemicals as the combustion of organic chemicals takes place quickly and generates an exothermic peak.[27] Following this, almost stable state is achieved up to the end of the analysis. Decomposition illustrated by the loss of mass in the temperature range 280–580°C may be due to the liberation of gaseous fragments and removal of surfactant.

The same nature of the thermogram was observed for *n*-butyl THPM nanocrystalline particles even after 6 months, which suggests good stability of samples suitable for pharmaceutical applications. Similar results were observed by Vyas *et al.*[28] for cholesterol nanocrystalline particles, where cholesterol nanocrystalline particles exhibited slightly more thermal stability than the crystalline cholesterol sample.

3.6. *Kinetic and thermodynamic study*

In the present study, authors evaluate the thermodynamic and kinetic parameters for the decomposition of the *n*-butyl THPM nanoparticles at 240°C using the thermo-gram data of Fig. 4. There are many mathematical relations available to evaluate kinetic parameters for dehydration and decomposition from thermogram.[29,30] The kinetic parameters of decomposition process of *n*-butyl THPM nanocrystalline particles were calculated by the Coats and Redfern relation.[30]

$$\log_{10}\left(\frac{1-(1-\alpha)^{1-n}}{(1-n)T^2}\right) \equiv \left[\log_{10}\left(\frac{AR}{\alpha E}\right)\left(1-\frac{2RT}{E}\right)-\left(\frac{E}{2.3RT}\right)\right], \quad (2)$$

where, α is $(W_0 - W)/(W_0 - W_f)$, W_0 is Initial weight, W is Weight at time t, W_f is Final weight, n is Order of reaction, A is Frequency factor, E is Activation energy of the reaction, R is Gas constant and a is Heating rate.

To determine the kinetic parameters, a plot of $\log_{10}[\{1-(1-\alpha)^{1-n}\}/\{T^2(1-n)\}]$ versus $1/T$ is drawn for different values of order of reaction (n). The best linear fit gives the correct value of n and the value of activation energy is calculated by using the slope of linear plot.

The thermodynamic parameters of decomposition have been evaluated for the sharp decomposition stage at 240°C temperature by using the standard formulae discussed by Laidler[31] and Parikh,[32] which

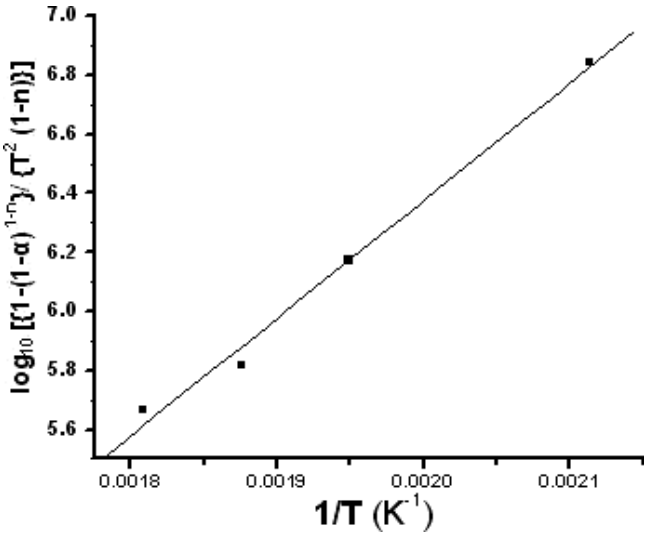

Fig. 5. Linear fitted plot of C−R relation for *n*-butyl THPM nanoparticles.

Table 1. Kinetic parameters of *n*-butyl THPM.

Kinetic parameters	
Order of reaction (n)	0.75
Activation energy (E)	76.15 kJK^{-1} mol^{-1}
Frequency factor (A)	6.77×10^{20}

Table 2. Thermodynamic parameters of *n*-butyl THPM.

Thermodynamic parameters	
Standard change in entropy ($\Delta^{\#}S^{\circ}$)	149.38 JK^{-1} mol^{-1}
Standard change in enthalpy ($\Delta^{\#}H^{\circ}$)	67.62 kJmol^{-1}
Standard change in Gibbs free energy ($\Delta^{\#}G^{\circ}$)	−9.01 kJmol^{-1}
Standard changes in internal energy ($\Delta^{\#}U^{\circ}$)	71.88 kJmol^{-1}

are given in Table 2. The positive value of standard change in entropy ($\Delta^{\#}S^0$) and standard change in enthalpy ($\Delta^{\#}H^0$) as well as the negative value of standard change in Gibbs free energy ($\Delta^{\#}G^0$) suggest that the reaction will be spontaneous at higher temperatures.[33]

3.7. *FT−IR spectral study*

The FT−IR spectral analysis was carried out to confirm the chemical bonds and functional groups present in the nanomaterial. FT−IR spectrum of *n*-butyl THPM nanocrystalline particles is shown in Fig. 6. The analysis of spectrum suggests that the absorptions occurring at 3282.4 cm^{-1} and 3171.9 cm^{-1} show −NH bending, the absorption

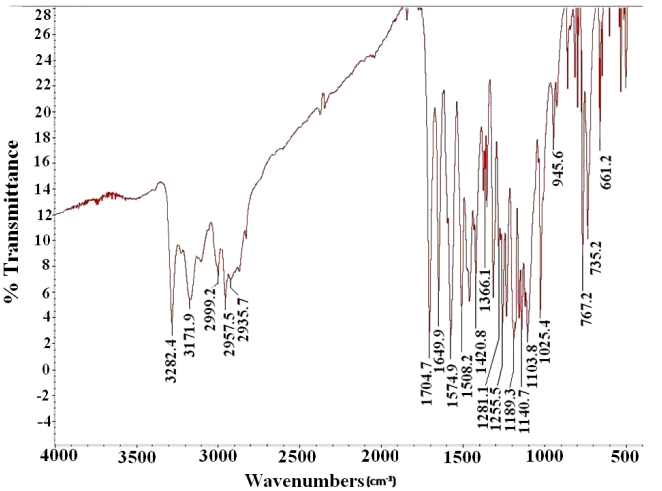

Fig. 6. FT−IR spectrum of *n*-butyl THPM nanoparticles.

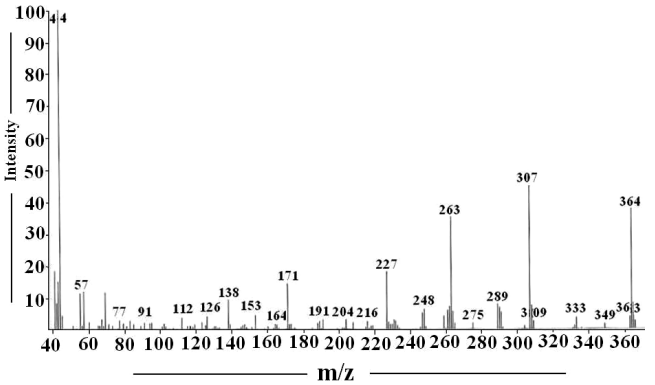

Fig. 7. Mass spectrum of *n*-butyl THPM nanoparticles.

occurring at 2999.2 cm^{-1} is due to C−H stretching vibration of $-CH_3$, the absorption taking place at 2957.5 cm^{-1} is due to C−H stretching vibration of $-CH_2$ and the absorption at 1704.7 cm^{-1} is due to C=O stretching vibration of ester. Whereas, the absorptions situated at 1649.9 cm^{-1}, 1574.9 cm^{-1} and 1508.2 cm^{-1} show C=C aromatic ring skeleton vibrations. The absorption at 1420.8 cm^{-1} is assigned to C−H bending vibration of $-CH_2$ and the absorption at 1366.1 cm^{-1} is due to C−H bending vibration of $-CH_3$. Altogether, the absorptions occurring at 1281.1 cm^{-1}, 1255.5 cm^{-1}, 1189.3 cm^{-1}, 1140.7 cm^{-1}, 1103.8 cm^{-1} and 1025.4 cm^{-1} are due to C−O stretching vibrations of esters and the absorptions at 945.6 cm^{-1}, 767.2 cm^{-1}, 735.2 cm^{-1} and 661.2 cm^{-1} are attributed to the out-of-plane bending vibration or aromatic substitution.

3.8. *Mass spectrum*

In order to study the formation of nanoparticles of proper compound through fragmentation process, a mass spectrum was recorded. The mass spectrum of *n*-butyl THPM nanocrystalline particles is shown in Fig. 7. By comparing the mass spectrum of nanocrystalline particles of *n*-butyl THPM with crystalline *n*-butyl THPM material, it is found that there is no change in the mass spectrum. However, fragmentation process of *n*-butyl THPM crystals is discussed in detail elsewhere.[14]

3.9. *Dielectric studies*

The capacitance of pelletized sample at different frequency of applied field has been measured at room temperature within the frequency range from 50 Hz to 5 MHz. Figure 8 is a plot of variation of dielectric constant with frequency of applied field.

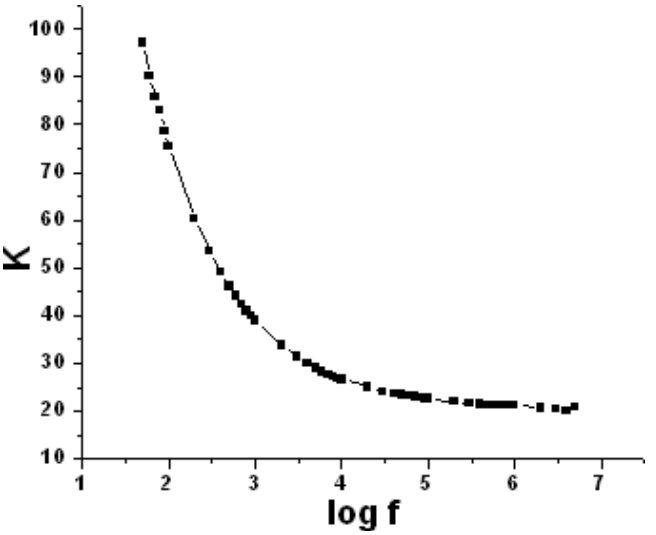

Fig. 8. Plot of dielectric constant versus log f.

From this plot, one can notice that as the frequency increases the dielectric constant initially decreases rapidly and then above 10 kHz range decreases very slowly. This type of behavior suggests higher space charge polarizability at lower frequency region. This may be because the electronic exchange in the ions of the nanocrystalline sample gives the local displacement of electrons in the direction of applied field, which results into the polarization. As the frequency of applied field increases the dipoles cannot comply with the varying field and hence the reduction in dielectric constant is observed. The nanostructured materials have enhanced crystal field due to its surface bond contraction and the rise in surface area to volume ratio. As the particle size decreases, the crystal field increases and subsequently the dielectric constant decreases. Several authors found that as the particle size increases, the dielectric constant increases.[34] In contrast to this, very less dielectric response of 4-(2 hydroxyphenylamino)-pent-3-e*n*-2-one (HPAP) crystal with frequency was observed.[35] Also, low dielectric response was reported for photosensitive polyimide.[36]

Figure 9 shows the plot of dielectric loss ($\tan\delta$) of *n*-butyl THPM nanocrystalline particles versus log f at room temperature. From this plot, one can observe that as the frequency increases, the dielectric loss decreases. The ac conductivity (σ_{ac}) was calculated from the following formula

$$\sigma_{ac} = \frac{2\pi f C D t}{A}, \tag{3}$$

where, f denotes Frequency of the applied field, C denotes Capacitance, D denotes Dissipation factor,

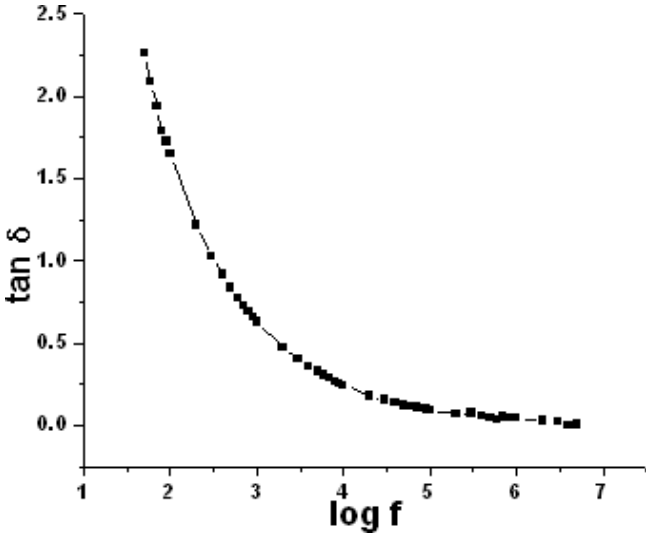

Fig. 9. Plot of dielectric loss versus log f.

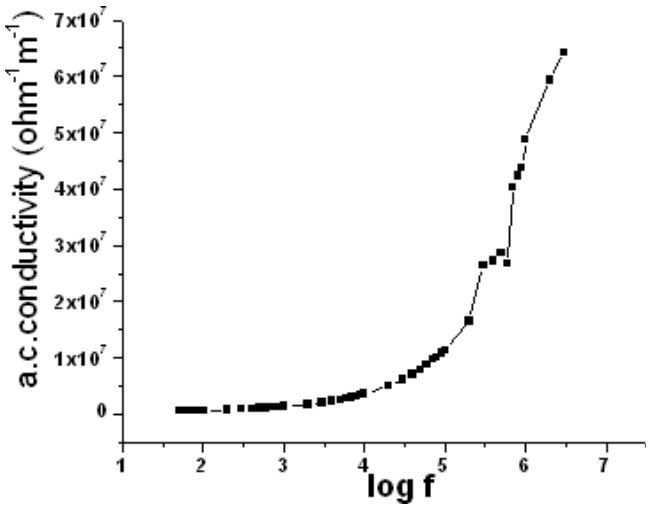

Fig. 10. Plot of ac conductivity versus log f.

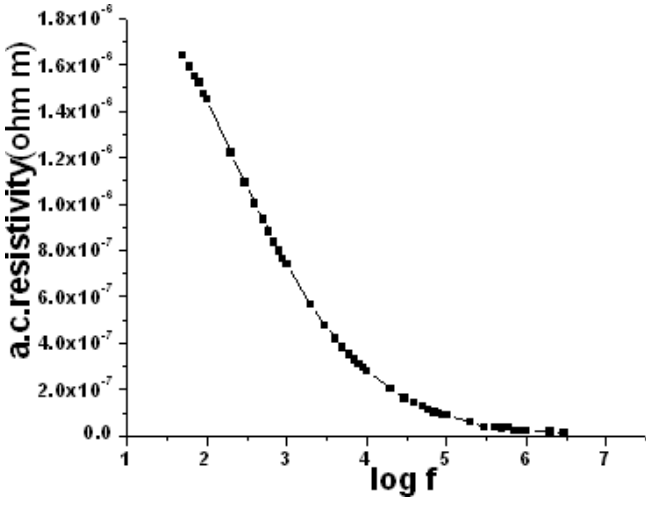

Fig. 11. Plot of ac resistivity versus log f.

A denotes Area of the pellet and t denotes Thickness of the sample.

The ac resistivity is calculated by

$$\rho_{ac} = \frac{1}{\sigma_{ac}} \tag{4}$$

The variation of ac conductivity with frequency of applied field is shown in Fig. 10 and the variation of ac resistivity with frequency of applied field is shown in Fig. 11. This shows that as the frequency of the applied field increases the ac conductivity increases. The nature of the ac resistivity is just opposite to the nature of the ac conductivity.

4. Conclusion

The *n*-butyl acetoacetate was obtained by transesterification of ethyl acetoacetate with *n*-butyl alcohol using Biginelli condensation. By using this powder the *n*-butyl 4-(3, 4-dimethoxyphenyl)-6-methyl-2-thioxo-1,2,3,4 tetrahydropyrimidine-5-carboxylate (*n*-butyl THPM) nanocrystalline particles were synthesized by using water/oil microemulsion. Broadening of the powder XRD peaks indicated the nanostructured nature of the material and the average particle size was determined by using the Scherrer's formula, which was found to be 35 nm. The crystal structure of *n*-butyl THPM nanocrystalline particles was solved and found to be triclinic crystal system with the unit cell parameters as, $a = 7.198$ Å, $b = 10.3378$ Å, $c = 10.2246$ Å, $\alpha = 103.78°$, $\beta = 107.56°$ and $\gamma = 92.66°$. The particle size was also measured by TEM, which varied from 15 nm to 65 nm. From the TGA it was found that the nanoparticles of THPM were stable up to 280°C. The minor weight loss was observed between 160°C and 180°C accompanied by endothermic peak, which could be due to phase transition occurring on heating nanoparticles. The FT−IR study confirmed the presence of −NH, C=O, C−H, C−O stretching as well as aromatic substitution. The mass spectrum confirmed the formation of *n*-butyl THPM nanocrystalline particles. Dielectric study suggested that as frequency increased the dielectric constant, the dielectric loss and the ac resistivity decreased.

Acknowledgments

The authors are thankful to the Government of Gujarat for sanctioning grants to develop

experimental facilities under the project "Nanoscience and Technology and Environmental Physics." The authors are thankful to Prof. Surekha Devi for useful discussion and Profs. K. N. Iyer, H. H. Joshi and P. H. Parsania for their encouragements. The author (PMV) is thankful to UGC, New Delhi, for sanctioning the Fellowship under the Meritorious Research Student Scheme. Authors are thankful to Prof. P. Sagayaraj, Physics Department, Loyola College, Chennai, for helping in dielectric data collection.

References

1. C. O. Kappe, *Tetrahedron* **49**, 6937 (1993).
2. C. G. Rovnyak *et al.*, *J. Med. Chem.* **35**, 3254 (1992).
3. E. L. Khania, G. O. Sillisnietse, Ya Ya Ozel, G. Dabur and A. A. Yakimenis, *Khim. Pharm. Zh.* **78**, 1321 (1978).
4. H. Cho *et al.*, *J. Med. Chem.* **32**, 2399 (1989).
5. M. A. Bruce, G. S. Pointdexter and G. Johnson, PCT Int. WO, 9833791 (1998).
6. B. B. Snider and Z. Shi, *J. Org. Chem.* **58**, 3828 (1993).
7. A. D. Patil, N. V. Kumar, W. C. Kokke, M. F. Bean, A. J. Freyer, C. DeBrosse, S. Mai, A. Truneh, D. J. Faulkner, B. Carte, A. L. Breen, R. P. Hertzberg, R. K. Johnson, J. W. Westley and B. C. M. Potts, *J. Org. Chem.* **60**, 1182 (1995).
8. Y. Kashman, S. Hirsh, O. J. McConnel, I. Ohtani, K. Takenori, K. Kakisawa and A. Ptimycolin, *J. Am. Chem. Soc.* **111**, 8925 (1989).
9. K. S. Atwal, B. N. Swanson, S. E. Unger, D. M. Floyd, S. Moreland, A. Hedberg and B. C. O'Reilly, *J. Med. Chem.* **34**, 806 (1991).
10. G. C. Rovnyak, K. S. Atwal, A. Hedberg, S. D. Kimball, S. Moreland, J. Z. Gougoutas, B. C. O'Reilly, J. Schwartz and M. F. Malley, *J. Med. Chem.* **35**, 3254 (1992).
11. G. J. Grover, S. Dzwonczyk, D. M. McMullen, D. E. Normandin, C. S. Parham, P. G. Sleph and S. J. Moreland, *Cardiovasc. Pharmacol.* **26**, 289 (1995).
12. D. Dallinger and C. O. Kappe, *Nat. Protoc.* **2**, 317 (2007).
13. I. G. Saez, S. Debones, R. Lopez, F. Trucco, B. Rousseau, P. Thery and F. Kozielski, *J. Biol. Chem.* **282**, 9740 (2001).
14. P. M. Vyas, A. M. Pansuriya, Y. T. Naliapara and M. J. Joshi, Synthesis and Characterization of *n*-Butyl 4-(3, 4-dimethoxyphenyl)-6-methyl-2-thioxo-1,2,3,4 tetrahydropyrimidine-5-carboxylate crystals, *Proc. Nat. Symp. Growth of Detector — Grade Single Crystals* (2009), pp. 118−121.
15. P. M. Vyas, A. M. Pansuriya, Y. T. Naliapara, B. B. Parekh and M. J. Joshi, Thermal and Dielectric studies of *n*-Butyl 4-(3, 4-dimethoxyphenyl)-6-methyl-2-thioxo-1,2,3,4 tetrahydropyrimidine-5-carboxylate crystals, *9th Int. Workshop on Crystal Growth of Organic Materials* (2010), pp. 105.
16. S. P. Moulik, L. G. Digout, W. M. Aylward and R. Palepu, *Langmuir* **16**, 3101 (2000).
17. B. K. Paul and S. P. Moulik, *Curr. Sci.* **80**, 990 (2001).
18. B. K. Pal and S. P. Moulik, *J. Disp. Sci. Technol.* **18**, 301 (1997).
19. S. P. Moulik and B. K. Paul, *Adv. Colloid. Inter. Sci.* **78**, 99 (1998).
20. C. Destree, J. Ghijsen and J. B. Nagy, *Langmuir* **23**, 1965 (2007).
21. L. Jeunieau, F. Debuigne and J. B. Nagy, *J. Ed. Surfactant Sci. Ser.* **100**, 609 (2001).
22. F. Debuigne, L. Jeunieau, M. Wiame and J. B. Nagy, *Langmuir* **16**, 7605 (2000).
23. Y. Bayrak and M. Iscan, *J. Surf. Deter.* **7**, 363 (2004).
24. T. H. Quiroz, S. H. Ortega and M. S. García, *Anal. Chem.* **15**, 105 (1999).
25. M. N. Marino and J. M. Salas, *J. Therm. Anal.* **29**, 1053 (1984).
26. R. L. Garzón, D. G. Valero, C. Valenzuela, C. N. Cruzpèrez and A. G. Rodriguez, *Mono. Für Chem.* **118**, 553 (1987).
27. F. Teng, Y. Man, S. Liang, B. Gaugue, Y. Zhu, W. Han, Z. Wang, P. Xu, G. Xiong and Z. Tian, *J. Alloys. Compol.* **461**, 516 (2008).
28. P. M. Vyas, S. R. Vasant, R. R. Hajiyani and M. J. Joshi, Synthesis and Characterization of Cholesterol Nanoparticles by Using w/o microemulsion Technique, *Int. Conf. Adv. Nanomaterials and Nanoscience* (2009), pp. 289.
29. A. H. Horowitz and B. G. Metzger, *Anal. Chem.* **35**, 1464 (1963).
30. A. W. Coats and J. P. Redfern, *Nature* **201**, 68 (1964).
31. K. J. Laidler, *Chemical Kinetics* (Harper and Row, New York, 1987).
32. K. D. Parikh, D. J. Dave, B. B. Parekh and M. J. Joshi, *Cryst. Res. Technol.* **45**, 603 (2010).
33. K. D. Parikh, D. J. Dave, B. B. Parekh and M. J. Joshi, *Bull. Mater. Sci.* **30**, 105 (2007).
34. H. Ye, C. Q. Sun and P. Hing, *J. Appl. Phys.* **33**, 23 (2000).
35. B. B. Parekh, D. H. Purohit, P. Sagayraj, H. S. Joshi and M. J. Joshi, *Cryst. Res. Technol.* **42**, 407 (2007).
36. A. Mochizuki, N. Kurata and T. Fukuoka, *J. Photopolym. Sci. Technol.* **14**, 17 (2001).

Acta Crystallographica Section E
Structure Reports Online
ISSN 1600-5368
Editors: **W. T. A. Harrison, H. Stoeckli-Evans, E. R. T. Tiekink and M. Weil**

(*E*)-*N*′-{7-Methoxyspiro[chromeno[4,3-*d*]thiazole-4,1′-cyclohexan]-2-yl}-*N*,*N*-dimethylacetimidamide

Kamini Kapoor, Vivek K. Gupta, Rajni Kant, Poorvesh M. Vyas, Mihir J. Joshi, Kalpesh M. Menpara and Kartik D. Ladva

Acta Cryst. (2011). E**67**, o2855–o2856

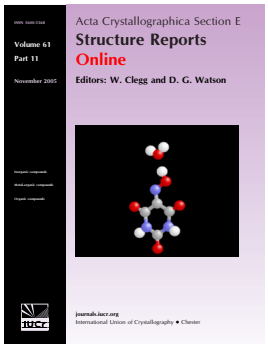

Acta Crystallographica Section E
Structure Reports Online
ISSN 1600-5368

(*E*)-*N*′-{7-Methoxyspiro[chromeno-[4,3-*d*]thiazole-4,1′-cyclohexan]-2-yl}-*N*,*N*-dimethylacetimidamide

Kamini Kapoor,[a] Vivek K. Gupta,[a] Rajni Kant,[a]* Poorvesh M. Vyas,[b] Mihir J. Joshi,[b] Kalpesh M. Menpara[c] and Kartik D. Ladva[c]

[a]X-ray Crystallography Laboratory, Post-Graduate Department of Physics, University of Jammu, Jammu Tawi 180 006, India, [b]Physics Department, Saurashtra University, Rajkot 360 005, India, and [c]Shri M. N. Virani Science College, Rajkot 360 005, India
Correspondence e-mail: rkvk.paper11@gmail.com

Received 19 September 2011; accepted 30 September 2011

Key indicators: single-crystal X-ray study; T = 293 K; mean σ(C–C) = 0.003 Å; R factor = 0.043; wR factor = 0.113; data-to-parameter ratio = 12.0.

In the chromenothiazole ring system of the title molecule, $C_{20}H_{25}N_3O_2S$, the pyran ring is in a half-chair conformation. The dihedral angle between the thiazole and benzene rings is 14.78 (6)°. The cyclohexane ring is in a chair conformation. The crystal structure is stabilized by weak intermolecular C—H···N and C—H···O hydrogen bonds.

Related literature

For the biological activity of heterocyclic compounds containing nitrogen and sulfur, see: Bishayee *et al.* (1997); Cruz *et al.* (1995); Chitamber & Wereley (1997). For the biological activity of thiazoles, see: Pawar *et al.* (2009). Schiff bases and acetamidine play an important role in many biological processes and are of great importance for the preparation of various pharmaceuticals, see: More *et al.* (2001); Sutariya *et al.* (2007); Murza *et al.* (1999); Dong *et al.* (2006); Jayashree *et al.* (2005); Modi *et al.* (1971); Vicini *et al.* (2003). For standard bond-length data, see: Allen *et al.* (1987). For ring conformations, see: Duax & Norton (1975).

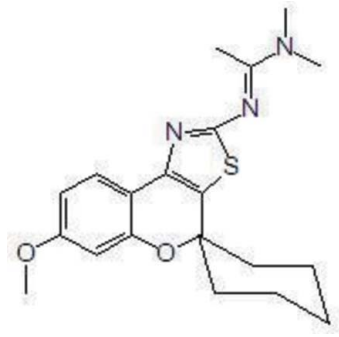

Experimental

Crystal data

$C_{20}H_{25}N_3O_2S$
M_r = 371.49
Monoclinic, $P2_1/n$
a = 9.2510 (2) Å
b = 20.0273 (4) Å
c = 10.7301 (2) Å
β = 90.840 (2)°
V = 1987.78 (7) Å^3
Z = 4
Mo $K\alpha$ radiation
μ = 0.18 mm^{-1}
T = 293 K
0.3 × 0.2 × 0.1 mm

Data collection

Oxford Diffraction Xcalibur Sapphire3 diffractometer
Absorption correction: multi-scan (*CrysAlis RED*; Oxford Diffraction, 2009)
T_{min} = 0.892, T_{max} = 1.000
56290 measured reflections
3482 independent reflections
2835 reflections with $I > 2\sigma(I)$
R_{int} = 0.041

Refinement

$R[F^2 > 2\sigma(F^2)]$ = 0.043
$wR(F^2)$ = 0.113
S = 1.02
3482 reflections
291 parameters
H atoms treated by a mixture of independent and constrained refinement
$\Delta\rho_{max}$ = 0.18 e Å^{-3}
$\Delta\rho_{min}$ = −0.19 e Å^{-3}

Table 1
Hydrogen-bond geometry (Å, °).

D—H···A	D—H	H···A	D···A	D—H···A
C19—H19*B*···O5^{i}	0.96	2.41	3.335 (3)	161
C6—H61···N1^{ii}	0.95 (2)	2.59 (2)	3.441 (3)	149.3 (15)

Symmetry codes: (i) $x-\frac{1}{2}, -y+\frac{1}{2}, z+\frac{1}{2}$; (ii) $x+\frac{1}{2}, -y+\frac{1}{2}, z-\frac{1}{2}$.

Data collection: *CrysAlis PRO* (Oxford Diffraction, 2009); cell refinement: *CrysAlis PRO*; data reduction: *CrysAlis PRO*; program(s) used to solve structure: *SHELXS97* (Sheldrick, 2008); program(s) used to refine structure: *SHELXL97* (Sheldrick, 2008); molecular graphics: *ORTEP-3* (Farrugia, 1997); software used to prepare material for publication: *PLATON* (Spek, 2009) and *PARST* (Nardelli, 1995).

RK acknowledges the Department of Science & Technology for the single-crystal X-ray diffractometer sanctioned as a National Facility under project No. SR/S2/CMP-47/2003. He is also thankful to the UGC for research funding under research project F.No. 37–4154/2009 (J&K) (SR).

Supplementary data and figures for this paper are available from the IUCr electronic archives (Reference: LH5340).

References

Allen, F. H., Kennard, O., Watson, D. G., Brammer, L., Orpen, A. G. & Taylor, R. (1987). *J. Chem. Soc. Perkin Trans. 2*, pp. S1–19.

Bishayee, A., Karmaker, R., Mandal, A., Kundu, S. N. & Chaterjee, M. (1997). *Eur. J. Cancer Prev.* **6**, 58–70.

Chitamber, C. R. & Wereley, J. P. (1997). *J. Biol. Chem.* **272**, 12151–12157.

Cruz, T. F., Morgon, A. & Min, W. (1995). *Mol. Biochem.* **153**, 161–166.

Dong, Y. B., Wang, L., Ma, J. P. & Zhao, X. X. (2006). *Cryst. Growth Des.* **6**, 2475–2485.

Duax, W. L. & Norton, D. A. (1975). *Atlas of Steroid Structures*, Vol. 1. New York: Plenum.

Farrugia, L. J. (1997). *J. Appl. Cryst.* **30**, 565.

Jayashree, B. S., Anuradha, D. & Venugopala, K. N. (2005). *Asian J. Chem.* **17**, 2093–2097.

Modi, J. D., Sabnis, S. S. & Deliwala, C. V. (1971). *J. Med. Chem.* **14**, 450–451.

More, P. G., Bhalvankar, R. B. & Patter, S. C. (2001). *J. Indian Chem. Soc.* **78**, 474–475.

Murza, M. M., Kuvatov, Z. K. & Safarov, M. G. (1999). *Chem. Heterocyl. Compd*, **35**, 1097–1103.

Nardelli, M. (1995). *J. Appl. Cryst.* **28**, 659.

Oxford Diffraction (2009). *CrysAlis RED* and *CrysAlis PRO*. Oxford Diffraction Ltd, Yarnton, England.

Pawar, M. J., Burungale, A. B. & Karale, B. K. (2009). *Arkivoc*, **xiii**, 97–107.

Sheldrick, G. M. (2008). *Acta Cryst.* A**64**, 112–122.

Spek, A. L. (2009). *Acta Cryst.* D**65**, 148–155.

Sutariya, B., Raziya, S. K., Mohan, S. & Rao, S. V. S. (2007). *Indian J. Chem. Sect. B*, **465**, 884–887.

Vicini, P., Geronikaki, A., Incerti, M., Busonera, B. & Poni, G. (2003). *Bioorg. Med. Chem.* **11**, 4785–4789.

supplementary materials

Acta Cryst. (2011). E**67**, o2855-o2856 [**doi:10.1107/S1600536811040359**]

(*E*)-*N*'-{7-Methoxyspiro[chromeno[4,3-*d*]thiazole-4,1'-cyclohexan]-2-yl}-*N*,*N*-dimethylacetimidamide

K. Kapoor, V. K. Gupta, R. Kant, P. M. Vyas, M. J. Joshi, K. M. Menpara and K. D. Ladva

Comment

Heterocyclic compounds containing nitrogen and sulfur are used for medical purposes for the treatment of different kinds of fungal and bacterial infection along with treatment of e.g. gastric ulcers and cancer (Bishayee *et al.*, 1997; Cruz *et al.*, 1995; Chitamber & Wereley, 1997). Thiazoles exhibit a wide range of biological activities (Pawar *et al.*, 2009). Schiff bases and acetamidine play an important role in many biological processes. They are of great importance for the preparation of various pharmaceuticals and are used in many other areas of chemistry as starting materials. Their facile synthesis and numerous biological activities contribute greatly to their Schiff bases and acetamidine popularity (More *et al.*, 2001; Sutariya *et al.*, 2007; Murza *et al.*, 1999; Dong *et al.*, 2006; Jayashree *et al.*, 2005; Modi *et al.*, 1971; Vicini *et al.*, 2003). Therefore, Schiff bases and acetamidine of amino thiazoles are expected to be biologically active. We report herein the X-ray crystallographic studies of a novel acetamidine base derived from substituted 8-methoxyspiro[chromeno[4,3-*d*] [1,3]thiazole-4,1-cyclohexan]-2-amine as a possible hybrid antimicrobial agent. In the title compound (Fig. 1), the methoxy substituent at the C7 atom forms the torsion angle of 178.4 (2) ° [(+) antiperiplanar conformation] with the atom set O10/C7/C8/C9. The benzopyran ring has a half-chair conformation with asymmetry parameter: ΔC2(C4—O5) = 4.49 (Duax *et al.*, 1975). The cyclohexane ring has a chair conformation. The asymmetry parameters are: ΔCs(C4)=0.24; ΔC2(C4—C12)= 0.88. The dihedral angle between the best least squares planes through the thiazole and benzene rings is 14.75 (7)°. The stabilization of crystal packing (Fig. 2) is influenced by intermolecular C—H···N and C—H···O hydrogen bonding [C6—H61···N1 (symmetry code: *x* + 1/2, -*y* + 1/2, *z* - 1/2); C19—H19B···O5 (symmetry code: *x* - 1/2, -*y* + 1/2, *z* + 1/2)]. These interactions link the molecules into chains that run parallel to [-1 0 1].

Experimental

An ice cold solution of phosphorus oxychloride (0.85 mmol) in dry toluene(20 ml) was added to the suitable amount of acetamide (0.47 mmol), and the mixture was stirred for 30 min at room temperature. At the end of the reaction, 7-methoxyspiro[4,3-*d*][1,3]thiazole-4,1-cyclohexan]-2-amine (0.42 mmol) dissolved in dry toluene was added drop wise and the reaction mixture was refluxed for 6 h. The solution was then cooled, carefully poured into the ice-water, and made alkaline with 1 N NaOH solution. The organic layer was extracted with $CHCl_3$, washed to neutrality with water, dried over sodium sulfate, filtered and then evaporated *in vacuo*. The crude material was purified by column chromatography on silica gel eluting with a hexane/ethyl acetate(7:3) mixture. Single crystals suitable for X-ray measurements were obtained by crystallization from $CHCl_3$ at room temperature.

Refinement

All H atoms (except methyl H atoms) were located in a difference Fourier map and refined freely. Methyl H atoms were positioned geometrically and refined using a riding model with C—H = 0.96 Å. The U_{iso}(H) values were constrained to be 1.5U_{eq}(C methyl).

Figures

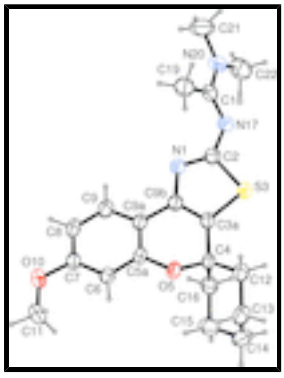

Fig. 1. The molecular sreucture with ellipsoids are drawn at the 40% probability level. H atoms are shown as small spheres of arbitrary radii.

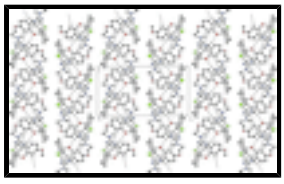

Fig. 2. The packing arrangement of molecules. The broken lines show weak intermolecular hydrogen bonds.

(*E*)-*N*'-{7-Methoxyspiro[chromeno[4,3-*d*]thiazole- 4,1'-cyclohexan]-2-yl}-*N*,*N*-dimethylacetimidamide

Crystal data

$C_{20}H_{25}N_3O_2S$	$F(000) = 792$
$M_r = 371.49$	$D_x = 1.241$ Mg m^{-3}
Monoclinic, $P2_1/n$	Mo $K\alpha$ radiation, $\lambda = 0.71073$ Å
Hall symbol: -P 2yn	Cell parameters from 24440 reflections
$a = 9.2510$ (2) Å	$\theta = 3.5$–$29.0°$
$b = 20.0273$ (4) Å	$\mu = 0.18$ mm^{-1}
$c = 10.7301$ (2) Å	$T = 293$ K
$\beta = 90.840$ (2)°	Plate, light-brown
$V = 1987.78$ (7) Å^3	0.3 × 0.2 × 0.1 mm
$Z = 4$	

Data collection

Oxford Diffraction Xcalibur Sapphire3 diffractometer	3482 independent reflections
Radiation source: fine-focus sealed tube	2835 reflections with $I > 2\sigma(I)$
graphite	$R_{int} = 0.041$
Detector resolution: 16.1049 pixels mm^{-1}	$\theta_{max} = 25.0°$, $\theta_{min} = 3.5°$
ω scans	$h = -11 \rightarrow 11$
Absorption correction: multi-scan (*CrysAlis RED*; Oxford Diffraction, 2009)	$k = -23 \rightarrow 23$
$T_{min} = 0.892$, $T_{max} = 1.000$	$l = -12 \rightarrow 12$
56290 measured reflections	

Refinement

Refinement on F^2	Primary atom site location: structure-invariant direct methods
Least-squares matrix: full	Secondary atom site location: difference Fourier map
$R[F^2 > 2\sigma(F^2)] = 0.043$	Hydrogen site location: inferred from neighbouring sites
$wR(F^2) = 0.113$	H atoms treated by a mixture of independent and constrained refinement
$S = 1.02$	$w = 1/[\sigma^2(F_o^2) + (0.0521P)^2 + 0.884P]$ where $P = (F_o^2 + 2F_c^2)/3$
3482 reflections	$(\Delta/\sigma)_{max} = 0.001$
291 parameters	$\Delta\rho_{max} = 0.18$ e Å^{-3}
0 restraints	$\Delta\rho_{min} = -0.19$ e Å^{-3}

Special details

Experimental. *CrysAlis PRO*, Oxford Diffraction Ltd., Version 1.171.34.40 (release 27–08-2010 CrysAlis171. NET) (compiled Aug 27 2010,11:50:40) Empirical absorption correction using spherical harmonics, implemented in SCALE3 ABSPACK scaling algorithm.

Geometry. All e.s.d.'s (except the e.s.d. in the dihedral angle between two l.s. planes) are estimated using the full covariance matrix. The cell e.s.d.'s are taken into account individually in the estimation of e.s.d.'s in distances, angles and torsion angles; correlations between e.s.d.'s in cell parameters are only used when they are defined by crystal symmetry. An approximate (isotropic) treatment of cell e.s.d.'s is used for estimating e.s.d.'s involving l.s. planes.

Refinement. Refinement of F^2 against ALL reflections. The weighted *R*-factor *wR* and goodness of fit *S* are based on F^2, conventional *R*-factors *R* are based on *F*, with *F* set to zero for negative F^2. The threshold expression of $F^2 > \sigma(F^2)$ is used only for calculating *R*-factors(gt) *etc*. and is not relevant to the choice of reflections for refinement. *R*-factors based on F^2 are statistically about twice as large as those based on *F*, and *R*- factors based on ALL data will be even larger.

Fractional atomic coordinates and isotropic or equivalent isotropic displacement parameters (Å^2)

	x	*y*	*z*	U_{iso}*/U_{eq}
N1	0.33437 (18)	0.18039 (8)	0.41748 (15)	0.0474 (4)
C2	0.2587 (2)	0.12626 (10)	0.39594 (19)	0.0467 (5)
C3A	0.4732 (2)	0.12918 (9)	0.26463 (18)	0.0428 (5)
S3	0.33236 (6)	0.07336 (3)	0.28200 (5)	0.05248 (19)
C4	0.6032 (2)	0.12315 (9)	0.18332 (17)	0.0410 (4)
O5	0.64694 (14)	0.19099 (6)	0.14928 (11)	0.0428 (3)
C5A	0.65071 (19)	0.23902 (8)	0.24074 (16)	0.0368 (4)
C6	0.7445 (2)	0.29214 (9)	0.22330 (18)	0.0395 (4)
C7	0.7481 (2)	0.34279 (9)	0.3113 (2)	0.0459 (5)
C8	0.6590 (3)	0.34051 (11)	0.4146 (2)	0.0551 (6)
C9	0.5632 (3)	0.28851 (11)	0.4276 (2)	0.0539 (5)
C9A	0.5568 (2)	0.23671 (9)	0.34111 (17)	0.0419 (4)
C9B	0.4543 (2)	0.18148 (9)	0.34258 (17)	0.0421 (4)
O10	0.83754 (17)	0.39732 (7)	0.30446 (15)	0.0619 (4)
C11	0.9325 (3)	0.40072 (13)	0.2026 (3)	0.0766 (8)

H11A	0.9927	0.3617	0.2020	0.115*
H11B	0.9919	0.4398	0.2104	0.115*
H11C	0.8772	0.4029	0.1262	0.115*
C12	0.5715 (3)	0.08891 (13)	0.0596 (2)	0.0562 (6)
C13	0.7053 (3)	0.08381 (14)	−0.0209 (3)	0.0693 (7)
C14	0.8293 (3)	0.05035 (14)	0.0475 (3)	0.0818 (9)
C15	0.8642 (3)	0.08530 (14)	0.1699 (3)	0.0693 (7)
C16	0.7304 (2)	0.08994 (12)	0.2511 (2)	0.0535 (5)
N17	0.13926 (19)	0.10532 (9)	0.45830 (17)	0.0537 (5)
C18	0.0370 (2)	0.14748 (11)	0.4842 (2)	0.0501 (5)
C19	0.0168 (3)	0.21331 (12)	0.4193 (2)	0.0657 (6)
H19A	0.0794	0.2155	0.3489	0.099*
H19B	0.0400	0.2489	0.4761	0.099*
H19C	−0.0818	0.2176	0.3915	0.099*
N20	−0.06057 (19)	0.12955 (11)	0.56983 (19)	0.0650 (5)
C21	−0.1802 (3)	0.17228 (18)	0.6067 (3)	0.0986 (11)
H21A	−0.1614	0.2174	0.5812	0.148*
H21B	−0.1900	0.1707	0.6956	0.148*
H21C	−0.2680	0.1569	0.5675	0.148*
C22	−0.0438 (4)	0.06674 (15)	0.6362 (3)	0.0923 (10)
H22A	−0.1023	0.0331	0.5963	0.139*
H22B	−0.0739	0.0723	0.7208	0.139*
H22C	0.0558	0.0533	0.6352	0.139*
H61	0.803 (2)	0.2918 (9)	0.1512 (18)	0.044 (5)*
H81	0.664 (2)	0.3751 (11)	0.477 (2)	0.058 (6)*
H91	0.499 (3)	0.2877 (11)	0.494 (2)	0.064 (7)*
H161	0.698 (2)	0.0457 (12)	0.275 (2)	0.061 (6)*
H162	0.752 (2)	0.1132 (11)	0.328 (2)	0.058 (6)*
H121	0.537 (2)	0.0441 (12)	0.079 (2)	0.061 (6)*
H122	0.493 (3)	0.1108 (13)	0.017 (2)	0.076 (8)*
H131	0.679 (3)	0.0603 (13)	−0.093 (3)	0.076 (8)*
H132	0.734 (3)	0.1291 (13)	−0.046 (2)	0.063 (7)*
H141	0.913 (3)	0.0497 (14)	−0.006 (3)	0.092 (9)*
H142	0.801 (3)	0.0054 (16)	0.064 (3)	0.093 (9)*
H151	0.942 (3)	0.0618 (14)	0.216 (3)	0.092 (9)*
H152	0.897 (3)	0.1321 (13)	0.153 (2)	0.068 (7)*

Atomic displacement parameters (Å^2)

	U^{11}	U^{22}	U^{33}	U^{12}	U^{13}	U^{23}
N1	0.0512 (10)	0.0403 (9)	0.0512 (10)	−0.0060 (8)	0.0149 (8)	−0.0058 (7)
C2	0.0484 (11)	0.0394 (11)	0.0525 (12)	−0.0010 (9)	0.0098 (9)	−0.0008 (9)
C3A	0.0480 (11)	0.0324 (10)	0.0482 (11)	−0.0054 (8)	0.0072 (9)	−0.0044 (8)
S3	0.0512 (3)	0.0383 (3)	0.0684 (4)	−0.0089 (2)	0.0148 (3)	−0.0121 (2)
C4	0.0488 (11)	0.0285 (9)	0.0460 (11)	−0.0059 (8)	0.0086 (8)	−0.0056 (8)
O5	0.0580 (8)	0.0311 (7)	0.0395 (7)	−0.0040 (6)	0.0085 (6)	−0.0047 (5)
C5A	0.0429 (10)	0.0281 (9)	0.0393 (10)	0.0018 (7)	0.0003 (8)	−0.0033 (7)
C6	0.0408 (10)	0.0331 (10)	0.0446 (11)	0.0024 (8)	0.0035 (8)	0.0001 (8)

C7	0.0455 (11)	0.0329 (10)	0.0592 (12)	−0.0027 (8)	−0.0015 (9)	−0.0045 (9)
C8	0.0649 (14)	0.0389 (11)	0.0617 (13)	−0.0051 (10)	0.0081 (11)	−0.0193 (10)
C9	0.0628 (14)	0.0459 (12)	0.0534 (12)	−0.0069 (10)	0.0144 (11)	−0.0144 (10)
C9A	0.0479 (11)	0.0340 (10)	0.0438 (10)	−0.0021 (8)	0.0053 (8)	−0.0050 (8)
C9B	0.0475 (11)	0.0362 (10)	0.0428 (10)	−0.0028 (8)	0.0075 (8)	−0.0027 (8)
O10	0.0637 (10)	0.0431 (8)	0.0791 (11)	−0.0182 (7)	0.0083 (8)	−0.0145 (7)
C11	0.0684 (16)	0.0602 (15)	0.102 (2)	−0.0289 (13)	0.0216 (15)	−0.0149 (14)
C12	0.0602 (14)	0.0509 (14)	0.0579 (13)	−0.0119 (11)	0.0102 (11)	−0.0201 (11)
C13	0.0826 (18)	0.0614 (16)	0.0645 (16)	−0.0119 (14)	0.0242 (14)	−0.0268 (13)
C14	0.0795 (19)	0.0494 (15)	0.118 (3)	0.0057 (14)	0.0509 (19)	−0.0093 (15)
C15	0.0494 (14)	0.0596 (16)	0.099 (2)	0.0071 (12)	0.0135 (13)	0.0161 (15)
C16	0.0531 (13)	0.0411 (12)	0.0665 (15)	−0.0008 (10)	0.0051 (11)	0.0067 (11)
N17	0.0493 (10)	0.0446 (10)	0.0677 (11)	−0.0064 (8)	0.0177 (9)	−0.0025 (9)
C18	0.0402 (11)	0.0526 (12)	0.0575 (12)	−0.0095 (9)	0.0004 (9)	−0.0127 (10)
C19	0.0538 (13)	0.0627 (15)	0.0801 (16)	0.0048 (11)	−0.0125 (12)	−0.0052 (13)
N20	0.0440 (10)	0.0762 (14)	0.0753 (13)	−0.0106 (9)	0.0150 (9)	−0.0155 (11)
C21	0.0528 (16)	0.137 (3)	0.106 (2)	0.0069 (17)	0.0207 (15)	−0.033 (2)
C22	0.092 (2)	0.086 (2)	0.100 (2)	−0.0273 (17)	0.0405 (18)	0.0049 (17)

Geometric parameters (Å, °)

N1—C2	1.309 (3)	C12—H121	0.97 (2)
N1—C9B	1.380 (2)	C12—H122	0.96 (3)
C2—N17	1.366 (2)	C13—C14	1.510 (4)
C2—S3	1.762 (2)	C13—H131	0.94 (3)
C3A—C9B	1.353 (3)	C13—H132	0.98 (2)
C3A—C4	1.501 (3)	C14—C15	1.519 (4)
C3A—S3	1.7292 (19)	C14—H141	0.97 (3)
C4—O5	1.465 (2)	C14—H142	0.95 (3)
C4—C12	1.519 (3)	C15—C16	1.527 (3)
C4—C16	1.526 (3)	C15—H151	0.98 (3)
O5—C5A	1.374 (2)	C15—H152	1.00 (3)
C5A—C6	1.387 (3)	C16—H161	0.97 (2)
C5A—C9A	1.394 (3)	C16—H162	0.97 (2)
C6—C7	1.386 (3)	N17—C18	1.301 (3)
C6—H61	0.95 (2)	C18—N20	1.346 (3)
C7—O10	1.373 (2)	C18—C19	1.501 (3)
C7—C8	1.391 (3)	C19—H19A	0.9600
C8—C9	1.376 (3)	C19—H19B	0.9600
C8—H81	0.96 (2)	C19—H19C	0.9600
C9—C9A	1.393 (3)	N20—C22	1.452 (4)
C9—H91	0.94 (2)	N20—C21	1.458 (3)
C9A—C9B	1.457 (3)	C21—H21A	0.9600
O10—C11	1.414 (3)	C21—H21B	0.9600
C11—H11A	0.9600	C21—H21C	0.9600
C11—H11B	0.9600	C22—H22A	0.9600
C11—H11C	0.9600	C22—H22B	0.9600
C12—C13	1.523 (3)	C22—H22C	0.9600
C2—N1—C9B	110.04 (16)	C14—C13—C12	111.8 (2)

N1—C2—N17	127.00 (18)	C14—C13—H131	111.6 (16)
N1—C2—S3	114.16 (14)	C12—C13—H131	107.3 (16)
N17—C2—S3	118.62 (15)	C14—C13—H132	109.5 (14)
C9B—C3A—C4	122.24 (17)	C12—C13—H132	108.6 (14)
C9B—C3A—S3	109.23 (14)	H131—C13—H132	108 (2)
C4—C3A—S3	128.48 (14)	C13—C14—C15	111.5 (2)
C3A—S3—C2	89.18 (9)	C13—C14—H141	109.2 (17)
O5—C4—C3A	107.26 (14)	C15—C14—H141	110.7 (16)
O5—C4—C12	104.56 (16)	C13—C14—H142	107.4 (17)
C3A—C4—C12	113.46 (17)	C15—C14—H142	109.4 (18)
O5—C4—C16	108.01 (16)	H141—C14—H142	109 (2)
C3A—C4—C16	112.13 (17)	C14—C15—C16	110.9 (2)
C12—C4—C16	110.92 (18)	C14—C15—H151	110.9 (17)
C5A—O5—C4	118.37 (13)	C16—C15—H151	109.5 (17)
O5—C5A—C6	116.73 (16)	C14—C15—H152	109.6 (14)
O5—C5A—C9A	121.25 (16)	C16—C15—H152	107.3 (14)
C6—C5A—C9A	121.85 (16)	H151—C15—H152	109 (2)
C7—C6—C5A	118.55 (18)	C4—C16—C15	112.4 (2)
C7—C6—H61	123.5 (12)	C4—C16—H161	106.8 (13)
C5A—C6—H61	117.9 (12)	C15—C16—H161	110.5 (13)
O10—C7—C6	123.63 (18)	C4—C16—H162	110.4 (13)
O10—C7—C8	115.69 (17)	C15—C16—H162	110.8 (13)
C6—C7—C8	120.68 (18)	H161—C16—H162	105.7 (19)
C9—C8—C7	119.71 (19)	C18—N17—C2	120.09 (18)
C9—C8—H81	120.0 (13)	N17—C18—N20	118.0 (2)
C7—C8—H81	120.3 (13)	N17—C18—C19	123.8 (2)
C8—C9—C9A	121.1 (2)	N20—C18—C19	118.1 (2)
C8—C9—H91	120.6 (14)	C18—C19—H19A	109.5
C9A—C9—H91	118.2 (15)	C18—C19—H19B	109.5
C9—C9A—C5A	118.01 (18)	H19A—C19—H19B	109.5
C9—C9A—C9B	125.40 (18)	C18—C19—H19C	109.5
C5A—C9A—C9B	116.51 (16)	H19A—C19—H19C	109.5
C3A—C9B—N1	117.40 (17)	H19B—C19—H19C	109.5
C3A—C9B—C9A	119.39 (17)	C18—N20—C22	119.9 (2)
N1—C9B—C9A	123.18 (16)	C18—N20—C21	123.2 (2)
C7—O10—C11	117.49 (17)	C22—N20—C21	116.8 (2)
O10—C11—H11A	109.5	N20—C21—H21A	109.5
O10—C11—H11B	109.5	N20—C21—H21B	109.5
H11A—C11—H11B	109.5	H21A—C21—H21B	109.5
O10—C11—H11C	109.5	N20—C21—H21C	109.5
H11A—C11—H11C	109.5	H21A—C21—H21C	109.5
H11B—C11—H11C	109.5	H21B—C21—H21C	109.5
C4—C12—C13	112.2 (2)	N20—C22—H22A	109.5
C4—C12—H121	106.7 (13)	N20—C22—H22B	109.5
C13—C12—H121	109.2 (13)	H22A—C22—H22B	109.5
C4—C12—H122	110.2 (16)	N20—C22—H22C	109.5
C13—C12—H122	112.2 (16)	H22A—C22—H22C	109.5
H121—C12—H122	106 (2)	H22B—C22—H22C	109.5
C9B—N1—C2—N17	174.7 (2)	C4—C3A—C9B—N1	−176.95 (18)

C9B—N1—C2—S3	0.3 (2)	S3—C3A—C9B—N1	0.5 (2)
C9B—C3A—S3—C2	−0.26 (16)	C4—C3A—C9B—C9A	5.1 (3)
C4—C3A—S3—C2	176.97 (19)	S3—C3A—C9B—C9A	−177.50 (15)
N1—C2—S3—C3A	0.00 (17)	C2—N1—C9B—C3A	−0.5 (3)
N17—C2—S3—C3A	−174.98 (18)	C2—N1—C9B—C9A	177.41 (18)
C9B—C3A—C4—O5	−32.2 (3)	C9—C9A—C9B—C3A	−170.1 (2)
S3—C3A—C4—O5	150.85 (15)	C5A—C9A—C9B—C3A	13.4 (3)
C9B—C3A—C4—C12	−147.2 (2)	C9—C9A—C9B—N1	12.1 (3)
S3—C3A—C4—C12	35.9 (3)	C5A—C9A—C9B—N1	−164.47 (18)
C9B—C3A—C4—C16	86.2 (2)	C6—C7—O10—C11	−1.2 (3)
S3—C3A—C4—C16	−90.7 (2)	C8—C7—O10—C11	178.4 (2)
C3A—C4—O5—C5A	44.4 (2)	O5—C4—C12—C13	63.2 (3)
C12—C4—O5—C5A	165.17 (16)	C3A—C4—C12—C13	179.8 (2)
C16—C4—O5—C5A	−76.6 (2)	C16—C4—C12—C13	−53.0 (3)
C4—O5—C5A—C6	154.00 (16)	C4—C12—C13—C14	54.4 (3)
C4—O5—C5A—C9A	−30.6 (2)	C12—C13—C14—C15	−55.2 (3)
O5—C5A—C6—C7	177.88 (16)	C13—C14—C15—C16	55.1 (3)
C9A—C5A—C6—C7	2.6 (3)	O5—C4—C16—C15	−60.5 (2)
C5A—C6—C7—O10	179.29 (18)	C3A—C4—C16—C15	−178.52 (19)
C5A—C6—C7—C8	−0.3 (3)	C12—C4—C16—C15	53.5 (3)
O10—C7—C8—C9	178.4 (2)	C14—C15—C16—C4	−54.7 (3)
C6—C7—C8—C9	−2.0 (3)	N1—C2—N17—C18	45.0 (3)
C7—C8—C9—C9A	2.1 (4)	S3—C2—N17—C18	−140.69 (18)
C8—C9—C9A—C5A	0.1 (3)	C2—N17—C18—N20	−164.45 (19)
C8—C9—C9A—C9B	−176.4 (2)	C2—N17—C18—C19	18.9 (3)
O5—C5A—C9A—C9	−177.56 (18)	N17—C18—N20—C22	4.1 (3)
C6—C5A—C9A—C9	−2.4 (3)	C19—C18—N20—C22	−179.0 (2)
O5—C5A—C9A—C9B	−0.7 (3)	N17—C18—N20—C21	−179.9 (2)
C6—C5A—C9A—C9B	174.37 (17)	C19—C18—N20—C21	−3.1 (3)

Hydrogen-bond geometry (Å, °)

D—H···*A*	*D*—H	H···*A*	*D*···*A*	*D*—H···*A*
C19—H19B···O5^{i}	0.96	2.41	3.335 (3)	161
C6—H61···N1^{ii}	0.95 (2)	2.59 (2)	3.441 (3)	149.3 (15)

Symmetry codes: (i) *x*−1/2, −*y*+1/2, *z*+1/2; (ii) *x*+1/2, −*y*+1/2, *z*−1/2.

Fig. 1

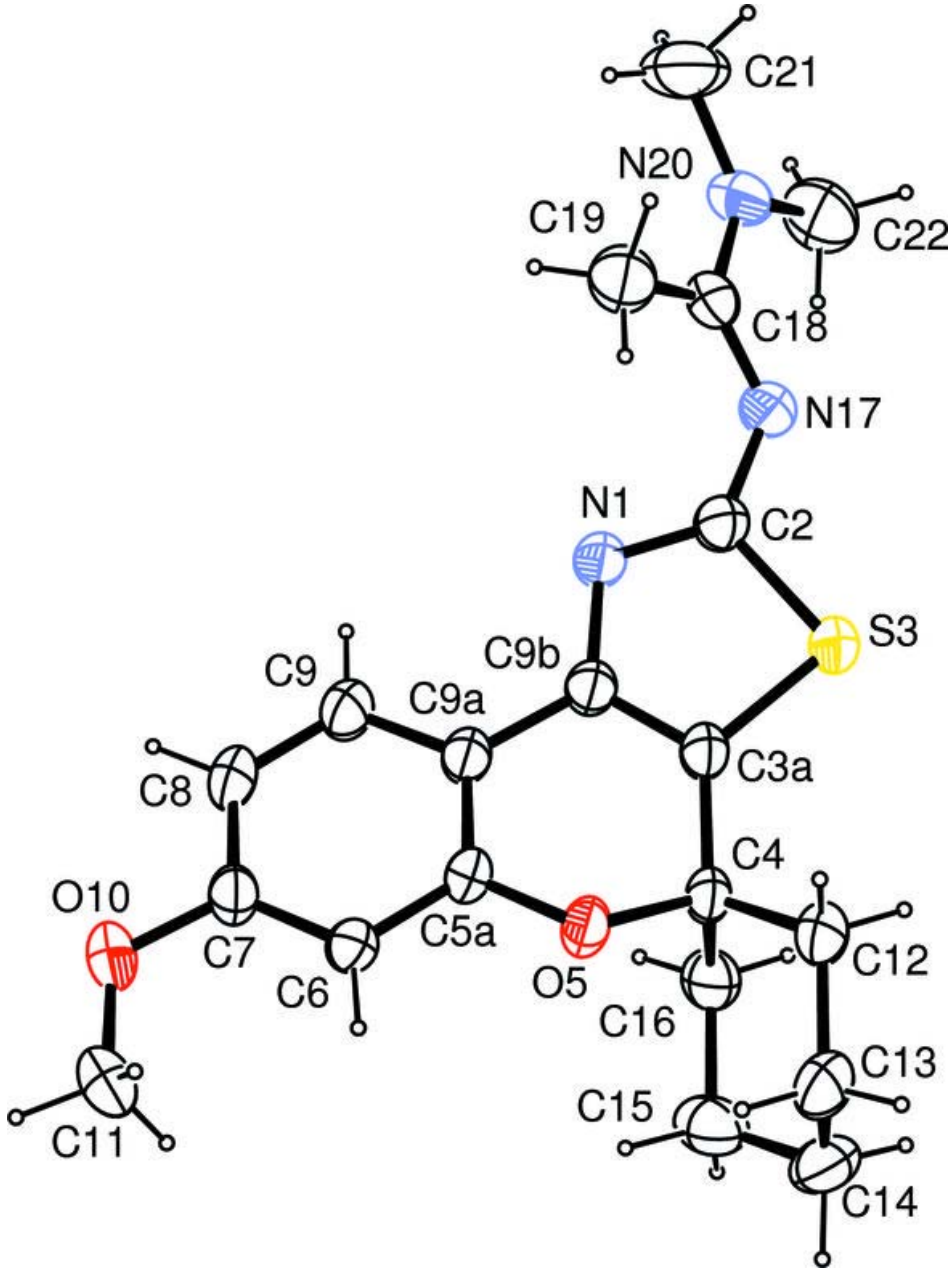

Fig. 2

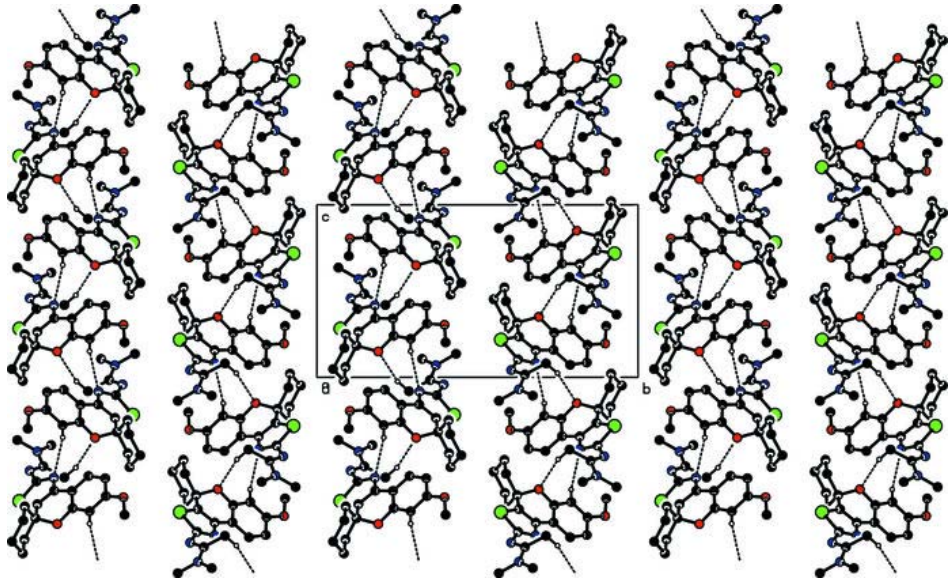

X-ray Structure Analysis Online

Cocrystallization of Two Tautomers: 1-Phenyl-3-(propan-2-yl)-1,2-dihydro-pyrazol-5-one and 1-Phenyl-3-(propan-2-yl)-1*H*-pyrazol-5-ol

Kamini KAPOOR,* Vivek K. GUPTA,* Rajnikant,*† Poorvesh M. VYAS, Mihir J. JOSHI,** Satish D. TADA,*** Satish M. SAROTHIA,*** H. S. JOSHI*****

**X-ray Crystallography Laboratory, Post-Graduate Department of Physics, University of Jammu, Jammu Tawi - 180 006, India*
***Physics Department, Saurashtra University, Rajkot - 360 005, Gujarat, India*
****Chemistry Department, Saurashtra University, Rajkot - 360 005, Gujarat, India*

Two different tautomeric forms, namely the *keto* [1-phenyl-3-(propan-2-yl)-1,2-dihydro-pyrazol-5-one] and the *enol* form, [1-phenyl-3-(propan-2-yl)-1*H*-pyrazol-5-ol], $C_{12}H_{14}N_2O{\cdot}2C_{12}H_{14}N_2O$, are present in the crystal in a 1:2 ratio. During crystallization, 1-phenyl-3-(propan-2-yl)-1,2-dihydro-pyrazol-5-one undergoes tautomerization to afford a corresponding *enol via* proton transfer reaction. The compound crystallizes in the triclinic space group $P\bar{1}$ with the following unit-cell parameters: a = 11.1593(3)Å, b = 11.2247(3)Å, c = 14.1140(4)Å, α = 73.333(3)°, β = 88.286(2)°, γ = 82.767(2)°, Z = 2. The crystal structure was solved by direct methods and refined by full-matrix least-squares procedures to a final R-value of 0.0405 for 4611 observed reflections. The dihedral angles between the mean planes through the phenyl ring and the pyrazole ring are: 28.04(5)°, 47.38(5)° and 49.32(6)° for molecules I, IIA, IIB, respectively. The crystal structure is stabilized by intermolecular N–H···N, O–H···O, O–H···N, C–H···O and C–H···π hydrogen bonds.

(Received July 28, 2011; Accepted August 22, 2011; Published on web October 10, 2011)

Pyrazoles are a class of heterocyclic compounds whose members exhibit a wide range of interesting biological properties *viz.* antibacterial,[1] insecticidal,[2] anticancer,[3] anti-HIV,[4] herbicidal[5] and anti-inflammatory[6] *etc.* and are quite useful to the pharmaceutical industry for new drug formulations. The biological properties of pyrazole derivatives have propitiated the development of synthesis methods for these, and also for precursors and analogous compounds. Considering the importance of pyrazole derivatives, it was thought to be worthwhile to synthesize a compound incorporating a pyrazole moiety. The compound has been synthesized by a mixture of methyl-isobutylacetate (0.01 mol) and phenylhydrazine (0.01 mol) in methanol (10 mL). In this reaction mixture, two drops of acetic acid were added and the solution was refluxed for 5 h. After completion of the reaction, the solvent was removed under vacuum, and the resulting solid was crystallized from methanol to afford crystals of suitable size for X-ray work. This compound undergoes tautomerism by proton transfer between

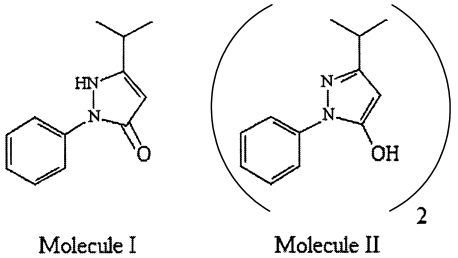

Fig. 1 Chemical structure of 1-phenyl-3-(propan-2-yl)-1,2-dihydro-pyrazol-5-one (molecule I) and 1-phenyl-3-(propan-2-yl)-1*H*-pyrazol-5-ol (molecule II).

Table 1 Crystal and experimental data

Chemical formula: $C_{12}H_{14}N_2O{\cdot}2C_{12}H_{14}N_2O$	
Formula weight = 606.76	
T = 293 K	
Crystal system: triclinic	Space group: $P\bar{1}$
a = 11.1593(3)Å	α = 73.333(3)°
b = 11.2247(3)Å	β = 88.286(2)°
c = 14.1140(4)Å	γ = 82.767(2)°
V = 1680.13(8)Å^3	Z = 2
D_x = 1.199 g/cm^3	D_m (floatation) = not measured
Radiation: Mo K_α (λ = 0.71073 Å)	
μ(Mo K_α) = 0.078 mm^{-1}	F(0 0 0) = 648
Crystal size = 0.3 × 0.2 × 0.1 mm^3	
No. of reflections collected = 23149	
No. of independent reflections = 5862	
θ range for data collection: 3.44 to 24.99°	
Data/Restraints/Parameters = 5862/0/542	
Goodness-of-fit on F^2 = 1.016	
R indices [$I > 2\sigma(I)$]: $R1$ = 0.0405, $wR2$ = 0.0966	
R indices (all data): $R1$ = 0.0556, $wR2$ = 0.1044	
$(\Delta/\sigma)_{max}$ = 0.001 for y H83	
$(\Delta\rho)_{max}$ = 0.194 eÅ^{-3}	$(\Delta\rho)_{min}$ = –0.188 eÅ^{-3}
Measurement: *X'calibur system—Oxford diffraction make*,	
Programs system: SHELXL-97, Crysalis *RED*	
Structure determination: SHELXS-97	
CCDC deposition number: 824525	

† To whom correspondence should be addressed.
E-mail: rkvk.paper11@gmail.com

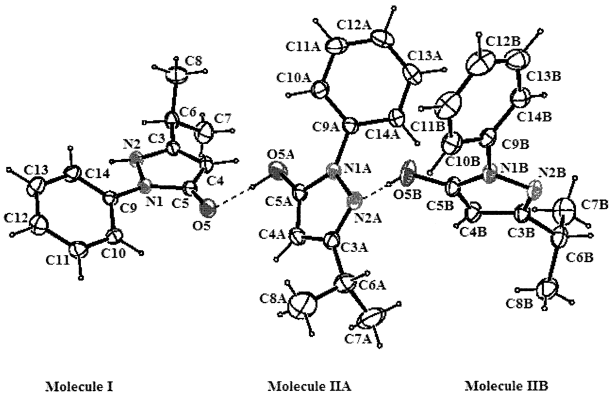

Fig. 2 *ORTEP* view of the molecules, showing the atom-labeling scheme. Displacement ellipsoids are drawn at the 40% probability level and H atoms are shown as small spheres of arbitrary radii.

the hydroxyl O atom and the N2 atom forming two tautomers, *keto* form (molecule I) and *enol* form (molecule II) (Fig. 1), and the two different tautomeric forms of the same molecule cocrystallized in a 1:2 ratio.

The crystallographic data are summarized in Table 1.

An ORTEP view of all the three molecules[8] [molecule I (*keto* form); molecule IIA and IIB (*enol* form with two independent molecules in the asymmetric unit)] is shown in Fig. 2. Selected bond lengths, bond angles and torsion angles are given in Table 2. When compound I undergoes tautomerisation during crystallization to afford corresponding *enol* via proton transfer reaction, an appreciable decrease in the N2–C3 and C4–C5 distance is observed [N2–C3 = 1.346(2)Å *versus* N2A–C3A = 1.326(2)Å; N2B–C3B = 1.327(2)Å and C4–C5 = 1.411(2)Å *versus* C4A–C5A = 1.368(2)Å; C4B–C5B = 1.368(2)Å]. A concomitant increase in the C3–C4 and C5–O5 distance has also been observed [C3–C4 = 1.366(2)Å *versus* C3A–C4A = 1.397(2)Å; C3B–C4B = 1.399(2)Å and C5–O5 = 1.261(2)Å *versus* C5A–O5A = 1.326(2)Å; C5B–O5B = 1.325(2)Å]. Hence the above-mentioned C–C, C–N, and C–O bond lengths (Table 2) help to establish the *keto* form of molecule I and the *enol* form of molecule IIA and molecule IIB, respectively. In addition, the magnitude of planarity for the molecules in *keto* and *enol* forms is different. The pyrazole and the phenyl rings are inclined at an angle of 28.04(5)° in molecule I, 47.38(5)° in molecule IIA and 49.32(6)° in molecule IIB.

The six C–C bond lengths in the phenyl ring lie in the range 1.378(2)Å – 1.386(2)Å, molecule I; 1.370(3)Å – 1.387(2)Å, molecule IIA; 1.371(3)Å – 1.390(3)Å, molecule IIB. The pyrazole ring and the phenyl ring are individually planar with maximum deviations from the respective least-squares planes of: –0.023(1)Å for C5 and –0.008(2)Å for C14 (molecule I); –0.004(2)Å for C3A and –0.008(2)Å for C14A (molecule IIA); 0.006(1)Å for C3B and 0.011(2)Å for C14B (molecule IIB). Both intrá- and intermolecular hydrogen bonds are found in the crystal structures of the tautomers. The two tautomers are connected *via* intermolecular N–H···N, O–H···O, O–H···N and C–H···O hydrogen bonds. Despite the rich availability of aryl rings, there are no aromatic π-π stacking interactions in the structure. However, C–H···π hydrogen bonds are present. Details of N–H···N, O–H···O, O–H···N, C–H···O and C–H···π hydrogen bonds are given in Table 3S.

Table 2 Selected bond lengths (Å), bond angles (°) and torsion angles (°) for non hydrogen atoms (e.s.d.'s are given in parentheses)

	Molecule I	Molecule IIA	Molecule IIB
N1-N2	1.382(1)	1.377(1)	1.384(1)
N2- C3	1.346(2)	1.326(2)	1.327(2)
C3-C4	1.366(2)	1.397(2)	1.399(2)
C4-C5	1.411(2)	1.368(2)	1.368(2)
N1- C5	1.387(2)	1.358(2)	1.352(2)
C5 -O5	1.261(2)	1.326(2)	1.325(2)
C3- N2- N1	108.4(1)	105.6(1)	104.7(1)
C5 -N1 -N2	108.6(1)	110.3(1)	110.8(1)
C5 -N1 -C9	130.0(1)	129.3(1)	127.0(1)
N2 -N1 -C9	119.6(1)	120.3(1)	121.1(1)
O5 -C5 -N1	122.4(1)	119.1(1)	118.8(1)
N1 -C5 -C4	105.5(1)	107.3(1)	107.4(1)
N2 -C3 -C4	108.9(1)	110.9(1)	111.5(1)
N2 -C3 -C6	119.1(1)	120.2(1)	121.2(1)
C5 -N1 - C9 -C10	-38.0(2)	49.2(2)	54.7(2)
N2 - N1 - C9 - C10	159.0(1)	-133.7(1)	-138.1(1)
N2 - N1 - C9 - C14	-19.8(2)	45.8(2)	42.8(2)
C4 - C3 - C6 - C7	-82.4(2)	75.0(2)	69.2(2)
N2 - C3 - C6 - C8	-142.3(2)	128.9(2)	125.4(2)

In conclusion, a crystal structure of a pyrazole derivative has been determined by X-ray crystallographic techniques. Two different tautomeric forms are found in the solid state, and these are hydrogen bonded to one another.

Acknowledgements

One of the authors (Rajnikant) acknowledges the Department of Science & Technology for single crystal X-ray diffractometer sanctioned as a National Facility under Project No. SR/S2/CMP-47/2003. He is also thankful to UGC for research funding under a research project F. No. 37-4154/2009 (J & K) (SR).

References

1. A. Tanitame, Y. Oyamada, and K. Ofuji, *J. Med. Chem.*, **2004**, *47*, 3693.
2. Y. Kondo, T. Kiji, M. Noguchi, and Y. Manabe, Jpn. Kokai Tokkyo Koho JP 08, 311, 036, Chem Abstr., **1997**, *126*, 89367r.
3. D. Berta, E. Felder, A. Valpetti, and M. Villa, PCT Int. Appl. WO 02 62804 (Cl.CO7D498/04; Chem Abstr., **2002**, *137*, 169517g.
4. S. D. Bhardwaj and V. S. Jolly, *Oriental J. Chem.*, **1996**, *12(2)*, 185 (Eng.); Chem. Abstr. **1997**, *126*, 1442174.
5. Siddal, T. Lyman, B. Zaltan, and G. Gail, PCT Int. Appl. WO 98, 52, 926, Chem Abstr., **1999**, *130*, 25068u.
6. A. Kumar, R. S. Verma, and B. P. Jagu, *J. Ind. Chem. Soc.*, **1990**, *67*, 120.
7. G. M. Sheldrick, *Acta Cryst.*, **2008**, *A64*, 112.
8. L. J. Farrugia, *J. Appl. Cryst.*, **1997**, *30*, 565.

www.crt-journal.org

Crystal Research and Technology

Journal of Experimental and Industrial Crystallography
Zeitschrift für experimentelle und technische Kristallographie

WILEY-VCH

Cryst. Res. Technol. **47,** No. 7, 763–770 (2012) / **DOI** 10.1002/crat.201100536

Synthesis and characterization of 1-phenyl-3-(propan-2-yl)-1*H*-pyrazol-5-ol single crystals

P. M. Vyas*[1], J. D. Akbari[2], S. D. Tada[2], H. S. Joshi[2], and M. J. Joshi[1]

[1] Crystal Growth Laboratory, Department of Physics, Saurashtra University, Rajkot–360 005, Gujarat, India
[2] Department of Chemistry, Saurashtra University, Rajkot–360 005, Gujarat, India

Received 10 November 2011, revised 24 February 2012, accepted 10 April 2012
Published online 6 June 2012

Key words Solution Growth, X–Ray diffraction, TG–DTA–DSC, Dielectric Study.

The synthesis of pyrazoles and its derivatives remains of great interest due to their wide applications in pharmaceutical and agrochemical industry. The 1-phenyl-3-(propan-2-yl)-1*H*-pyrazol-5-ol was synthesized. The 1-phenyl-3-(propan-2-yl)-1*H*-pyrazol-5-ol single crystals were grown by slow solvent evaporation technique using mixture of chloroform and methanol as a solvent. Yellowish and transparent crystals having maximum dimensions of 0.005 m × 0.004 m × 0.002 m were grown. The crystals were characterized by powder XRD, FT–IR, TG–DTA–DSC and dielectric study. The crystals remained stable up to 160 °C and then start decomposing. The DSC suggested both endothermic and exothermic reactions. One broad exothermic peak was observed at 558.1 °C due to complete decomposition of the sample into the gaseous phase and reaction within the products. Thermodynamic and Kinetic parameters of decomposition were calculated by Coats–Redfern formula. The dielectric study was carried out in the frequency range from 50 Hz to 5 MHz at room temperature. The dielectric constant decreased as the frequency of the applied field increased. The variations of dielectric loss, a.c. conductivity and a.c. resistivity also studied with the frequency of the applied field. Jonscher's power law was verified for a.c. conductivity.

1 Introduction

The synthesis of pyrazoles remains of great interest due to the wide applications of such heterocycles in the pharmaceutical and agrochemical industry. Pyrazole derivatives were reported to possess significant antibacterial [1], p - 38α MAP kinase inhibitory [2], monoamine oxidase inhibitory [3], insecticidal [4], anticancer [5], anti–HIV [6], herbicidal [7], etc. activities. This gave a great impact to search for potential pharmacologically active drugs carrying pyrazole substituent. Pyrazolyl pyrazolone derivatives were found to possess potent activities such as anti-inflammatory [8], antimicrobial [9], antiallergic [10], antidiabetic [11], cardio–vascular [12], diuretic [13,14], antioxidant agent [15] and brain connabinoid receptor (CB1) [16].

Several physical and spectroscopic characterizations are important for pharmaceutical compounds and crystals for determining their thermal stability, shelf–life, reactivity and their production point of view. Thermogravimetry is used for pharmaceutical compounds as well as crystals for assessing thermal stability and content of water either in moisture form or in crystallization form. Using DSC a polymorph of compound can be predicted. Moreover, DSC can be used for determination of solid–solid transition occurring before melting, melting point of compound and associated moisture. Dielectric properties relate to the ability of a material to polarize under the influence of an electric field. The polarizability of the materials depends on the structure and molecular properties, therefore, the dielectric study can provide informations on these terms. The application of dielectric study for pharmaceuticals are mainly focused of four aspects; analysis of water, estimation of molecular mobility, estimation of the distribution of materials throughout the system and general formulation characterization [17]. Generally, crystallization is carried out in the final stage during the manufacture of active pharmaceutical ingredients (API),

* Corresponding author: e-mail: pm_crystal123@yahoo.co.in

Fig. 1 Grown single crystals.

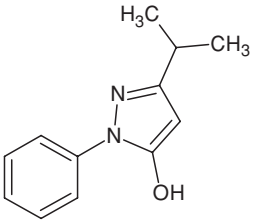

Fig. 2 Molecular structure.

that is, the drug substance. Moreover, the structure based approach requires effectively designed and commercially viable crystalline substances for optimal drug performance.

Considering various applications of pyrazolyl pyrazolone derivates, in the present study the authors have synthesized 1-phenyl-3-(propan-2-yl)-1*H*-pyrazol-5-ol and attempted to grow its single crystals. As many properties are governed by the crystalline nature the grown crystals were characterized by using powder XRD, FT–IR spectroscopy, TG–DTA–DSC, thermodynamic and kinetic parameters for decomposition process and dielectric study. Moreover, the 1-phenyl-3-(propan-2-yl)-1*H*-pyrazol-5-ol crystals show tautomerism in two forms, i.e. keto and enol, which is reported by the present authors in a collaborative manner elsewhere[18]. It has been reported earlier that enol form shows good antimicrobial activity compared to keto form by one of the present authors [19].

2 Experimental

2.1 Synthesis of material and crystals 1-phenyl-3-(propan-2-yl)-1H-pyrazol-5-ol has been synthesized by a mixture of methyl-isobutyl acetate (0.01 mole) and phenyl hydrazine (0.01 mole) in methanol (10 ml). In this mixture two drops of acetic acid were added and the solution was reflux for 5 h. After completion of the reaction, the solvent was removed under vacuum and the resulting solid was air dried in to a powder form, which was used for the further growth of single crystals. All AR grade chemicals were used for the synthesis. For the growth of single crystals, the synthesized material was dissolved in the mixture of chloroform and methanol, in the ratio of chloroform: methanol selected 8: 2, as a solvent after trying different organic solvents. The growth of 1-phenyl-3-(propan-2-yl)-1*H*-pyrazol-5-ol crystals was carried out by using slow solvent evaporation technique. Glass container of 50 ml was selected as crystallization apparatus containing saturated solution of 1-phenyl-3-(propan-2-yl)-1*H*-pyrazol-5-ol, this was covered by lid to allow slow and controlled evaporation of solvent. This was placed in a constant temperature water bath of accuracy $\pm$ 0.01 °C. After the 20 days yellowish, transparent, crystals were grown having maximum dimensions 0.005 m $\times$ 0.004 m $\times$ 0.002 m, which are shown in figure 1. Figure 2 shows the molecular structure of 1-phenyl-3-(propan-2-yl)-1*H*-pyrazol-5-ol.

2.2 Characterizations The 1-phenyl-3-(propan-2-yl)-1*H*-pyrazol-5-ol crystals were characterized by powder XRD using PHILIPS X'Pert system using Cu K_α radiation and the data were analyzed by using computer software powder X. The FT–IR spectrum was recorded for powdered samples by employing Thermo Nicolet–6400 spectrophotometer within the frequency range from 400 cm^{-1} to 4000 cm^{-1} in KBr medium. The simultaneous TG–DTA–DSC was carried out on Linseis STA PT - 1600 set up from room temperature to 900 °C at a heating rate of 15 K/min. The dielectric measurements were carried out on pelletized crystalline powder samples at room temperature by using HIOKI 3532 LCR HITESTER, in the frequency range from 50 Hz–5 MHz.

3 Results and Discussion

There are varieties of organic molecular crystals grown and characterized, for example, some recent work on 4-(2-hydroxyphenylamino)–pent-3en–2–one (HPAP) single crystals [20], bis [2-(5-trifluoromethyl-3-ferrocenyl) pyrazolyl] methane single crystals for its metal to ligand charge transfer properties in UV - Visible range [21]. Several pyrazole based compounds have been successfully synthesized and their structures are solved by X–Ray diffraction techniques, for instance, ethyl 1–(4–chlorobenzyl)-3–(4–flurophenyl)-

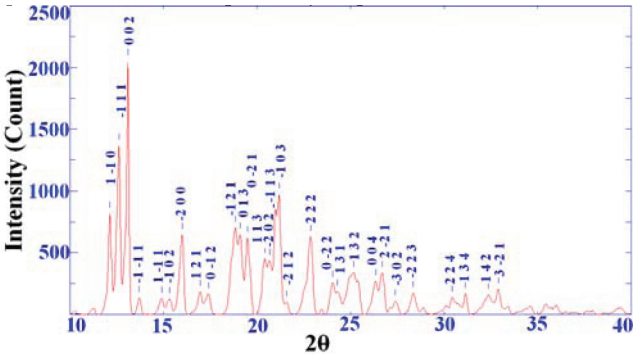

Fig. 3 Powder XRD pattern of 1-phenyl-3-(propan-2-yl)-1*H*-pyrazol-5-ol crystals.

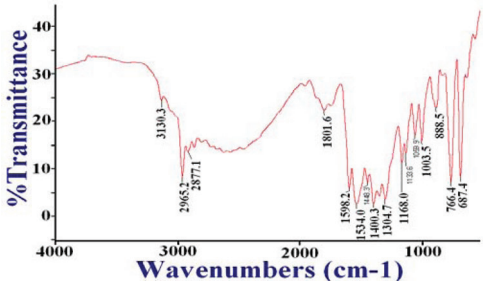

Fig. 4 FT–IR Spectrum of 1-phenyl-3-(propan-2-yl)-1*H*-pyrazol-5-ol crystals.

1H-pyrazole–5–carboxylate [22], ethyl–1–(4-methoxybenzyl)–3–p–tolyl–1H-pyrazole–5–carboxylate [23], 1-(2,4-dinitrophenyl)–3-(2-hydroxyphenyl)-1H-pyrazole-4–carbaldehyde [24] and 4–(1,3–Diphenyl–1H–Pyrazol–5- yl) pyridine [25]. Several metal compounds of pyrazole based ligands have been studied for various applications such as low temperature antiferromagnetic properties of manganese–pyrazole ligands [26], Palladium and platinum pyrazole based ligands for catalytic activity [27] and silver pyrazole complexes with tunable liquid crystals and luminescent properties having electro optic devices applications [28]. Various characterization studies of 1-phenyl-3-(propan-2-yl)-1*H*-pyrazol-5-ol crystal are reported hereby.

3.1 Powder X–Ray Diffraction Study The single crystal X–Ray Diffraction study was carried out on good quality single crystals of 1-phenyl-3-(propan-2-yl)-1*H*-pyrazol-5-ol by Kapoor et al. [18]. In order to study the crystalline nature and obtain the unit cell parameters the powder XRD study was carried out on 1-phenyl-3-(propan-2-yl)-1*H*-pyrazol-5-ol crystals. Figure 3 shows the powder XRD pattern of 1-phenyl-3-(propan-2-yl)-1*H*-pyrazol-5-ol. The crystal structure was solved by using software powder X. All major reflections in the XRD pattern were fitted and assigned the corresponding planes. The 1-phenyl-3-(propan-2-yl)-1*H*-pyrazol-5-ol crystals exhibited triclinic system with the estimated unit cell parameters as, a = 11.1593 Å, b = 11.2247 Å, c = 14.1140 Å, $\alpha = 73.333^\circ$, $\beta = 88.286^\circ$, $\gamma = 82.767^\circ$, which corresponds to the values reported by Kapoor et al. [18].

3.2 FT–IR Study Figure 4 shows the FT–IR spectrum of 1-phenyl-3-(propan-2-yl)-1*H*-pyrazol-5-ol crystals. There are mainly three groups of absorption alkane (- CH_3), aromatic substitution and pyrazole observed. The detailed analysis of the spectrum is given in table 1.

3.3 TG–DTA–DSC Thermal study of different pyrazole compounds have been reported by several authors [29,30]. The thermal decomposition behavior of 1-phenyl-3-(propan-2-yl)-1*H*-pyrazol-5-ol was similar to the reported other pyrazole based compounds. Figure 5 shows the thermo-gram of 1-phenyl-3-(propan-2-yl)-1*H*-pyrazol-5-ol crystalline powder. The TG plot shows that the sample remains stable up to 160 °C and then it starts decomposing rapidly up to 280 °C and beyond that it decomposes slowly up to 610 °C, where complete decomposition is observed. The DTA plot indicates that the decomposition process of 1-phenyl-3-(propan-2-yl)-1*H*-pyrazol-5-ol occurs through an endothermic reaction at 105.2 °C and two exothermic peaks observed at 278.2 °C and 558.1 °C, respectively. From the DSC plot several thermodynamic parameters were calculated by using the software TA evaluation available with the set up. For the first endothermic reaction

Table 1 Analysis of FT–IR Spectrum.

Type	Validation Mode	Frequency (cm^{-1})
Alkane–CH_3	C–H stretching (asym.)	2965.2
	C–H Stretching (sym.)	2877.1
	C–H in plane bending (asym.)	1448.3
	C–H out of plane bending (sym.)	1400.3
Aromatic	C–H stretching	3130.3
	C = C (skeleton)	1534.0
	C–H in plane bending	1003.5
	C–H out of plane bending	888.5
Pyrazole	= N–N–	1133.6
	- C = O stretching	1801.6

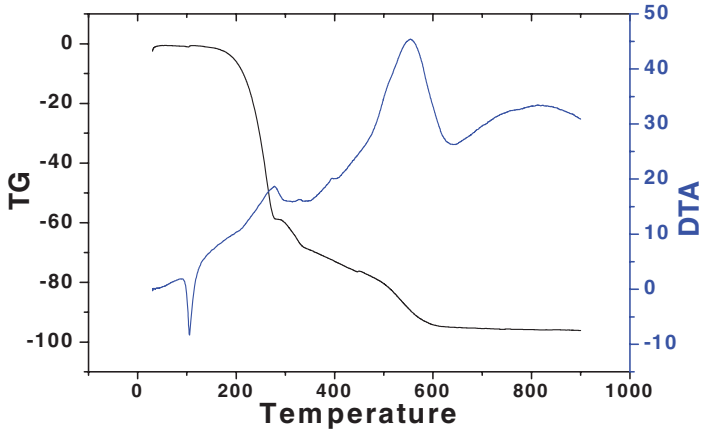

Fig. 5 TG–DTA of 1-phenyl-3-(propan-2-yl)-1*H*-pyrazol-5-ol crystals.

at 105.2 °C the enthalpy and the change in heat capacity are calculated and found to be −119964.9 J/kg and 866.9 J/kgK, respectively. This may be due to some phase change occurring without significant breaking of the bonds resulting into marginal weight loss, which may be due to melting of a sample. The melting point of 1-phenyl-3-(propan-2-yl)-1*H*-pyrazol-5-ol is 90 °C. After the endothermic reaction, minor exothermic reaction is observed at 278.2 °C and values of the enthalpy and the change in heat capacity are found to be 77457.6 J/kg and 1362.4 J/kgK, respectively. Similarly, the second exothermic reaction occurring at 558.1 °C, may be due to complete decomposition of the sample into the gaseous phase and reaction within the products. For this reaction values of the enthalpy and the change in heat capacity are found to be 2636717 J/kg and 10891.7 J/kgK, respectively.

3.4 Thermodynamic and Kinetic Parameters In the present study, authors evaluate the thermodynamic and kinetic parameters for the decomposition of the 1-phenyl-3-(propan-2-yl)-1*H*-pyrazol-5-ol at 200 °C, i.e., the on set of decomposition, using the thermo-gram data. There are many mathematical relations available to evaluate kinetic parameters for dehydration and decomposition from thermo-gram [31,32]. The kinetic parameters of decomposition process of 1-phenyl-3-(propan-2-yl)-1*H*-pyrazol-5-ol were calculated by using Coats and Redfern relation [32]:

$$\log_{10}\left(\frac{1-(1-\alpha)^{1-n}}{(1-n)\,T^2}\right) \approx \left[\log 10\left(\frac{AR}{\alpha E}\right)\left(1-\frac{2RT}{E}\right)-\left(\frac{E}{2.3RT}\right)\right] \quad (1)$$

Where, $\alpha = (W_0 - W) / (W_0 - W_f)$, W_0 = Initial weight, W = Weight at time t, W_f = Final weight, n = Order of reaction, A = Frequency factor, E = Activation energy of the reaction, R = Gas constant and a = Heating rate.

To determine the kinetic parameters, a plot of $\log_{10}$ $[\{1-(1-\alpha)^{1-n}\}/\ \{T^2\ (1-n)\}]$ versus 1/T is drawn for different values of order of reaction (n). The best linear fit gives the correct value of n and the value of activation energy can be calculated by using the slope of linear plot. Figure 6 shows the linear plot for Coats and Redfern

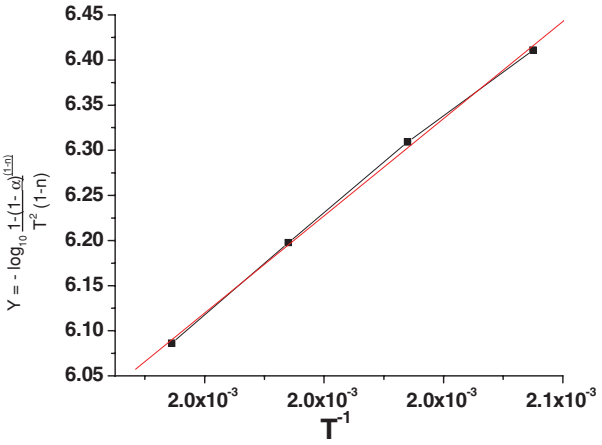

Fig. 6 Plot of Coats–Redfern relation for 1-phenyl-3-(propan-2-yl)-1*H*-pyrazol-5-ol crystals.

Table 2 Kinetic and Thermodynamic parameters of 1-phenyl-3-(propan-2-yl)-1*H*-pyrazol-5-ol crystals by using C–R relation.

Kinetic Parameters		Thermodynamic Parameters	
Order of Reaction (n)	0	Standard Change in Entropy ($\Delta^{\#}S^0$)	114.10 $JK^{-1}mol^{-1}$
Activation Energy (E)	51.54 $kJK^{-1}mol^{-1}$	Standard Change in Enthalpy ($\Delta^{\#}H^0$)	43.34 $kJmol^{-1}$
Frequency Factor (A)	9.36×10^{18}	Standard Change in Gibbs free energy ($\Delta^{\#}G^0$)	-12.90 $kJmol^{-1}$

relation for 1-phenyl-3-(propan-2-yl)-1*H*-pyrazol-5-ol. Table 2 shows the values of different kinetic parameters, viz., Order of Reaction, Frequency Factor and Activation Energy.

The thermodynamic parameters of decomposition have been evaluated for the sharp decomposition stage at 200 °C by using the formulae discussed by Laidler [33].

The Standard Change in Entropy is calculated by the relation,

$$\Delta^{\#}S^0 = 2.303 \times R \times \log_{10}\left[\frac{Ah}{kT_m}\right] \tag{2}$$

Where, k = Boltzmann constant, h = Planck's constant, T_m = Temperature and A = Frequency Factor

The Standard change in Enthalpy can be calculated by,

$$\Delta^{\#}H^0 = E - 2RT \tag{3}$$

The Standard Change in Gibbs free energy is calculated as,

$$\Delta^{\#}G^0 = \Delta^{\#}H^0 - T\Delta^{\#}S^0 \tag{4}$$

Table 2 shows the values of different thermodynamic parameters calculated for the sharp stage of decomposition at 200 °C, this temperature indicates the onset of precipitous decomposition process. The positive value of standard change in entropy ($\Delta^{\#}S^0$) and standard change in enthalpy ($\Delta^{\#}H^0$) as well as the negative value of standard change in Gibbs free energy ($\Delta^{\#}G^0$) suggest that the reaction will be spontaneous at higher temperatures [34].

3.5 Dielectric Study Dielectric study of Active Pharmaceutical Ingredients (API), amino acids and carbohydrates has been reported [35]. The dielectric study of amorphous pharmaceutical drugs has been reported in correlation with molecular mobility and isothermal crystallization kinetics [36]. A broadband dielectric spectroscopic study of Verapamil Hydrochloride (VH), a calcium channel blocker by Adrjanowicz et al. [37] is carried out to understand its molecular dynamics. Usually there are four contributions playing important role in the value of dielectric constant (ε'); which are from electronic, ionic, dipolar and space-charge polarizations. However, all these may be active in low frequency region. The nature of the variation of ε' with frequency suggests which contribution is prevailing. The space-charge contribution depends on the purity and perfection

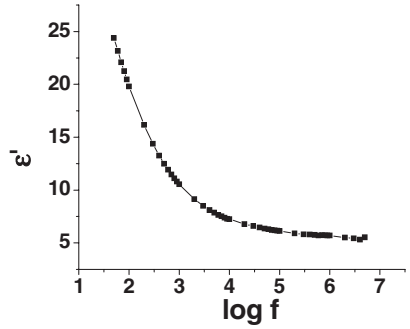

Fig. 7 plot of Dielectric Constant versus log f.

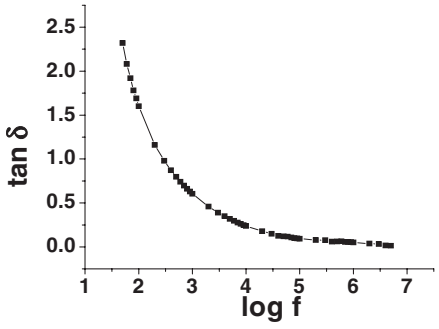

Fig. 8 plot of Dielectric loss versus log f.

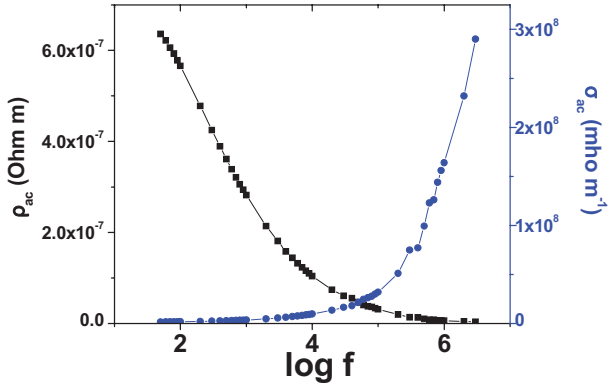

Fig. 9 Plot of a. c. conductivity and a. c. resistivity versus log f.

of the crystal. The dipolar orientational effect can be seen up to 10^{10} Hz. Moreover, the ionic and electronic polarizations always exist below 10^{13} Hz [38]. Figure 7 shows the variation of ε' with frequency of applied field. The dielectric constant decreases rapidly as frequency increases. The nature of the plot in the figure 7 suggests that the space-charge polarization is active in low frequency region, which is reflected in terms of rapid decrease in the value of dielectric constant with increase in frequency. This also further suggests that the dipoles can not comply with the varying field and hence the decreasing nature is exhibited, which is a common feature in 4-(2-hydroxyphenylamino)-pent-3-en-2-one [20] and zinc tartrate crystals [39]. More-or-less, the same type of nature is observed for the variation of dielectric loss (tan δ) with the frequency of applied field as shown in the figure 8. Recently, an a.c. conductivity and dielectric constant measurements of bulk pyronine G (Y) is reported by Yaghmour [40]. The author observed that the dielectric constant and dielectric loss decreased by increasing frequency and the a.c. conductivity was due to the correlated barrier hopping.

Usually, typical current carriers in organic solids are through π- conjugated systems and the electrons can move via π-electron cloud, especially, by hopping, tunneling and other related mechanisms. Figure 9 shows that the a. c. conductivity σ_{ac} increases as the frequency increases and the opposite nature is observed for a. c. resistivity. In case of the a. c. conductivity if the angular frequency of applied field is represented as

$$\omega = 2\pi\upsilon \tag{5}$$

The Jonscher's equation [41,42] can be written as follows,

$$\sigma_{ac}(\omega, \mathrm{T}) = \sigma_{dc}(\mathrm{T}) + \mathrm{a}(\mathrm{T})\omega^n \tag{6}$$

Where, σ_{dc}(T) (or static, $\omega = 0$) is the dc conductivity due to excitation of electrons from a localized state to the conduction band, a(T)ω^n is the ac conductivity due to the dispersion phenomena occurring in the material, a(T) is a temperature dependent constant and n is the power law exponent, which generally varies between 0 and 1 depending on temperature. The exponent n represents the degree of interaction between mobile ions with the

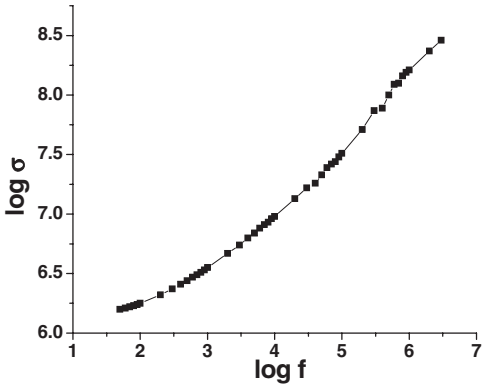

Fig. 10 Plot of a. c. conductivity versus log f.

lattice around them. A typical frequency dependence of conductivity spectrum shows three distinguish regions, namely, (a) low frequency dispersion, (b) an intermediate frequency plateau and (c) an extended dispersion at high frequency. Figure 10 shows plot of log σ_{ac} versus log f which shows that as the frequency increases conductivity increases. The exponent n is calculated from the slope of the plot for room temperature, which is 0.6, from this we conclude that a. c. conductivity follows Jonscher's power law.

4 Conclusion

The crystals of 1-phenyl-3-(propan-2-yl)-1*H*-pyrazol-5-ol were grown by slow solvent evaporation technique. Pale yellowish and transparent crystals were grown. The powder XRD analysis suggested that crystals were having triclinic crystal system with the unit cell parameters as, a = 11.1593 Å, b = 11.2247 Å, c = 14.1140 Å, $\alpha = 73.333^\circ$, $\beta = 88.286^\circ$, $\gamma = 82.767^\circ$. The FT–IR study confirmed the presence of C–H, C = C, N–N and C = O stretching. The TG analysis indicated that the sample remained stable up to 160 °C and then decomposed rapidly up to 280 °C, thereafter; it decomposed slowly up to 610 °C. The DTA and DSC study showed an endothermic peak at 105.2 °C may be due to melting of a substance, while the exothermic reactions were observed at 278.2 °C and 558.1 °C may be due to decomposition of the sample and reaction within the gaseous phase. Dielectric study of 1-phenyl-3-(propan-2-yl)-1*H*-pyrazol-5-ol indicated that as the frequency increased the dielectric constant, dielectric loss and a. c. resistivity decreased while a. c. conductivity increased. At room temperature the Jonscher's power law was followed by a.c. conductivity.

Acknowledgments The authors are thankful to UGC, New Delhi, for the SAP. The authors are thankful to State Government of Gujarat for providing financial assistance to develop characterization facilities and Prof. H.H. Joshi (HOD of Physics Dept.), Prof. P.H. Parsania (HOD of Chemistry Dept.) for their keen interest. The author (PMV) is thankful to UGC, New Delhi, for JRF under Meritorious Research Students Scheme.

References

[1] A. Tanitame, Y. Oyamada, K. Ofuji, M. Fujimoto, N. Iwai, Y. Hiyama, K. Suzuki, H. Ito, H. Terauchi, M. Kawasaki, K. Nagai, M. Wachi, and J. Yamagishi, J. Med. Chem. **47**, 3693 (2004).
[2] A. L. Gill, M. Frederickson, A. Cleasby, S. J. Woodhead, M. G. Carr, A. J. Woodhead, M. T. Walker, M. S. Congreve, L. A. Devine, D. Tisi, M. O'Reilly, L. C. A. Seavers, D. J. Davis, J. Curry, R. Anthony, A. Padova, C. W. Murray, R. A. E. Carr, and H. Jhoti, J. Med. Chem. **48**, 414 (2005).
[3] F. Chimenti, A. Bolasco, F. Manna, D. Secci, P. Chimenti, O. Befani, P. Turini, V. Giovannini, B. Mondovi, R. Cirilli, and F. La Torre, J. Med. Chem. **47**, 2071 (2004).
[4] T. Singh, S. Sharma, V. K. Srivastava, and A. Kumar, Archiv der Pharma. **339**, 24 (2006).
[5] I. Bouabdallah, L. A. M'Barek, A. Zyad, A. Ramdani, I. Zidane, and A. Melhaoui, Nat Prod Res. **20**, 1024 (2006).
[6] J. J. Vora, D. R. Patel, A. R. Patel, and Y. S. Patel, Asian J. of Biochem. & Pharm. Res. **1**, 108 (2011).
[7] H. G. McFadden, J. L. Huppatz, M. Couzens, C. H. L. Kennard, and D. E. Lynch, Pesticide Sci. **36**, 247 (1997).
[8] A. A. Bekhit, H. M. Ashour, Ael–D Bekhit, and S. A. Bekhit, Med Chem. **5**, 103 (2009).
[9] K. N. Sarma, M. C. S. Subbha, and K. C. Rao, Eur. J. of Chem. **7**, 745 (2010).

[10] M. T. Di Parsia, C. Suárez, M. J. Vítolo, V. E. Márquez, B. Beyer, C. Urbina, and I. Hurtado, J. Med Chem. **24**, 117 (1981).
[11] R. Soliman, J. Med. Chem. **22**, 321 (1979).
[12] M. M. Mohy El-Din, A. M. Senbel, A. A. Bistawroos, A. El-Mallah, N. A. Nour El-Din, A. A. Bekhit, and H. A. Abd El Razik, Basic Clin Pharmacol Toxicol. **108**, 263 (2011).
[13] A. Chauhan, P. K. Sharma, and N. Kaushik, Int. J. of Chemtech Res. **3**, 11 (2011).
[14] P. T. Chovatia, J. D. Akabari, P. K. Kachhadia, P. D. Zaalavadia, and H. S. Joshi, J. Serb. Chem. Soc. **71**, 713 (2007).
[15] J. Lertvorachon, J. P. Kim, D. V. Soldatov, J. Boyd, G. Roman, S. J. Cho, T. Popek, Y. S. Jung, P. C. K. Lau, and Y. Konishi, Bioorg. Med. Chem. **13**, 4627 (2005).
[16] R. Lan, Q. Liu, P. Fan, S. Lin, S. R. Fernando, D. McCallion, R. Pertwee, and A. Makriyannis, J. Med. Chem. **42**, 769 (1999).
[17] R. A. Storey and I. Ymèn, Solid State Characterization of Pharmaceuticals, (John Wiley & Sons Ltd, West Sussex, United Kingdom, 1988), p. 187
[18] K. Kapoor, V. Gupta, Rajnikant, P. M. Vyas, M. J. Joshi, S. D. Tada, S. M. Sorathia, and H. S. Joshi, X–ray Stru. Anal. Online **27**, 59 (2011).
[19] S. D. Tada, Studies on Heterocyclic Compounds of Medicinal Interest, (Ph. D. Thesis, Saurashtra University, India 2009).
[20] B. B. Parekh, D. H. Purohit, P. Sagayraj, H. S. Joshi, and M. J. Joshi, Cryst. Res. Technol. **42**, 407 (2007).
[21] Q. Zhang, W. L. Song, A. M. Showkot Hossain, Z. D. Liu, G. J. Hu., Y. P. Tian, J. Y. Wu, B. K. Jin, H. P. Zhou, J. X. Yang, and S. Y. Zhang, Dalton Trans. **40**, 3510 (2011).
[22] Y. Q. Ge, J. M. Zhang, G. L. Wang, H. Xu, and B. Shi, Acta Cryst.E **67**, O1387 (2011).
[23] C. X. Shi and Y. M. Xie, Acta Cryst. E **67**, O1084 (2011).
[24] S. S. S. Raj, J. Jeyakanthan, S. Selvi, D. Velumurugan, H. K. Fu, and P. T. Perumal, Acta Cryst. C **55**, 1667 (1999).
[25] T. N. Mahadeva Prasad, B. Raghava, M. A. Sridhar, K. S. Rangappa, and J. Shashidhara Prasad, X–Ray Stru. Anal. Online **26**, 75 (2010).
[26] M. V. Chumillas, M. G. Marqu, S. Tanase, M. Evangelisti, I. Mutikainen, U. Turpeinen, J. M. M. Smits, R. de Gelder, L. Jose de Jongh, and J. Reedijk, J. Phy. Chem. C **112**, 20525 (2008).
[27] J. A. Perez, J. Pons, X. Solans, M. Font–Bardia, and J. Ros, Inorganic Chimica Acta **358**, 617 (2005).
[28] M. J. Mayoral, P. Ovejero, J. A. Campo, J. V. Heras, M. R. Torres, C. Loderio, and M. Cano, New J. Chem. **34**, 2766 (2010).
[29] Z. K. Jacimovic, G. A. Bogdanovic, B. Hollo, V. M. Leovac, and K. M. Szecsenyi, J. Serb. Chem. Soc. **74**, 1259 (2009).
[30] K. M. Szecsenyi, V. M. Leovac, Z. K. Jacimovic, and G. Pokol, J. Ther. Anal. Calo. **74**, 943 (2003).
[31] A. H. Horowitz and B. G. Metzger, Anal. Chem. **35**, 1464 (1963).
[32] A. W. Coats and J. P. Redfern, Nature **201**, 68 (1964).
[33] K. J. Laidler, Chemical Kinetics, (Harper and Row, New York, 1987), p. 112.
[34] K. D. Parikh, D. J. Dave, B. B. Parekh, and M. J. Joshi, Bull. of Mater. Sci. **30**, 105 (2007).
[35] D. R. Mantheni, M. P. K. Maheswaran, H. F. Sobhi, N. I. Perea, A. T. Riga, M. E. Matthews, and K. Alexander, J. Term. Anal. Calorim., DOI: 10.1007/s10973-011-1423-y.
[36] J. Menegotto, J. Alie, C. Lacabanne, and M. Bauer, Dielectric News Lett. **19**, 1 (2004).
[37] K. Adrjanowicz, K. Kaminski, M. Paluch, P. Wlodarczyk, K. Grzybowska, Z. Wojnarowska, L. Hawelek, W. Sawicki, P. Lepek, and R. Lunio, J. of Pharma. Sci. **99**, 828 (2010).
[38] D. Enakshi and K. V. Rao, J. Mater. Sci. Lett **4**, 1298 (1985).
[39] R. M. Dabhi, B. B. Parekh, and M. J. Joshi, Ind. J. Phys. **79**, 503 (2005).
[40] S. J. Yaghmour, Eur. Phys. J. Appl. Phys. 49, 10402 (2010).
[41] A. K. Jonscher, Nature. **267**, 673 (1977).
[42] J. O. Lòpez and R. G. Aguilar, Rev. Mex. Fis. **49**, 529 (2003).

